



Thomson, Hannah (2023) *Ultrasonic differentiation of healthy and cancerous neural tissue*. PhD thesis.

<https://theses.gla.ac.uk/83670/>

Copyright and moral rights for this work are retained by the author

A copy can be downloaded for personal non-commercial research or study, without prior permission or charge

This work cannot be reproduced or quoted extensively from without first obtaining permission from the author

The content must not be changed in any way or sold commercially in any format or medium without the formal permission of the author

When referring to this work, full bibliographic details including the author, title, awarding institution and date of the thesis must be given

Enlighten: Theses

<https://theses.gla.ac.uk/>
research-enlighten@glasgow.ac.uk



Ultrasonic Differentiation of Healthy and Cancerous Neural Tissue

Hannah Thomson

Submitted in fulfilment of the requirements for the
Degree of Doctor of Philosophy (PhD)

School of Engineering

College of Science and Engineering

University of Glasgow

Centre for Medical and Industrial Ultrasonics

Author's Declaration

I, Hannah Thomson, hereby declare that this thesis entitled, "Ultrasonic Differentiation of Healthy and Cancerous Neural Tissue," submitted in partial fulfilment of the requirements of the University of Glasgow for the degree of Doctor of Philosophy represents my own work. No part of the work referred to in this thesis has been supported in application of another degree or qualification of this university or any other university or institute of learning.

Signed: Hannah Thomson

Date: 12/05/2023

Abstract

It is well documented that intraoperative ultrasound offers improvements to the extent of tumour resected in neurosurgery but currently fails to depict the boundaries of more invasive tumours. Quantitative ultrasound (QUS) is a technique that models ultrasound scattering in tissue mathematically. It can act as a quantitative tool to identify cancerous regions and be used to define features which can train a machine learning (ML) classifier. The use of QUS to differentiate healthy and malignant brain tissue is the objective of this thesis.

This work began with a proof of concept study which saw the effective implementation of QUS with a linear array transducer, at conventional frequencies, on phantom materials. The results were then used to train a K-nearest neighbours (KNN) binary classifier to differentiate between two soft tissues. Insight into the most practical parameters for near real time tissue identification was achieved, as well as the opportunity to produce parametric images for various QUS parameters. The effects of freezing and fixation of tissue on QUS results were also considered.

The experimental design was developed to obtain a higher lateral spatial resolution before applying it to *ex vivo* human samples of ten healthy and eight high-grade glioma (HGG) tissues. This was accomplished with both a linear array and a single element scanning system, at centre frequencies of 25 and 74 MHz, respectively. The SoS and attenuation were found to be higher, on average, in the tumour samples than in the healthy tissue. The homodyned K-distribution (HK) parameters alone could distinguish between healthy and HGG tissue to 96% accuracy at 74 MHz, suggesting this is a viable solution for residual HGG detection.

To explore the potential of ML with a larger data set, and to extend the study to low grade glioma (LGG) tissue, acoustic impedance maps based on 300 previously recorded microscope histology images of each tissue type were created. The interaction with high frequency (HF) ultrasound was explored using finite element analysis and QUS parameters were obtained. A classification algorithm was able to differentiate healthy and HGG to near perfect accuracy, but a significantly lower accuracy of 79% was found when distinguishing LGG from healthy tissue maps.

This research represents a step forward in the otherwise unexplored landscape of HF QUS in brain tissue which necessitates further work to transition from laboratory based experiments to *in vivo* QUS to aid intraoperative glioma detection.

Acknowledgement

I am, and will always be, grateful for the experience of being under the supervision of Professor Sandy Cochran. His scientific guidance, relentless support and encouragement kept me motivated and curious in my research, even when experiments became challenging. Combine this with his sense of humour and kindness made him truly the best supervisor I could have asked for.

I would also like to thank Dr Shufan Yang, whom I have considered as my 2nd supervisor throughout this journey- though this was never official! As well as her assistance in the machine learning aspects of the project, I would like to thank her on a personal level for her positivity and for pushing me to achieve a peer reviewed publication. This would not have been possible if not for you.

Thanks go to the staff of the Edinburgh Brain Bank who assisted in the process of obtaining the *ex vivo* tissue samples and supplied a source of microscope images for the simulation study in this thesis. I am grateful for the expertise and clinical guidance from my industrial supervisors from Stryker Medical devices: Mitch Baldwin and Thomas Stritch who spent many Friday afternoons with me discussing the latest challenges and how to solve them.

I am appreciative of everyone in the Centre for Medical and Industrial Ultrasonics at the University of Glasgow for creating an inclusive and friendly research environment. Particular thanks go to Dr Nicola Fenu, Dr Nathan Giles-Donovan, Dr Mat Wilkie and Lisa McMenamain with whom I have made lifelong friendships, blossoming from our (too!) frequent breaks from the office for second breakfasts and pub lunches. I would also like to thank Dr Mihnea Turcanu for his expertise with biological tissue despite my squeamishness and Dr Alex Moldovan for finally getting the Verasonics to listen to us.

I would like to give thanks to the mental health support team at the University of Glasgow as the support I received here made finishing my degree possible.

Finally, I would like to thank all my friends and family for helping me accomplish one of the most difficult challenges I have ever undertaken. Particularly, my mum who was simultaneously my number one supporter, often telling me to 'get my a*** in gear' (AIG), and my best friend, knowing exactly when to invite me for a walk with the dogs to clear my head. Plus, she is kindly proofreading this thesis, despite having no interest in ultrasound... or mathematics, so I had best put her in! I would like to thank my partner, Stuart for being my rock throughout this entire journey, despite me disappearing for weeks at a time to write.

Table of Contents

1	Introduction.....	1
1.1	Chapter Aim	1
1.2	Overview of Thesis	1
1.2.1	Current Standard of Care in Glioma Patients.....	1
1.2.2	Ultrasound Techniques.....	2
1.2.3	Introduction to QUS.....	3
1.3	Motivation	5
1.4	Thesis Aims and Objectives	6
1.5	Contributions to Knowledge	7
1.6	Thesis Structure.....	7
1.7	Publications Arising	8
1.7.1	Peer Reviewed.....	8
1.7.2	Conference Proceedings.....	8
1.7.3	Conference Presentations	9
2	Clinical Background	10
2.1	Chapter Aim	10
2.2	Current Standard of Care For GBM	10
2.2.1	Brain Tumours	10
2.2.2	Limitations of Current Imaging	12
2.2.3	Introduction to Ultrasound	14
2.2.4	History of Medical Ultrasound for Brain Imaging.....	15
2.3	Ultrasound Propagation in Tissues.....	17
2.3.1	Wave Propagation	17
2.3.2	Attenuation.....	19
2.3.3	Acoustic Properties of Brain and Brain Tumour.....	22
2.3.4	Scattering.....	25
2.4	The Role of IUS in Neuro-Oncology- A Literature Review	27

2.4.1	Conventional B-mode	27
2.4.2	3D/ Neuro-navigation.....	30
2.4.3	Harmonic Imaging	31
2.4.4	Doppler and Contrast Enhanced Ultrasound.....	31
2.4.5	Elastography.....	32
2.5	Quantitative Ultrasound	35
2.5.1	Introduction.....	35
2.5.2	Spectral- based QUS	36
2.5.3	Statistical-based QUS.....	37
2.5.4	Additional QUS parameters	38
2.5.5	Use in Neural Tissue	38
2.5.6	Combination of QUS Techniques and Machine Learning.....	39
2.6	Conclusions	40
2.7	Chapter Summary.....	42
3	Technical Background	44
3.1	Chapter Aim	44
3.2	Spectral QUS Parameter Estimation	44
3.2.1	Theoretical Description of Backscattered Power Spectrum.....	45
3.2.2	Attenuation Compensation.....	47
3.3	Statistical Parameters	49
3.3.1	Introduction to echo envelope statistics.	49
3.3.2	The Nakagami Distribution.....	50
3.3.3	Homodyned K-Distribution	51
3.3.4	Solving for QUS parameters from the HK-distribution.....	52
3.3.5	Other statistical parameters	56
3.4	Machine Learning.....	56
3.4.1	Binary classification.....	57
3.4.2	K-nearest neighbours	57

3.4.3	Support Vector Machine	58
3.4.4	Evaluating the performance of a classifier.....	59
3.5	Conclusions	61
3.6	Chapter Summary	61
4	Quantitative Ultrasound Differentiates Phantoms of Brain and Brain Tumour	63
4.1	Chapter Aims.....	63
4.2	Introduction	63
4.2.1	The Need for Acoustic Phantoms	63
4.2.2	Ultrasound Phantoms	64
4.3	Methodology	65
4.3.1	Validation of Acoustic Phantoms	65
4.3.2	QUS Analysis.....	69
4.3.3	Machine Learning Implementation	73
4.3.4	Effect of Freezing and Fixation.....	75
4.4	Results and Discussion	75
4.5	Conclusions	87
4.6	Chapter Summary	88
5	High Frequency Quantitative Ultrasound Differentiates Healthy And Glioblastoma Samples Ex Vivo.....	90
5.1	Aim of Chapter	90
5.2	Introduction	90
5.3	Methodology	92
5.3.1	Sample Preparation	92
5.3.2	Verasonics Data Acquisition.....	95
5.3.3	LNO Data Acquisition	97
5.3.4	B-mode Image Formation	99
5.3.5	Acoustic Characterisation	99
5.3.6	QUS analysis.....	101

5.3.7	Machine Learning Capabilities.....	102
5.4	Results and Discussion.....	103
5.4.1	Acoustic Characterisation.....	103
5.4.2	B-mode Images.....	107
5.4.3	QUS Results using Linear Array.....	124
5.4.4	LNO QUS Results.....	129
5.4.5	Limitations of this study.....	134
5.5	Conclusions.....	135
5.6	Chapter Summary.....	136
6	Differentiation of Low- and High-Grade Glioma From Healthy Brain in Finite Element Analysis.....	137
6.1	Chapter Aim.....	137
6.2	Introduction.....	137
6.2.1	FEA Software.....	137
6.2.2	Acoustic Impedance of Brain Microstructure.....	138
6.3	Methodology.....	139
6.3.1	Pathology Image Preparation.....	139
6.3.2	Meshing.....	142
6.3.3	Time-varying Pressure Input.....	143
6.3.4	Running the simulation.....	144
6.3.5	QUS analysis.....	144
6.3.6	Machine Learning Classification.....	146
6.4	Results and Discussion.....	146
6.4.1	Running the Simulation.....	146
6.4.2	QUS Results.....	147
6.4.3	Classification Performance.....	149
6.4.4	Comparison to <i>ex vivo</i> results.....	154
6.4.5	Limitations of this study.....	154

6.5	Conclusions	155
6.6	Chapter Summary	156
7	Conclusions and Future Work	157
7.1	Aim of chapter	157
7.2	Conclusions	157
7.2.1	Machine Learning-enabled QUS for Tissue Characterisation	157
7.2.2	Acoustic Characterisation	158
7.2.3	Differentiating Healthy and HGG Neural Tissue using QUS	158
7.2.4	Microultrasound Analysis	158
7.2.5	QUS in FEA	159
7.3	Recommendations for Future work	159
7.3.1	<i>In vivo</i> QUS	159
7.3.2	Further FEA Exploration	162
7.3.3	Reference Free QUS	162

List of Figures

<i>Figure 1.1: (a) A case of a temporal high-grade glioma is shown using 7 MHz IUS. The lesion appears hyperechoic on the IUS image but the margins surrounding the cancerous region are not well delineated and the image is of significantly lower resolution than the preoperative MRI in (b) [19].</i>	2
<i>Figure 1.2: Characterisation of rat mammary tumours using the ESD and EAC parameters, showing significant differences in the malignant case (a) and the benign case (b).</i>	4
<i>Figure 2.1: a) Coronal view of T1 weighted MRI image showing contrast in white and grey matter [42]. b) Schematic of brain structures in the brain.[43]</i>	11
<i>Figure 2.2: a) Preoperative MRI, b) Intraoperative MRI taken during tumour resection [67]. Red arrow indicates tumour site.</i>	14
<i>Figure 2.3: Dussik and his “Hyperphonic” apparatus [64].</i>	15
<i>Figure 2.4: First diagnostic ultrasound image of a living human brain [24]. Red arrow indicates ventricles.</i>	16
<i>Figure 2.5: Longitudinal sound wave [67].</i>	17
<i>Figure 2.6: Attenuation of various biological tissues, with associated power law of frequency dependence, from [79].</i>	22
<i>Figure 2.7: Summary from the literature of acoustic attenuation of healthy and cancerous brain tissue in human and animal studies.</i>	24
<i>Figure 2.8: Diagram showing the formation of scattering over 3 timesteps when ultrasound is incident on a material containing scattering sources. The image on the right shows (top right) a typical received signal from these interactions, from [87].</i>	26
<i>Figure 2.9: Comparison of RF ultrasound data (red) and echo envelope data (blue) from chicken liver tissue.</i>	26
<i>Figure 2.10: Ultrasound probes currently being used in neuro-surgery [89].</i>	27
<i>Figure 2.11: a) Resection cavity showing a light shadow (red arrows), which is an artefact, not residual tumour. This is due to differences in acoustic impedance of saline-filled cavity and brain tissue[27]. b) Intraoperative HGG image where tumour margins are difficult to fully delineate.</i>	28
<i>Figure 2.12: a) Application of a hockey stick-shaped linear array probe [18]. b) High resolution (15 MHz) image of GBM showing necrosis (dark areas) and diffuse infiltration surrounding them [19].</i>	29

<i>Figure 2.13: Chart displaying the different imaging modalities currently being researched in neuro-oncology. The modalities are arranged depending on which biomarker (Echogenicity, vascularisation or stiffness) is being utilised.</i>	<i>30</i>
<i>Figure 2.14: Real-time B-mode images superimposed on preoperative MRI to ease the surgeon's image interpretation [19].</i>	<i>30</i>
<i>Figure 2.15: Intraoperative CEUS image of GBM case. In arterial phase, the main veins feeding the tumour can be seen, in peak and parenchymal phase it is possible to differentiate more viable and necrotic or cystic areas. In venous phase, multiple small veins draining towards the ventricle are visible [103]</i>	<i>32</i>
<i>Figure 2.16: Comparison between strain elastography image and ECG. The red arrow indicates tumour in elastography image; note the delay in pressure as blood travels from the heart to the brain, causing pressure on transducer [110].</i>	<i>33</i>
<i>Figure 2.17 a) SWE vs B-mode, stiff (cancerous) regions are shown in red.</i>	<i>34</i>
<i>Figure 2.18: Scattering in tissues due to incident ultrasound source from the left. Structures of a similar size to λ will contribute to radial source of scattering as depicted by scattered beam.</i>	<i>35</i>
<i>Figure 2.19: Classification of cancerous regions in excised lymph node (left) and histopathology image (right) [36].</i>	<i>40</i>
<i>Figure 3.1: Illustration of higher perceived scattering in Region A due to bulk attenuation.</i>	<i>47</i>
<i>Figure 3.2: Flow chart describing the steps needed to obtain model parameters from output voltage from a transducer to obtain the spectral QUS parameters.</i>	<i>49</i>
<i>Figure 3.3: Pictorial summary of the various scattering situations and corresponding statistical distributions, from [147].</i>	<i>50</i>
<i>Figure 3.4: Algorithm for computing the function $\gamma(\alpha, X)$, from [125].</i>	<i>54</i>
<i>Figure 3.5: Algorithm solving $X_{HK} = X$ and $U_{HK} = U$ simultaneously, from [125]</i>	<i>55</i>
<i>Figure 3.6: Algorithm for estimating the parameters ε^2, σ^2, α of the HK-distribution with the constraint that α is less than an upper bound α_{max}, adapted from [125].</i>	<i>55</i>
<i>Figure 3.7: 2-D visualisation of the KNN framework for binary classification. In this case it is important to consider the number of neighbours as it may change the predicted class of the test point.</i>	<i>58</i>
<i>Figure 3.8: Example of a linear kernel SVM showing optimal hyperplane as a solid black line with support vectors on positive and negative cases, from [154].</i>	<i>59</i>
<i>Figure 4.1: Sample sections of chicken liver (left), and gizzard (right) for acoustic characterisation.</i>	<i>66</i>

<i>Figure 4.2: Speed of sound measurement showing (a) Sample of chicken gizzard placed on transducer for pulse-echo testing, (b) typical transducer response from experimental set-up.</i>	67
<i>Figure 4.3: Experimental set-up for attenuation measurement via TL.</i>	68
<i>Figure 4.4: (a) Experimental set-up of data acquisition from tissue using Verasonics Vantage system. (b) Typical B-mode image of tissue placed on top of quartz flat submerged in water.</i>	70
<i>Figure 4.5: Diagram showing the sliding window technique for QUS parametric image formation.</i>	71
<i>Figure 4.6: Confusion matrix for liver and gizzard classification.</i>	74
<i>Figure 4.7: Attenuation values, with error bars showing uncertainty in chicken liver and gizzard over 1 – 10 MHz range.</i>	77
<i>Figure 4.8: B-mode images of liver and gizzard samples obtained with Verasonics L15-8 array.</i>	78
<i>Figure 4.9: QUS parameter results for 1 mm x 1 mm regions. a) Two echogenicity parameters showing distinct clustering of results for liver and gizzard. b) Spectral parameter results highlighting the very small intra-sample variance. c) The X and U statistics used to estimate the HK parameters. d) The results for the scatter clustering parameter and structure parameter.</i>	79
<i>Figure 4.10: QUS images from two samples of both liver and gizzard. Parameters shown are scatterer size, scatter clustering parameter, echogenicity variance and skewness, with colour bars based on maximum and minimum values for both individual tissue types</i>	80
<i>Figure 4.11: Effect of ROI size on HK-distribution parameters showing approach of the true value when ROI size exceeds 3mm.</i>	81
<i>Figure 4.12: Pixel prediction of liver and gizzard. Binary results from fold 6 of the classification algorithm are superimposed on B-mode image.</i>	82
<i>Figure 4.13: Computation time for HK parameters for various tolerance values in both α and γ.</i>	84
<i>Figure 4.14: Percentage error in γ estimation for varying tolerance values.</i>	84
<i>Figure 4.15: Boxplot of results from fresh, frozen and fixed liver and gizzard. a) scatterer size, b) acoustic concentration, c) scatterer clustering parameter d) structure parameter.</i>	85
<i>Figure 5.1: Region of healthy human brain used for this study. Image courtesy of Edinburgh Brain Bank.</i>	91

<i>Figure 5.2: Effect of time on submerged tissue over 30-minute time interval. a-c shows the tissue thickness increasing over the 30-minute period when using water. e-f shows almost no absorption by the tissue over the same time interval.</i>	92
<i>Figure 5.3: A typical sample of healthy white matter.</i>	93
<i>Figure 5.4: Samples for data acquisition using the Verasonics linear arrays. a) Whole healthy sample with LF transducer. b) Smaller section of a healthy sample with HF transducer. c) GBM sample with HF transducer. For scale, the quartz flat is 2.5cm in diameter.</i>	94
<i>Figure 5.5: Event sequence for individual element transmit and receive with linear array.</i>	96
<i>Figure 5.6: Pulse echo response from one array element of the Verasonics L11-5v transducer.</i>	97
<i>Figure 5.7: Plan view of stepped scanning system over the entire tissue volume using LNO transducer (Tx).</i>	98
<i>Figure 5.8: Example of B-mode image with selected ROI used in acoustic characterisation highlighted in yellow.</i>	100
<i>Figure 5.9: Examples of the received signals from the quartz flat with (red) and without (blue) the brain tissue present.</i>	101
<i>Figure 5.10: Average attenuation of healthy and GBM samples using L35-16 and L11-5 probes. a) The dotted line indicates a single ideal linear fit. b) Polynomial fit with zero intercept.</i>	105
<i>Figure 5.11: Pulse-echo response from LNO scanning set-up highlighting clipped data acquisition. a) Response with intervening tissue, as indicated in the red arrow. b) Reference response from only quartz flat.</i>	106
<i>Figure 5.12: Six B-mode images of Healthy human brain tissue from the LF Verasonics linear array. The scan number for a specific sample is indicated by the subscript of the sample number.</i>	107
<i>Figure 5.13: B-mode images of smaller samples of healthy tissue and GBM using L36-16 probe elements excited individually and 80 dB dynamic range.</i>	109
<i>Figure 5.14: B-mode images of healthy tissue and GBM with LNO microultrasound scanning.</i>	110
<i>Figure 5.15: QUS parameters boxplots indicating the QUS results over each tissue scan for healthy (n = 48) and GBM (n = 40).</i>	125
<i>Figure 5.16: Compensated power spectrum of two samples of healthy tissue. a) Typical compensated power spectrum from soft tissue. b) Atypical power spectrum, seen in two</i>	

<i>samples of healthy tissue and eleven samples of GBM caused by a non-linear attenuation compensation function.</i>	127
<i>Figure 5.17: Scatter plots of several combinations of QUS parameters for healthy and GBM samples. a) ESD vs EAC. b) HK statistics. c) General statistics of pixel intensity. .</i>	128
<i>Figure 5.18: Statistical results of LNO QUS analysis. a) The mean value was significantly higher in tumour tissue. b) The echogenicity varied more in GBM. c) The kurtosis also showed to depend on tissue type. d) The structure parameter was significantly higher in healthy tissue.</i>	130
<i>Figure 5.19:., HK parameter results from LNO B-scans. a) α, κ and mean value. b) X and U statistics.</i>	132
<i>Figure 6.1: Acoustic impedance microscopy image from rat brain tumour model from [180]. a) healthy glial tissue and b) GBM tissue.</i>	138
<i>Figure 6.2: H&E stained diagnostic slide image of A) healthy brain tissue, B) LGG and C) HGG, from [182].</i>	139
<i>Figure 6.3: Selection of 30 500 micron² tiles in a LGG image, avoiding blood vessels (black arrow) and tissue breakages (white areas within tissue).</i>	140
<i>Figure 6.4: Binary image creation for 3 example tiles. The original image must be normalised to account for interlaboratory differences before filtering cell nuclei and creating a binary image.</i>	141
<i>Figure 6.5: Optimised resolution of material geometry within simulation with gridlines representing model mesh size.</i>	143
<i>Figure 6.6: Steps involved for meshing pathology image into a binary acoustic impedance map for HGG. a) Original Image. b) Greyscale image filtered with Haematoxylin staining. c) Image smoothed with Gaussian filter. d) Final binary map in lower resolution used for acoustic impedance assignment in FEA.</i>	143
<i>Figure 6.7: Pressure excitation used in pulse-echo simulation.</i>	144
<i>Figure 6.8: Pulse-echo responses of pressure waves incident from the left, showing interaction with tissue microstructure for the three tissue types over the entire simulation timeframe.</i>	147
<i>Figure 6.9: Paired QUS parameter results for healthy tissue (green), LGG (blue), and HGG (red). a) Attenuation Midband fit vs value at centre frequency. b) Lizzi parameters: BSPS intercept vs slope. c) Intensity statistics, variance vs mean. d) X-statistic vs Nagakami shape parameter.</i>	148
<i>Figure 7.1: MI from Verasonics using acoustic pressure measurements from needle hydrophone. Image courtesy of Dr Alex Moldovan.</i>	161

List of Tables

Table 2.1: 5-year survival percentage for most commonly occurring brain tumours, 2015-2017, UK. Data retrieved from Cancer Research UK, 2020 [5].	12
Table 2.2: Reported values of acoustic properties of human brain tumours measured <i>ex vivo</i> .	24
Table 2.3: Advantages and limitations of ultrasound sub-modalities in neuro-oncology.	42
Table 3.1: Validation of algorithm implementation for 3 pairs of X and U values.	53
Table 4.1: Summary of Tissue Exploration Options.	64
Table 4.2: Summary of QUS parameters used in machine learning training algorithm.	74
Table 4.3: Results of acoustic impedance measurements for liver and gizzard.	75
Table 4.4: Accuracy and F1-score for various parameter sets.	82
Table 4.5: P-values from t-test comparing frozen and fixed QUS parameters.	86
Table 5.1: Details of Human Tissue Samples.	93
Table 5.2: Classification Results with Gaussian SVM	129
Table 5.3: Classification results using only HK model parameters, α and κ .	133
Table 5.4: Classification results using only X and U statistic.	133
Table 6.1: Acoustic Properties of Materials in the Model	142
Table 6.2: Summary of QUS Parameters used in Classification Algorithms.	149
Table 6.3: Classifier results for healthy (negative) vs HGG (positive).	150
Table 6.4: Classifier results for healthy (negative) vs LGG (positive)	151
Table 6.5: Classifier results for healthy (negative) vs glioma (positive)	152

List of Abbreviations Used

A-Scan	Amplitude Scan
B-mode	Brightness Mode
BSC	Backscatter Coefficient
dB	Decibels
EAC	Effective Acoustic Concentration
ESD	Effective Scatterer Diameter
FFT	Fast Fourier Transform
FN	False Negative
FP	False Positive
GBM	Glioblastoma Multiforme
H&E	Haematoxylin and Eosin
HF	High Frequency
HGG	High Grade Glioma
HK	Homodyned K-
IEC	International Electrotechnical Committee
IQR	Interquartile Range
LF	Low Frequency
LGG	Low Grade Glioma
LNO	Lithium Niobate
MRI	Magnetic Resonance Imaging
OR	Operating Room
PBS	Phosphate Buffer Saline
PVDF	Polyvinylidene Fluoride
QUS	Quantitative Ultrasound
RF	Radiofrequency
ROC	Receiver Operating Characteristics
ROI	Region of Interest
TL	Transmission Loss
TN	True Negative
TP	True Positive
WHO	World Health Organisation

List of Symbols Used

A	Echo envelope signal amplitude
a	Attenuation
α	Scatter clustering parameter (HK)
a_{eff}	Effective scatterer diameter
c	Speed of sound
φ	Digamma function
E	Echogenicity
ε^2	Coherent signal power
f	Frequency
γ_E	Euler constant
I	Intensity
J_0	Bessel Function of the first kind
K_p	Modified Bessel Function of order p
K	Stiffness
k	Wavenumber
κ	Structure parameter (HK)
L	Gate length
M_S	Spectral gradient
θ_k	Phase shift
ω	Angular frequency
P	Probability distribution
p	Pressure
ρ	Density
n_z	Acoustic concentration
q	Ratio of transducer aperture to focal length
R	Reflection coefficient
σ^2	Diffuse signal power
σ	Standard deviation
t	Time
V_{Tis}	Voltage signal received from tissue
W	Power
X	RF data signal amplitude
x	Propagation distance
λ	Wavelength

1 INTRODUCTION

1.1 CHAPTER AIM

This chapter aims to introduce the thesis, beginning with a general overview of the complex problem of intraoperative glioma identification. The use of ultrasound in the neurosurgical theatre is discussed and the limitations of current established techniques are stated as motivation for this study. The aims and objectives for the project are put forward, followed by the contributions to knowledge. Finally, the publications arising from this thesis are given.

1.2 OVERVIEW OF THESIS

1.2.1 Current Standard of Care in Glioma Patients

Gliomas are common primary brain tumours of the central nervous system and grow invasively from the white matter regions of the human brain [1]. Unlike metastatic or meningioma tumours, which can have well defined boundaries, gliomas are extremely difficult to localise intraoperatively and so are nearly impossible to completely resect [2]. In the malignant case, remaining tumour cells will eventually form a new tumour and patient prognosis generally predicts death within 1 - 5 years, depending on malignancy [3]. This is graded by the World Health Organisation (WHO) I to IV where IV represents the Glioblastoma Multiforme (GBM) which is the most malignant and aggressive tumour, and I is a slower growing, but still dangerously invasive tumour [4]. In the surgical management of gliomas, maximum possible tumour resection is critical to improve prognosis in both LGG [5], and HGG [6]. Typically, high resolution preoperative Magnetic Resonance Imaging (MRI) is carried out to inform surgical decisions on craniotomy location. This provides a full 3D representation which can be implemented into a neuro-navigation system to allow the surgeon to easily map the surgical path for safest resection.

However, for subsurface gliomas, after removal of the skull and piercing of the dura matter, the pressure released causes the brain to shift inside the skull, rendering the preoperative image locations inaccurate [7]. Furthermore, the physical structure of the brain is such that it tends to fold in on itself to fill the resection cavity and this in turn causes discrepancies in the boundaries of the tumour [8]. At this stage, a real-time image update is necessary for the surgeon to safely resect as much tumour as possible. Intraoperative MRI is a possibility, however, the safety practicalities and costs associated with a non-ferromagnetic operating

theatre environment mean it has not been widely adopted [9]. Furthermore, acquiring the MRI image still takes some time, and there could be a huge disruption to surgical workflow if multiple images are required [10].

1.2.2 Ultrasound Techniques

Ultrasound, on the other hand, is an attractive option that is less costly, portable and provides real-time images in a time- efficient manner. It is an imaging modality which has been used in the neurosurgical theatre for several decades, not only for tumour localisation but in a range of guidance based applications, including ventricular shunt placements, and needle and catheter guidance [11]. Ultrasound imaging is based on the reflections arising when mechanical waves encounter a boundary of different acoustic impedance, which occurs in the various structures in human tissue. In summary, a voltage drives a piezoelectric device, or transducer, to produce a sound wave with frequency typically $>1\text{MHz}$, which is coupled to the tissue so the waves can propagate through the material, reflecting off various structures and substructures. A brightness mode (B-mode) image is formed which portrays the amplitude of the reflected signals detected by the transducer [12]. In present terms, conventional ultrasound refers to a curvilinear array typically operating in the frequency range 3 - 10 MHz, offering a resolution of 500 – 1,300 μm at depths of 2 - 8 cm from the transducer [13]. There has been significant evidence showing intraoperative ultrasound (IUS) can greatly improve the extent of resection in glioma surgery [14–16] and recent advances are showing an improvement, particularly when IUS is integrated with a neuronavigation system [17] and using HF linear arrays [18]. The tumour appears as a hyperechoic, or brighter, region in the IUS image, usually with unclear boundaries, as the lesion in Figure 1.1a shows. The comparable MRI is also displayed in Fig. 1.1b.

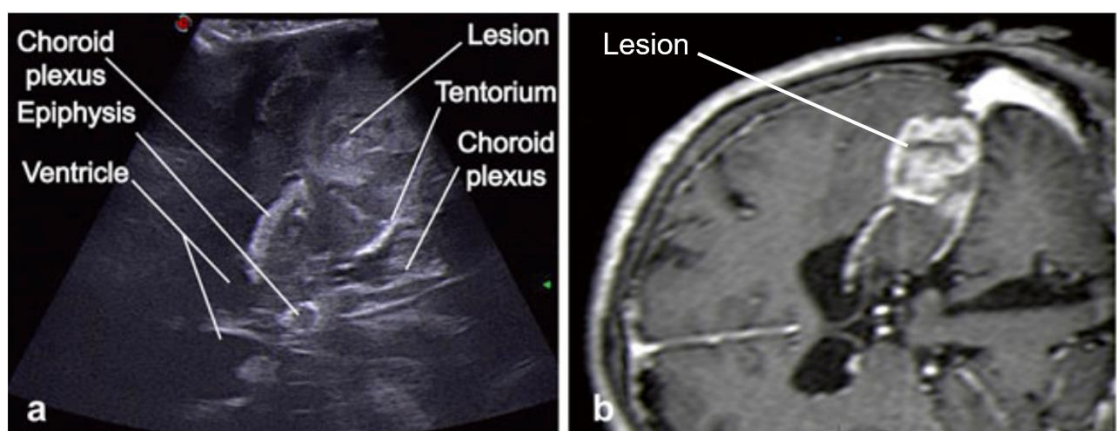


Figure 1.1: (a) A case of a temporal high-grade glioma is shown using 7 MHz IUS. The lesion appears hyperechoic on the IUS image but the margins surrounding the cancerous region are not well delineated and the image is of significantly lower resolution than the preoperative MRI in (b) [19].

The major disadvantage of ultrasound is the limited resolution and lack of acoustic contrast between healthy brain and glioma tissue, which causes the margins of the tumour to be unclear, as is reported often in the early literature [20]. Advancements in technology have allowed the manufacturing of smaller probes with higher frequency, which will improve the resolution, at the cost of a reduced penetration depth. This is caused by attenuation, where the tissue absorbs ultrasound energy as it travels through, at a rate proportional to the frequency, usually around $0.5 \text{ dB MHz}^{-1} \text{ cm}^{-1}$. Typically, in brain tissue, if the frequency were to be increased to 30 MHz, this would result in a maximum imaging depth of 2 – 3 cm, which would not be suitable for deep seated lesions. However, with the introduction of probes with smaller footprint, this can be overcome by inserting the probe into the resection cavity.

While the increase of resolution may improve the image quality, there is still a distinct lack of acoustic contrast between healthy and glioma tissue, meaning the margins of the tumour are not clear in the conventional B-mode image. Some recent advances try to optimise image quality by reducing the grainy appearance of the ultrasound image but, crucially, there may be information contained in the speckle pattern which can be used for tissue characterisation. The speckled, or grainy, appearance is typical in an IUS image and is caused by scattering of waves within the tissue. Scattering arises when ultrasound encounters an acoustic inhomogeneity smaller than the wavelength itself [21]. This is where a region within the tissue has slightly different acoustic properties to the bulk acoustic properties of the material. Within brain tissue, the wavelength of ultrasound at 10 MHz is $155 \mu\text{m}$ and so the complex neuronal microstructures will contribute to scattering. It is hypothesised that regions with higher cell density, such as cancerous regions, will cause ultrasound to scatter more chaotically than in healthy areas which may have fewer scattering sources and be more structured. The measurement of scattering from tissue can be quantified in several ways, including the backscatter coefficient (BSC) and statistical model parameters. The blanket term given to the field where any parameter may be used to describe scattering is QUS, which is commonly sub-divided into spectral and statistical aspects [22].

1.2.3 Introduction to QUS

The field of QUS was pioneered by Lizzi and Felleppa in the 1980s when studying ocular tumours [23]. They developed a theoretical framework to account for system dependent effects, so user-independent parameters can be measured [24]. The backscattered power spectrum (BSPS) measures the amount of signal scattered back to the transducer from the tissue region over the bandwidth of the transducer. The dependence on frequency was shown

to give useful parameters for tissue characterisation, termed ‘Lizzi-Fellepa parameters’ [23]. Their parameters were based on the slope and intercept of the BSPS, when plotted against frequency, and launched work towards a theoretical description for scattering within tissues [25]. Extended by Oelze et. al in the early 2000s, this enabled the experimental measurement of the effective scatterer diameter (ESD) and effective acoustic concentration (EAC), the product of the number of scatterers per mm^3 and the acoustic impedance mismatch [25]. These parameters have since been used to detect different tumour grades in rat mammary tumours [26], human breast masses [27] and in the detection of fatty liver disease [28].

The values of these parameters may be used to form a parametric image over the original B-mode image to give additional information on tissue microstructure, which can be extremely useful for tissue characterisation [29]. Fig. 1.2 shows an example of parametric images where significant differences in ESD are seen in the malignant and benign cases for rat mammary tumours [26].

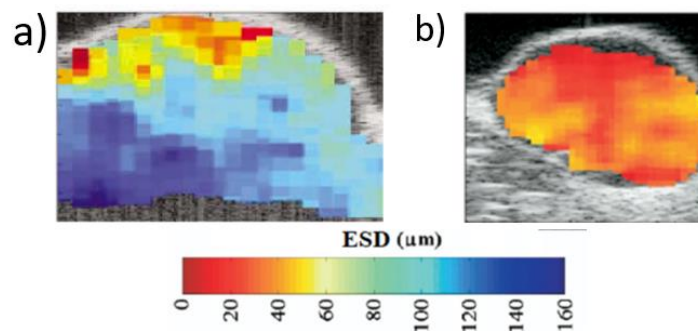


Figure 1.2: Characterisation of rat mammary tumours using the ESD and EAC parameters, showing significant differences in the malignant case (a) and the benign case (b).

In parallel to developments in the spectral domain of QUS, advances were made in the statistical description of scattering [30]. Early work used statistics of the speckle from ultrasound images directly to characterise tissue [31] and recent studies are still adopting the simple approach to analyse the first order statistics of the echogenicity values to gain quantitative insight into scattering properties [32]. A sophisticated model came by investigating the amplitude of the echo envelope of the ultrasound signal scattered back from tissue [33]. Initially, the scattering sources were assumed to be randomly arranged, so were described by the Rayleigh distribution [34]. However, the HK distribution is the most commonly adopted for tissue characterisation due to its accuracy and mean invariant parameters [35]. This can describe ultrasound scattering in general from complex shapes and patterns and does not rely on the assumption of randomly placed spherical scatterers, which

brain tissue is unlikely to include. The key parameters for tissue characterisation are α , the scatter clustering parameter which gives a level of organisation of the scatterers, and, κ , the structure parameter, which measures the ratio of diffuse to coherent scatterers [33].

The real benefit of QUS comes from its parameter-based nature, and most successful studies have adopted a multi-parametric approach where they include some or all the parameters detailed above to train a binary classification algorithm for tissue characterisation. The use of ML to aid diagnosis is ever increasing and has already achieved high sensitivity and specificity in a range of diseases using a QUS approach. This includes characterisation of breast masses [32], metastatic lymph nodes [36] and diagnosing of fatty liver disease [37].

Despite this success in other tissues, there have been no reports of QUS analysis of human brain tissue, except a study of *in vivo* attenuation and BSC measurements over a frequency range of 2 - 6 MHz in healthy brain and meningioma [38]. This study saw success differentiating the two tissues, suggesting that the field of QUS should be explored fully in glioma tissue, as these are the most infiltrative tumours and are difficult to localise with conventional US.

1.3 MOTIVATION

It is imperative, for improved patient prognosis, to remove as many of the glioma cells as possible during surgery. The preoperative images taken before tumour removal surgery become outdated and inaccurate as soon as the surgery begins. There is a need for an interoperative tool to provide real time imaging to the neurosurgeon to indicate whether a region is cancerous or healthy. Conventional ultrasound probes are limited by size and frequency for this application.

There is a lack of understanding of the acoustic attenuation properties of brain tissue at frequencies greater than 10 MHz. This is particularly important for the BSPS, as it needs to be corrected for attenuation for an accurate spectral parameter result. This gap is not specific only to neural tissue research but applies to the field of QUS in soft tissues in general, which is why, presently, there are limited reports of QUS parameters above 25 MHz in any tissue analysis [39].

Furthermore, the statistics of the echo envelope signals, which can provide detailed information about tissue microstructure, have been successful for tissue characterisation yet only utilised in a handful of studies to date. There has been no measurement of HK parameters from animal or human brain tissue. These parameters could be key to aiding differentiation of healthy and cancerous neural tissue, so it is imperative they are obtained,

and statistical QUS parameters are explored fully. Moreover, the parametric nature of the QUS analysis allows for easy implementation into simple binary classification algorithms, the use of which has not been implemented in the context of neural tissue characterisation to date.

In summary, there is motivation to explore QUS in general at frequencies higher than 15 MHz and there is incentive to apply this technique to the differentiation of healthy and cancerous brain tissue. Due to the ever-increasing use of ML to aid clinical decisions, it would be advantageous to incorporate this into the analysis to allow QUS to reach its full potential in a clinical setting.

1.4 THESIS AIMS AND OBJECTIVES

The overall goal of this thesis is to add to the extremely limited field of QUS for brain tumour detection and explore some of the gaps in current literature, such as backscatter analysis at HF and use of statistical models. This can be divided into three more specific aims:

1. To implement and assess the real-time classification capability of QUS techniques using readily available phantom materials and animal brain tissue.
2. To explore HF QUS (>15 MHz) for the application of human brain tumour identification, for the first time, by obtaining measurements on *ex vivo* samples.
3. To investigate the potential of ML and QUS when given a larger dataset to identify varying levels of malignant gliomas in an *in silico* study.

To achieve these aims, the following objectives are detailed below:

1. To arrive at suitable phantom materials to mimic brain and brain tumour to allow experimental procedures to be implemented in a preliminary study, aligning with Aim 1.
2. To set-up a research ultrasound system for array and single element transducers, both low and HF, which can obtain a full set of QUS parameters, required for Aims 1 and 2.
3. To accurately measure the attenuation and QUS parameters from human brain tissue, as well as human glioma at frequencies greater than 15 MHz for Aim 2.
4. To compare the QUS parameters from healthy and cancerous tissue and assess the classification performance for tissue differentiation on *ex vivo* samples.
5. To realistically model healthy and cancerous brain tissue *in silico* to fully exploit the data driven ML approach for tissue characterisation.

1.5 CONTRIBUTIONS TO KNOWLEDGE

This thesis has contributed both to the wider field of QUS, and specifically QUS in brain tissue in several ways, with the most significant contributions outlined below.

1. Low frequency QUS parameters measured in brain tissue-like materials. This work describes the simultaneous measurement of spectral and statistical parameters from chicken liver and gizzard muscle and shows the ability of QUS to differentiate the two soft tissue phantoms.
2. The ability of QUS to differentiate between *ex vivo* samples of human brain and brain tumour was assessed at 25 MHz. This firstly adds to the field of HF acoustic characterisation, then to both spectral and statistical QUS.
3. Samples of human brain tissue and tumour were studied at atypical frequencies, including analysis using a 74MHz single element transducer for acoustic characterisation and full QUS analysis for an initial investigation at the feasibility of implementing the technique using micro ultrasound.
4. The use of diagnostic microscope images of healthy and cancerous brain tissue was investigated and adds to the discipline of tissue modelling in FEA. This allowed the exploration of QUS parameters for cancer detection without the limitation of a small sample set.

1.6 THESIS STRUCTURE

The remaining chapters of the thesis are outlined below.

Chapter 2 provides context for the research from a clinical perspective, by presenting a literature review of the use of ultrasound in neurosurgery, with particular focus on intraoperative glioma imaging and limitations in the current practice. The field of QUS for tissue characterisation is introduced and the shortcomings of this field in neural tissue and at HF are discussed.

Chapter 3 describes the underlying theory of QUS parameter estimation for tissue characterisation. Firstly, the mathematics of tissue attenuation are explained, followed by the BSC and mathematical models of tissue scattering. Then, echo envelope statistics and methods to estimate the distribution parameters are described. This is followed by a presentation of the principles of ML for binary classification.

Chapter 4 presents phantom work carried out to implement and optimise the QUS technique previously described at conventional frequencies. This involved acoustic characterisation of

chicken liver and gizzard, followed by full QUS parametric image formation. The ability of QUS to differentiate the two phantoms was assessed using a binary classification.

Chapter 5 includes preliminary work on *ex vivo* bovine brain before it examines the ability of QUS to differentiate samples of snap-frozen healthy cortical white matter and GBM *ex vivo*. A research ultrasound machine and linear array transducer were used to conduct a full QUS analysis and assess the differentiation potential. There was also a full analysis using the highest frequency recorded via a 74 MHz single element transducer.

Chapter 6 explores tissue microstructure in more detail by modelling human brain tissue and tumour in FEA software. Microscope images of human healthy white matter and glioma tissue were used to create an acoustic impedance map where wave interaction can be studied in more detail, and QUS parameters obtained. These were combined to investigate the data driven research approach for classification.

Chapter 7 presents the conclusions drawn from the results obtained in this thesis, highlighting the key contributions to this field as well as the main challenges experienced throughout the project. This leads to a discussion on improvements and details of the steps required in the future to further assess the potential of QUS as an intraoperative aid in neuro-oncology.

1.7 PUBLICATIONS ARISING

1.7.1 Peer Reviewed

Thomson H, Yang S, Cochran S (2022). Machine Learning enabled Quantitative Ultrasound for Tissue Characterisation. *Journal of Medical Ultrasonics*.

DOI: <https://doi.org/10.1007/s10396-022-01230-6>

1.7.2 Conference Proceedings

Thomson H, Yang S, Baldwin M, Stritch T, Cochran S (2020). The Effect of Freezing and Fixation on QUS parameters. 2020 IEEE International Ultrasonics Symposium (IUS).

DOI: <https://doi.org/10.1109/ULTSYM.2019.8925982>

Thomson H, Yang S, Baldwin M, Stritch T, Cochran S (2019). Quantitative Ultrasound Differentiates Brain and Brain Tumour Phantoms. 2019 IEEE International Ultrasonics Symposium (IUS). DOI: 10.1109/ULTSYM.2019.8925982

Lemke C, **Thomson H**, Lay H, Cox F, Yongqiang Q, Clutton E, Cochran S. 2019 IEEE International Ultrasonics Symposium (IUS). DOI: 10.1109/ULTSYM.2019.8925827

1.7.3 Conference Presentations

'Applications of Intraoperative Ultrasound to Improve Brain Tumour Resection: A Literature Review' – **Poster presentation**, Inaugural Brain Tumour Conference (Cancer Research UK), first – 3rd May 2018, London.

'Applications of Intraoperative Micro-Ultrasound to Improve Brain tumour resection'- **Poster Presentation** 10th Annual Scientific Meeting of SINAPSE (Scottish Imaging Network: A Platform for Scientific Excellence), 25th June 2018, Edinburgh.

'Multiparametric Quantitative Ultrasound Measurements for Differentiating Brain and Brain Tumour Phantoms with Binary Classifier' – **Invited Talk**, Nanjing University of Science and Technology, 7th August 2020.

'Quantitative Micro-Ultrasound Differentiates High Grade Glioma and Healthy White Matter in Ex Vivo Tissue Samples'– **Oral Presentation**, IEEE International Ultrasonics Symposium (IUS), 11th-16th September 2021, Online Conference.

'Microultrasound-Based Machine Learning Classifier Differentiates Low- and High-Grade Glioma via Acoustic Impedance Maps in Finite Element Analysis'– **Oral Presentation**, IEEE International Ultrasonics Symposium (IUS), 11th-16th September 2021, Online Conference.

2 CLINICAL BACKGROUND

2.1 CHAPTER AIM

The aim of this chapter is to examine current ultrasound technologies aiding brain tumour delineation in the neurosurgical theatre and identify which areas hold potential for the focus of this thesis. To fully realise this aim, the chapter begins with a clinical introduction to brain tumours and discusses the current standard of care for glioma patients before establishing what place intraoperative QUS should have in this. The history of IUS in neuro-oncology is reported, including recent advances and clinical trials from a range of ultrasound sub-modalities. Finally, the chapter introduces the field of QUS and examines the literature surrounding its use in tissue characterisation to explain why it is a suitable focus for the remainder of the thesis.

2.2 CURRENT STANDARD OF CARE FOR GBM

2.2.1 Brain Tumours

*“To confront cancer is to encounter a
parallel species, one perhaps more adapted
to survival than even we are.”*

The Emperor of all Maladies [40]

The treatment of cancer remains one of humanity’s greatest challenges. Since medieval times, surgeons have been devising aggressive treatments for cancer, through radical resections, but only in the last sixty years has cell biology advanced enough to understand the underlying mechanisms which cause cells to divide so relentlessly.

The brain contains two primary types of cells: neurons and neuroglia. Neurons are responsible for receiving, processing and communicating information to other neurons via electrical and chemical excitations, or synapses [41]. These are located on the cerebral surface, or grey matter, as shown in Fig. 2.1. Neurons are incapable of mitosis (cell division) as the body of the cell lacks a pair of organelles which are essential for cell division, known as centrioles. This means when neuron cells die, they are not replaced, and they are thus unable to become cancerous.

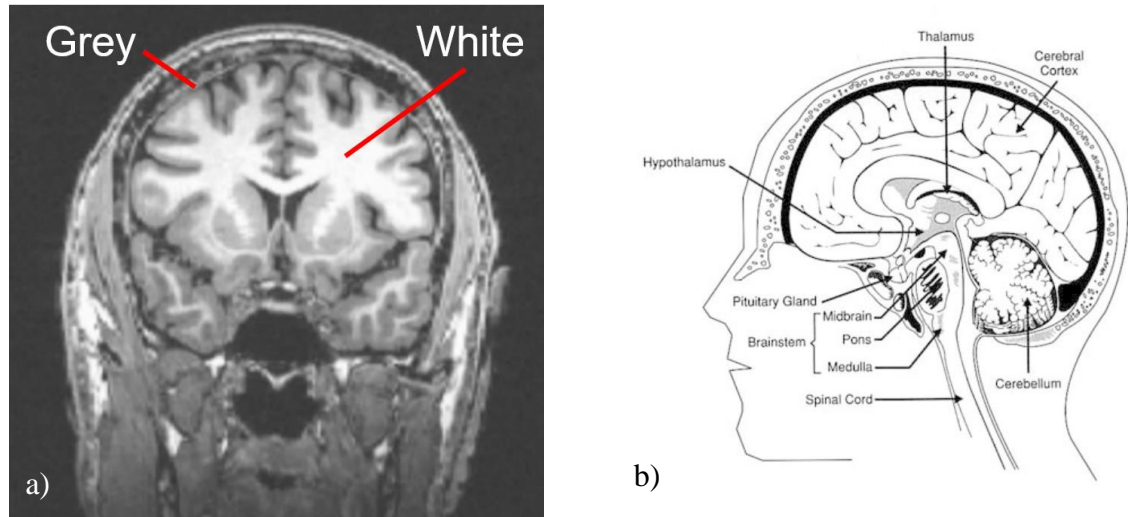


Figure 2.1: a) Coronal view of T1 weighted MRI image showing contrast in white and grey matter [42]. b) Schematic of brain structures in the brain.[43]

Neuroglia, or glial cells, are essentially the glue of the nervous system and are found in both white and grey matter. They consist of a variety of different cell types that provide functions to protect and nourish surrounding neurons. The most abundant are astrocytes which have numerous projections that link neurons to their blood supply [41]. They also regulate the external chemical environment of neurons and recycle neurotransmitters released during synapses. Oligodendrocytes, ependymal cells and microglia have different purposes and are located in different areas of the brain [44]. All these glial cells can become cancerous and are then labelled gliomas. The normally useful, infiltrative nature of glial cells then makes the cancer they develop one of the most difficult to cure.

Brain tumours are relatively rare in comparison with other cancers in that they constitute approximately 3% of all cancer cases worldwide [45]. However, the mortality rate is extremely high and it is ‘the biggest cancer killer of children and adults under 40’ [46]. Patient survival is highly dependent on a variety of parameters (age, sex, malignancy, time of diagnosis [47],[48]) but on average only 12% of patients survive more than 5 years after diagnosis of an intrinsic brain tumour [49]. There are currently over 100 categories of brain tumours identified by the WHO, with the most prevalent being gliomas; then meningiomas, which form in the outer layers protecting the brain; and finally metastases, cancers from another part of the body that spread into the brain [50].

A more complete breakdown of the most frequent cancer types is shown in Table 2.1. WHO Classification gives a level of malignancy to tumours from (**I - IV**) with **I** indicating benign and **IV** indicating an aggressive, rapidly growing tumour. Survival rates decrease rapidly with malignancy classification for all tumour types, but GBM, which is the name given to

all gliomas with a WHO classification of IV, has a very low survival rate, with average survival time after diagnosis of only 16 months [3].

Table 2.1: 5-year survival percentage for most commonly occurring brain tumours, 2015-2017, UK. Data retrieved from Cancer Research UK, 2020 [5].

5-YEAR SURVIVAL % FOR MOST PREVALENT BRAIN TUMOURS

Astrocytoma	Grade I	90%
	Grade II	50%
	Grade III	20%
GBM	Grade IV	5%
Ependymoma	Grade I	90%
	Grade II	70%
	Grade III	50%
Meningiomas	Grade I	80%
	Grade II	80%
	Grade III	40%
Pituitary gland	Grade I	70%

Cancers of the brain are particularly challenging to treat for several reasons. Firstly, the brain and spinal cord are insulated by a tight cellular seal, called the blood brain barrier, which prevents foreign chemicals from easily entering the brain, making it almost unreachable by chemotherapy [51]. As well as this, the surgical resection of brain tumours is extremely complex, as a mass resection is rarely possible as it would result in irreversible neurological damage [52]. The presence of the skull also introduces the need for craniotomy (removal of part of the skull) which causes additional trauma to the head, so the section removed is generally minimised. In some cases, ‘burrhole’ surgery is used, in which a small hole, typically less than 3 cm in diameter, is cut through the skull to allow the surgery to be performed [53]. The advantages of such minimally invasive approaches include decreased surgical times, and lower blood loss and complication rates, resulting in shorter hospital stays [54]. However, they leave a limited field of view for the surgeon, which restricts the instrumentation or diagnostic tools that can be used to aid resection.

2.2.2 Limitations of Current Imaging

Tumours are typically detected via a MRI after symptoms begin. These vary from a mass effect (headache caused by tumour mass increasing pressure to the brain) to neuronal specific effects such as personality changes, confusion, vision and hearing problems [55]. Surgical

management depends on whether the tumour is intra-axial (growing from within the brain substance) or extra-axial (growing externally). Extra-axial tumours are mostly benign, cause symptoms by mass effect on the surrounding brain and are easier to resect. They usually have a well-defined boundary and complete surgical excision is the aim. On the other hand, intra-axial tumours are malignant and diffuse, and are more challenging to remove completely, such as metastatic tumours and gliomas.

This thesis will focus on the challenge of delineating intra-axial tumours, specifically HGG, from healthy tissue. These tumours are particularly challenging as they typically have similar colour and texture to the surrounding healthy brain parenchyma, making them hard to distinguish during surgery. It is clear from Table 2.1 that the most difficult to treat is the aggressive and infiltrative GBM. It is the proliferating nature of its cells, causing a microscopic invasion while still aggressively multiplying, which causes it to be classed as an incurable disease [56].

There have been several studies concluding a positive correlation between percentage of tumour resected and patient survival time [5], even in HGG growing in areas which are essential for basic functioning [6]. Maximum safe resection is the standard treatment for most GBM cases. Typically, the surgeon will refer to the preoperative MRI, perform a real time image update to reorientate, and navigate to the tumour site. Then the tumour bulk will be resected, mainly using palpation to identify it. A tissue ablator is used to destroy cancerous regions which, interestingly, will utilise high power ultrasonics to ablate the tissue. These typically consist of an ultrasonic aspirator, which has a tip diameter of around 2 mm, such as the SonoPet[®] (Stryker Medical Devices, USA). After tumour debulking, the margins between healthy and cancerous tissue become unclear and the surgeon may use magnification and injection of contrast agents to aid in achieving clean margins [52]. They may also use several biopsy samples taken throughout the procedure to achieve an accurate diagnosis; however, this is time consuming and labour intensive.

After surgery, treatment is followed by a multimodal regimen of radiotherapy and / or chemotherapy, but ultimately limitations in drugs accessing the brain mean any tumour regions left are unresponsive to this treatment so begin to proliferate again [6]. Survival time has modestly increased in recent years, owing to advances in surgical techniques and intraoperative imaging [5]. Preoperative MRI is seen as the gold standard of image quality, however, these images are rendered inaccurate after craniotomy and dural opening as the brain undergoes the phenomenon of brain shift [57]. This is a well-documented occurrence in which structures change shape and position as a result of the procedure [7]. Depending on

intracranial pressure before craniotomy, the brain and lesion will bulge toward, or away from the surgical site. This is further exacerbated by opening the dura mater and, during the process of the whole operation, where cerebral spinal fluid loss and gravity will cause further shift. This means the preoperative images become inaccurate and there is a need for interoperative imaging.

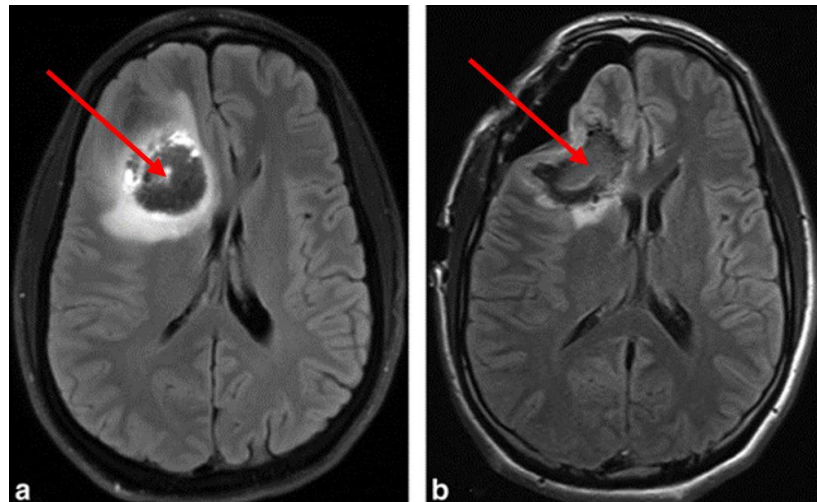


Figure 2.2: a) Preoperative MRI, b) Intraoperative MRI taken during tumour resection [67]. Red arrow indicates tumour site.

Fig. 2.2 shows an example of brain shift, with a) being taken preoperatively, while b) is taken with intraoperative MRI, after craniotomy. Not only is the surface of the brain deformed, but the entire left hemisphere has undergone some distortion.

Intraoperative MRI provides the highest quality imaging method for brain tumour visualisation, however it has several drawbacks which have prevented it from being widely used [52]. Positron emission tomography (PET) scans are also used in the brain, but mostly for functional imaging or for monitoring the effects of radiotherapy treatment in cancer [58]. Computerised Tomography (CT) scans are also used for brain tumour visualisation, but are of lower resolution, so are more commonly used as an initial diagnosis tool for cancer, as well as stroke or head trauma [59].

Ultrasound is a real-time, cost-effective imaging system in neurosurgery, but artefacts, low spatial resolution and image orientation are amongst the most important challenges to overcome [60]. Improvements to IUS in neurosurgery are imperative in contributing to the ultimate aim of improved glioma resection.

2.2.3 Introduction to Ultrasound

Medical diagnosis by ultrasound is possible due to the physical interactions between ultrasonic waves and biological materials. Ultrasonic waves propagate through tissue and reflect or scatter from tissue interfaces and structures. B-mode ultrasound is utilised often in

the clinical environment and makes use of the piezoelectric effect: the conversion of electrical energy to mechanical energy. When an electrical signal is sent to the transducer, it causes the piezoelectric material to expand and contract which, in turn, generates an ultrasound wave. This wave propagates through the material until it encounters a boundary of different acoustic impedance. Then, some of the energy from the wave is transmitted across the boundary into the different material and some is reflected back to the source where it is converted back into a voltage and detected by the system. The time delay between the emission of the pulse and reception of the echo by the ultrasound probe enables the depth of the reflecting structure to be deduced. Using an array of transducers, multiple echoes are represented and processed into a greyscale image - the stronger the echo from a particular tissue boundary, the brighter the pixel. The resulting 2D image enables visualisation of anatomical structures, the most common example being obstetrics imaging, but the same technique can be used to obtain diagnostic information in other areas such as the heart, breast, thyroid, kidneys and abdominal organs [61].

Tumour tissue has a higher local density (hence impedance) so will appear lighter on an US image compared to surrounding brain. The use of ultrasound predates MRI and has seen significant advances in the last four decades, involving improved image resolution, smaller probe sizes and navigated 3-D techniques [62].

2.2.4 History of Medical Ultrasound for Brain Imaging

The first medical use of ultrasound on a human subject was reported in 1937 in Austria by Theodore Dussik and his brother, investigating the detection of brain abnormalities [63]. The experimental set-up is shown in Fig. 2.3 and the Dussik brothers were able to produce an image based on the differential attenuation of sound during its passage through the head.

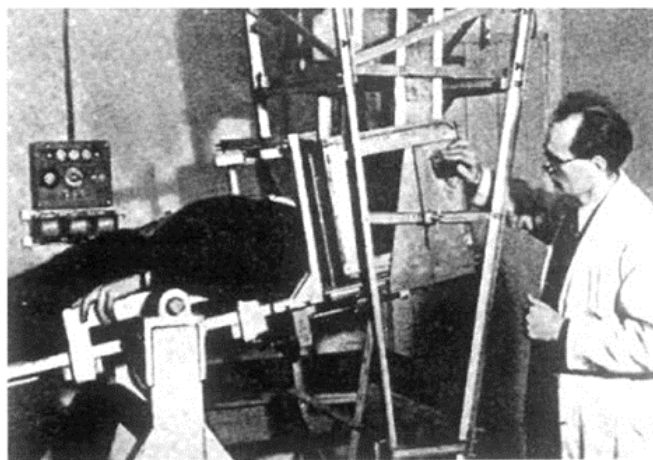


Figure 2.3: Dussik and his “Hyperphonic” apparatus [64].

The Dussik's paper, which translates to 'On the way to Brain Hyperphonography' was published in 1947 [65] and included the first diagnostic image of part of a living human being ever recorded [66]. The dark spaces are what the authors believed to be ventricles, the spaces in the brain where cerebral spinal fluid can enter, so appear hypoechoic, or black in an ultrasound image.

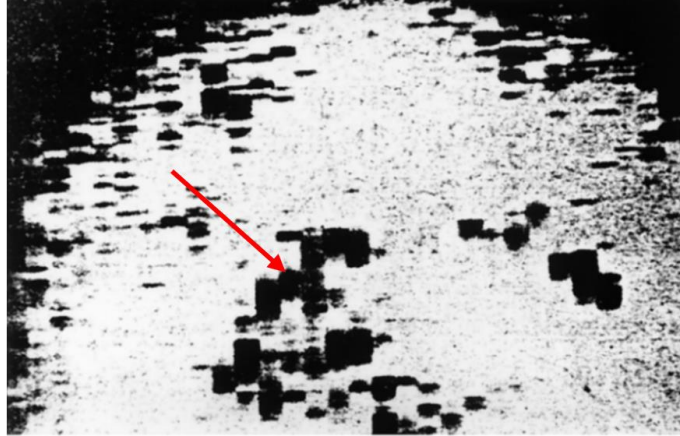


Figure 2.4: First diagnostic ultrasound image of a living human brain [24]. Red arrow indicates ventricles.

In the 1970s, B-mode US was introduced in the OR for foetal imaging, however, the acoustic properties of the skull halted its progress as a non-invasive technology in neurosurgery. The skull comprises material with very high ultrasonic attenuation, so it is particularly challenging to achieve a high-resolution image through it. MRI was therefore introduced and adopted into routine clinical diagnostic practice for tumour diagnosis and localisation. However, advancements in surgical techniques allowed the removal of the skull to become routine practice and essential for tumour removal surgery. This allowed the first reported use of ultrasound in neurosurgery for tumour localisation in 1982 [11].

Soon, the problem of brain shift was encountered and a need for real-time intraoperative image updates was evident. The main advancement specifically in IUS technology was the development of small ultrasound probes for superficial lesions which eliminated the necessity for a large cranial window. B-mode ultrasound is a real-time, cost-effective imaging system in neurosurgery but artefacts, low spatial resolution and image orientation are amongst the most important challenges to overcome [60]. Due to the non-ionising nature of ultrasound and the ability to image in real time with a portable machine, ultrasound is used in a range of applications, including brain tumour identification. IUS is a powerful tool in tumour surgery for resection control and future developments are likely to widen its scope.

An extensive review of the various uses of IUS in neurosurgery has been produced [19] but only its use for cancer detection is discussed in the review which follows.

2.3 ULTRASOUND PROPAGATION IN TISSUES

2.3.1 Wave Propagation

A sound wave, as considered here, is a longitudinal displacement wave, causing the particles to oscillate back and forth in the direction of propagation. This results in regions of compression and rarefaction. Hence, at each point the pressure oscillates from maximum to minimum as the wave passes, as visualised in Fig. 2.5.

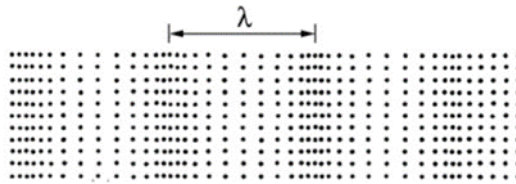


Figure 2.5: Longitudinal sound wave [67].

The speed of propagation depends on material density, ρ , and stiffness, K :

$$c = \sqrt{\frac{K}{\rho}} \quad (2.1)$$

The speed, frequency and wavelength are related by $c = f\lambda$. For a sound wave to be deemed ultrasonic, its frequency must be higher than the physical limit of human hearing (i.e. >20 kHz).

Ultrasonic waves are generated by the transducer, which usually consists of one or many piezoelectric elements which can convert electrical into mechanical energy via the converse piezoelectric effect. The material allows the wave to be produced by supplying a voltage across the material surface. The direct piezoelectric effect is also observed; when ultrasound is incident on the surface of the material, this will translate into a voltage which can be recorded.

If the transducer is operating in “pulse echo” mode, which it usually is for medical imaging and in the work in this thesis, it will first generate a short pulse to propagate away from the transducer. If there is any boundary, or material with different properties, in the wave’s path, it reflects the wave, changing the direction of propagation, and so a smaller signal may be received by the same transducer if it is incident on the surface.

The acoustic impedance of a material, Z , is the product of the density and the speed of sound (SoS), c , so is a fundamental property of the material:

$$Z = \rho c \quad (2.2)$$

When an ultrasound wave propagates through a material and reaches a point where a boundary exists in acoustic impedance, reflection of the ultrasound wave will occur at this boundary. Specular reflections result where the boundary is smooth and the sizes of irregularities at a tissue boundary are much larger than the wavelength of the ultrasound [68]. Diffuse reflections are observed when the ultrasound wave meets a rough boundary while scattering directs ultrasound waves into various directions as a result of irregularities within the medium material [69].

The amount of energy reflected normally from a specific boundary between materials of Z_1 and Z_2 is proportional to the difference in acoustic impedance:

$$R = \frac{(Z_1 - Z_2)^2}{(Z_1 + Z_2)^2} \quad (2.3)$$

where R is the energy (or intensity) reflection coefficient, measured in MRayl ($\text{kg}\cdot\text{s}^{-1}\cdot\text{m}^{-2}$). Typical acoustic impedance of soft tissue is 1.3 – 1.7 MRayl, with differences between blood vessels, fatty layers and muscle causing relatively strong reflections [70]. The reflection coefficient between water and quartz, as a representative material of high density and SoS, is 0.8 [71]. This means 80% of the energy is reflected back towards the transducer, which is useful as a reference pulse-echo signal.

The voltage signal converted from the ultrasound reflections incident upon a single element transducer is called an A-scan, and has its own uses in medical diagnostics. A-scans are more widely adopted for non-destructive testing in an industrial setting. An array of elements, for example 64 or 128, is used in imaging, where the A-scans from all elements are displayed beside each other and a 2-D image can be formed.

Basic ultrasound analysis uses the knowledge of the SoS in a material and, by measuring the time delay, Δt , between the emission of the pulse and echo received, the depth, d , of the reflecting tissue boundary can be calculated by

$$d = \frac{c\Delta t}{2} \quad (2.4)$$

In this equation, d is the depth of the reflection and the factor of two is required to account

for the wave travelling to and from the target, back to the transducer face. Several methods exist to experimentally measure the SoS using a transducer; a review of these methods is given in [72].

Though tissue can be heterogeneous, the SoS is usually assumed to be constant within a material at a specific temperature. It is taken to be 1540 ms^{-1} for soft tissues but can range from $1350 - 1700 \text{ ms}^{-1}$, with fat having a much lower SoS than cartilage [73]. Due to its higher stiffness, bone can have c up to 4000 ms^{-1} [74].

While there is no particular relationship between the SoS and frequency set by the ultrasonic system, there was slight dispersion noted in human brain samples and this is attributed to relaxation theory [75]. In one of the few records of ultrasonic measurements of fresh human brain, Kremkau et. al found that the SoS varied from 1561 ms^{-1} to 1566 ms^{-1} at $37 \text{ }^\circ\text{C}$ [76]. Temperature may also affect the results of SoS in brain tissue, though this has not been published in brain tissue yet. However, the SoS in other soft tissues was observed to increase with temperature (by around 10 ms^{-1}) when conducting experiments at room temperature as opposed to 40°C [77]. Furthermore, rarely are speeds of sound reported above 30 MHz, as attenuation makes it difficult to use a sufficiently large tissue sample to examine the macroscopic propagation of ultrasound through it, due to the amplitude of the signal decaying away as it travels through the attenuating medium.

2.3.2 Attenuation

In all biological tissues, refraction, dispersion, scattering and absorption all contribute to the total signal loss, or attenuation, of the tissue [12]. The mechanisms behind absorption and dispersion of ultrasound in biological media were studied extensively in the 1970s and collated by Bamber et. al in 1986 [74]. Understanding attenuation is of the utmost importance throughout this project, because of the HF systems studied, as these lead to very high signal losses, even when the tissue sample is only a few centimetres thick. Besides, QUS analysis requires a separation of the scattering component from the total attenuation, in turn requiring attenuation compensation, which needs accurate measurement of attenuation in the tissue under investigation at the operating frequency of the transducer. The theory behind why attenuation occurs is only briefly discussed before focusing on methods to accurately measure it at high frequencies.

Absorption of ultrasound wave energy occurs as molecules of the material have gained kinetic energy from the wave as it propagates through. Signal amplitude will degrade into heat when the density fluctuations in the material become out of phase with the sound

pressure fluctuation. As frequency increases, the molecules become more out of phase, losing more energy to heat. At frequencies higher than the relaxation frequency, the wave cannot perturb the equilibrium of the media and there is very little energy able to propagate in its translational form, leading to the majority of the wave energy being absorbed by the material [74].

Modelled simply, attenuation is a constant loss, a , of the wave power, which is uniform for each centimetre of path length. If the initial wave power is W_0 , then the corresponding power, W , throughout the material, as a function of time and depth, can be written as:

$$W(x, t) = W_0 e^{-ax} e^{i(kx - \omega t)} \quad (2.5)$$

where k is the wave number and ω is the angular velocity, related by:

$$k = \frac{2\pi}{\lambda} = \frac{2\pi f}{c} = \frac{\omega}{c} \quad (2.6)$$

By simply taking the natural logarithm of Equation 2.5, the attenuation, in nepers per cm, is

$$a_{Nepers} = -\frac{1}{x} \log_e \left(\frac{W}{W_0} \right) \quad (2.7)$$

For many purposes, it is more convenient to report this in terms of the pressure, or signal amplitude, V and to express the attenuation in decibels.

$$a_{dB} = -\frac{20}{x} \log_{10} \left(\frac{V}{V_0} \right) \quad (2.8)$$

This is a measurable quantity if the signal amplitude can be determined before and after travelling through a distance, x , within the tissue.

Whilst attenuation is in theory a measurable quantity for biological materials, the practical application of measurement techniques can be challenging. The most widely adopted method in general acoustics is the transmission loss (TL) method, where the received signal from a system is measured before and after insertion of a tissue sample. This requires the propagation distance to be determined accurately, which may be difficult when dealing with extremely soft tissues, of which brain is an example.

Two main approaches adopted in the literature are broadband and narrowband techniques. The choice usually depends on the usable bandwidth of the transducer, which depends on its design. A 10 MHz narrowband transducer has most of the waves' energy concentrated at the centre frequency, with rapid spectral decay on either side, so it may have a usable frequency

range only from 8 - 12 MHz. On the other hand, a broadband transducer will have its energy spread over a range of frequencies, such as 5 – 15 MHz, but still peak at the centre frequency.

The narrowband technique will find the TL, which is the difference in the natural logarithm of the voltage received by the transducer with and without the tissue sample present. Using Equation 3.8, this will give an attenuation result at a specific frequency, but it can be repeated at several different frequencies, if multiple transducers are available, to build up an understanding of the attenuation of the tissue over a larger bandwidth. Broadband techniques, on the other hand, utilize the whole range of energy spread across the bandwidth of the transducer, using the power spectrum from the received signal before and after insertion of the tissue. Typically, in such spectral analysis, a windowing, or apodization, function is used to remove side lobes in the frequency domain. A Hamming window is often used, defined in Equation 2.9:

$$Ham(t, L) = \begin{cases} \frac{1}{2} \left[1 - \cos\left(\frac{2\pi t}{L}\right) \right], & 0 \leq x \leq L \\ 0 & \text{otherwise.} \end{cases} \quad (2.9)$$

where L is the gate length of the signal, which should be the length of the full received pulse in this case. The power spectrum from the received signal is given by:

$$W(f) = |FFT(V(t, L) * Ham(t, L))|^2 \quad (2.10)$$

i.e., the squared magnitude of the fast Fourier transform (FFT) of the received signal with tissue present. The voltage can be replaced with the power spectrum in Equation 2.8 and, to account for the use of squared magnitude in Equation 2.10, the final value for attenuation should be divided by 2.

In this case, the attenuation derived will be a continuous function over the usable frequency range, which will show an increase with frequency. However, the relationship is not straightforward. In the simplest approximation, which is still regularly adopted, the attenuation is assumed to increase linearly with frequency, i.e. an attenuation coefficient, a_c , measured in $\text{dB MHz}^{-1} \text{ cm}^{-1}$ can be used to estimate the attenuation value of tissue at any given frequency. Therefore, the total attenuation of the tissue through a distance, d, will be given as:

$$a_{Total} = a_c f d \quad (2.11)$$

This can be a useful approach to compare different tissues, as often a range of frequencies is used in the literature to measure attenuation.

Another approach is to plot the attenuation per centimetre over a range of frequencies, as shown in Fig. 2.6 for various biological media. Water has a much lower attenuation than tissue as it is easier to displace molecules in liquids than solids. Bone, and high-density materials, attenuate ultrasound rapidly, whereas soft tissues including liver and brain have moderate attenuation. The majority of the data available in the literature on attenuation are measured between 1 and 10 MHz, including for brain tissue.

A recent study by Rabell-Montiel et. al measured attenuation values using a broadband technique from 12 - 35 MHz in murine brain, liver and kidney and found a combination of linear and frequency squared dependence to most accurately fit the results over the entire bandwidth [78]. This study indicates the attenuation of murine brain to be 10 dB cm^{-1} at conventional imaging frequencies, increasing to 25 dB cm^{-1} at 30 MHz. This is a very important consideration as information can be lost if useful signals are not detected by the transducer.

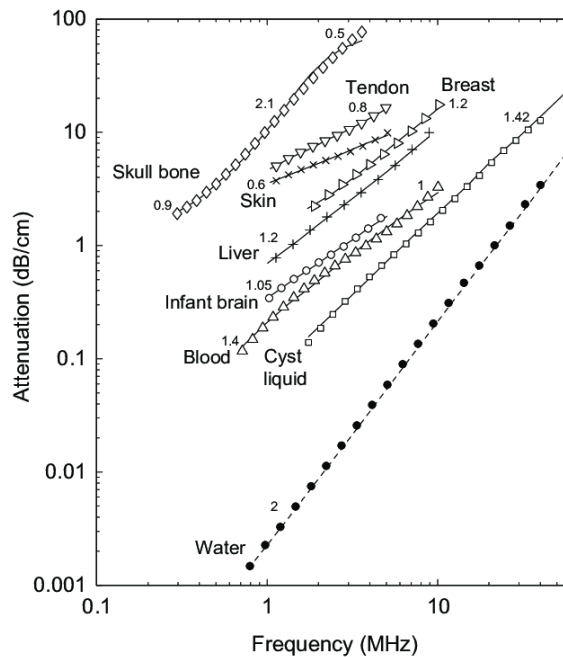


Figure 2.6: Attenuation of various biological tissues, with associated power law of frequency dependence, from [79].

2.3.3 Acoustic Properties of Brain and Brain Tumour

This section presents a summary of the acoustic properties of brain and brain tumour from the literature as these are key to the development of suitable phantom materials described in

Chapter 4. The complexity of human brain tissue makes it an extremely heterogeneous subject. For example, different acoustic properties have been measured between white and grey matter [76]. Nonetheless, it is accepted that the average density of normal human brain is 1040 kg m^{-3} and the acoustic velocity is 1550 ms^{-1} [80].

A realistic brain tissue phantom was constructed for ultrasound thermal therapy using bovine gelatine powder dissolved in ethylene glycol. The density and acoustic velocity of this phantom were, respectively, $1040 \pm 40 \text{ kgm}^{-3}$ and $1545 \pm 44 \text{ ms}^{-1}$, with an attenuation value of 0.6 dB at 1 MHz [81]. Furthermore, a study in 2008 reported calculation of the acoustic attenuation of brain tissue and meningioma intraoperatively, to highlight the diagnostic capabilities of quantitative ultrasound parameters [38].

The authors found the attenuation of healthy brain, 4.5 dB cm^{-1} , to be significantly higher than the figure for benign tumour, 2.5 dB cm^{-1} , at a frequency of 6 MHz. However, this conflicts with the results of a large study from 1968 which measured the properties of brain and several different types of brain tumours *ex vivo* [82]. It found that meningioma has a greater attenuation than healthy brain, and glioma (tumour of glial tissue) has an attenuation coefficient similar to but slightly more than for healthy tissue over the frequency range 5 - 10 MHz. A summary of attenuation results reported in the literature can be seen in Fig. 2.7 [38], [76], [78], [82], [83]. Standards have been prepared for commercial phantoms by the International Electro-technical Commission (IEC) which recommend an acoustic velocity of 1540 ms^{-1} and attenuation coefficients of 0.5 - 0.7 dB cm^{-1} for a frequency range of 2 - 15 MHz, with a linear relationship between attenuation and frequency [84]. It is clear that the IEC standard, shown as a dotted line, would not adequately describe the acoustic properties of healthy brain tissue.

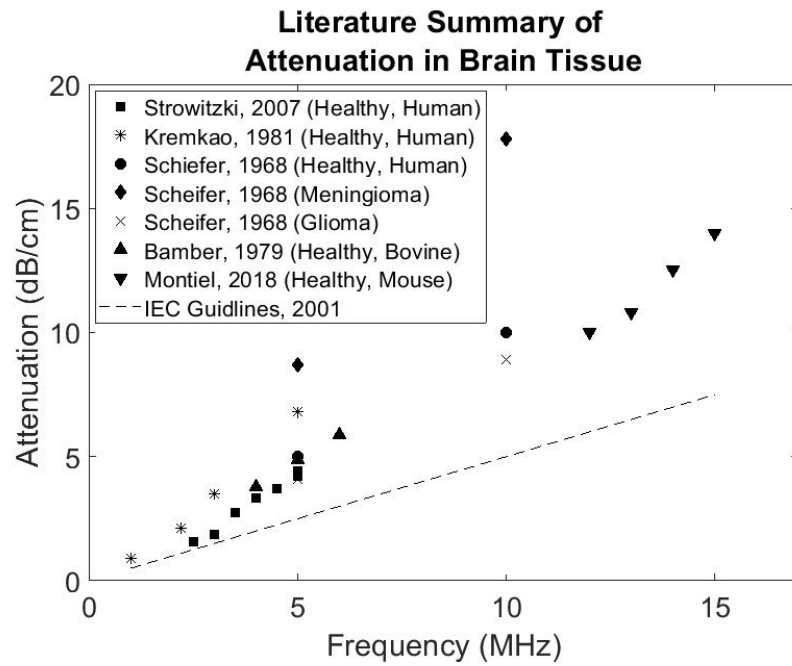


Figure 2.7: Summary from the literature of acoustic attenuation of healthy and cancerous brain tissue in human and animal studies.

There is scarce literature available on the acoustic properties of brain tumour to aid in the development of a brain tissue specific phantom. One study measured the density, velocity and attenuation of a range of primary brain tumours and these results are displayed in Table 2.2[85].

Table 2.2: Reported values of acoustic properties of human brain tumours measured *ex vivo*.

	Cases	Density (kg/m^3)	Velocity (m/s)	Acoustic Impedance (MRayl)	Attenuation at 5MHz (dB cm^{-1})	Attenuation at 10 MHz (dB cm^{-1})
<i>Meningioma</i>	15	1061	1546	1.64	8.7	17.8
<i>Astrocytoma</i>	12	1040	1503	1.56	3.9	8.5
<i>GBM</i>	7	1041	1511	1.57	4.1	8.9
<i>Metastasis</i>	7	1044	1519	1.57	6	11.9
<i>Normal Brain</i>	62	1040	1550	1.61	5.0	10.0

An accurate measurement of the bulk acoustic properties of brain tissue is imperative as attenuation must be compensated for in subsequent QUS analysis.

2.3.4 Scattering

Attenuation measures all energy lost by insertion of the tissue into the acoustic path. However, the specific process which causes ultrasound to lose energy to the surroundings that is of interest here is through scattering. This occurs when ultrasound travels through a material with sub-wavelength inhomogeneities, such as any biological medium. Diffuse scattering is observed when the ultrasound wave meets a rough boundary of acoustic impedance mismatch, as a result of irregularities within the medium material, and diffracts ultrasound waves in various directions [86].

A spherical wavefront is produced from a scattering source, or 'scatterer', which in turn may be incident on other scatterers in the material. The result is a speckled pattern in the B-mode image, such as in Fig. 1.1a. A schematic of this situation is shown in Fig. 2.8, which also shows an A-scan of the resulting ultrasound energy returning to the transducer from these interactions. The unprocessed ultrasound signal is referred to as the RF signal and is often filtered to try to improve the image quality. However, there is information contained in the small scattering signals which is crucial for tissue characterisation at a microscopic level.

Any biological material will contain inhomogeneities and brain tissue is an organ of considerable microscopic complexity, so there will be significant variations in tissue microstructure [41]. Furthermore, tumour pathology observed using an optical microscope showed various sources of scattering including tumour nodules often arranged in clusters of 50 - 150 μm diameter. Given this complexity, it is not possible to model every fluctuation and inhomogeneity in tissues, so a statistical approach is taken to describe the size and distribution of scatterers within the material.

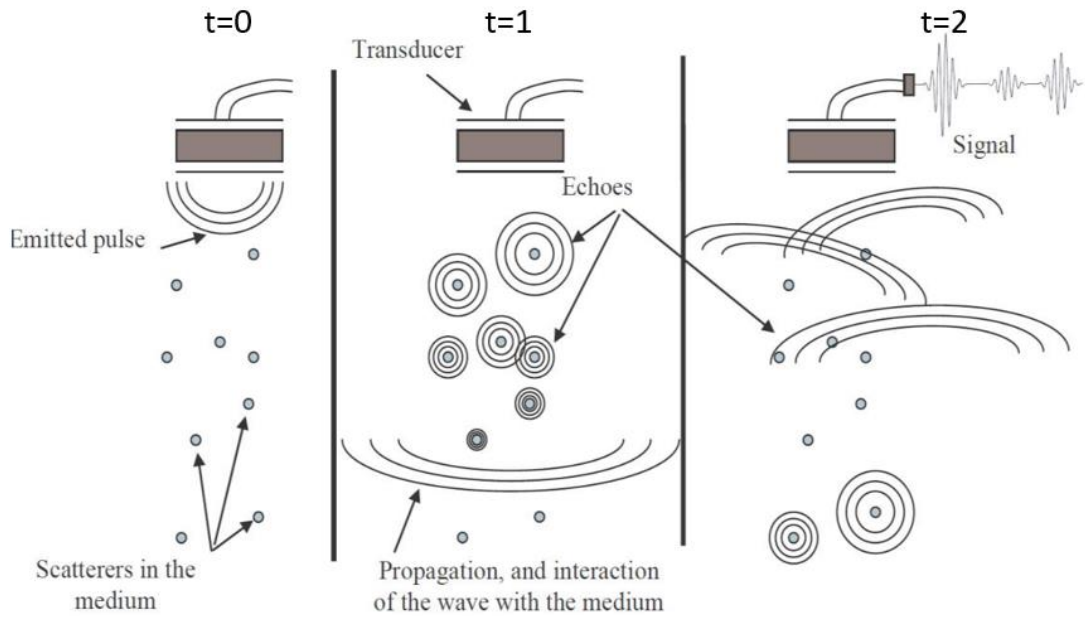


Figure 2.8: Diagram showing the formation of scattering over 3 timesteps when ultrasound is incident on a material containing scattering sources. The image on the right shows (top right) a typical received signal from these interactions, from [87].

There are two different approaches to obtain information about tissue microstructure from the RF data: spectral parameters can be used to analyse the RF data in the frequency domain, and echo envelope statistics compare the amplitude of the echo envelope of the RF data to statistical distributions. A typical RF data set and echo envelope signal for a tissue scattering region are shown in Figure 2.9, which highlights the difference between the RF data and echo envelope.

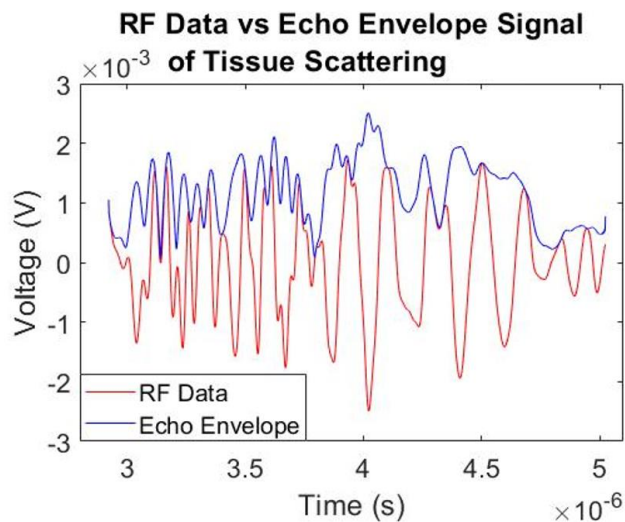


Figure 2.9: Comparison of RF ultrasound data (red) and echo envelope data (blue) from chicken liver tissue.

The RF data is the voltage signal from the transducer from a tissue scattering region, $V(t)$, and is measured experimentally. The echo envelope signal, A , is then the magnitude of the Hilbert transform of the signal response, defined for discrete time signals as [88]:

$$A(nT) = |H(V(nT))| = \left\{ \begin{array}{ll} \left(\frac{2}{\pi} \sum_{n \text{ odd}} \frac{V(nT)}{k-n} \right); & k \text{ even} \\ \left(\frac{2}{\pi} \sum_{n \text{ even}} \frac{V(nT)}{k-n} \right); & k \text{ odd} \end{array} \right\} \quad (2.12)$$

where T is the sampling period, the time difference between two sampling instants of an analogue signal. This relates to the sampling frequency, f_s , determined by the experimental set-up and should be at least twice the maximum frequency in the bandwidth of the ultrasound source to satisfy Nyquist's sampling theorem:

$$T = \frac{1}{f_s} \quad (2.13)$$

2.4 THE ROLE OF IUS IN NEURO-ONCOLOGY- A LITERATURE REVIEW

2.4.1 Conventional B-mode

The bandwidth of a transducer is the usable frequency range and is typically 2 - 10 MHz which will allow an imaging depth of 12 - 5 cm. Probe shape is an important consideration as only a small opening of the skull – a ‘burr hole’ - is normally used to access the brain tissue. A summary of the different probes used currently in neurosurgery is shown in Fig. 2.10. The lines represent the excitation and reception paths of ultrasound waves outside the transducer which will form the shapes of the images produced.


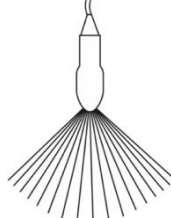
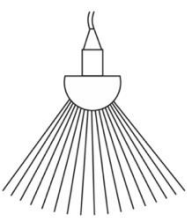
	Linear Array	Sector (Phased) Array	Curved Linear Array
			
Frequency range	Higher (8–15 MHz)	Lower (2–6 MHz)	Higher (2–12 MHz)
Depth of imaging	Superficial (1–4 cm)	Deeper (4–8 cm)	Intermediate (2–6 cm)
Field of view	Linear, limited (depends on footprint)	Trapezoidal, wider at depth, narrow at the surface	Trapezoidal, wide at surface and depth

Figure 2.10: Ultrasound probes currently being used in neurosurgery [89].

In this thesis, HF is considered to be above 15 MHz, with bespoke commercial HF ultrasound transducers typically operating with a centre frequency of 25 – 40 MHz. However, there have been limited reports of use in brain tissue [13]. No instances of ultrasound of frequencies higher than this regime being utilised for brain tumour detection were identified during the literature search. There have been many studies which concluded that conventional B-mode ultrasound is useful for visualising the tumour and boundary intra-operatively [14] [20] [3] though all studies agreed that the brain-tumour boundary is difficult to locate in glioma patients. In a large patient study, Chacko et al. demonstrated that all tumours appeared hyperechoic, however clear margins were seen in only 71% of cases [16]. As surgery proceeds, artefacts make the boundary harder to visualise and often ultrasound images over-estimate tumour margins (Fig. 2.6a) [90]. Furthermore, in HGG, the invasive nature of the cancer and limited acoustic contrast between healthy and malignant tissue prevents the delineation of the two tissue types with conventional ultrasound, as illustrated in Fig. 2.11b.

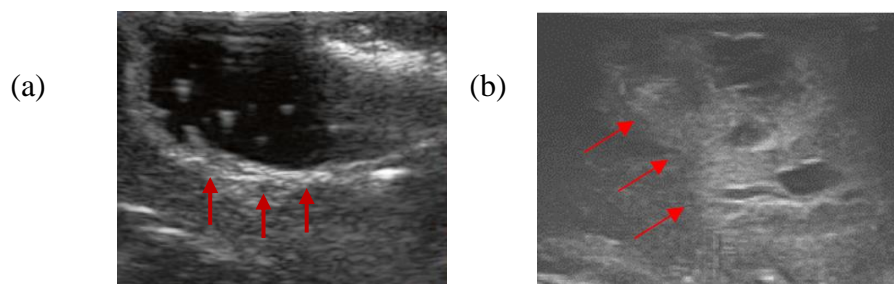


Figure 2.11: a) Resection cavity showing a light shadow (red arrows), which is an artefact, not residual tumour at 5MHz. This is due to differences in acoustic impedance of saline-filled cavity and brain tissue[27]. b) Intraoperative HGG image where tumour margins are difficult to fully delineate at 7 MHz.

Coburger et al. investigated the use of a 15 MHz miniature linear array probe after near total resection in GBM patients (Fig. 2.12a) [18][91]. Sensitivity and specificity were calculated based on biopsy samples and histopathological correlation and then compared for HF IUS, conventional IUS and intraoperative MRI. The highest sensitivity for residual tumour detection was found in intraoperative MRI (83%), followed by HF IUS (79%), and finally conventional IUS at 5 MHz (21%). This shows HF ultrasound gives image quality approaching that of intraoperative MRI, which could be due to the reduction in image artefacts as the probe is small enough to be placed inside the resection cavity. An example of the resolution capability at this frequency in visualising a GBM resection *in vivo* is shown in Fig. 2.12b.

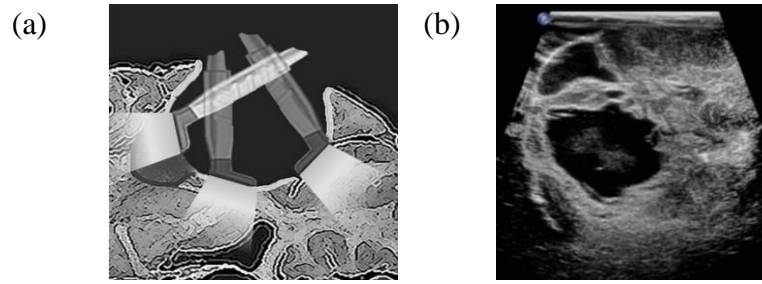


Figure 2.12: a) Application of a hockey stick-shaped linear array probe [18]. b) High resolution (15 MHz) image of GBM showing necrosis (dark areas) and diffuse infiltration surrounding them [19].

A trade-off exists between image resolution and penetration depth due to the frequency dependence of attenuation. This is discussed in more detail in Chapter 3 but, in summary, as the wave propagates through the tissue, energy is absorbed through scattering and heat, so signals are significantly weaker at greater depths. Modern ultrasound machines maximise image depth by applying a time-gain control (TGC) to the image, meaning signals from deeper in the tissue are amplified more than those nearer the transducer [92]. At 30 MHz in brain tissue, typically the maximum penetration depth is 3 cm, which may prevent IUS from being used routinely in the operating room.

The flexibility in the manufacturing of ultrasound probes means there are innovative ways to overcome these limitations. This is of use in transsphenoidal surgery, in which the surgery is carried out via the patients nose, by using a miniature probe [93]. It was also shown to be important in aiding in resection of superficial gliomas through a burr hole [54]. There are still challenges associated with manufacturing of small microultrasound arrays [94], as well as orientation problems for the surgeon. Alternatively, images of vasculature in the brain have been taken through the skull using a helmet containing 512 array elements operating at 1 MHz [95] and transcranial low-frequency ultrasound has been used to distinguish brain tumours through suitable sections of the skull [96]. Furthermore, the use of ultrasound in neuro-oncology is not limited to conventional grayscale images. Ultrasound offers multiple sub-modality possibilities and recent studies have highlighted the potential of these additional approaches through clinical trials. Summarised in Fig. 2.13, these sub-modalities of IUS will be briefly introduced in the following section.

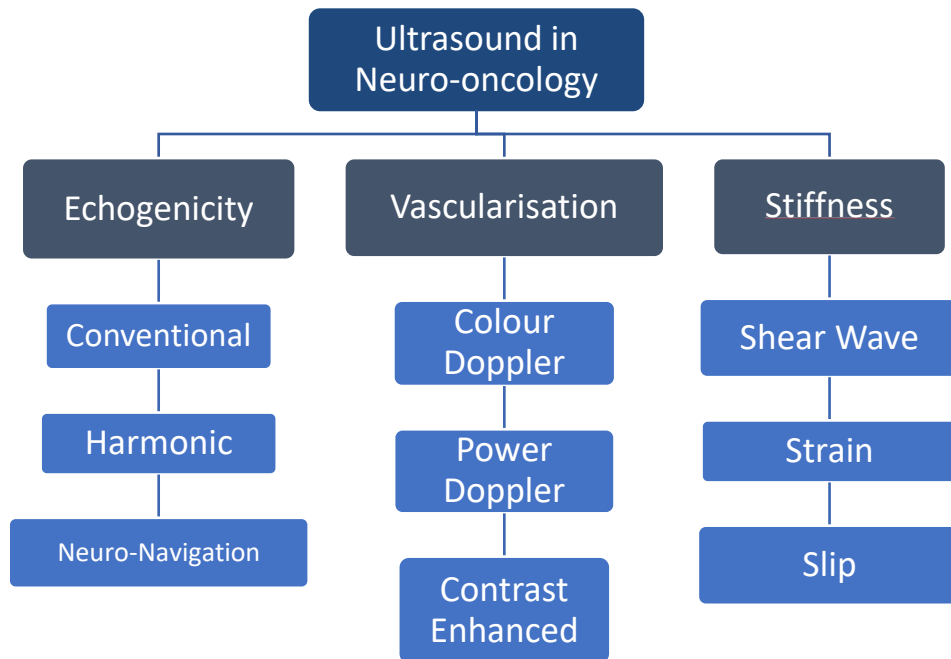


Figure 2.13: Chart displaying the different imaging modalities currently being researched in neuro-oncology. The modalities are arranged depending on which biomarker (Echogenicity, vascularisation or stiffness) is being utilised.

2.4.2 3D/ Neuro-navigation

Neuro-navigation superimposes 3D MRI images into a coordinate system within the patient's head. Real-time 3D ultrasound images are now being incorporated into such systems [19][97]. The SonoWand system (SonoWand, Trondheim, Norway) acquires a series of 2 - 300 2D images that are computed automatically into a 3D volume that can be displayed in any plane, including the familiar axial, coronal and sagittal views, which is beneficial to the surgeon (Fig. 2.8) [98].

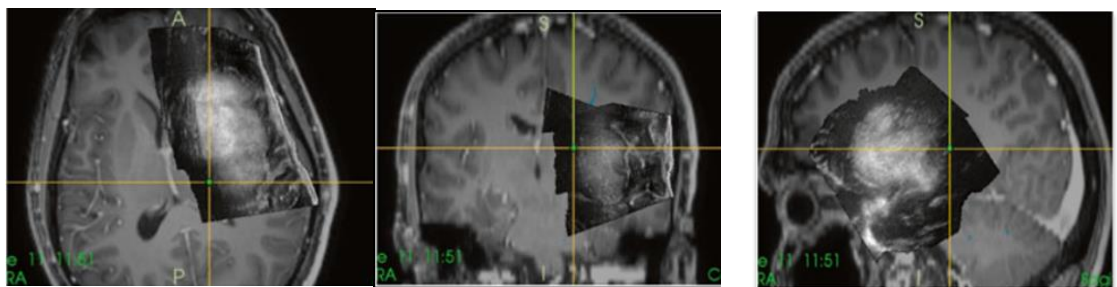


Figure 2.14: Real-time B-mode images superimposed on preoperative MRI to ease the surgeon's image interpretation [19].

Unsgaard et al. documented improved accuracy of 3D ultrasound in GBM surgery, owing to the team's experience with ultrasound over time [99]. Before resection, both specificity and sensitivity were as high as 95% using real-time ultrasound. However, as resection began,

sensitivity became poor (26%) which meant a larger amount of tumour tissue appeared normal on the ultrasound image and may have been missed by the surgeon [100].

2.4.3 Harmonic Imaging

Harmonic imaging makes use of the non-linear propagation of ultrasound in tissues. By selectively filtering out the fundamental frequency, it allows the transducer to receive only the (higher) harmonic frequencies. This comes with the advantages of higher frequency US, including increased axial and lateral resolution, decreased reverberation and side-lobe artifacts [19].

2.4.4 Doppler and Contrast Enhanced Ultrasound

Due to their rapid formation, tumours have a more prolific blood supply than healthy tissue and will often have a main feeding artery [19]. Ultrasound undergoes the Doppler effect, so it can be used to image moving targets, giving a quantitative value of blood flow velocity. Many studies have concluded that Doppler imaging is useful to visualise tumour pathology and avoid damage to the main blood vessels during surgery [45]. Doppler imaging is a well-established technique, and it has seen recent implementation with miniature probes in neurosurgery [18].

Contrast enhanced ultrasound (CEUS) involves the injection into the bloodstream of contrast agents, or microbubbles, which can then amplify signals coming from the blood vessels, as an improvement to traditional Doppler [15]. When excited by an ultrasound wave, these bubbles undergo contractions and expansions with a frequency depending on their radius. They then act like radial ultrasound sources themselves, with their behaviour detected and displayed overlaid on an original B-mode image.

CEUS is well established in hepatology where it is considered to give the same image quality as MRI and CT, therefore being superior to B-mode imaging [101]. Prada et al. have published several studies observing that CEUS is able to highlight residual tumour masses in glioma surgery, especially when tumours have an ill-defined border in a conventional B-mode image [102]. An example of the CEUS sequence of images is shown in Fig. 2.15, from one of the studies of Prada et al. in a GBM patient, and it is concluded that resolution is improved and allows imaging of microvasculature systems in glioma patients intraoperatively [103]. There are some limitations of this modality, for example, only one portion of the lesion can be analysed at a time and the probe must be accurately placed to gain as much information as possible in the limited time available. Care must also be taken with preparation and injection of contrast enhancement agent [101].

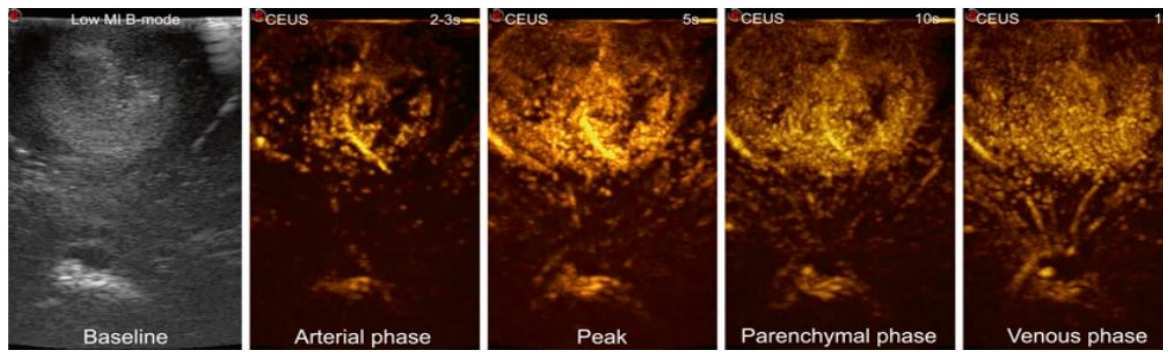


Figure 2.15: Intraoperative CEUS image of GBM case. In arterial phase, the main veins feeding the tumour can be seen, in peak and parenchymal phase it is possible to differentiate more viable and necrotic or cystic areas. In venous phase, multiple small veins draining towards the ventricle are visible [103].

2.4.5 Elastography

Most tumours have different mechanical properties to surrounding tissue. Surgeons make use of this during surgery by palpating tissue to determine which to remove, with cancerous tissue being stiffer than healthy. The extent of which may depend on malignancy [104]. These differences in stiffness do not arise from the cells themselves, but from the material in the space in between cells: the extracellular matrix [105]. Elastography provides an image of tissue elasticity, either qualitatively or quantitatively. The main methods under investigation in neurosurgery are strain elastography and shear wave elastography (SWE).

Strain elastography can provide an image showing the relative stiffness of one type of tissue compared to another. It makes use of the radiofrequency (RF) data pairs from conventional B-mode images, one of which is obtained with the transducer placed on the surface of the tissue and the other a compressed signal obtained by manually compressing the target [106]. In 2012, Selbekk et al. compared the contrast of B-mode imaging to strain elastography in gliomas [107]. The operator identified the tumour boundary and local maximum and minimum values of the amplitude were used to calculate contrast ratio. Strain elastography was shown to have a significantly higher contrast than B-mode alone, however images were still processed offline. The first real-time elastography images in neurosurgery were obtained in 2009 by Uff et al. [108] and the results showed excellent correlation with the surgeon's assessment of stiffness. It was also noted that areas of high axial strain corresponded to slip locations on the brain-tumour boundary. The same team has further characterised this phenomenon, termed 'slip elastography' with experimentation and simulation to visualise the tumour margin [109]. Selbekk et al. also showed that the pulsations of the brain due to arterial pressure variations provided sufficient tissue movement to enable strain to be calculated [110]. Strain imaging could be used to differentiate between solid tumour and normal brain qualitatively, as indicated by the arrows in Fig. 2.16. However, this technique

is highly dependent on the user and possible side effects of compressing brain tissue are not well understood.

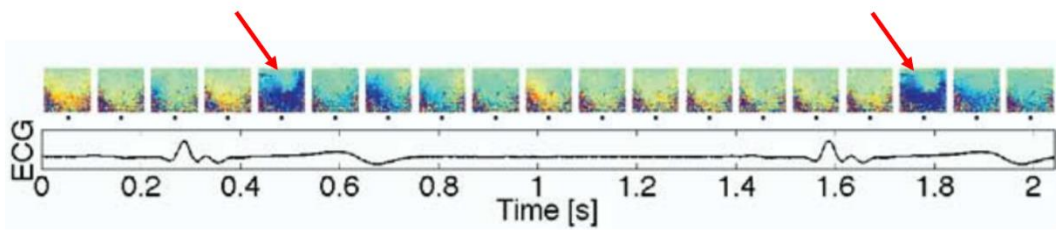


Figure 2.16: Comparison between strain elastography image and ECG. The red arrow indicates tumour in elastography image; note the delay in pressure as blood travels from the heart to the brain, causing pressure on transducer [110].

Shear wave elastography (SWE) allows a quantitative measurement of stiffness by calculation of Young's Modulus, a quantity used to measure stiffness of linearly elastic soft tissue. Instead of using external compression, shear waves are generated in the tissue by acoustic radiation force [111]. The propagation speed of the shear wave, typically only around 10 ms^{-1} , is tracked using an ultra-fast US scanner [112]. Young's modulus can be estimated once shear wave velocity is known. The Aixplorer system (Supersonic Imagine, Aix-en-Provence, France) was used *in vivo* during tumour neurosurgery to obtain values for the shear modulus of brain tissue and several types of brain tumours [113]. The mean Young's modulus of healthy brain was found to be 7.1 kPa while both malignant and benign tumours were found to be stiffer, ranging from 11.4 kPa - 33.3 kPa. However, the anisotropy in stiffness of healthy brain tissue was illustrated using SWE in rat brains *in vivo*, for which the values varied from 2 - 25 kPa depending on location and orientation in the brain [114]. In his PhD thesis, Chan optimised the use of SWE in neurosurgery, assessing the effect that system settings had on the resulting image [115]. He found SWE to be superior to B-mode imaging and comparable to MRI in brain tumour visualisation (Fig. 2.17). In comparison to histopathology, the use of SWE yielded a sensitivity of 94% and a specificity of 77%. The value of specificity is low compared to standard B-mode imaging (around 90%) and it corresponds to an overestimation in tumour volume, which could be especially problematic in neuro-oncology. However, this method is highly sensitive - there have been reports of SWE detecting MRI-negative lesions [116].

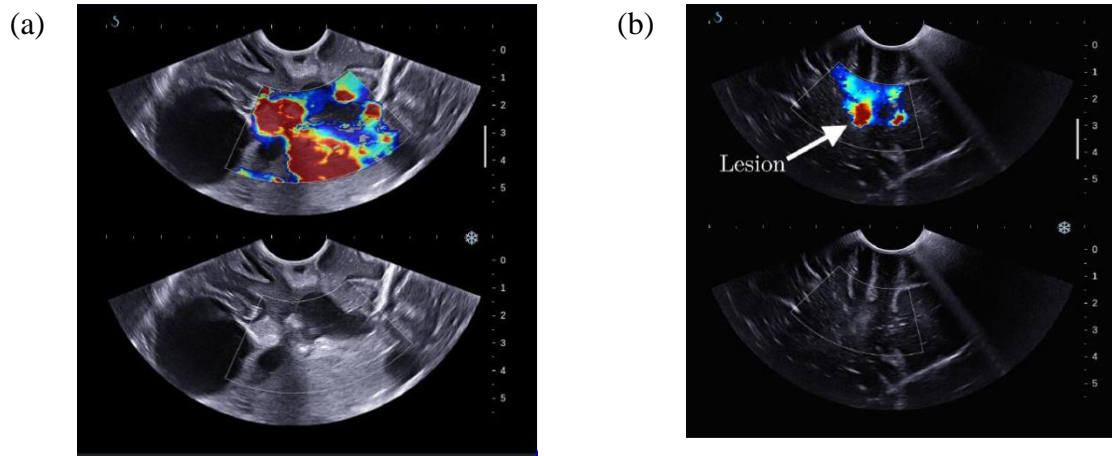


Figure 2.17 a) SWE vs B-mode, stiff (cancerous) regions are shown in red. b) SWE vs B-mode highlighting a lesion which is almost invisible on standard B-mode image [116].

SWE is promising as an improvement to B-mode ultrasound; however, only high-end ultrasound systems have the capability of ultrafast detection to measure the shear wave speed, which means the technique is not easily accessible to the majority of surgeons.

Ultrasound has gone through considerable developments in recent years and can now offer a range of new imaging modalities as standard on many machines such as those produced by BK Medical[®] (GE Healthcare, USA), Canon Medical[®] and Siemens Healthineers[®]. These companies offer a range of equipment but all will include B-mode imaging, harmonic imaging, Doppler ultrasound and strain elastography, with the high-end machines also offering shear wave elastography [117]. As an example, the SonixTouch Q+ (BK Medical, 2015) is a mid-range commercial machine that supports probes with centre frequencies of 2 - 30 MHz. It also offers colour Doppler and strain elastography. Appendix I gives an insight into the capabilities of current clinical machines to image porcine brain *in situ* and *ex vivo*.

An ultrasound-related method in early development is photoacoustic imaging, which allows interrogation of matter at the molecular level. A laser is used to excite molecules and, with photon activation, the molecules then undergo characteristic non-radiative decay, producing ultrasonic waves dependent on the molecules excited [118]. In 2017, Dahal and Cullum investigated the ability of multiphoton photoacoustic spectroscopy to distinguish between healthy and malignant (WHO III glioma) brain tissue *ex vivo* at two different wavelengths [119]. The multiphoton (in this case two-photon) excitation is achieved by using a near infrared radiation source, and has been developed as it can reach molecules at greater depths (up to 1.4 cm) than conventional photoacoustic imaging [120]. The exact chemical species

responsible is unknown but the authors demonstrate photoacoustic imaging has a clear ability to distinguish between the samples.

QUS is another sub-modality of ultrasound which has not yet been realised in glioma detection. It seeks to overcome the limitations of conventional ultrasound, such as the lack of acoustic contrast between healthy and cancerous regions, by extracting information on tissue microstructure from the ultrasound signal for tissue characterisation purposes. Some methods exploit the frequency dependence of the backscattered signal, while others focus on modelling the amplitude distribution of scattering to the physical distribution of scatterers. The following section presents a review of QUS as a diagnostic tool in other tissues and diseases.

2.5 QUANTITATIVE ULTRASOUND

2.5.1 Introduction

QUS can be considered as assigning some numeric values to certain characteristics of the received tissue signal from the tissue scattering region. Scattering occurs when an ultrasound wave encounters an acoustic inhomogeneity at a scale similar to or smaller than its wavelength, λ . This occurs throughout many biological tissues, with the incident beam scattered in all directions, as visualised in Fig. 2.18.

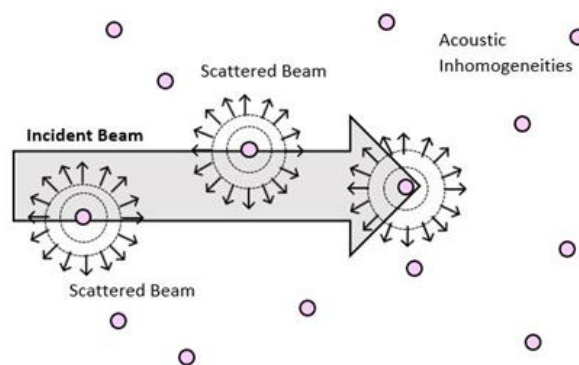


Figure 2.18: Scattering in tissues due to incident ultrasound source from the left. Structures of a similar size to λ will contribute to radial source of scattering as depicted by scattered beam.

This causes the grainy, or speckled, appearance of B-mode ultrasound images. Alternative approaches of analysing the scattering component of the RF data were largely due to the work of Frederic Lizzi, whose group developed the theoretical framework behind ultrasound scattering in tissues [121]. The BSPS measures the amount of signal scattered back to the

transducer from the tissue region over the bandwidth of the transducer. The dependence on frequency was shown to give useful parameters for tissue characterisation, termed ‘Lizzi-Fellepa parameters’ [23]. These parameters were based on the slope and intercept of the BSPS, when plotted against frequency, and can be used as system-dependent QUS parameters on their own. However, further work was done to relate them to a theoretical description for scattering within tissues [25].

Biological tissue can be modelled as a homogeneous medium with randomly distributed spheres of a slightly different acoustic impedance to the surrounding medium [24]. The exact size and location of each individual scatterer cannot be determined but a statistical description of the average properties in a region of interest (ROI) may be extracted [122]. Specifically, ESD and EAC are key parameters that have shown significant differences in healthy and cancerous tissues. As they are derived from the power spectrum obtained from the tissue, they are often referred to as spectral-based QUS parameters. A comprehensive review of the areas in which both spectral and statistical QUS have contributed to diagnostic ultrasound was published by Oelze and Mamou in 2016 [123]. Studies of significant notability and relevance are discussed in the following sections, as well as the latest publications in the field since the review was released.

2.5.2 Spectral- based QUS

Compelling evidence has been published on the ability of spectral based QUS to detect cancerous regions in several soft tissues [26][124]. Early studies include work from Felleppa et al. who used the frequency-dependent backscatter to obtain estimates of scatterer size and concentration from ocular tumours [23]. Mamou et al. had great success characterising cancerous lymph nodes using this technique and found that metastatic nodes had an ESD larger than that in cancer free nodes (37.1 ± 1.7 mm versus 26 ± 3.3 mm) [36]. This trend can be seen through various studies; notably in 2003, Oelze et al. illustrated that overall estimates of scatterer size were 44% larger inside rat mammary tumours than outside [25].

However, as momentum began to grow in the technique, researchers pushed to a higher frequency range, which meant attenuation compensation became very important. Briefly, as attenuation is energy lost to the tissue as the wave propagates through it, to isolate the energy lost by scattering only, the bulk attenuation through absorption and reflection must be estimated and subtracted from the total attenuation. Moreover, the frequency dependence of the attenuation must be considered over the bandwidth of the transducer. Understanding of this complex issue has developed over the last 15 years and there are still controversies

around the appropriateness of the estimation today so it is discussed in mathematical detail in Section 3.3.3.

2.5.3 Statistical-based QUS

With the published successes of spectral-based QUS, interest grew in the analysis of the RF data in different ways to conventional B-mode processing. Researchers began to explore novel ways of describing the ultrasonic signals from the echo envelope of tissue regions. This envelope is obtained from the magnitude of the Hilbert transform of the RF data from a tissue scattering region [30] and is statistical in nature as it arises from the interference of a large number of randomly distributed scatterers [35]. This signal is then modelled mathematically to yield parameters to describe the organisation structure, density and concentration of scattering components [125]. Various models have been used in the literature to describe the echo envelope statistics, the most fundamental being the Rayleigh distribution which describes randomly located and densely packed scatterers [31]. Others include, but are not limited to, the Rice distribution [126], the K-distribution [127], the HK distribution [35] and the Nakagami distribution [128].

The Nakagami distribution approximates the HK distribution and is the most commonly used model for tissue characterisation, due to its relative simplicity. The Nakagami shape parameter, m , has shown to be an accurate diagnostic tool in a wide range of applications, including parotid-gland injury detection, ophthalmology and vascular flow imaging [34]. However, the most frequent instances of the distribution occur in breast tumour classification, owed to the pioneering work done by Shankar and Tsui in this specific application [127]. At the time of their work, the calculations involved for the HK parameters were problematic and computationally advanced, so they focused only on the Nakagami parameter. Their studies showed that the Nakagami shape parameter was significantly higher in the tumour, and thus sufficient to differentiate between healthy breast tissue and a fibroadenoma, which is a solid, benign mass [129].

Despite the clinical success of the Nakagami parameter, researchers were still concerned with the approximations used in the model and the lack of distinct physical meaning of the shape parameter. As computer technology advanced, work was done by Cloutier and Destremes in the 2010s to identify an accurate estimation method for the parameters of the HK-distribution. The two parameters used for tissue characterisation are the α parameter, which measures the number of scatterers per resolution cell, and the κ parameter, which is the ratio of coherent to diffuse scattering power [125]. These can give insight into the underlying tissue microstructure, but still maintain a reasonable computation time. The HK

distribution has also been used extensively in measuring severity of fatty liver disease [37]. In 2020, Zhou et. al evaluated the effectiveness of the Nakagami parameter and the α parameter from the HK-distribution for imaging of hepatic steatosis in rats. They found α parametric imaging provided significant information associated with fat droplet size, thus suggesting a promising statistic for grading of steatosis, but they did not report on the time taken to form a parametric image [130]. Other successful applications of the HK-distribution include assessment of carotid plaque [131] and classification of rat mammary tumours [132].

2.5.4 Additional QUS parameters

Many studies have used additional parameters to those stated above, which are extensions of a specific technique, e.g. the measurement of attenuation at the centre frequency of the transducer. Alternatively, there are additional parameters obtained from general statistics of the distribution of echogenicity within the ROI. There is often no theoretical grounding to justify the use of these parameters for the specific application, yet they can prove to be powerful for classification purposes. Examples include the mean value of the echo signal, and the variance of the grayscale value and the signal to noise ratio (SNR) [131]. There is an interesting divide between theorists and clinicians regarding the practicality of use of the additional QUS parameters as they hold no physical meaning yet could be efficient and practical to implement. A combination of all parameters will be explored in this thesis.

2.5.5 Use in Neural Tissue

There is a distinct lack of application of both spectral and statistical QUS in neural tissue. This may be due to the high demand for neural tissue in research, as it used in many fields such as clinical brain science. There is simply not enough availability of tissue to meet the demands of all researchers. Nonetheless, a study conducted in 2008 collected unprocessed RF data from 20 patients intra-operatively [133]. Values of attenuation and BSC were calculated by using 10 distinct frequencies between 2.5 - 7.5 MHz. The attenuation coefficient of white matter in the cerebral cortex was found to be $0.94 \pm 0.13 \text{ dBcm}^{-1}$, which is significantly higher than that of most tissue such as liver and muscle. The authors concluded that the differences in BSC in healthy and cancerous tissues occurred only in the upper frequency band of this analysis. Studies utilising spectral methods in the brain include the assessment of apoptosis in monkey [134] and Vlad et. al looked at simple spectral parameters to measure murine response to radiotherapy through the skull, with them found to be a reliable indicator of treatment [135]. Mouse skull is significantly thinner than human skull, so the same technique may not be feasible for human application. There have been no reports of statistical based QUS for brain tissue characterisation, however, the Nakagami

distribution was used to aid detection of landmarks in 2D ultrasound scans of the foetal brain [136].

Realising the different capabilities of spectral and statistical methods, researchers began to incorporate an analysis of both methods into their studies. This was explored at 40 MHz in the detection of thyroid cancer where both the ESD and HK parameters had significant differences in cancerous and healthy thyroid in a mouse model [137]. The study concluded that HF QUS may enhance the ability to detect and classify diseased thyroid tissues. However, a more robust combination of the parameters is required to fully enhance the diagnostic capability of the technique and one way to do this is through machine learning (ML), which is discussed in detail in Chapter 3.

2.5.6 Combination of QUS Techniques and Machine Learning

ML is revolutionising diagnostic imaging by reducing human error. Image recognition is a potential route for ML to aid in diagnosis in ultrasound. Many studies have shown that integrating computer aided diagnosis with clinician feedback improves performance in a range of areas, including recognising benign and malignant breast masses in ultrasound images [138]. However, this requires high quality training data and clearly segmented brain-tumour boundaries, which is not always possible with current ultrasound images, especially in glioma surgery.

Other researchers have utilized QUS to its full potential for tissue characterisation by taking advantage of its quantitative nature and drawing on supervised classification methods of ML. Often clinicians are interested in a binary classification (healthy or cancerous) which is a well-established approach in ML [139]. A range of methods exist but the common idea is to take a range of parameters from a dataset and label each instance as 'healthy' or 'cancerous'. This can be extended to a larger number of groups but binary classification is sufficient for the application. Next, a percentage of the labelled data is input to the classifier as training data. Then, the remaining data, which is unseen, can be used to test how well the classifier predicts the label. The most commonly adopted classification algorithms are KNN, SVM, random forest and decision trees [139]. The performance can be measured in terms of accuracy, or often a Receiver Operator Characteristics (ROC) curve will be used. The area under the curve (AUC) varies between 0 - 1, combining sensitivity and specificity to give the overall diagnostic performance [140].

Mamou et al. utilized a combination of spectral and statistical parameters to characterise healthy and cancerous lymph nodes and found the ESD and k parameter from the HK-

distribution to be the most reliable [36]. They were able to determine a ‘cancer likelihood percentage’ and then created a classification image by using the assigned score of each pixel and colour coding it according to: $<25\%$ = green, $>75\%$ = red and amber = otherwise. Fig. 2.19 shows the classification image, highlighting in red the areas of interest, which could then be compared to a stained section which the histopathologist could determine as correct.

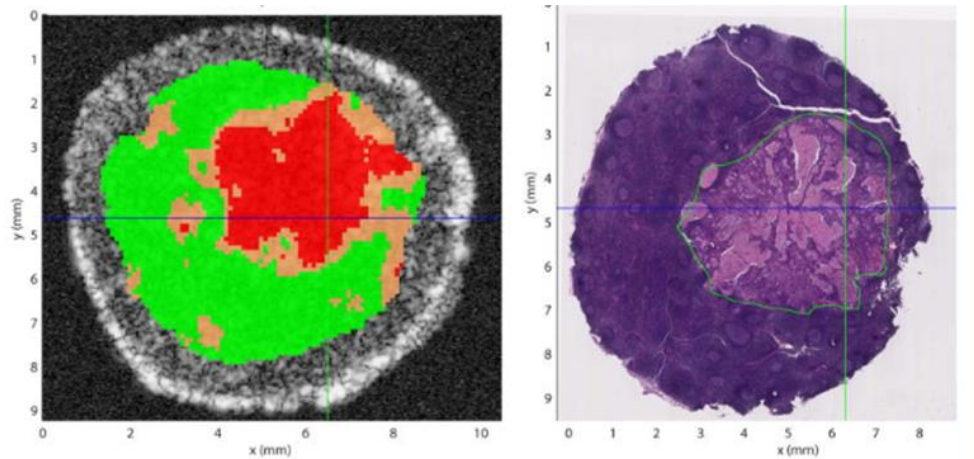


Figure 2.19: Classification of cancerous regions in excised lymph node (left) and histopathology image (right) [36].

In 2019 Nasief et. al exploited a total of 7 parameters, including the attenuation, Nakagami parameter and SNR to successfully classify carcinomas and fibroadenomas in excised breast masses [32]. Achieving a classification accuracy of 95% suggests this could become a non-invasive technique for determining benign and malignant breast tumours. Another recent instance of the effectiveness of QUS with machine learning was a 29 MHz scanning system which could successfully identify cancerous regions in the prostate using QUS [39]. Attenuation was assumed constant in both healthy and cancerous tissue. The authors calculated 15 parameters in total but, instead of using every one for the classification, they explored a variety of sets of parameter combinations. The SVM achieved good classification performance, with an AUC of 0.79, when combining envelope statistics and spectral parameters. At the same time, Roy-Cardinal et al. adopted a multimodal ultrasound approach, as the system used was capable of estimating shear wave velocity. A combination of elastography and statistical QUS was used for classification. This study used a random forest ML algorithm to classify carotid artery plaque components with 95% accuracy [131].

2.6 CONCLUSIONS

With research showing increased tumour resected correlates to marked improvements in patient prognosis, the challenge then becomes maximising the percentage of tumour resected in the OR. IUS has proven to be a useful adjunct in increasing tumour resection but still fails

to clearly depict the boundary as the surgery proceeds [13]. Higher frequency probes give greater resolution and hence can show clearer margins at the brain-tumour boundary. Trials thus far in neurosurgery have been conducted only up to 16 MHz, despite 71 MHz commercial probes being available for small animal use [141]. Elastographic techniques could offer additional contrast to improve differentiation. Strain elastography is easy to implement, however images acquired are operator dependent and there is unclear correlation with histopathology. SWE has a high sensitivity for identifying stiffer tissue, however it is only available in high end systems. CEUS and Doppler US are useful additions in instances where visualisation of tumour perfusion is sought.

QUS is a broad field which analyses RF data in a different way to conventional imaging, via spectral or statistical methods. Both have shown potential for soft tissue characterisation in liver and breast and may be translatable to brain tissue. There are still issues identified in the literature with implementing some of the QUS techniques, such as attenuation compensation at high frequencies and efficient algorithm implementation for the HK parameters. A summary of the advantages and disadvantages of these techniques is shown in Table 2.3. More research must be conducted on the impact of these developing technologies on clinical outcomes by performing clinical trials on tumour resection with a large number of patients. This will ensure the overall utility of US technology in neuro-oncology is accurately evaluated.

The results of the literature review suggest there are two key areas which offer potential to improve tumour delineation using ultrasound in the brain:

- HF (>15 MHz) imaging of healthy and cancerous tissue for improved resolution and to probe smaller microstructures with shorter wavelengths.
- QUS measurements of healthy and glioma tissue combined with ML classification to assess the differentiation capability of this technique.

Table 2.3: Advantages and limitations of ultrasound sub-modalities in neuro-oncology

Technology	Advantages	Limitations
<i>B-mode US</i>	Speed of image acquisition. Simplicity. Low cost.	High operator variability. Image artefacts give unclear diagnosis. Interpretation/ orientation problems.
<i>3D US</i>	Volumetric acquisition Possible with standard 3D US probes. Can be implemented into neuronavigation software.	Slower than 2D US. Diminished image quality.
<i>High Frequency US</i>	High spatial resolution. More reliable visualisation of tumour margins.	Poor depth of penetration. Smaller probes can cause orientation problems.
<i>Strain Elastography</i>	Visualises tumour elasticity variation. Gives greater contrast than B-mode alone.	Unclear correlation with pathology. Induced strain risks trauma to brain tissue. High operator variability.
<i>SWE</i>	Highly sensitive visualisation of tumour margins. Reduced operator variability.	High-end US system required. Over-estimation in tumour margins.
<i>CEUS</i>	Visualises tumour vascularity with greater contrast than Doppler.	Involves invasive delivery of contrast agents. Field of view is constant during injection.
<i>Photoacoustic imaging</i>	Significant differences in absorbance ratios.	No <i>in vivo</i> human trials. New technique, still needs established.
<i>Quantitative Ultrasound</i>	Visualises microscopic characteristics of tissue. Can be combined with a ML approach for user independent tissue characterisation.	Limited information on use in brain tissue. Resolution of parametric image is much less than conventional US.

2.7 CHAPTER SUMMARY

This chapter introduced the current standard of care in brain tumour patients and highlighted the particularly poor prognosis for HGG patients. Then, the need for a real-time imaging modality was given, followed by a comprehensive review of the use of ultrasound in neuro-oncology. This review highlighted the multimodality of ultrasound imaging and discussed the recent clinical trial successes of state-of-the-art imaging methods. Particularly, the manufacturing of HF probes with small footprints has allowed ultrasound to compete with the higher resolution imaging types for intraoperative tumour delineation. However, gliomas

are challenging to detect using B-mode images alone. The field of QUS, and its success in tissue characterisation was discussed, and importantly, its distinct lack of utilisation to date in brain tissue. It was concluded that the main focus in this PhD study should be the novel use of HF QUS applied to differentiation of healthy and cancerous neural tissue.

3 TECHNICAL BACKGROUND

3.1 CHAPTER AIM

This chapter describes the theory of both spectral and statistical QUS parameters, as well as providing an insight into ML algorithms for binary classification. First, the physics behind, the phenomenon of scattering within tissue is described mathematically, first in terms of the BSPS, which can be used to obtain spectral QUS parameters, and then by studying the statistics of the echo envelope. A general look at the various theoretical models of the echo envelope is given as context, before moving on to detailed explanation of the Nakagami and HK-distributions and their model parameters. The derivations of both spectral and statistical QUS parameters are provided; these have been studied for several decades but still have some controversies in practical implementation, which are also discussed. Finally, an insight into the mathematics of ML algorithms is provided, as these are used extensively in tissue characterisation, and the KNN and SVM techniques are introduced to provide a foundation for the binary classification work presented in this thesis.

3.2 SPECTRAL QUS PARAMETER ESTIMATION

Spectral parameters rely on the careful measurement of the frequency dependence of the BSPS. This is the amount of ultrasound energy received by the transmitting transducer operating in pulse-echo mode from a tissue scattering region [22]. It is obtained from the RF data from a transducer over a tissue ROI using Equation 3.10; however, it must be compensated to separate the scattering component from the total attenuation, as explained fully in Section 3.2.2.

To obtain the spectral parameters, first an experimental power spectrum is obtained. This is then compared to a theoretically derived power spectrum from a general tissue scattering model of the same size as the ROI. The mathematics behind the backscattered power spectrum have been well established since the work done by Lizzi et. al in the 1980s [24]. This includes the crucial discovery that the power spectrum depends only on two tissue parameters: the ESD and EAC, for a given frequency and size of ROI [24]. By comparing the theoretically derived power spectrum to a measured power spectrum, the tissue parameters can be estimated.

3.2.1 Theoretical Description of Backscattered Power Spectrum

Tissues can be modelled as random or structured distributions of small scatterers with slightly different acoustic impedance, Z , to the bulk tissue bulk, Z_0 , which depends on the location [23]:

$$z_{var} = \frac{(Z - Z_0)}{Z_0}. \quad (3.1)$$

The EAC, n_z , is the product of this acoustic impedance mismatch and the number of scattering sources in the material. When ultrasound is incident on this tissue, each scatterer will cause reflections in all directions, which will in turn interfere with other scatterer reflections as they return to the transducer. This will result in the received RF signal being the sum of the reflected echoes from each individual contribution.

The simplest model is to assume a random spatial distribution of scatterers throughout the tissue, and it has been shown this can be modelled as a random walk, equivalent to the sum of phasors [142]. Each contribution will have a random amplitude phase shift, depending on the size, distribution and relative acoustic impedance mismatch between scatterer and surrounding material [25].

The received signal amplitude, A , will be the phasor sum of the k individual components with initial angular frequency, ω_0 , with amplitudes A_k and phase shift θ_k :

$$A = \sum_{k=1}^{N-1} A_k e^{i\theta_k} \quad (3.2)$$

Under the assumption that the tissue contains a sufficiently large number of scatterers, the RF data can be modelled as a Gaussian distribution of zero mean and standard deviation, σ :

$$P_{A_r}(X) = \frac{1}{\sqrt{2\pi\sigma^2}} e^{-\frac{A^2}{2\sigma^2}} \quad (3.3)$$

Conceptually, if ultrasound from a 10 MHz narrowband transducer is incident on tissue, the power spectrum of the tissue will move slightly higher over the bandwidth of the transducer as a result of various interferences of randomly placed scatterers.

The frequency dependence of the RF data can be determined by finding an expression for the backscattered power spectrum, as a function of frequency, after assuming a Gaussian form factor. The acoustic form factor is determined by evaluating the Fourier transform of the spatial correlation function for the tissue medium.

In the special case of randomly positioned, spherical scatterers, the form factor is a function of the average ESD, a_{eff} , and the frequency [29]:

$$F_{Gauss}(2k) = e^{-0.827k^2 a_{eff}^2} \quad (3.4)$$

Lizzi et al. incorporated all relevant assumptions for beam pattern effects and the ROI size, L , to show that, in the frequency domain, the normalized, theoretical power spectrum is derived fully as [121]:

$$W(f) = \frac{185Lq^2 a_{eff}^6 n_z f^4}{[1 + 2.66(fqa_{eff})^2]} e^{-12.159f^2 a_{eff}^2} \quad (3.5)$$

where:

L = gate length (mm) (the size of ROI)

q = ratio of transducer aperture to distance to ROI

f = frequency (MHz)

n_z = EAC i.e. a product of n , the number of scatterers per mm^{-3} , and Z_{var} , the relative acoustic impedance of the scatterers and the surrounding medium.

The average ESD and EAC can be estimated by applying a linear fit to the measured power spectrum from the scattering echoes and direct comparison with Equation 3.5, as derived by Oelze et al [25].

First, the power spectrum from a scattering source is expressed on a decibel scale:

$$S(f) = 10 \log W(f) = 10 \log \left\{ \frac{185Lq^2 a_{eff}^6 n_z f^4}{[1 + 2.66(fqa_{eff})^2]} e^{-12.159f^2 a_{eff}^2} \right\} \quad (3.6)$$

Expanding this logarithm yields:

$$\begin{aligned} S(f) = & 10 \log(185Lq^2 a_{eff}^6 n_z) + 10 \log(f^4) \\ & - 10 \log(1 + 2.66(fqa_{eff})^2) - 10(12.159f^2 a_{eff}^2) \log e \end{aligned} \quad (3.7)$$

Typically, q is small for HF sources, so an approximation can be made by assuming $2.66(fqa_{eff})^2 \ll 1$:

$$\log(1 + 2.66(fqa_{eff})^2) \approx 2.66(fqa_{eff})^2 \log e \quad (3.8)$$

Subtracting the f^4 term and including this approximation yields:

$$S(f) - 10 \log(f^4) \approx M(a_{eff}^2) f^2 + I(a_{eff}^6 n_z) \quad (3.9)$$

where

$$M = -4.34[12.159 + 2.66q^2]a_{eff}^2 \quad (3.10)$$

and

$$I = 10\log [185Lq^2a_{eff}^2n_z] \quad (3.11)$$

Ultimately, if $S(f)$ is measured for a specific tissue region, $S_{meas}(f)$, the ESD and EAC can be found by equating $S_{meas}(f) = S(f)$ and modelling the left hand side of Equation 3.9 as a straight line in terms of the variable f^2 .

$S_{meas}(f)$ needs careful consideration and should be measured over the bandwidth of the transducer. Different equations are used for single element transducers and linear array probes respectively [83]. The specific formulas for transducer systems used in this work are given in the methods sections in the relevant chapters. If the attenuation caused by the tissue over the ROI is not negligible, which is the case in brain tissue, then a compensation function is needed to accurately obtain $S_{meas}(f)$. This is especially important at frequencies which will be used in the analysis here, higher than the conventional frequencies (>10 MHz), and thus needs particular attention.

3.2.2 Attenuation Compensation

Consider a tissue with an attenuation coefficient of $1 \text{ dB MHz}^{-1} \text{ cm}^{-1}$ being insonated at 10 MHz, such as that in Fig. 3.1. If there is a 2 cm difference between regions A and B and one is required to obtain the backscattered power section from the entire tissue sample with no correction, there would be a 40 dB difference in the amplitude of signal received from the upper and lower regions of the tissue.

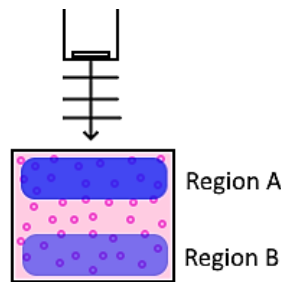


Figure 3.1: Illustration of higher perceived scattering in Region A due to bulk attenuation.

The difference between wavelets being scattered in Region A and Region B will be caused by frequency dependent losses, through absorption rather than the specific scattering the

modelled power spectrum can describe. Attenuation will diminish the contribution from scatterers in the deeper tissue region, reducing the phase components involved in the summation which will then be compared to the theoretical power spectrum. On top of this, the frequency dependence of attenuation must also be considered. This is the observation of increasing attenuation at increasing frequencies, such as that in Fig. 2.7, though there is debate around whether the relationship is linear, it is most commonly used in the literature. Both a linear model and experimentally derived attenuation function $a(f)$ is used in this work. If the effects of frequency-dependent attenuation are not carefully considered, estimations of the scatter size and acoustic concentration will be inaccurate [143].

A review of the evolution of attenuation compensation functions is given in [144], but for the present work, the state-of-the-art method for large attenuation values and a Hamming gating function is used, as derived by Oelze and O'Brian as [143]:

$$A_{OO}^{Ham}(f) = e^{4a_0(f)x_0} \left[\frac{2\alpha(f)L}{1 - e^{-2\alpha(f)L}} \right]^2 \left[1 + \left(\frac{2\alpha(f)L}{2\pi} \right)^2 \right]^2 \quad (3.12)$$

where x_0 is the distance between the source and gated region and $a_0(f)$ is the frequency dependent attenuation of the intervening tissue, typically water or phosphate buffer saline (PBS) solution. $\alpha(f)$ is the frequency dependent attenuation in the tissue under investigation. This is often approximated as linear and based on literature values and even assumed to be the same for healthy and cancerous tissues. The work described here will involve QUS at HF, where there are limited measurements of the attenuation of brain tissue. Therefore, the attenuation function will also be measured before any subsequent QUS analysis.

A summary of the various processes involved in determining the spectral based QUS parameters is given in Fig. 3.2.

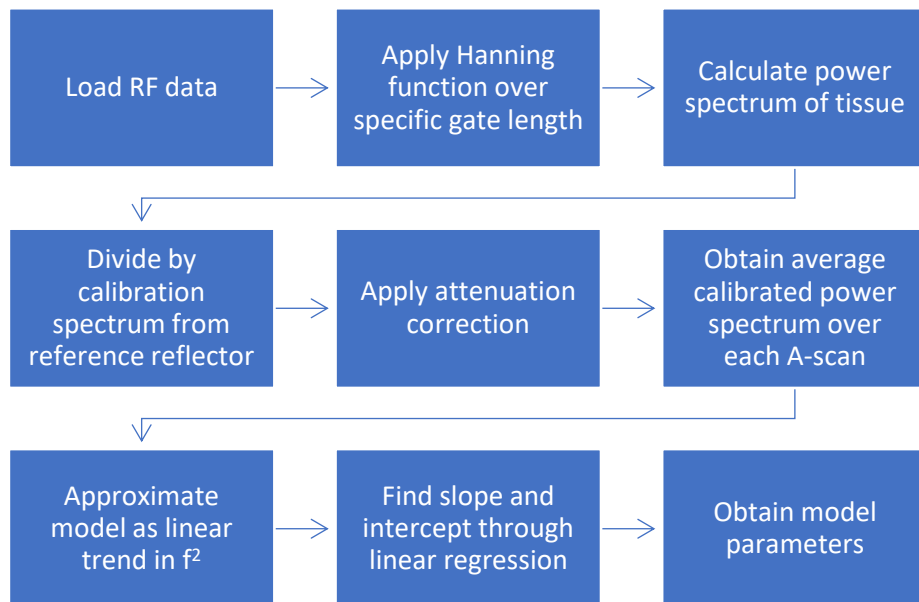


Figure 3.2: Flow chart describing the steps needed to obtain model parameters from output voltage from a transducer to obtain the spectral QUS parameters.

3.3 STATISTICAL PARAMETERS

3.3.1 Introduction to echo envelope statistics.

As discussed, scattering occurs when ultrasound is incident on random scatterers distributed within a tissue. This can be extended further to distinguish between coherent and diffuse scattering and there will often be a combination of these sources in any biological tissue.

- Diffuse scattering leads to speckle in the image and occurs when there is a large number of scatterers in the ultrasound beam resolution cell with random phase.
- Coherent scattering creates clear light and dark features and happens when the scatterers are in phase or there exists some periodicity to their organization.

Drawing from the randomness of backscattered ultrasound, a quantitative, statistical approach to describe the distribution of reflected signal amplitudes in various tissues has been useful for tissue characterisation [130]. The echo envelope statistics refer to a set of statistical parameters which are estimated based on modelling the echo envelope of ultrasound signals from a tissue scattering region [33].

In ultrasound imaging, the Rayleigh distribution corresponds to the distribution of amplitudes in an unfiltered B-mode image, in the case of a high density of random scatterers with no coherent signal component [31]. The Rayleigh distribution was first introduced in 1880 in the context of sound propagation. The Rice distribution also corresponds to a high

density of random scatterers (the diffuse signal component) but, in this case, combined with the presence of a coherent signal component of power [145]. The Nakagami distribution considers the same scatterers' configurations [146] but the two shape parameters of the HK distribution are intertwined into a single Nakagami parameter, m , as given in Equation 3.14 [19]. Due to its simplicity, the Nakagami distribution has become the most widely adopted statistical model for tissue characterisation [33].

A summary of the relationship between the theoretical distributions and scattering types is shown in Fig. 3.3. This diagram shows the types of ultrasound images that can be modelled by various distributions. The HK distribution can model images with any number of diffuse scatterers and any proportion of diffuse to coherent amplitude. The k distribution is appropriate for diffuse scattering alone and the Rician distribution only works when the number of diffuse scatterers tends to infinity. The Rayleigh distribution is applicable only for purely diffuse scattering from many scatterers [147]. Currently, the most relevant for tissue characterisation are the Nakagami distribution, for simplicity, and the HK-distribution, for a complete model [33].

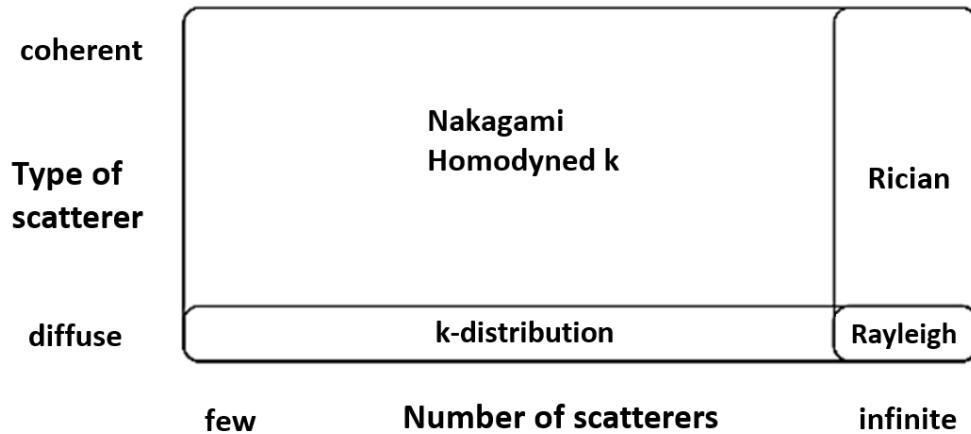


Figure 3.3: Pictorial summary of the various scattering situations and corresponding statistical distributions, from [147].

3.3.2 The Nakagami Distribution

The Nakagami distribution is a simplification of the HK-distribution and is defined by the following probability density function:

$$P_{Nak}(A|m, \Omega) = \frac{2m^m}{\Gamma(m)\Omega^m} A^{2m-1} \exp\left(-\frac{m}{\Omega} A^2\right) \quad (3.13)$$

where A represents the amplitude of the signal, $\Gamma(m)$ is the gamma function, Ω is the scale parameter and m is the shape parameter of the Nakagami distribution [34]. m can be deduced from a moment-based estimator as follows:

$$m = \frac{\overline{(A^2)^2}}{(\overline{A^2} - \overline{A^2})^2} \quad (3.14)$$

where $\overline{\quad}$ represents the expectation value operator. The parameter m will take values from 0 to 1, indicating changes in the envelope statistic from the pre-Rayleigh to the Rayleigh distribution [130].

3.3.3 Homodyned K-Distribution

The probability density for the echo amplitude when described by an HK-distribution is [35]:

$$P_{HK}(A|\varepsilon, \sigma^2, \alpha) = A \int_0^\infty u J_0(u\varepsilon) J_0(uA) \left(1 + \frac{u^2 \sigma^2}{2}\right)^{-\alpha} du \quad (3.15)$$

where J_0 is the Bessel function of the first kind and ε , σ^2 , and α are the model parameters.

Given an echo envelope signal measured experimentally from a tissue scattering region, the approach is to assume this signal follows the HK-distribution, with the goal to then solve for model parameters ε^2 , σ^2 and α .

If there exists a periodicity pattern in the position of the scatterers or if there exist strong specular reflections then a coherent (or deterministic) component, ε^2 , appears in the received signal, because of long-range organization (relative to the wavelength) [125]. The remaining power (from the total signal power) is called the diffuse signal power, $2\sigma^2\alpha$, and corresponds to the diffuse (or random) component, arising from a diffuse collection of scatterers.

The ratio of these two powers is a detailed description of the level of structure in a given material and is a system independent parameter, termed the structure parameter, defined as:

$$\kappa = \frac{\varepsilon^2}{(2\sigma^2\alpha)} \quad (3.16)$$

It is hypothesised that this will be key to understanding some differences between the microstructure of healthy growing tissues and rapidly forming cancers.

These parameters can have huge diagnostic potential for tissue characterisation but obtaining them from the RF data is computationally intensive. A variety of methods exists, including even moments of the backscattered envelope, the SNR, even and fractional moments of the intensity, and the XU statistics[35][148]. The latter has been deemed better overall than the other estimators in terms of fast and reliable performance [125] and it is therefore the method adopted in this thesis.

3.3.4 Solving for QUS parameters from the HK-distribution

The X and U statistics are defined in terms of the expectation value of the intensity, $I = A^2$:

$$U := \overline{\log I} - \log \bar{I} = U_{HK}(\varepsilon^2, \sigma^2, \alpha) \quad (3.17)$$

$$X := \frac{\overline{I \log I}}{\bar{I}} - \overline{\log I} = X_{HK}(\varepsilon^2, \sigma^2, \alpha) \quad (3.18)$$

where U_{HK} and X_{HK} are the theoretical expectation values obtained via evaluation of the integral from zero to infinity over the expressions of X and U, multiplied by the HK probability distribution given in Equation 3.15.

$$\begin{aligned} U_{HK}(\gamma, \alpha) = & -\gamma_E - \log(\gamma + \alpha) + \varphi(\alpha) \\ & -\gamma^\alpha \frac{\Gamma(-\alpha)}{\alpha \Gamma(\alpha)} {}_1F_2(\alpha; 1 + \alpha; 1 + \alpha; \gamma) + \gamma \frac{\Gamma(\alpha-1)}{\Gamma(\alpha)} {}_2F_3(1, 1; 2, 2, 2 - \alpha; \gamma) \end{aligned} \quad (3.20)$$

$$\begin{aligned} X_{HK}(\gamma, \alpha) = & \frac{(1 + 2\alpha)}{(\gamma + \alpha)} - \frac{2\gamma^{\frac{\alpha}{2} + \frac{1}{2}}}{(\gamma + \alpha)\Gamma(\alpha)} K_{\alpha+1}(2\sqrt{\gamma}) \\ & + \frac{\gamma^\alpha}{(\gamma + \alpha)} \frac{\Gamma(-\alpha)}{\Gamma(\alpha)} {}_1F_2(\alpha; 1 + \alpha; 1 + \alpha; \gamma) \\ & - \frac{\gamma^{\alpha+1}}{(\gamma + \alpha)} \frac{\Gamma(-1 - \alpha)}{(1 + \alpha)\Gamma(\alpha)} {}_1F_2(1 + \alpha; 2 + \alpha; 2 + \alpha; \gamma) \\ & + \frac{\gamma}{(\gamma + \alpha)^2} {}_2F_3(1, 1; 2, 2, 1 - \alpha; \gamma) \\ & - \frac{\gamma}{(\gamma + \alpha)} \frac{\alpha \Gamma(-1 + \alpha)}{\Gamma(\alpha)} {}_2F_3(1, 1; 2, 2, 2 - \alpha; \gamma) \end{aligned} \quad (3.21)$$

The integration was performed by Destremes et. al (given as a proof in Appendix A of [125]) to give two equations in terms of hypergeometric functions which can then be solved to accurately obtain the model parameters.

First, a change of variables is used for convenience:

$$\mu = \varepsilon^2 + 2\sigma^2\alpha, \quad \gamma = \frac{\varepsilon^2}{2\sigma^2}. \quad (3.19)$$

Next, the theoretical expectation values for X and U are:

where γ_E is the Euler constant [149], φ is the digamma function [150], ${}_pF_q(a_1, \dots, a_p; b_1, \dots, b_q; z)$ is the generalised hypergeometric series and K_p denotes a modified Bessel function of the second kind of order p [151].

Despite their complexity, these two non-linear equations depend only on two model parameters λ and α , so can be solved if given values of X , U and \bar{I} , which are very easy to obtain experimentally from a tissue scattering region. An embedded binary search algorithm is used to solve for the required parameters, which must be done in three stages. The flowcharts that define this process are given in Figures 3.4-6 for convenience, and their translation into MATLAB code is given in Appendix II.

The model parameters can then be found using the identities as the final step:

$$\varepsilon^2 = \frac{\mu\gamma}{\gamma + \alpha}; \quad \sigma^2 = \frac{\mu}{2(\gamma + \alpha)} \quad (3.22)$$

Ultimately the goal is to create a function in computer code which takes the X , U and \bar{I} parameters and returns the parameters γ and α which can then be converted back to the model parameters using Equations 3.33 and 3.34. Implementation of these algorithms in the present work was achieved using MATLAB and they were validated with published values of α and γ , for a given input of X and U . The tolerance was set to 10^{-4} for algorithms 1 and 2, respectively and the results are shown in Table 3.1.

Table 3.1: Validation of algorithm implementation for 3 pairs of X and U values.

Input (X,U)	Output(α,γ) Published	Output (α, γ) - Present Algorithm
(0.7166, -0.3935)	(2.10, 3.10)	(2.09, 3.09)
(0.8, -0.3)	(0.0747, 0.1508)	(0.0743, 0.1497)
(4, -1.5)	(0.0287, 0.0059)	(0.0279, 0.0058)

There is good agreement with the published literature values and the algorithms developed in this study. This validation allows confidence in the computation of all subsequent work regarding HK parameters calculated from experimental data.

Input: $X > 0$ (the X -statistics) and $\alpha > 0$.
Assumption: $\alpha \leq \alpha_0 = 1/(X - 1)$ if $X > 1$; no restriction if $0 < X \leq 1$.

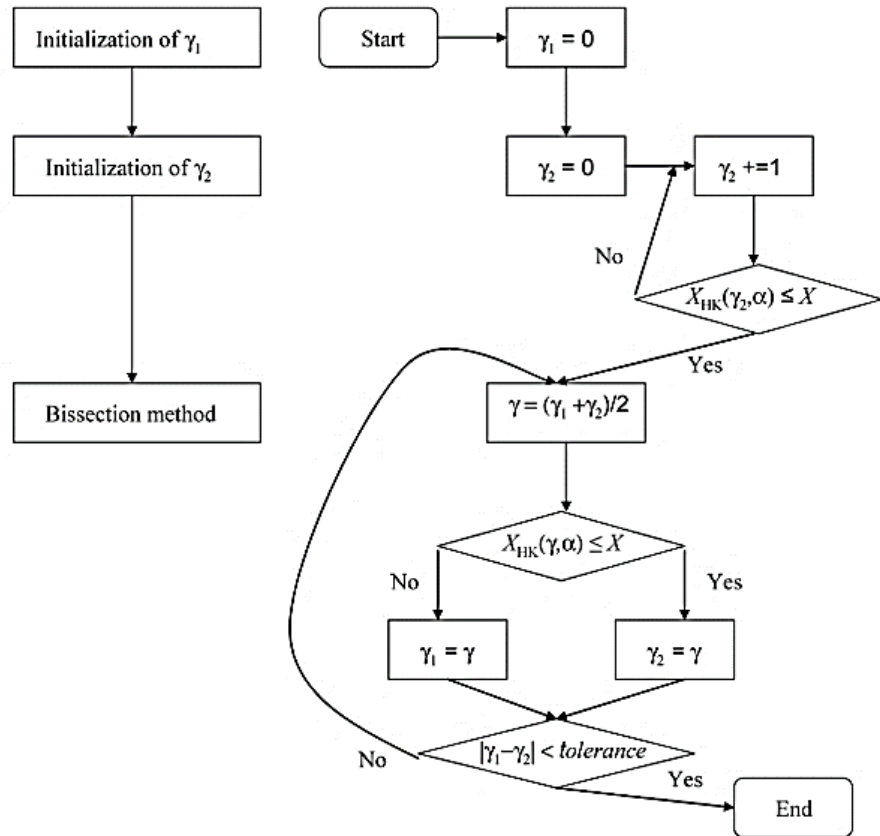


Figure 3.4: Algorithm for computing the function $\gamma(\alpha, X)$, from [125].

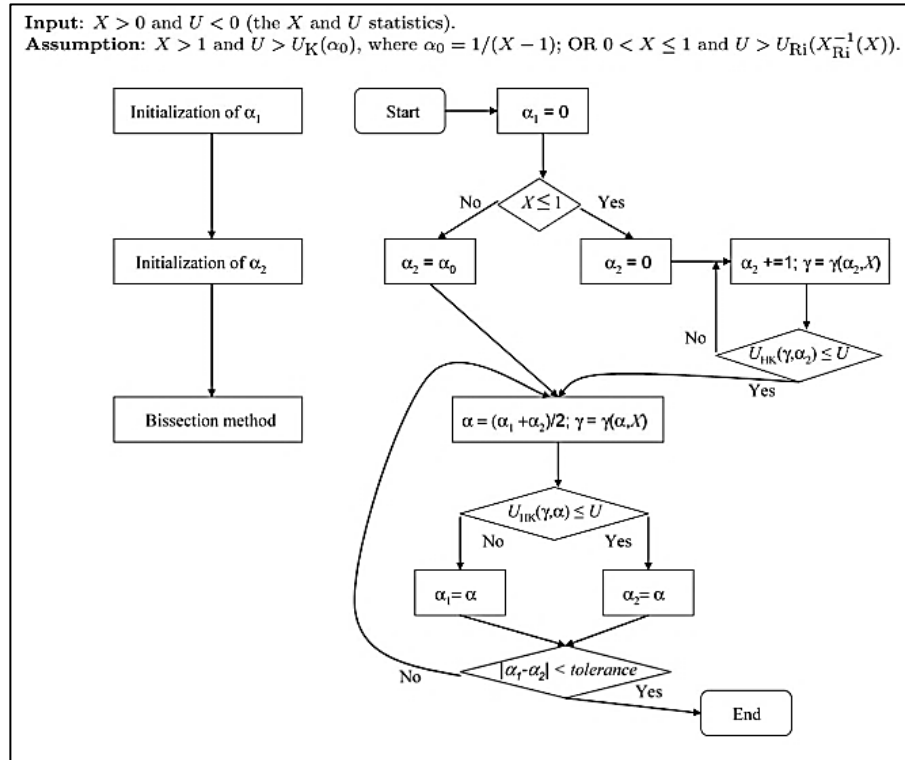


Figure 3.5: Algorithm solving $X_{HK} = X$ and $U_{HK} = U$ simultaneously, from [125].

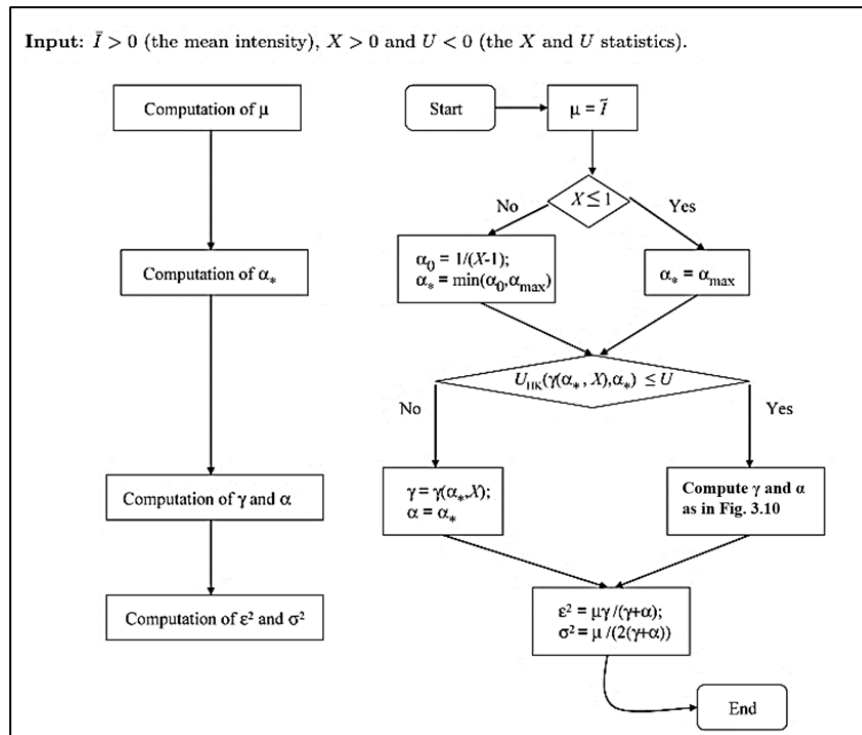


Figure 3.6: Algorithm for estimating the parameters ϵ^2 , σ^2 , α of the HK-distribution with the constraint that α is less than an upper bound α_{\max} , adapted from [125].

3.3.5 Other statistical parameters

Various other statistics which do not stem from a theoretical distribution can still be useful for tissue characterisation and are efficient to calculate in real time.

The echogenicity, E , of the signal amplitude can be thought of as a general statistical distribution. Moments of a distribution are quantitative measures related to the shape of the function's graph. The mean, or expectation value of E , is given by:

$$\mu = \bar{E} = \frac{1}{N} \sum_{i=1}^N E_i \quad (3.23)$$

The second central moment is the variance of the distribution, or standard deviation.

$$\sigma_{var}^2 = \frac{1}{N} \sum_{i=1}^N (\bar{E} - E_i)^2 \quad (3.24)$$

The third central moment, or skewness, measures the asymmetry of the distribution, and can take a positive or negative value depending on whether it skews to the left or right. The fourth central moment is a measure of the heaviness of the tail of the distribution, compared to the normal distribution of the same variance; it is always strictly positive.

The normalised n -th central moment is easily obtained via MATLAB and is given mathematically as [152]:

$$\frac{\mu_n}{\sigma_n} = \frac{\overline{(E - \mu)^n}}{[\overline{(E - \mu)^2}]^{\frac{n}{2}}} \quad (3.25)$$

for the random variable, E . Despite their simplicity, all central moments are dimensionless quantities, meaning they are representative of the distribution, independent of any linear change of scale. Although implicit, this means these values are invariant under scaling of the mean, or independent of the initial energy of the system.

The effect of frequency on the value of the higher order moments has not been reported. Regardless of their lack of physical relevance to underlying microstructure, they could still show changes in healthy and cancerous tissue and are often included as additional features in a ML algorithm.

3.4 MACHINE LEARNING

Developments in computing over the last few decades have allowed ML and artificial intelligence to increase the diagnostic potential of many medical imaging modalities.

Algorithms can be written to detect patterns in the numerical values of measured parameters in different tissue pathologies to predict which pathology a new set of measurements is most likely to come from. This can be applied to the current study which measures a range of QUS parameters and is interested in determining whether the tissue is healthy or cancerous.

3.4.1 Binary classification

Binary classification is a supervised type of ML in which a function uses a range of methods to make a prediction of a defined label based on the input data. It requires a labelled data set to train the classifier, for example, a selection of data which has already been categorised into healthy or cancerous. A function will then be created to recognise patterns between the parameters in the specific categories and this function can be used to predict the label of uncategorised data.

For example, cancerous samples are usually considered as the ‘positive’ case and healthy tissue is considered a ‘negative’ result. The algorithm will predict if an unknown sample should be labelled positive or negative. The larger the training set, the more specific and accurate the algorithm tends to be. This is of huge clinical relevance as certain measurements could be collected in known healthy and cancerous tissues, which will then be used to train a classifier to predict whether an unknown tissue is more likely to be healthy or cancerous in a clinical setting. This is a powerful tool which can collapse several complex measurements around tissue characterisation into a single labelled prediction ‘healthy’ or ‘cancerous’. Often, ML technology is integrated into a clinical setting gradually, with ethical considerations needed. It should be seen as another aid to the surgeon, who should ultimately make the final decision.

3.4.2 K-nearest neighbours

The KNN algorithm is a simple algorithm for classification. It is based on calculating the Euclidean distance between a test point and k neighbouring labelled data points. Fig. 3.7 shows a 2-D illustration of this, where the test point is marked in black, and the two possible classes are shown in red (positive) and green (negative). The distance is not limited to 2-D space and, depending on the number of parameters, n , available, can be extended to n dimensions.

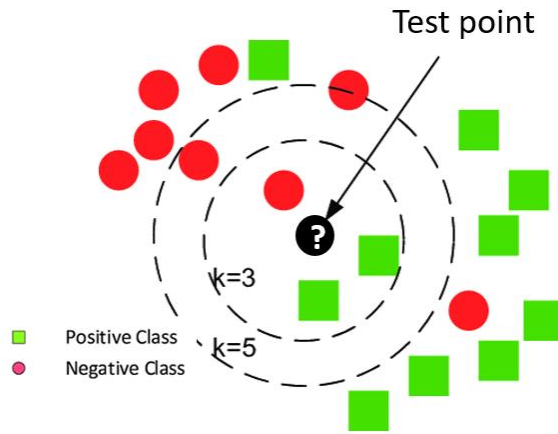


Figure 3.7: 2-D visualisation of the KNN framework for binary classification. In this case it is important to consider the number of neighbours as it may change the predicted class of the test point.

The number of neighbours is often an input to the model and should be optimised to give the most accurate results. Typically, between 5 - 50 data points are used, depending on the size of the dataset. Next, the Euclidean distance, d , is calculated between the test point, p , and a neighbour, q , by the n -space distance formula:

$$d(p, q) = \sqrt{\sum_{i=1}^n (p_i - q_i)^2} \quad (3.26)$$

The algorithm will then label the test point as whichever category is most commonly in closer proximity to the test point.

3.4.3 Support Vector Machine

A SVM is an algorithm which tries to find an optimal hyperplane, which separates two or more distinct data sets, so unseen data can be classified depending on its location relative to that hyperplane. A hyperplane is a subspace whose dimension is one less than its ambient space, which is the number of features considered in the algorithm [153]. Therefore, in a 2-D space, the hyperplane will be a line and in 3-D space it will be a 2-D plane. It is harder to visualise for higher dimensions, but they exist in n -space. The support vectors are the points that are closest to the hyperplane and are used to create a separating line, the margins between which should be maximised to generate optimal separation. An example of this in a 2-D space is shown in Fig. 3.8.

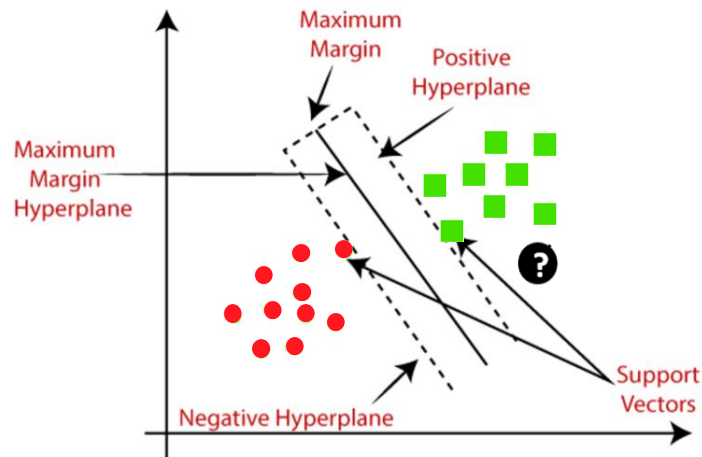


Figure 3.8: Example of a linear kernel SVM showing optimal hyperplane as a solid black line with support vectors on positive and negative cases, from [154].

Once the support vectors are found, the test data are labelled positive or negative according to their position relative to the optimal hyperplane, by use of the dot product with a vector perpendicular to the hyperplane [155]. For example, in Fig. 3.13, the test data point indicated in black would be labelled positive as its position has crossed the linear hyperplane into the positive sub-space.

Often the dataset will not have a linear separation and will require a kernel to find the optimum hyperplane. A kernel refers to a method that allows application of linear classifiers to non-linear problems by mapping non-linear data into a higher-dimensional space [156]. The mathematics behind minimising the empirical error on classification while considering the complexity of the hypothesis space require an algebraic topology framework to explain fully [157]. In this analysis it was restricted to linear, quadratic and Gaussian kernels.

3.4.4 Evaluating the performance of a classifier

After the classifier has predicted the label of the test data, the performance can be quantified to compare it to other methods or classifiers. This is achieved using a confusion matrix, which is an illustration of how the predicted results compare with reality. For the simple case of binary classification, there are four outcomes for each prediction. If a tumour sample is classified as a positive case, and if it is correctly labelled positive, it is a true positive (TP). However, if it is incorrectly labelled healthy (negative), this corresponds to a false negative (FN), and in this context, it may result in the unnecessary removal of healthy brain tissue. Similarly, a negative case classified correctly is a true negative (TN) but if it is incorrectly labelled positive it is a false negative (FP). This is summarised in Fig. 3.11.

Predicted Class	Tumor	True Positive (TP)	False Positive (FP)
	Healthy	False Negative (FN)	True Negative (TN)
		Tumor	Healthy
		True Class	

Figure 3.11: Confusion matrix for binary classification where tumour = positive case and healthy = negative case.

While other applications may look at a weighted analysis, aiming to maximise positive case detection, it may be argued that it is equally unfavourable to remove healthy brain tissue as it is to miss cancerous tissue. Therefore, the overall percentage accuracy of the classifier is considered in this thesis and maximised. The accuracy is given in terms of the outcomes in Equation 3.27.

$$Accuracy (\%) = \frac{TP + TN}{TP + TN + FN + TN} \quad (3.27)$$

$$F_1 = \frac{TP}{TP + \frac{1}{2}(FP + FN)} \quad (3.28)$$

The precision of a classifier is the ratio of correctly identified positive cases to the total number of cases and the recall is the ratio of correctly identified negative cases to total negative cases. The F_1 -score is the harmonic mean of the precision and recall of the classifier. This measures the effectiveness of retrieval when precision and recall have equal importance [158].

k-fold validation is a resampling procedure where the separation of training and testing data is repeated k times to remove any bias in the training vs testing data subsets. The accuracy and F_1 score are calculated for each ‘fold’ and the average results over k-folds are a more robust metric for algorithm performance; therefore, this is the method adopted in this thesis.

3.5 CONCLUSIONS

The main conclusions drawn from this chapter are as follows:

1. Biological materials are far more complex and heterogenous than allowed by descriptions with a bulk parameter such as speed of sound and attenuation. Nonetheless, these descriptions are necessary to make any sort of predictions about wave propagation and are the basis of medical imaging and QUS parameter estimation.
2. The frequency dependence of the BSPS contains valuable information about the size and distribution of scattering within tissue, which links to tissue microstructure and so could be useful for cancer detection.
3. The simplest model of scattering in tissues is the Gaussian model (random walk) which is used to give the BPS in terms of physical parameters which describe scattering in tissues.
4. The HK-distribution is the most complete statistical model of the echo envelope, providing two system-independent parameters for tissue characterisation: α , the scatter clustering parameter, and the structure parameter, κ . The Nakagami distribution is an approximation, which yields one parameter that is still useful in some cases, and computation time is significantly less.
5. Any numeric parameter can be used to aid ML characterisation, including standardised moments of a general statistical distribution in the context of the B-mode pixel intensity.
6. Binary classification algorithms, such as KNN, and SVM see data as having the choice of two labels and will use the training data to determine whether it is more probable for a particular test point to be labelled positive or negative.

3.6 CHAPTER SUMMARY

This chapter presented a theoretical description of ultrasound scattering interaction with tissues. Bulk material properties, such as the speed of sound and attenuation were discussed for brain tissue in the literature. An appropriate estimation of these is crucial to accurately measure QUS parameters. An overview of scattering in tissues was given, followed by the mathematical framework for spectral based parameters. A key finding was that the frequency dependence of the BPS can be modelled to depend only on the ESD and EAC. The theory

underpinning statistical analysis of the echo envelope was given, with a review of several distributions which have been used in an ultrasound context. Notably, the HK-distribution is the most accurate model but the estimation method for the model parameters is complex. However, it is repeatable as the values obtained agree with published results. All QUS parameters may be combined to create an n-dimensional space in which ML algorithms can predict the outcome of a specific measurement, using previous results as training data.

4 QUANTITATIVE ULTRASOUND DIFFERENTIATES PHANTOMS OF BRAIN AND BRAIN TUMOUR

4.1 CHAPTER AIMS

This chapter has three key aims which relate to using phantom materials as a substitute for brain tissue to explore QUS analysis. Firstly, the aim was to identify suitable acoustic phantoms to represent brain and brain tumour via a literature search and acoustic characterisation of bulk properties then, secondly, to provide a proof-of-concept study by using QUS to differentiate the two tissue types. Finally, work was done to study the effect of freezing and fixation of the QUS parameters via measurements from fresh and preserved tissues, in order to determine if preserved tissues can be used as reasonable models for *in vivo* application of QUS.

4.2 INTRODUCTION

4.2.1 The Need for Acoustic Phantoms

Fresh samples of human brain and brain tumour of an adequate size are difficult to obtain for various logistical, safety and ethical reasons. Firstly, it can be difficult to obtain fresh samples of healthy tissue due to the rapid deterioration of brain tissue when removed from the body, as neuronal cells die very quickly in the absence of glucose and oxygen [159]. This limits the tissue sources available geographically while conducting laboratory-based experiments. Secondly, tumour tissue of an adequate size is difficult to obtain as the tumour is often ablated in small sections and the tumour bulk should be retained for pathology tests and further cancer research [160]. While there is still a possibility to conduct an *ex vivo* trial in the OR, the feasibility of a new technique must have sufficient evidence to take it to clinical trial stage. It was therefore important to consider other tissue options for the exploration stage of the present project. A summary of the options for sources of brain tissue is displayed in Table 4.1, with colour indicators representing key factors to consider, namely, suitability, cost and ease of supply. The colour coding refers to ‘ideal’ = green, ‘moderate’ = orange and ‘not ideal’ = red’ for this work.

Table 4.1: Summary of Tissue Exploration Options

	<i>In vivo</i> Human Tissue	Fresh Human Tissue	Frozen Human Tissue	Animal Brain Tissue	Acoustic Phantoms
<i>Suitability</i>	High	High	Moderate	Low	Low
<i>Cost</i>	High	High	Moderate	Moderate	Low
<i>Ease of Obtaining</i>	Low	Low	Moderate	Moderate	High

It would be ideal to test the technique on *in vivo* human tissue; however, given the lack of exploration of QUS in brain tissue and the time needed to go through ethical approval for a clinical trial, it was considered unlikely this could occur within the time constraints of the PhD. Excised tissues are another option, where measurements could be taken adjacent to the OR and the tissue would be fresh, *ex vivo*. However, the impact of the Covid-19 pandemic caused further safety restrictions on and collaborations with medical centres. It is possible to obtain human tissue samples from tissue banks, which was achieved with results presented in Chapter 5, but this may not have been possible without the preliminary phantom work, which may also have value in other research.

In tissue banks, the tissue is preserved in some way, typically done by either fixation with formaldehyde or freezing at -80°C . Research on the effects of freezing and fixation on QUS parameters has been limited, but it is known that some acoustic properties, such as the attenuation and BSC, change significantly in soft tissues after preservation [83]. These tissues may thus have a problem with *in vivo* translatability. Another solution may be to use an animal brain as it is easier to obtain fresh tissue or even to conduct a study *in vivo*. However, there are problems associated with animal tumour models, as typically a murine model is used which comes with limitations such as: much smaller brain size, different thickness of skull and extensive ethical steps involved to conduct the study. Therefore, the best course of action for a proof-of-concept study as part of the present project was to find and use the most suitable ultrasound phantoms to mimic brain and brain tumour and create a QUS-based characterisation tool.

4.2.2 Ultrasound Phantoms

Ultrasound phantoms are necessary for the advancement of medical ultrasound techniques as it is complicated and expensive to obtain human tissue on a regular basis. In contrast, phantoms are materials made to mimic the material under investigation in terms of acoustic velocity, acoustic impedance and attenuation [161]. They are easier and cheaper to obtain

and often have a shelf-life of at least several months [162]. Common phantoms for soft tissues can be manufactured in the laboratory, for example agarose or polyvinyl alcohol (PVA) –based materials. Alternatively, commercial phantoms can be purchased which are primarily used for training and quality monitoring of developing and operational US system, with examples of suppliers including CIRS® Inc [163] and Blue Phantom [164]. These are usually expensive and application specific. Currently there is no company which offers a brain tissue specific phantom, but Delta Neurosurgical, which manufactures ultrasound neurosurgical simulators [165], suggest the use of ‘children’s jelly food’ to act as brain tissue [166]. It is crucial that the phantoms are ultrasound-specific and approach an equivalence to human tissue in the desired frequency range of interest.

Section 3.2.3 gave a review of the acoustic properties of healthy and cancerous brain tissue. Recently, Stewart et al. set out to determine which readily available tissue or phantom has similar mechanical properties to brain and brain tumour [104]. Through testing many tissue mimicking materials, they found that chicken liver and chicken gizzard muscle gave the greatest likeness to brain and brain tumour, respectively. In addition, several neurosurgeons agree with the finding that these tissues are mechanically similar, just by using palpation, and Stryker Medical uses chicken liver regularly for quality testing of their ultrasonic aspirator [167]. Furthermore, these tissues are available at many Halal butchers at very low cost.

The work described in the next section aims to validate the use of these materials for ultrasonic testing purposes, with the acoustic properties measured and compared with values from the literature for healthy brain and glioma tissue.

4.3 METHODOLOGY

The following sections explain the methodology for experimentally measuring and calculating the acoustic impedance and attenuation of soft tissue samples, followed by the procedure for obtaining RF data using a research ultrasound system for QUS analysis. A study is also described which measured the effect of freezing and fixation on QUS parameters.

4.3.1 Validation of Acoustic Phantoms

4.3.1.1 Acoustic Impedance

The acoustic impedance was determined via measurement of density and speed of sound then using Equation 3.2.

Fresh chicken liver and gizzard were purchased from a Halal butcher on the first day of delivery, meaning tissue were harvested less than 24 hours since death. They were then cut into small sample sections with a typical size of 1 cm (D) x 2 cm (W) x 2 cm (L) with a scalpel as shown in Fig. 4.1. Each sample was then placed on a 4-digit scale to accurately determine the mass.



Figure 4.1: Sample sections of chicken liver (left), and gizzard (right) for acoustic characterisation.

The volume of each sample was estimated via the Archimedes Method, i.e., from the volume of water displaced by the tissue when fully submerged. The mass of a test tube with water in it was measured, which allowed the starting volume to be calculated. The tissue was then placed in the test tube and the combined weight was measured. The volume of the tissue is simply the volume difference between the full container and the volume of water present with tissue, which could be calculated using the mass of tissue and the density of water, $\rho_{Water} = 997 \text{ kg m}^{-3}$.

The process is summarised in Equation 4.2 which gives the full calculation for the density of tissue sample.

$$\rho_{Tissue} = \frac{m_{Tissue}}{V_{Tissue}} = \frac{m_{Tissue}}{V_{Total} - V_{Water}} = \frac{m_{Tissue}}{\rho_{Water}(m_{Water} - (m_{Total} - m_{Tissue}))} \quad (4.1)$$

where m_{Tissue} , m_{Water} , m_{Total} are the masses of the tissue, of the container with only water, and of the water and tissue combined, respectively. This procedure was repeated for 15 samples of both liver and gizzard and the mean and standard deviation were obtained.

For speed of sound calculation, tissue was again cut into slices, however this time care was taken to ensure two sides were as parallel as possible to ensure a uniform thickness, as shown in Fig. 4.2. Each sample was placed on a sample holder, which was designed to surround the transducer and allow the sample to sit parallel to the transducer face as shown in Fig. 4.2a. The experiments were conducted at room temperature. A single-element 10 MHz immersion transducer was used for pulse-echo testing, connected to an ultrasonic pulser-receiver

(DPR300, JSR – Imaginant, NY, USA) operating in pulse echo mode. The receiver output from the pulser-receiver was connected to an oscilloscope (InfiniiVision 2000 X-Series, 200 MHz, Keysight Technologies, CA, USA). Once a steady reflection pattern was seen, the oscilloscope was paused and the time, Δt , between peak positive values in successive echoes was measured using the oscilloscope measuring function. A typical transducer response from the oscilloscope is shown in Fig. 4.3b, with Δt indicated. The echoes correspond to the pulse reflecting from the top and bottom surface of the tissue. The speed of sound in the tissue, c , can then be calculated by:

$$c = \frac{2d}{\Delta t} \quad (4.2)$$

where d is the thickness of the sample.

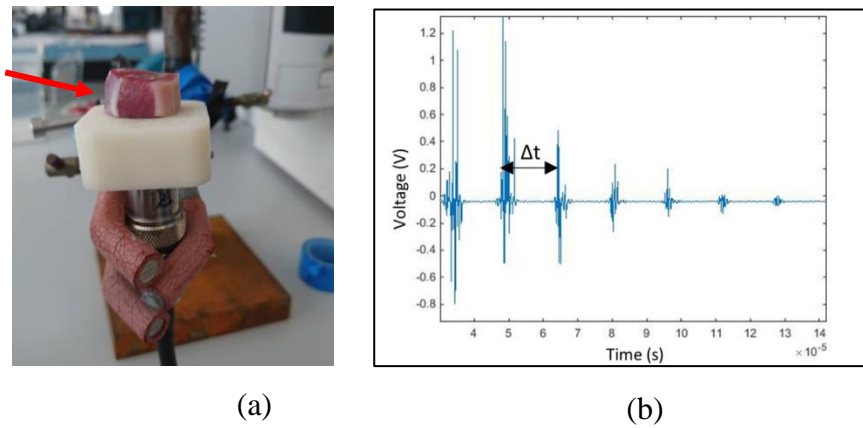


Figure 4.2: Speed of sound measurement showing (a) Sample of chicken gizzard placed on transducer for pulse-echo testing, (b) typical transducer response from experimental set-up.

This procedure was repeated for fifteen samples of both liver and gizzard and the average value was taken. The relative error on the acoustic impedance is calculated by the sum of the relative errors from the density and acoustic velocity:

$$\Delta Z = Z \sqrt{\left(\frac{\Delta \rho}{\rho}\right)^2 + \left(\frac{\Delta c}{c}\right)^2} \quad (4.3)$$

4.3.1.2 Attenuation

Calculation of attenuation was based on a narrowband TL measurement [168]. This gives a relative measure of the frequency-dependent *decrease* in amplitude of an ultrasound pulse,

expressed in decibels, incurred when a sample is inserted in the path of an acoustic propagating beam.

The study was performed in a water bath with a needle hydrophone (0.2 mm diameter, with 8 dB preamplifier, Precision Acoustics Ltd, Dorset, UK) positioned at 10 cm from the transducer in a tank of degassed water as shown in Fig. 4.4.

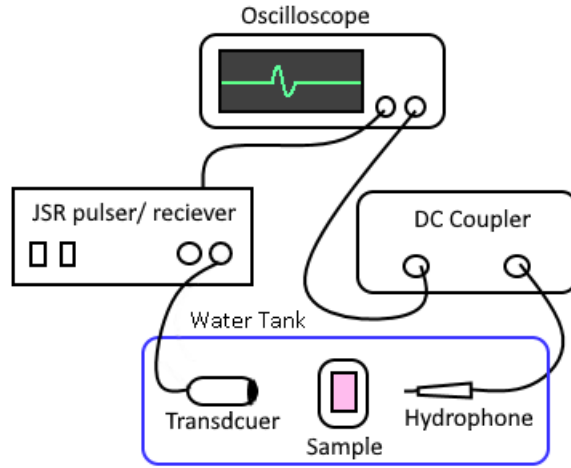


Figure 4.3: Experimental set-up for attenuation measurement via TL.

A needle hydrophone is a narrow and submersible polyvinylidene fluoride (PVDF) transducer designed to provide a highly sensitive voltage signal proportional to the acoustic pressure experience by the active element [169]. An empty sample holder was placed in the acoustic path and measurements were taken for the reference voltage, V_{REF} . Next, a tissue sample of known thickness was encased in agar to hold it securely in the sample holder and a reduced voltage was recorded by the hydrophone, V_{SAMPLE} . The TL, in dB, due to the insertion of the tissue sample via the through-transmission method can then be calculated:

$$TL = -10 \log_{10} \frac{V_{SAMPLE}}{V_{REF}} \quad (4.4)$$

The attenuation caused by a sample at a specific frequency can be calculated (in dB cm^{-1}) by dividing the TL by the sample thickness and correcting for the attenuation due to the displaced water of identical thickness, given by [170].

$$\alpha = \frac{TL}{d} + \alpha_{WATER} \quad (4.5)$$

This procedure was carried out using immersion transducers designed to operate at three different frequencies: 1 MHz, 5 MHz and 10 MHz (all unfocused immersion transducers,

Olympus Scientific Solutions Technologies, MA, USA). Measurements were repeated five times for each of the fifteen samples at each frequency and the attenuation coefficient was estimated as the gradient of a best-fit straight line through the average values found for each frequency. The attenuation of agar due to the very thin layer at these frequencies was assumed negligible.

4.3.2 QUS Analysis

4.3.2.1 QUS Data Acquisition

For the QUS study, the tissue was prepared in the same way as for the acoustic characterisation study. The experimental set-up consists of the tissue sample submerged in water and placed on a quartz flat below the centre of a 5 - 11 MHz linear array probe (Verasonics, Inc., WA, USA) connected to a Vantage 128 ultrasound research system (Verasonics, Inc. WA, USA) as shown in Fig. 4.6a. The probe has 128 elements and a centre frequency of 8 MHz. The ultrasound research system is a completely programmable imaging system which varies from commercial systems in that users can access the RF data, a feature which is imperative for QUS. Furthermore, all aspects of image processing can be customised by the user using the MATLAB (The Mathworks, Cambridge, UK) environment.

The system was programmed to provide a plane wave by excitation of all elements simultaneously then to acquire and store the RF data received by each element. A gain of 20 dB was applied to the entire received signal, and no TGC was used in this study, as compensation for attenuation is done during spectral analysis. One pulse-echo acquisition is referred to as a 'frame' of data. The sampling rate was 31.25 MHz, and the imaging depth was 5 cm. 64 frames were stored in each acquisition as a .mat file with dimensions 4096 x 128 x 64 samples in the host computer.

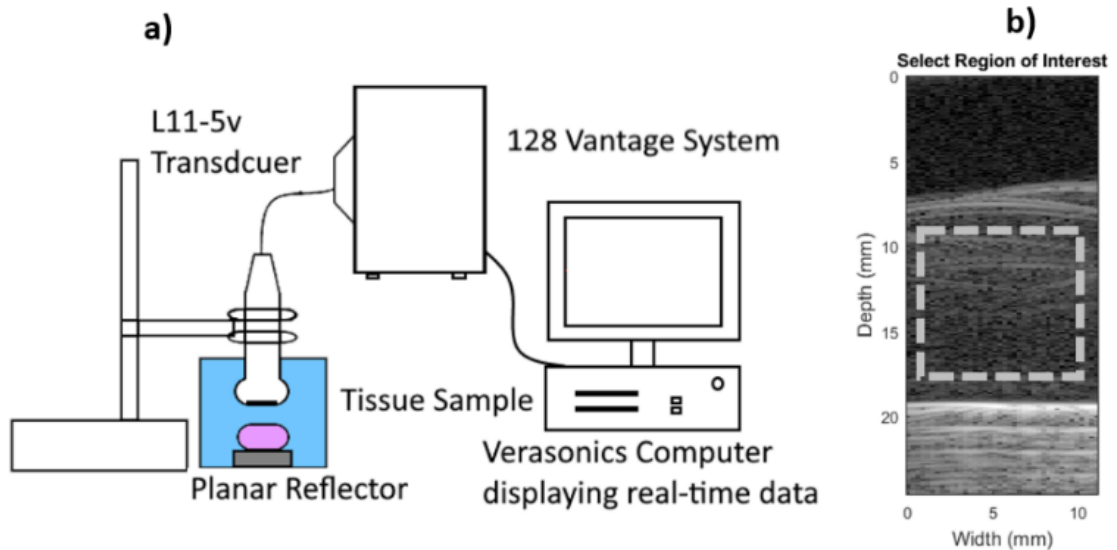


Figure 4.4: (a) Experimental set-up of data acquisition from tissue using Verasonics Vantage system. (b) Typical B-mode image of tissue placed on top of quartz flat submerged in water.

For processing, the RF data sets were loaded into a custom MATLAB framework and the averages of the 64 frames were taken. The echo envelopes of the resulting dataset were compressed using a suitable dynamic range to display a B-mode image, allowing the user to select a tissue ROI as shown as a dashed square in Fig. 4.4b. The water-tissue interface occurs at a depth of around 7 mm, and an example of tissue ROI is marked, measuring around 12 mm x 12 mm, with the strong reflections and reverberations from the quartz flat evident in the lower region of the image.

4.3.2.2 Parametric Image Formation

To obtain a parametric image, the ROI was divided into windows of 3 mm x 3 mm, corresponding to at least 10 wavelengths in the axial direction, and 12 transducer elements in the lateral direction. The windowed RF data were input into an algorithm which calculates 13 QUS parameters for that specific window location.

To increase the resolution of the parametric image, a sliding window was used with 66% overlap. This percentage was chosen so parameters to be calculated for the larger window, which satisfies the minimum of 10 wavelengths requirement, but the resulting parametric image has a pixel value for each 1 mm x 1 mm region, which is sufficient resolution for binary classification. This was achieved by measuring the QUS parameters for the top left 3 mm x 3 mm region, then sliding the window over 4 elements, which corresponds to a width of ~ 1 mm, and measuring subsequent QUS parameters for the new 3 mm x 3 mm window. After the entire width of the image was covered, the window returned to the left-hand side

but slid down 1mm in depth and a set of QUS parameters for the new window was calculated. The process was repeated until the entire ROI was covered.

Once the larger sections had associated results, a spatial average could be computed from the overlapping regions to achieve a pixel resolution of 1mm, as shown in Fig. 4.5, albeit with some correlation between values in successive pixels. Details of the calculation of parameters from the windowed RF data are provided in the following sections.

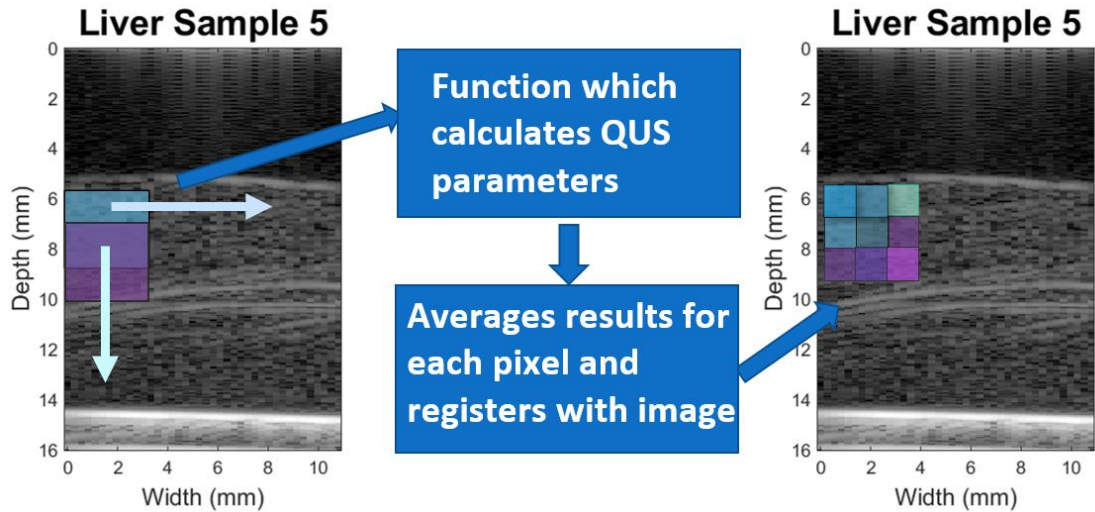


Figure 4.5: Diagram showing the sliding window technique for QUS parametric image formation.

4.3.2.3 Scatterer size and acoustic concentration

For each window location, calculation of scatterer size and acoustic concentration begins by multiplying each line segment in the ROI voltage data, V_{Tis} , by a time gated Hamming weighting function to adequately window the region while suppressing spectral lobes [23]. The gate length, L , was 3 mm as this corresponds to the window size. Then, an FFT algorithm is applied to compute power spectra as a function of frequency. The limits of the frequency of interest were specified by the bandwidth of the transducer (5 – 11 MHz). The squared magnitudes of the resultant spectra from each scan line are then averaged to estimate an average power spectrum from the region, W_{Tis} :

$$W_{Tis}(f) = |FFT(V_{Tis}(t, L) * Ham(t, L))|^2 \quad (4.6)$$

This spectrum is then divided by a reference spectrum to remove system dependence on the measurements, specifically the transfer function of the transducer elements and the excitation of the pulse. The reference spectrum, W_{ref} , is obtained by following the same analysis to obtain the tissue power spectrum but using the voltage from the reflection from a quartz flat situated in a water bath with no tissue present.

The average experimental BSPS coefficient, $S_{meas}(f)$ of the tissue was estimated using the formula derived by Insana et. al. for array transducers [171]:

$$S(f) = \frac{6(Y + \frac{L}{2})^2 p^2 R^2}{DLw^2 h} \frac{1}{4} A(f, L) \frac{1}{N} \sum_1^N \frac{W_{Tis}(f)}{W_{Ref}(f)} \quad (4.7)$$

where Y is the axial distance from the transducer to the centre of the ROI, D is the active area of the 12 transducer elements, and p, w and h are the pitch, width and height of the elements, respectively. R is the reflection coefficient of a water and quartz interface, calculated from Equation 3.3. A(f, L) is an attenuation compensation function for a Hamming gated signal [172], given in Equation 3.19.

The ESD and EAC were estimated by expressing the compensated power spectrum in decibel form and applying linear regression to solve for slope and intercept values in MATLAB, as described in Section 3.3.1.

4.3.2.4 Statistical Methods

By assuming the echo envelope signal amplitude is distributed according to the HK-distribution (Equation 3.27), more descriptive statistics can provide additional QUS parameters. For tissue characterization, two parameters in particular are commonly quoted, as noted previously, as they are invariant under scaling of the mean intensity: the scatterer clustering parameter, α , and the structure parameter κ [33]. The algorithms necessary were coded using three separate functions in MATLAB, corresponding to the flowcharts in Section 3.5. The main parametric imaging system calls these functions to populate the QUS parameter array for each window. In summary, the experimental results for X and U, from the intensity of the signal within the windowed region, are used to solve for the model parameters using the non-linear equations for X and U. The X and U statistics, all 3 model parameters and κ are included for machine learning classification.

More general statistics, based on the pixel intensity of the B-mode image were also included in the analysis. After log compression of the RF data, the image is displayed according to the dynamic range. In this study, a dynamic range of 80 dB was used and the distribution of

echogenicity values was modelled to yield the variance and higher moments of the values for a given windowed region. This dynamic range was most suitable for optimum image quality after experimenting with a sliding scale between 50 – 100 dB. The expectation value of the echogenicity, E , can be written as \bar{E} , and the higher moments of these first order statistics are written as \bar{E}_n for the n -th central moment.

4.3.2.5 Tolerance Optimisation

A further study of the efficiency of the algorithm which solves for the HK parameters was explored by optimising the tolerance levels in the binary search algorithm. The initial values were chosen as stated in the original publication as 10^{-4} [125]. However, this was explored further to minimise computation time as this affects whether these parameters are suitable for real-time characterisation. The analysis was conducted on a PC with the following specification: Windows 10 64-bit operating system, Intel Core i7-9700K CPU @ 3.60 GHz, 16 GB RAM.

One set of X,U statistics was used to evaluate the effect of changing the tolerance level on the computed values of α and γ . These were based on typical values from soft tissue ($X = 1.4106$, $U = -0.7031$). The reference result for these parameters was found using the initial tolerance values to give $\alpha = 0.5123$, $\gamma = 0.0469$ in a time of 22.3 seconds. Next, the tolerance levels were incrementally increased from 0.0001 to 0.01 and the varying results for α and γ for these levels were saved. The time taken and percentage error from the original value were also recorded.

4.3.3 Machine Learning Implementation

The KNN classification algorithm was trained using $k = 5$ and all QUS pixel data as features. The number of neighbours was chosen to be 5 after inspection of the data and quick experiments with $k=5$, $k=20$ and $k=50$. It was found the smallest number of neighbours (fine KNN) was most appropriate for this specific dataset. A 6 fold validation method was used, where the data from 10 of the 12 samples of each tissue type, were randomly chosen and used as training data for the machine learning classifier, as then repeated for the other 5 permutations. This resulted in 800 sets of training data for liver and 650 for gizzard, as liver was thicker on average, so had a larger ROI, and more associated pixel results. The QUS pixel results are used as features for binary classification. The pixel results from the remaining two samples were not seen by the classifier, and they were used to test the classifiers' ability to correctly label a result as 'liver' or 'gizzard', with the label 'liver' (phantom healthy tissue) taken as being the positive outcome. These labels were used to generate a confusion matrix which can then describe the sensitivity and specificity of a

classifier as shown in Fig. 4.6. A good classifier aims to maximise the TP and TN values, while minimising the off-diagonal elements.

Predicted Class	Gizzard	True Positive (TP)	False Positive (FP)
	Liver	False Negative (FN)	True Negative (TN)
		Gizzard	Liver
		True Class	

Figure 4.6: Confusion matrix for liver and gizzard classification.

This process was repeated six times and an average confusion matrix was obtained from which accuracy and F1-score could be calculated.

To investigate which of the thirteen parameters held most diagnostic potential, different subgroups were created. Parameters were separated by statistical and spectral methods, but also a consideration was made as to which ones would be obtained in real-time. A summary of the groups of QUS parameters is shown in Table 4.2. The binary classification process was repeated for each subgroup, including calculation of accuracy and F1-score.

Table 4.2: Summary of QUS parameters used in machine learning training algorithm.

		Symbol	Description
<i>Near real-time</i>	<i>Spectral</i>	a_{eff}	ESD
		n_z	EAC
	<i>Statistical</i>	\bar{E}	Mean of pixel intensity
		\bar{E}^2	Variance of pixel intensity
		\bar{E}^3	Skewness of pixel intensity
		\bar{E}^4	Kurtosis of pixel intensity
		\bar{E}^6	6 th moment of pixel intensity
		X	X-statistic
		U	U-statistic
		ϵ^2	Coherent signal power
		σ^2	Diffuse signal power
		α	Scatter clustering parameter
		κ	Structure parameter

4.3.4 Effect of Freezing and Fixation

In a separate study, further fresh chicken liver and gizzard were purchased from a Halal butcher. 30 samples of each tissue type were prepared using a surgical scalpel as in Section 4.3.1.1. Ten samples of each tissue type were analysed fresh, while ten were frozen and ten were placed in a sealed container with 4% paraformaldehyde for 24 hours. The experimental set-up is the same as that displayed in Fig. 4.5a and the data acquisition and QUS analysis are the same as those described in the previous sections. However, instead of a parametric imaging approach, the gate length, or depth, was set at 1 cm for all samples to take measurements over the whole tissue thickness. A larger gate length will improve statistical accuracy, but results in only one set of QUS parameters for each sample.

The parameters from fresh liver and gizzard were measured first. 24 hours after sample preparation, the frozen tissue was removed from a -20°C freezer and allowed to defrost in a tepid water bath while still in their packaging. The fixed samples were handled wearing gloves, but were analysed using the same procedure outlined above, and this was repeated once more when the frozen samples had fully defrosted.

Four key QUS parameters which are system independent and have physical meaning behind them were investigated in this study, which is imperative for tissue characterisation. The parameters measured were ESD, EAC, α and κ , the calculation procedures for which have already been discussed. These were calculated for samples of fixed, fresh, and frozen tissue and a t-test was used to determine if there were significant differences in the results from preserved tissues compared to fresh tissue.

4.4 RESULTS AND DISCUSSION

4.4.1.1 Acoustic Impedance

The mean and variance of the measured results for density and acoustic velocity are shown in Table 4.3.

Table 4.3: Results of acoustic impedance measurements for liver and gizzard

	Density (kg m ⁻³)	Acoustic velocity (m s ⁻¹)	Acoustic Impedance (MRayl)
<i>Chicken Liver</i>	1047 ± 23	1539 ± 85	1.64 ± 0.09
<i>Chicken Gizzard</i>	1051 ± 8	1510 ± 44	1.59 ± 0.05

Most tumours and healthy brain tissue fall in the density range $1040 - 1091 \text{ kg m}^{-3}$ and velocity within $1503 - 1550 \text{ ms}^{-1}$. The values observed for liver and gizzard certainly do fall within these brackets.

The uncertainties in the acoustic impedance values may be from the uncertainties in the volume calculation, resulting from limitations in the Archimedes method. As the test-tube had to be full of water, even filling the container by eye could result in discrepancies in the amount of water present in each measurement due to surface tension. However, the difficulties involved in cutting soft tissue to a perfect geometric shape outweighed this concern. Soft tissue slicing machines do exist and should be considered in further studies in this field.

In general, there was a larger uncertainty in the speed of sound calculation than in volume, which most likely comes from the thickness measurement of the sample. An accurate measurement of the thickness of fresh tissue was difficult using callipers as the material can easily deform. Maximising the size of tissue sample used would diminish the contribution of these errors.

4.4.1.2 Attenuation

The results for the attenuation via the TL method are shown in Fig. 4.7 for each frequency under investigation. The error bars indicate the variance on the mean at each point. A linear frequency response was assumed in this study, which utilised conventional ultrasound frequencies, so the attenuation coefficient, α_C , measured in $\text{dB MHz}^{-1} \text{ cm}^{-1}$, is the gradient of the line of best fit through the results at each frequency.

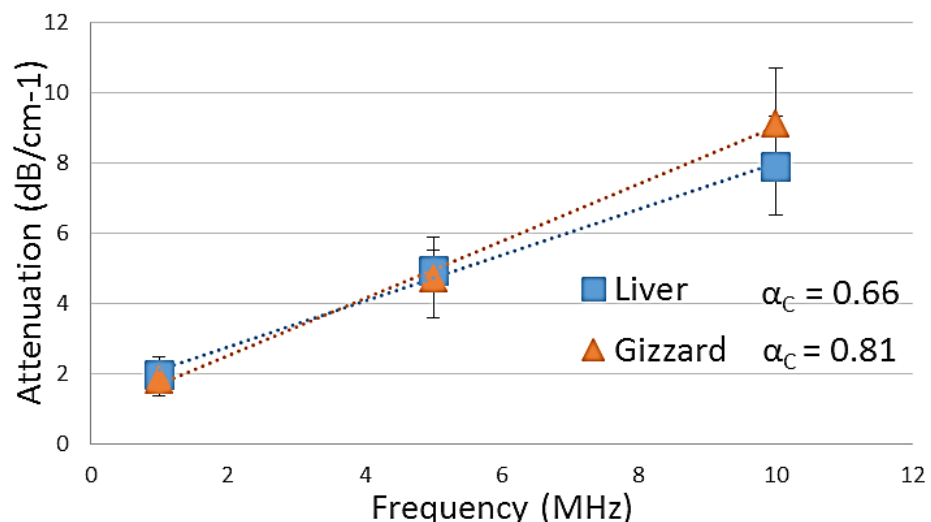


Figure 4.7: Attenuation values, with error bars showing uncertainty in chicken liver and gizzard over 1 – 10 MHz range.

The error in the attenuation coefficient is the error in the gradient of the line of best fit. This is calculated by finding the line of best fit through the extremes of the error bars, so as to find maximum, m_{\max} , and minimum, m_{\min} , values of gradient. The uncertainty in the gradient is then given by:

$$\Delta\alpha_c = \frac{m_{\max} - m_{\min}}{2} \quad (4.8)$$

The attenuation coefficients were 0.66 ± 0.16 and 0.81 ± 0.18 dB MHz⁻¹ cm⁻¹ for liver and gizzard respectively. When compared to the results of the literature review in Fig. 3.2, the results for liver agree well at 5 MHz with those for healthy brain *in vivo* and it would be expected that there would be further agreement if the data were extrapolated to 10 MHz with a linear trend [133]. Chicken gizzard figures agree well with the *ex vivo* results for GBM, further evidencing its suitability as a malignant tumour phantom [85]. The results emphasise the similarity between the two tissue types in terms of acoustic characterisation and the error analysis highlights the heterogeneity of the tissue samples.

Values in the literature for human samples manifest significant variation and, importantly, the two reported instances of *ex vivo* cancerous brain tissue show attenuation in glioma to be only slightly above the values for healthy brain, whereas meningioma shows a larger difference. Chapter 5 shows that GBM has a slightly higher attenuation than healthy brain tissue at 25 MHz. As attenuation is derived mainly from an absorption component and a scattering component, it is a good macroscopic measure of scattering within a tissue. It is thus possible to conclude that the results here are evidence that liver and gizzard are reasonable phantoms for white matter and glioma tumour over the present frequency range of interest. This is in agreement with Stewart et al., who concluded these were suitable phantoms in terms of steady-state mechanical properties. On a microscopic level these phantoms may not be adequate to describe the complex nature of brain tissue, but they are suitable for proof-of-concept studies.

4.4.1.3 B-mode Images

B-mode images of liver and gizzard were created from the RF data and are displayed in Figure 4.8. The acoustic similarity in these two tissue types is evident in the conventional ultrasound image as it is difficult to distinguish between the liver and gizzard samples from the B-mode images alone.

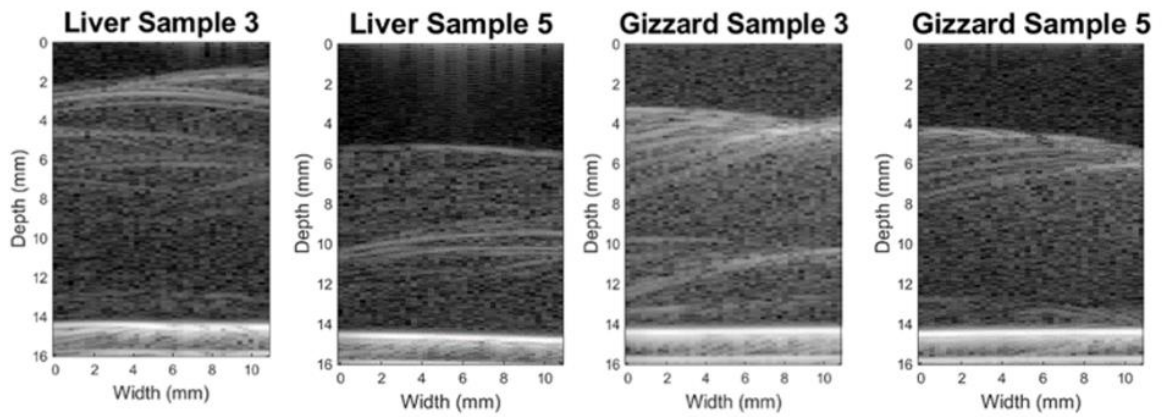


Figure 4.8: B-mode images of liver and gizzard samples obtained with Verasonics L15-8 array.

4.4.1.4 QUS Results

Fig. 4.9 shows the numerical results for some QUS parameters for all 1 mm x 1 mm sections of tissue via the sliding window technique. Results for liver samples are displayed in blue, whereas gizzard is coloured red. There is a distinct clustering of data into liver and gizzard regions, even when considering the 2-dimensional visualisation here. The echogenicity has a higher variance in liver samples than in gizzard but there was generally a spread over all samples. The spectral parameter saw very distinct regions of values for each sample, as shown in the small clusters in Fig. 4.9b. This indicates the parameters are very dependent on the sample used, which may indicate issues with alignment between measurements.

The X and U parameters for HK-distribution analysis give a reasonable separation on their own, before the complex algorithms have been used to solve for the model parameters, which is an interesting result. α tends to take a higher value in gizzard samples than in liver which suggests there is higher organisation in gizzard tendons. There is notable discretisation of results for κ which may be due to the tolerance values of the algorithms involved in solving the non-linear equations of X and U. The algorithm was tested using published values of α and γ , for a given input of X and U, with the tolerance set to 10^{-4} for both algorithms 1 and 2, respectively. The tolerance level can be optimised for the specific application to ensure a trade-off between accuracy and computation speed; this will be discussed in Section 4.4.2.5.

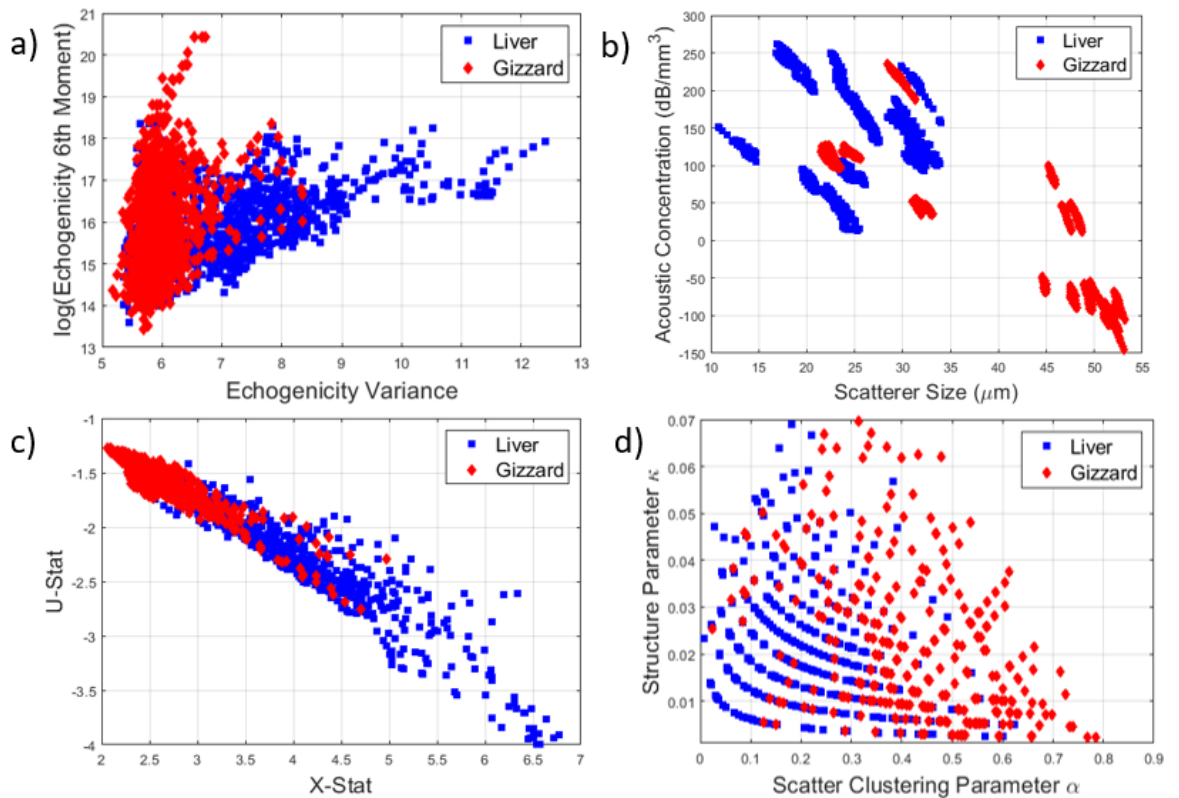


Figure 4.9: QUS parameter results for 1 mm x 1 mm regions. a) Two echogenicity parameters showing distinct clustering of results for liver and gizzard. b) Spectral parameter results highlighting the very small intra-sample variance. c) The X and U statistics used to estimate the HK parameters. d) The results for the scatter clustering parameter and structure parameter.

4.4.1.5 Parametric Images

Parametric B-mode images are formed by assigning each pixel a colour based on the parameter value in that ROI, with reasonable colour bar axes. This type of image was produced for all thirteen QUS parameters for all samples. Examples of four parametric images for two samples of liver and gizzard are displayed in Fig. 4.10 The images highlight the significant differences in the parameter values for liver and gizzard for selected spectral, statistical and echogenicity parameters. The scatterer size was found to be significantly higher in gizzard, suggesting that the scattering sources are larger agglomerations of scatterers, further evidenced by a higher clustering parameter. There was also a larger variance in echogenicity values in gizzard and a lower value of skewness of the echogenicity distribution.

The images show that all the parameters exhibit classification potential, but there are still some outlying pixel results for some parameters. Whilst pixel values were seen to be fairly consistent throughout relatively large regions within each sample, the “edge effect” was observed. This is an artefact of the sliding window method that exists because the pixel values around the edge tend to be different to those in the bulk of the sample. It is particularly

evident in the liver samples and could be reduced by using a larger window percentage overlap. The parametric image alone would provide additional information to the conventional B-mode image in this case to aid in tissue identification.

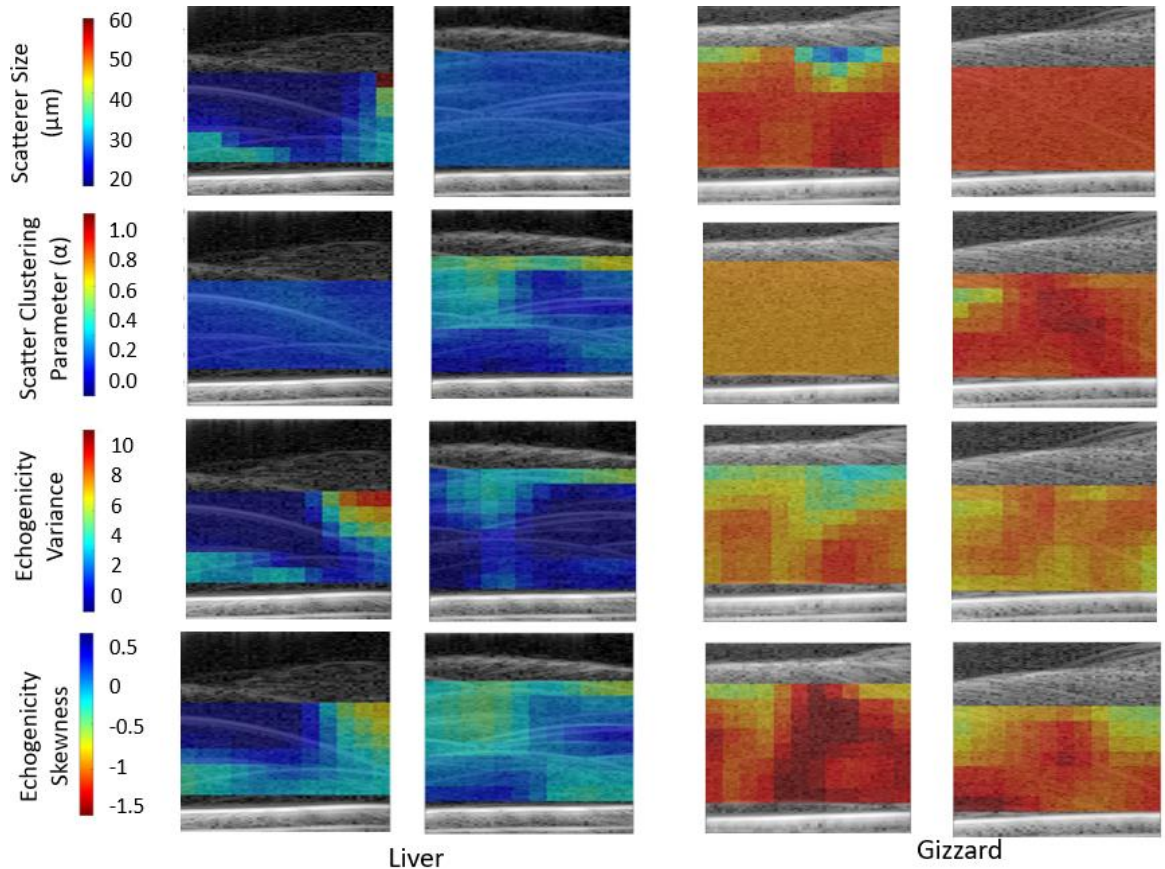


Figure 4.10: QUS images from two samples of both liver and gizzard. Parameters shown are scatterer size, scatter clustering parameter, echogenicity variance and skewness, with colour bars based on maximum and minimum values for both individual tissue types

There will always exist a trade-off between parametric image spatial resolution and confidence in statistical QUS measurements. At the frequency used here, it is possible to obtain reliable estimates over 3 mm sections of tissue, however increasing the frequency of the ultrasound will result in shorter wavelength. Hence, there will be a smaller restriction on the window size and a higher resolution parametric image could be produced. The ideal window size, or gate length, has been considered in various studies of spectral parameters [25], [173] but there are fewer studies relating to HK parameters. In the present study, Fig. 4.11 shows the effect of ROI size on the HK parameters, α and κ in a) and b) respectively. The results approach a limiting value at around the 3 mm window dimension, which corresponds approximately to 10 times the wavelength of ultrasound in tissue at 5 MHz, supporting the present choice.

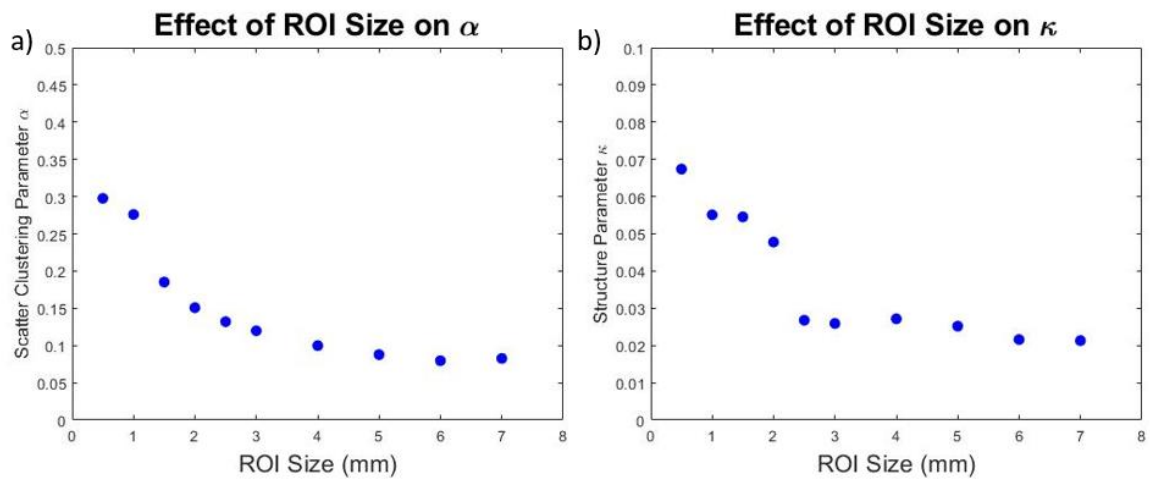


Figure 4.11: Effect of ROI size on HK-distribution parameters showing approach of the true value when ROI size exceeds 3mm.

4.4.1.6 Machine Learning Classification

Initially, all 13 QUS parameters were used to train a binary classifier. The method chosen was the KNN algorithm, using 5 neighbours. The number of neighbours was chosen as 5 as this was a low number of neighbours with regards to this data set, and could have been increased and optimised if required, but this was not necessary as $k=5$ was sufficient. After inspecting the data, various parameter sets were chosen in an attempt to reduce the number needed for analysis. These subsets were all tested using randomly chosen training and testing samples, and this process was cross-validated by repeating it six times to avoid over-fitting. The accuracy and F1-score for various parameter sets over 6 folds are shown in Table 5, along with the mean value. Unsurprisingly, the classifier with the highest accuracy, on average, used all 13 parameters, which achieved an accuracy of 95.5% and an F1-score of 0.944. This is compelling evidence for QUS as a means of tissue characterisation, though the question of the match between the phantom materials and human tissue remains.

To demonstrate this further, the binary classification results for the pixels of each test sample were superimposed on the original B-mode images, as shown in Fig. 4.12. This highlights how a classification image can provide useful information to the B-mode image which aids tissue differentiation in tissues which are indistinguishable by B-mode image alone.

Table 4.4: Accuracy and F1-score for various parameter sets.

	All parameters		Near-real time		Spectral		Statistical	
	Accuracy	F1-score	Accuracy	F1-score	Accuracy	F1-score	Accuracy	F1-score
<i>Fold 1</i>	90.3%	0.870	90.6	0.876	79.9%	0.767	80.5%	0.762
<i>Fold 2</i>	97.9%	0.974	97.9	0.974	61.8%	0.525	85.1%	0.814
<i>Fold 3</i>	96.3%	0.951	92.0	0.887	79.3%	0.642	66.3%	0.76
<i>Fold 4</i>	96.7%	0.956	97.7	0.970	80.7%	0.678	71.0%	0.664
<i>Fold 5</i>	95.4%	0.940	935	0.914	82.4%	0.725	84.3%	0.819
<i>Fold 6</i>	96.9%	0.968	97.8	0.979	95.7%	0.957	67.3%	0.639
Average	95.5%	0.944	94.9%	0.933	79.9%	0.715	75.7%	0.743

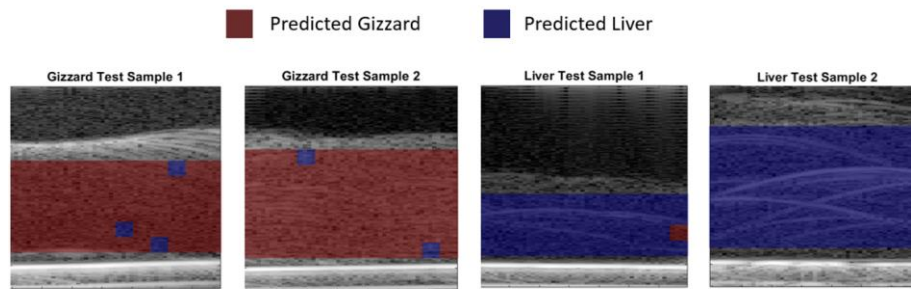


Figure 4.12: Pixel prediction of liver and gizzard. Binary results from fold 6 of the classification algorithm are superimposed on B-mode image.

The classification images in particular testing samples were from fold 6, corresponding to an accuracy of 96.9%, with almost all of the incorrectly identified pixels located at the edges of the images. This may be due to the ‘edge effect’ where these pixels use less data to calculate the results, so may be less accurate. As noted previously, this problem could be overcome in the future by using a larger window overlap or a higher frequency of ultrasound to allow more wavelengths within a smaller window to provide greater statistical accuracy. More often gizzard was incorrectly labelled as liver, which may be due to inhomogeneities of different acoustic properties to the majority of gizzard samples. The classifier would assume that particular pixel came from a liver sample as the QUS parameters, which were used as features, are much closer to the results of the training data for liver.

Despite these promising imaging results, the time it took to form them was around 25 min. due to the complexity of the algorithms involved in estimating the HK-distribution parameters. An interesting alternative would be to omit these and look only at parameters which could be obtained in a timely manner, i.e. quasi-real time parameters, Table 4.2, taking

into account the target application of real time tissue categorisation intraoperatively. Taking this approach, the accuracy dropped only from 95.5% to 94.9% when considering these parameters, which would still be sufficient for real-time characterisation.

From Table 4.4, another approach studied was using only spectral parameters and it was intriguing to see the high variance in classification accuracy and F1-score results. This indicates an algorithm which is too finely tuned to the dataset, and given the small sample set here, the random choosing of the test samples had a huge effect on the classification performance. However, on average the spectral results still performed better than the statistical results alone. Looking at the results from the statistical methods, a high number of pixels were incorrectly labelled. This indicates an overlap in the numerical results in the HK statistics from liver and gizzard, meaning these parameters are not suitable for differentiation at this frequency. It is important to note that the *combination* of all QUS parameters provides more dimensionality in the classification algorithm, achieving higher results, but using all parameters comes at a cost.

4.4.1.7 Computational Cost

The computational cost is important if QUS is to be used as a real-time imaging tool for intraoperative tissue identification. The time taken to image a 1 cm x 1 cm region, similar to the images shown here, was calculated for the various parameter sets: echogenicity values alone were the quickest, with an average time of 4.7 seconds, followed by spectral parameters which took 6.3 seconds.

The algorithms involved in solving for parameters of the HK distribution require a tolerance value, which can be tuned to give more accurate or faster results. The tolerance value used in this study was 0.0001 for both α and γ estimations. This resulted in a total time for a 1 cm x 1 cm QUS image of 22 minutes. To reduce computation time, the tolerance values were explored and the results in Fig. 4.15 show the time in sec. it took to compute α and γ while varying both tolerance levels. It can be seen that the time taken reduces linearly while the tolerance values increase exponentially.

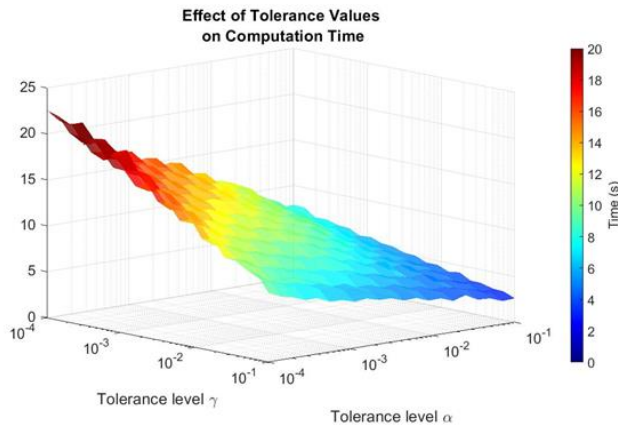


Figure 4.13: Computation time for HK parameters for various tolerance values in both α and γ .

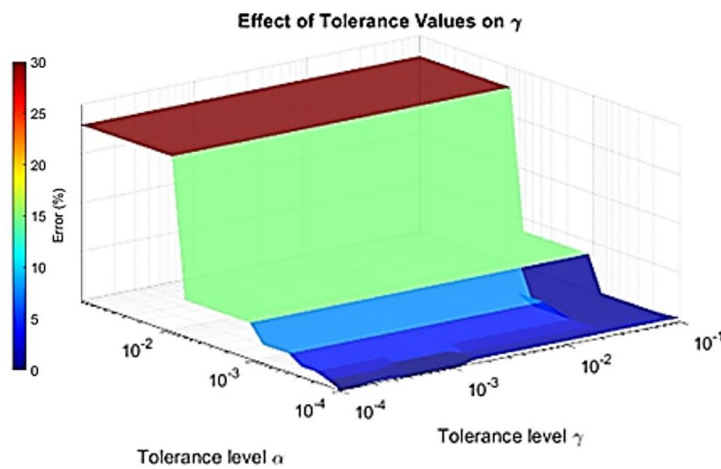


Figure 4.14: Percentage error in γ estimation for varying tolerance values.

The percentage error in γ is shown in Fig. 4.14 against both tolerance levels. There are two key observations from this result: areas of sudden decrease in accuracy are seen, and the results are far more dependent on the α tolerance value than the γ . With a threshold of maintaining a 5% accuracy in γ , the point on the graph with the highest tolerance values which satisfies this is indicated as $t1 = 0.01778$ and $t2 = 0.0001995$. Using the previous figure, it can be seen that these tolerance values correspond to a computation time of 10.78 s. This is less than half of the original time with minimum tolerance values, which will speed up analysis dramatically; however, it is still a slow computation on a standard PC. In terms of computational cost, it would be optimal to use only spectral and echogenicity parameters while working towards real-time application.

It is clear from these results that the overall estimator is not suitable for real-time imaging. Considering even a small ROI with limited resolution, for example around 60 pixels, the

parametric image will take 11 minutes 10 seconds to form. The estimation of parameters would deviate too greatly from the best estimate if the tolerance values were reduced any further. Given the quick calculation of the X and U statistics and that there is no classification improvement when including these results, one can conclude that parametric imaging of the model parameters of the HK-distribution is not feasible in real-time. However, they may still be useful in the OR if only one set of model parameters are obtained for a specific ROI. Simple statistics of the echogenicity and spectral parameters can provide adequate tissue differentiation for these specific tissues.

4.4.1.8 Effect of Freezing and Fixation

The results for the four QUS parameters of interest in the three tissue states, i.e. fresh, frozen and fixed, are displayed in Fig. 4.15.

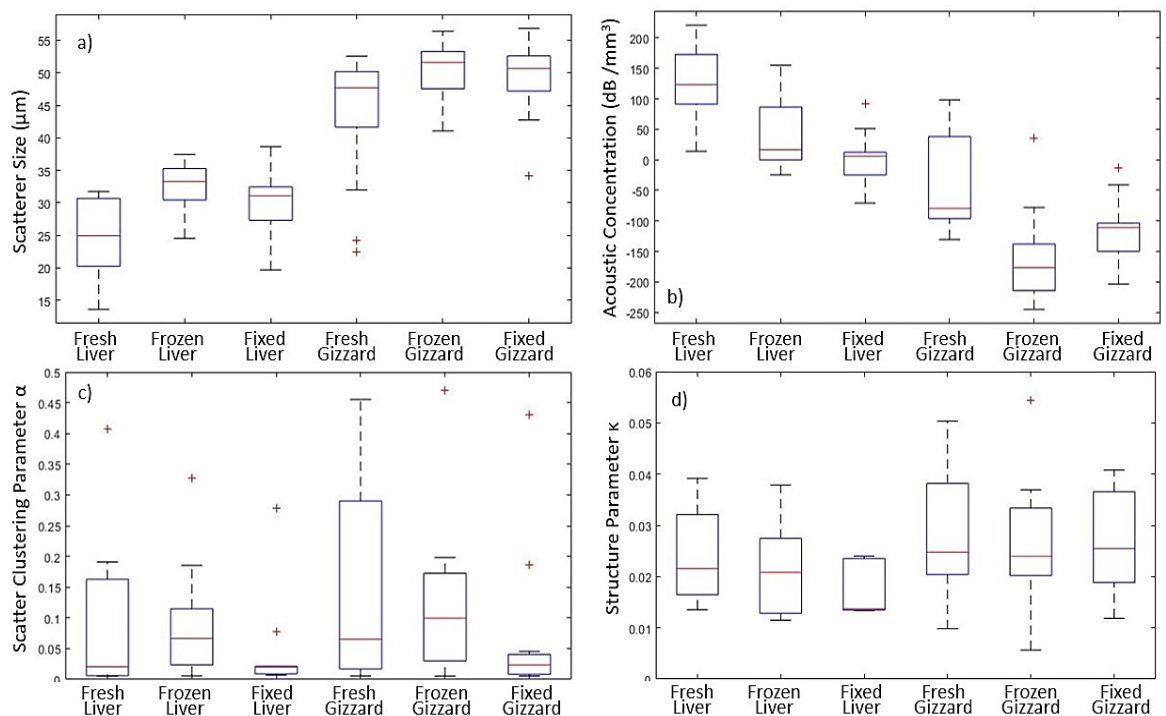


Figure 4.15: Boxplot of results from fresh, frozen and fixed liver and gizzard. a) scatterer size, b) acoustic concentration, c) scatterer clustering parameter d) structure parameter.

Some parameters were affected more than others due to fixation or freezing. The scatterer sizes in all instances of liver were around 15 - 35 microns, while gizzard remains much higher at around 40 - 55 microns, in agreement with the results from Section 4.4.1.4. The key observation here is that the interquartile range, indicated by the box, does not move considerably when the tissue is preserved via freezing or fixation. This makes sense

physically as both freezing and fixation should not alter the cell size significantly. On the other hand, the acoustic concentration, Fig. 4.15b, sees a marked decrease in frozen and fixed tissue, in both liver and gizzard. This parameter relates physically to the acoustic impedance mismatch between the scattering sources and surrounding material in the tissue. Under manual palpation, the tissue felt noticeably stiffer after fixation, corresponding to an increase in speed of sound and therefore in acoustic impedance in the whole tissue, which will alter the acoustic concentration parameter. The scatter clustering parameter and structure parameter relate to the microstructure distribution of scatterers and they varied slightly depending on the tissue state.

These results provide another view to highlight the differentiation power of specific parameters. For example, the values of scatterer size and κ are noticeably different in liver and gizzard, whereas the scatter clustering parameter does not show much distinction between tissues.

In order to provide a quantitative measure of whether QUS parameters were significantly affected by preservation, P-values comparing results from fixed and frozen tissue to the values for fresh tissues were calculated for each parameter and a P-value of 0.005 was used in a t-test to test for significance. Table 4.5 shows that the majority of QUS parameters were not significantly changed by the process of preservation, but those highlighted in bold were.

Table 4.5: P-values from t-test comparing frozen and fixed QUS parameters.

QUS Parameter	Liver		Gizzard	
	Fixed	Frozen	Fixed	Frozen
<i>ESD</i>	0.069	0.052	0.047	0.270
<i>EAC</i>	0.001	0.006	0.057	0.011
α	0.539	0.677	0.457	0.987
κ	0.953	0.683	0.834	0.601

It is expected that the acoustic concentration parameter produced significant changes to the results of fresh tissue and, interestingly, this occurred for frozen tissue more often than fixed. There must therefore be alteration to the mechanical properties of cells during the freezing process which causes this. It was also helpful to observe that while there were some slight differences in the HK-distribution parameters, the results for α and κ were not significantly altered by preservation. This indicates that most QUS measurements on frozen and fixed samples should not significantly change the results, which gives promise to utilize frozen

and fixed samples of human brain and brain tumour tissue in a future study with direct clinical application. However, not all parameters followed this promising trend, as evident in the acoustic concentration parameter. This may be due to the change in acoustic impedance which has been reported to occur during freezing and fixation.

4.5 CONCLUSIONS

Determination of Acoustic Phantoms

This chapter covered the available literature on the acoustic properties of human brain and brain tumour tissue and found there are limited results *in vivo*, and the tissues are heterogeneous so cannot be characterised generally. It is concluded the acoustic properties for brain and brain tumour depend significantly on the region of the brain and the type of tumour tissue, so it is difficult and inaccurate to say one can find materials which are acoustic phantoms for brain and brain tumour in general. However, the results of acoustic characterisation of chicken liver and gizzard muscle have indicated that liver is a reasonable model for healthy, white matter and gizzard is a reasonable model for malignant brain tumours, such as GBM.

This finding is further evidenced by mechanical properties [104] and by medical device manufacturers who use liver to test brain tissue ablaters. However, the accuracy of the underlying tissue microstructures as models of human brain tissue may be limited. It is still unclear if the complex sub-resolution configurations of real brain tumour tissue can be simplified in this way. Nevertheless, the macroscopic acoustic properties indicate that these materials are suitable for preliminary studies of QUS for tissue characterisation and parametric imaging.

The ability of QUS to aid classification

The work described in this chapter implemented a variety of QUS methodologies for chicken liver and gizzard. Firstly, RF data was collected from 1.2 cm x 1.2 cm samples of liver and gizzard and used to form conventional B-mode images, in which the tissues were almost indistinguishable. Two QUS parameters came from the tissue power spectrum. All statistics involved in the HK model estimation were included and simple statistics based on the echogenicity values were assigned to give 13 in total. The differences in QUS parameters were enough to correctly classify the two tissue types using an unsupervised machine learning approach. This demonstrates that QUS and binary classifications can correctly differentiate two materials which are acoustically similar. In terms of diagnostic value and real-time optimisation, the combination of echogenicity and spectral parameters reduced the

parametric imaging time to 6.3 seconds, while still achieving a high classification accuracy for the ultimate goal of real-time tissue differentiation.

The present study assumed that a good macroscopic ultrasound phantom corresponds to a good QUS phantom. It is not clear if the complex sub-resolution configurations of real brain tumour tissue can be simplified in this way. Nevertheless, a framework has been demonstrated which can classify phantom materials using a research ultrasound system, with encouraging results. Chapter 5 will utilise this framework to measure QUS parameters from *ex vivo* human brain tissue and GBM to fully test the capability of ML assisted tissue differentiation.

The effect of freezing and fixation on QUS parameters

The ESD, EAC, α and κ can be used to describe tissue microstructure independent of the ultrasonic system used, and thus have potential for clinical diagnosis. However, it is not clear whether parameter results from *ex vivo* trials are directly translatable to *in vivo* tissue. It was found that the EAC was significantly altered after the preservation process, however statistical parameters from the HK-distribution and ESD were not altered. This is most likely due to the mechanical changes which take place during freezing and fixation altering the acoustic impedance of the entire tissue, which has a direct effect on the EAC. Thus, care should be taken when interpreting results of this parameter in the *ex vivo* work, while there is confidence the other parameters are clinically relevant. It is important to note that the way in which the microstructure of liver and gizzard changes due to fixation may not necessarily be the same as in brain tissue; however, it is of interest to observe the effects on QUS parameters in these two soft tissues.

4.6 CHAPTER SUMMARY

This chapter began by introducing the importance of phantoms in medical research due to the difficulties in obtaining fresh human tissue to work with. The first aim of the chapter was to review the literature to identify suitable phantoms for brain and brain tumour. Having identified chicken liver and gizzard as possible materials, a full acoustic characterisation, in terms of acoustic impedance and attenuation, was carried out to validate their use for subsequent exploration. Next, QUS techniques were implemented on the phantom tissues and used to form parametric images, which themselves were useful for characterisation. All QUS parameters were used to train a binary classifier to predict whether a sample was liver or gizzard. The potential of this technique is evidenced by the high average accuracy of the classifier. Finally, the effect of freezing and fixation on QUS parameters in the phantoms

were studied to aid decisions about obtaining tissue for further work. In such future work with preserved tissue samples, less emphasis should be placed on the EAC parameter as this would not have translatable *in vivo* results.

5 HIGH FREQUENCY QUANTITATIVE ULTRASOUND DIFFERENTIATES HEALTHY AND GLIOBLASTOMA SAMPLES EX VIVO

5.1 AIM OF CHAPTER

Chapter 4 saw successful implementation of QUS techniques in a linear array operating at conventional imaging frequencies in tissue phantoms. This chapter builds on previous methods and applies the techniques on *ex vivo* human brain and GBM samples. Specifically, the aim of this chapter is to assess the ability of QUS parameters to differentiate between the two tissue types using both linear array transducers and single element microultrasound sources in order to determine which frequency and configuration is optimal for classification. Therefore, the objective of this study is to obtain an accurate estimation of the parameters over the entire tissue sample volume and determine if there are significant differences in the two tissue types, which can be used for ML classification. It begins with the process of obtaining human tissue samples for medical research, followed by sample preparation and the estimation of speed of sound (SoS) and attenuation at LF. It then moves on to a full QUS analysis with a HF 25 MHz linear array, and finally a complete microultrasound analysis at 74 MHz.

5.2 INTRODUCTION

Tissue banks are a source of human tissue for scientists, where patients have donated their bodies for medical research. The samples must be preserved, so are typically available fixed in formalin, or frozen, which is done with liquid nitrogen vapour to ensure a fast-freezing process. There is far more availability of diagnostic slide samples, which measure 25mm (W) x 75mm (L) x 0.02 mm (D) and are used in clinical brain sciences, however the small dimensions are not useful for ultrasound tissue characterisation.

There is evidence showing fixing the tissue samples has a greater effect on the mechanical properties of brain tissue [83]. Section 4.5 explored the effect freezing and fixation had upon QUS parameters measured in chicken liver and gizzard and concluded there were only significant changes in the EAC in frozen and defrosted tissue. It is most suitable to obtain snap-frozen samples, which is possible through a brain tissue repository such as the Edinburgh Brain Bank (University of Edinburgh, UK) [174]. The largest available healthy tissue available for this study was determined to be $\sim 1 \text{ cm}^3$ samples of central white matter, from the brain as indicated in Fig. 5.1.

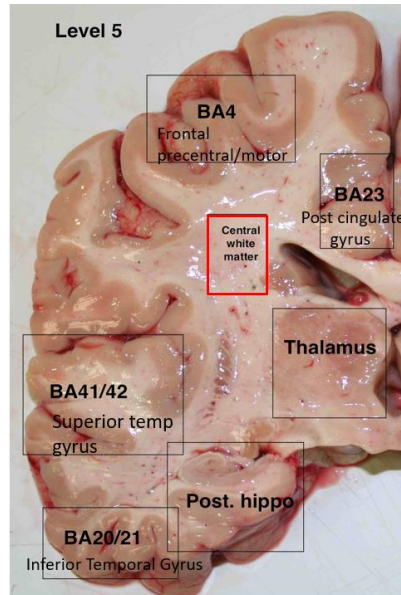


Figure 5.1: Region of healthy human brain used for this study. Image courtesy of Edinburgh Brain Bank.

This repository only holds samples of healthy brain, so cancerous tissue was obtained from Oxford Brain Bank (Oxford University Hospitals NHS Trust, UK), facilitated by Brain UK (University of Southampton, UK). Cancerous tissue is a precious resource for researchers and studies involving human tissues need sufficient evidence that it will be of benefit to patients. Therefore, use must be approved by the relevant ethics committee. The full application form which includes a lay summary, technical background, methods, and potential benefit for patients, which was approved by Brain UK, is given in Appendix III with ethical approval confirmation given in Appendix IV. Next, a risk assessment must be carried out when bringing human tissue into the university, with a particular duty of care needed to prevent blood borne infections such as Hepatitis B. Finally, tissue must be incinerated after use. After necessary considerations, the frozen tissue samples were delivered within the same day and on dry ice from the source institution to the university and immediately placed back into storage at -80°C .

There are some considerations to make in the experimental design when moving from phantom materials to human brain tissue. Currently tissue is placed in a water bath on a strong reflector, for several minutes during the scans. Brain tissue deteriorates very quickly at room temperature. If several scans must be acquired, this may alter the acoustic properties of the tissue over the course of the experiment. A preliminary study with lamb brain was conducted to find the optimal time brain tissue could spend in a water bath before deterioration. This is particularly important when using a motorised scanning system, as

there will be a trade-off between the number of scans acquired over the tissue volume and the time taken to do so. It would be beneficial from a statistical estimation standpoint to have as much data as possible however, this is only meaningful if the tissue has maintained its acoustic properties.

A small section of lamb brain was placed in a water bath. After 15 minutes, the tissue had begun to deteriorate as there were visible flakes of tissue separating from the main sample bulk. Furthermore, there was a noticeable increase in tissue thickness due to osmosis as shown in Fig. 5.2a-c. This is the spontaneous movement of water from a high to a low water potential through the semi-permeable membrane in the tissue cells [175]. A buffer solution such as PBS (ThermoScientific PH level = 7.4) can prevent this as it has the same osmolarity as that for human cells so should not result in any absorption; this was observed in Fig. 5.2d-f. The experiments were conducted at room temperature.

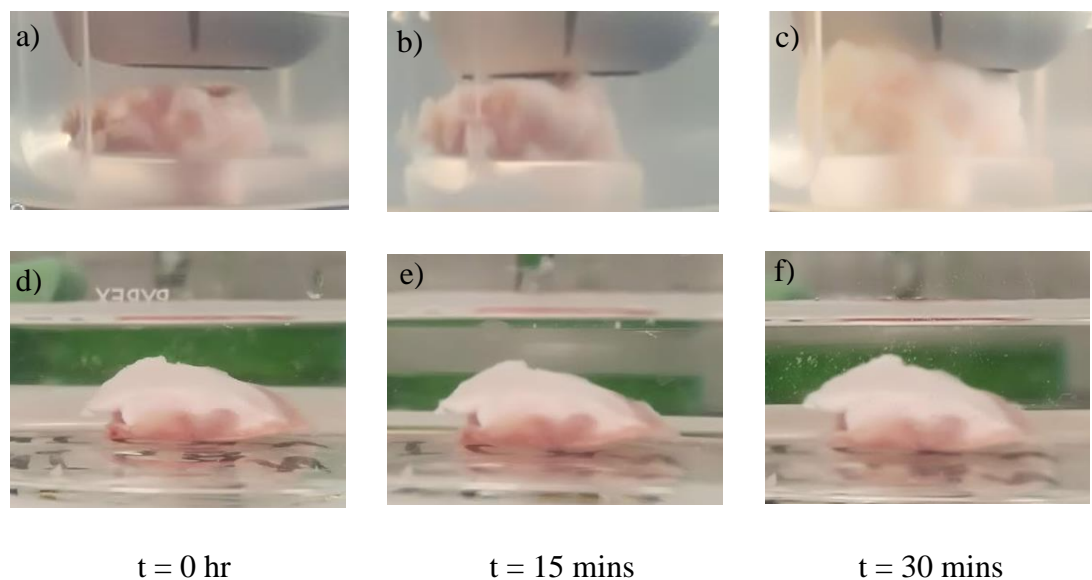


Figure 5.2: Effect of time on submerged tissue over 30-minute time interval. a-c shows the tissue thickness increasing over the 30-minute period when using water. e-f shows almost no absorption by the tissue over the same time interval.

For all QUS experiments involving human brain tissue or tumour, PBS was used instead of water and the maximum time tissue was submerged was limited to 15 min.

5.3 METHODOLOGY

5.3.1 Sample Preparation

Ten samples of healthy cortical white matter were obtained from the Edinburgh Brain Bank (Ref TR76/20) and eight GBM samples were obtained via Brain UK (Ref 20/013). The details of the human tissue samples are given in Table 5.1.

Table 5.1: Details of Human Tissue Samples.

IDENTIFIER	TISSUE	AGE	SEX
H1	Central White Matter	57	M
H2	Central White Matter	40	F
H3	Central White Matter	55	M
H4	Central White Matter	58	M
H5	Central White Matter	49	F
H6	Central White Matter	65	F
H7	Central White Matter	57	F
H8	Central White Matter	34	M
H9	Central White Matter	57	M
H10	Central White Matter	39	M
GBM1	GBM	66	M
GBM2	GBM	54	F
GBM3	GBM	44	F
GBM4	GBM	62	F
GBM5	GBM	48	M
GBM6	GBM	46	F
GBM7	GBM	64	M
GBM8	GBM	73	M



Figure 5.3: A typical sample of healthy white matter.

A typical sample is shown in Fig. 5.3. The dimension of the sample into the page is referred to as the thickness throughout this chapter for acoustic characterisation purposes. The maximum thickness of the samples was measured with digital callipers to four decimal

places. This was done when they were still frozen to ensure the tissue did not deform under the pressure of the callipers. The healthy samples had a mean thickness of 5.29 mm, ranging from 3.56 to 7.11 mm, whereas the GBM samples were smaller, on average, with a mean thickness of 2.01 mm, ranging from 1.56 mm to 2.36 mm.

It would not be possible to conduct a LF ultrasound analysis of the GBM samples due to the small sample size and recommendation of 10 wavelengths of thickness for QUS analysis [26]. However, it was considered useful to study the larger samples of healthy tissue over this frequency range to measure bulk acoustic properties. Furthermore, it would be advantageous for comparison purposes to have similar sample sizes for healthy tissue and GBM. Besides, the microultrasound scanning system was limited by the hardware to have a maximum imaging depth of 7 mm, which was not suitable for the available healthy brain samples. Smaller samples of healthy brain were therefore carefully cut from the larger healthy samples using a surgical scalpel to a comparable size to the GBM tissue (average thickness = 2 mm). Fig. 5.4 summarises the three cases of samples considered and shows the size of the tissue samples received.

To summarise, due to the limited thickness in the GBM sample, the data were obtained using three different acquisition systems as follows:

- Analysis of healthy brain tissue using Verasonics LF linear array (11 - 5 MHz)
- Analysis of healthy tissue and GBM using Verasonics HF linear array (35 – 16 MHz)
- Analysis of healthy tissue and GBM using single element LNO transducer in microultrasound scanning system (74 MHz)

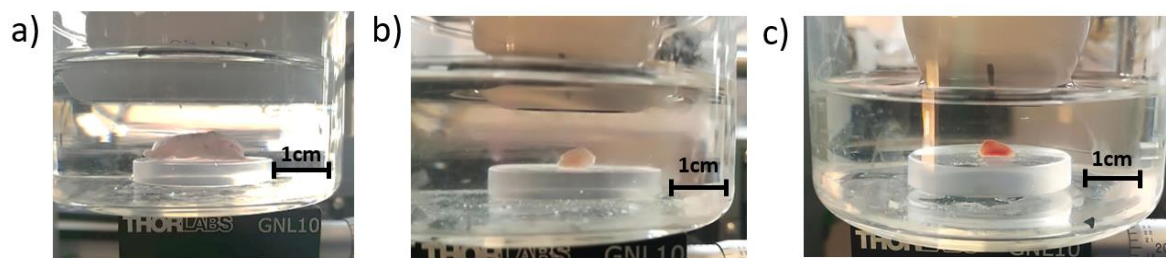


Figure 5.4: Samples for data acquisition using the Verasonics linear arrays. a) Whole healthy sample with LF transducer. b) Smaller section of a healthy sample with HF transducer. c) GBM sample with HF transducer. For scale, the quartz flat is 2.5cm in diameter.

All scans were completed within 6 hours of initial defrosting and samples were kept refrigerated while not being imaged. The Verasonics data acquisition was done first,

followed by LNO microultrasound scanning. Details of the data acquisition for each process are discussed in the following section.

5.3.2 Verasonics Data Acquisition

Due to the small sample size, there was less emphasis on parametric image formation for this procedure. Instead, the aim was to obtain an accurate measure of the QUS parameters from the whole tissue sample. The Vantage 128 Research Ultrasound system (Verasonics, Seattle, USA) was used in a novel way to insonate the tissue samples which could be used to form images and obtain QUS parameters by exciting and receiving on elements 1 – 128 of the linear array sequentially. This is in contrast to the use of the array in the traditional sense, where the elements are excited in specific patterns to focus the beam to a specific point or to steer it at a specific angle. The approach was beneficial for an initial study into QUS characterisation as the individual elements transmit signals of sufficient intensity to produce useful data in a simple protocol that permitted more straightforward analysis than would have been the case with conventional beamforming. Besides, the samples were smaller than the footprint of the probe so ultrasound from the elements where there was no tissue present would have caused unwanted interference and reflections from the quartz flat. The experimental set-up is the same for the LF and HF linear arrays, as displayed in Fig. 5.6. However, the sampling and post processing is slightly different for the HF measurements and will be discussed separately.

A quartz flat was placed in a clear plastic container and filled with PBS. This container was then secured to the surface of a goniometer to allow accurate alignment of the reflector. The probe was clamped approximately 2 cm above the quartz and was connected to a 3-axis manual motion stage. This allows the transducer to remain aligned to the quartz flat yet enables movement over a 1 cm region. To achieve alignment, a real time imaging script was used to display a B-mode image from the transducer as the goniometer was adjusted to ensure the bright reflection of the quartz flat in the B-mode image was a horizontal line. A reference scan was taken with only the quartz present, then the tissue was placed directly under the transducer face on the quartz flat for sample acquisition.

Sequential element excitation was achieved by programming additional ‘acquisition events’ into the software, giving enough time for the entire pulse-echo response to be recorded before moving on to the next element, as visualised in Fig. 5.5. The TGC was set to zero and the raw data were recorded into an empty receive buffer one column at a time, corresponding to each array element. After the 128 elements had each transmitted and received a signal, this was considered as one ‘frame’ of data and a near real time image was displayed on the

computer screen. A total of 50 frames were captured and the average result was used in the QUS analysis to reduce random noise.

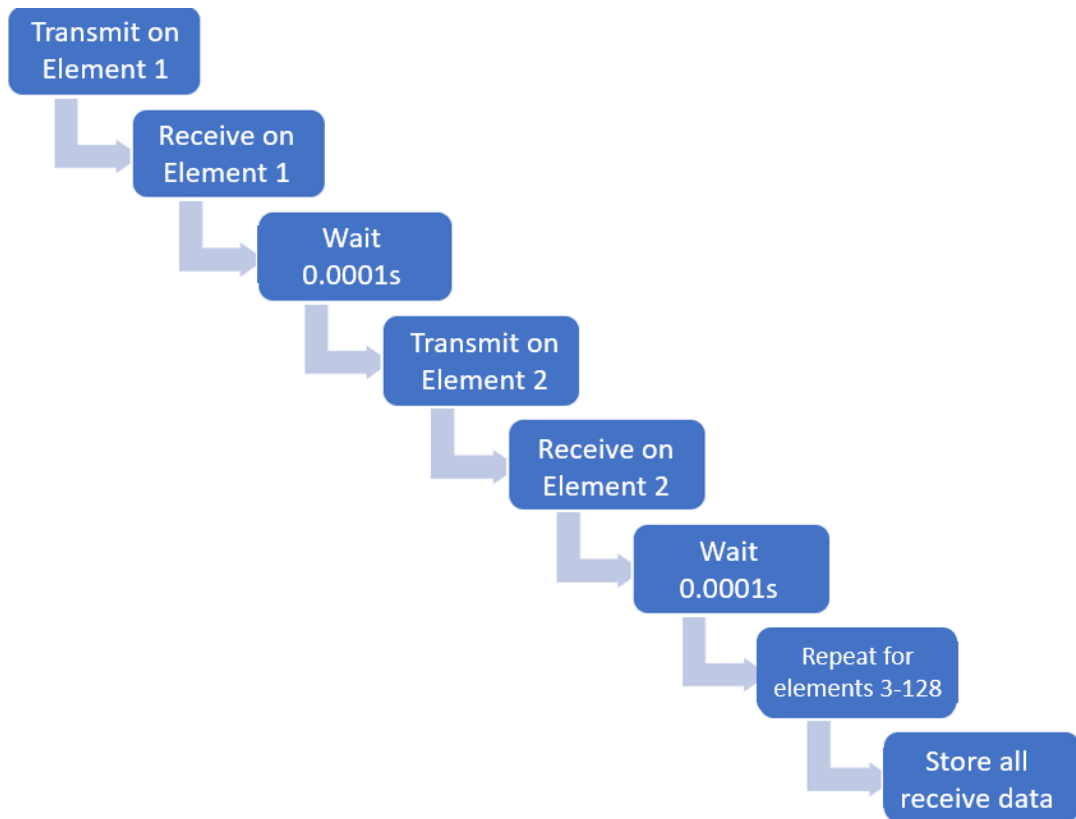


Figure 5.5: Event sequence for individual element transmit and receive with linear array.

For LF analysis, the transducer was excited by a burst with a centre frequency of 8 MHz as displayed in Fig. 5.6. The received signal from each element was sampled at 31.25 MHz, which satisfied the Nyquist limit for the whole transducer bandwidth. 2176 samples were stored, allowing an imaging depth of 5.36 cm, which was more than sufficient for the present application. This process was repeated 50 times until a receive data array containing the raw received data could be saved as a matrix data .mat file for all 128 elements for 50 frames. An initial set of data was recorded with the tissue placed so the transducer was insonating a slice of the tissue in the front region, then the transducer was moved 0.1 mm backwards. This process was repeated for eight different locations, or slices, through each healthy sample, to allow a manual full volume scan which maximised information while still minimising the time the tissue spent in the liquid. Then, the procedure was repeated for the ten samples of healthy tissue.

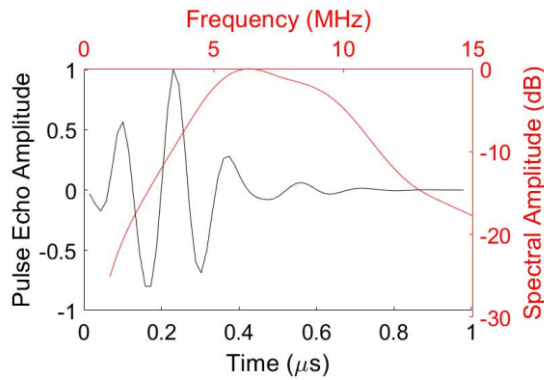


Figure 5.6: Pulse echo response from one array element of the Verasonics L11-5v transducer.

For HF data acquisition, the Verasonics was programmed in the same way as described above, however an interleaving sampling technique was used to achieve a sampling frequency of 125 MHz. This was done by effectively doubling the upper limit of the analogue to digital conversion process in the hardware (62.5MHz) by combining the receive data from two successive transmit and receive acquisitions, shifted by half of the sampling period relative to one another. This increased the time taken to form a B-mode image so 20 frames of receive data were saved during each scan. The scans were made at 5 different locations in the small tissue sample by moving the position of the transducer above the tissue with the manual stage after all 20 frames were saved. This was repeated for the ten samples of healthy tissue and eight samples of GBM, with a reference scan taking place before each sample.

5.3.3 LNO Data Acquisition

A 74 MHz LNO transducer, as displayed in Fig. 5.7a, was mounted to a pair of orthogonally positioned linear motors to collect RF data via a pulser/receiver unit (DPR500, JSR Ultrasonics, Pittsford, USA) at 800 MHz using a National Instruments device (NI 5772, National Instruments, Newbury, UK). The data were then transferred to the host computer as in Fig. 5.7b. There was no TGC; a constant gain of 40 dB was used in the pulser/receiver unit.

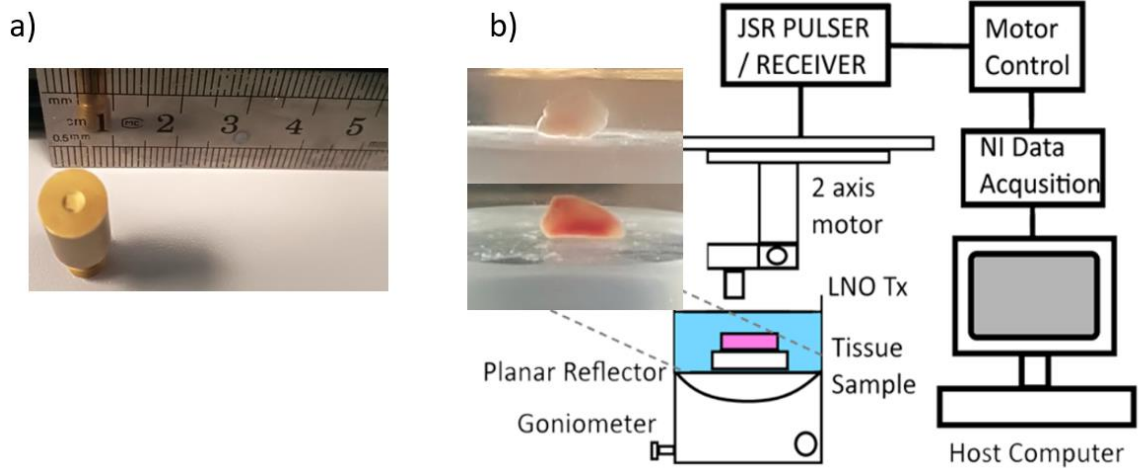


Figure 5.7: Experimental set-up for automated scanning of human brain tissue. a) 74 MHz LNO single element transducer. b) Diagram of data acquisition set-up.

A high-resolution volume scan of the tissue samples was achieved with a LabVIEW-based program written for the scanner. The samples were placed in a PBS bath atop a quartz flat and a stepped scanning approach was used to acquire A-scans over a $7 \times 10 \text{ mm}^2$ region. Scanning steps of 0.01 mm in the X-direction and 0.5 mm in the Y-direction were used, so it could be considered as a high-resolution B-scan, in the x-direction, for 20 different slices of the tissue, as visualised in Fig. 5.8. The total scan time was 12 minutes, which allowed acquisition of data precisely enough over the tissue volume, while minimising the time that the tissue spent in the liquid.

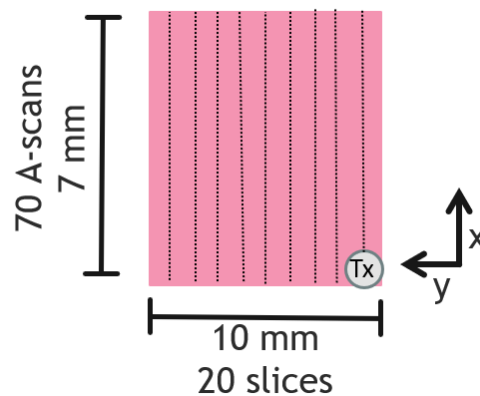


Figure 5.7: Plan view of stepped scanning system over the entire tissue volume using LNO transducer (Tx).

For each scan location, 32 pulse-echo acquisitions were performed, and the average of these independent acquisitions was saved. The data were saved in the filename convention

“Tissuetype_Ylocation_avg.txt” and contained the stepped scanned data over the entire X-direction for that particular Y-location. This continued until all Y-locations were covered. First, a reference signal was obtained which did not have tissue present, only PBS and the quartz flat, which was placed at the transducer’s focal distance of 7 mm. The pulse-echo response was obtained in order to account for the system settings. Then tissue samples were placed successively on top of the quartz flat and the scan was repeated, so each XY location had its respective reference and tissue signals for QUS analysis.

5.3.4 B-mode Image Formation

Formation of B-mode images followed a similar methodology, independent of the acquisition method used, however three custom Matlab scripts (Matlab 2019b, Mathworks, UK) were used for the three acquisition methods, named LF Verasonics, HF Verasonics and LNO for convenience. Each script contained the algorithms for the entire analysis, including B-mode image formation, acoustic characterisation and the various QUS methodologies.

Firstly, the tissue data for one slice were imported into the script to take the average over each frame in the Verasonics data. This was not a necessary step for the LNO data. Then the envelopes of the average received data were compressed and assigned echogenicity values using a dynamic range of 80 dB. This range was deemed most suitable for optimum image quality after using a sliding scale between 50 – 100 dB.

5.3.5 Acoustic Characterisation

The software used for acoustic characterisation and QUS parameters in this study was modified to account for the slight inconsistencies in tissue thickness. Firstly, the B-mode image was displayed and the user was asked to select a ROI which should be suitably chosen as the area where the maximum thickness remained uniform, such as that displayed in Fig. 5.9. This was the only region in which the absolute thickness could be reliably measured frozen. While this reduced the number of A-scans used in subsequent analysis, it had the benefit of preventing uncertainties in tissue thickness propagating into errors in speed of sound (SoS) and attenuation measurements, which would then lead to inaccuracies in the spectral parameter estimates.

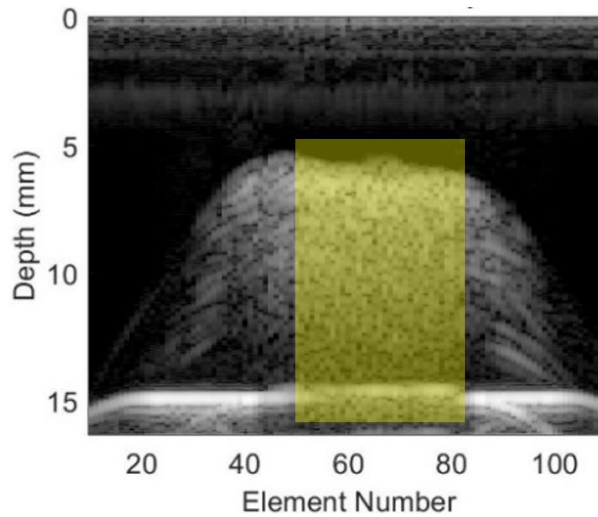


Figure 5.8: Example of B-mode image with selected ROI used in acoustic characterisation highlighted in yellow.

The A-scans from a suitable ROI were then displayed and the SoS was calculated using the difference in the times of flight between the received signal from the quartz with and without the tissue. This is shown in Fig. 5.10, where the signal has arrived sooner in the tissue sample, as the SoS in brain tissue is faster than in PBS. The difference in time between signals can be used to measure the SoS using the following equation:

$$c_s = \left(\frac{1}{c_{PBS}} - \frac{\Delta T}{2d} \right)^{-1} \quad (5.1)$$

where c_{PBS} is the SoS in PBS, taken as 1505 ms^{-1} [176].

An estimate for the SoS was made using the A-scans in each tissue slice and 5 slices were acquired in each sample, leading to $n = 50$ measured results for healthy tissue and $n = 40$ measurements for GBM. The mean and standard deviation were calculated for each tissue type.

Fig. 5.10 shows a marked decrease in signal amplitude due to the attenuation of the tissue, however a broadband substitution technique was used to obtain the frequency dependent attenuation function over the frequency range specified by the bandwidth of the linear arrays, and over the range 66 - 80 MHz for the LNO transducer.

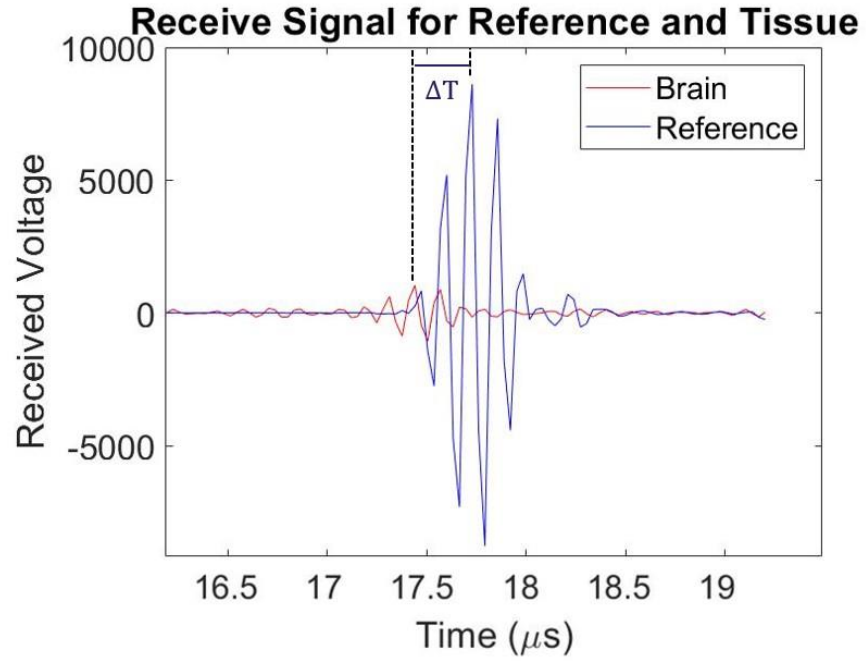


Figure 5.9: Examples of the received signals from the quartz flat with (red) and without (blue) the brain tissue present.

The attenuation function is calculated from the quotients of the power spectrum with and without tissue and is given as :

$$a(f) = \frac{10}{2d} \log_{10} \frac{W_{TIS}(f)}{W_{REF}(f)} + a_{PBS} \quad (5.2)$$

where W_{TIS} and W_{REF} are the power spectra of the reflections from the quartz flat with and without intervening tissue, respectively, and are found using Equation 3.10, where a_{WATER} is the attenuation of water displaced by insertion of the tissue. The factor of two on the denominator comes through the fact it is measured in a pulse-echo set up, so the total propagation distance is double the tissue thickness. The attenuation function was measured for each suitable element individually for the Verasonics arrays, using each slice and all samples.

5.3.6 QUS analysis

Spectral Parameters

The ESD and acoustic concentration were estimated in the procedure described in Section 3.3. The attenuation compensation used in each measurement was the attenuation function calculated in the tissue for that specific element from the TL method described above. In this

study, due to the small sample size, the gate length was taken as the whole tissue thickness. The calibrated power spectrum was found for each A-scan and the parameters were calculated based on the average power spectrum over the entire sample volume.

Statistical Parameters

The echogenicity values from the B-mode images provide a statistical dataset where centralised moments can be calculated and used for differentiation. The first six central moments of the pixel intensity in the tissue ROI were calculated for each slice of tissue, typically consisting of 40 - 60 A-scans.

The HK parameters were estimated using the algorithm described in Section 3.4.4, with a tolerance value of 10^{-4} for both algorithms to favour accuracy over speed. A modification was made to reduce computation time, which uses the whole ROI to obtain average X and U statistics instead of estimating the parameters in each individual A-scan as was done in Chapter 4. This meant an average parameter value for each B-mode image could be found in 10.2 s on average.

5.3.7 Machine Learning Capabilities.

A comparison between healthy tissue and GBM could be made using the parameters obtained in the HF Verasonics and microultrasound analyses. Firstly, a student's t-test was conducted on parameter results to test for significant differences using a confidence interval of 0.05. Then, the full set of QUS parameters, as given in Table 5.2, was used to train a ML classification algorithm using the Classification Learner Toolbox in MATLAB (Version 2019b). This was achieved by creating a table of all QUS results from both tissues, with an additional column containing the label 'Healthy' or 'Tumour'. This could then be imported into the Classification Learner Toolbox which launches a GUI where the user can select which QUS parameters should be used as features and which validation method to use. An 8-fold validation method was used and the overall performance in the confusion matrix was recorded.

Table 5.2: Summary of QUS parameters used as features for *ex vivo* study.

		Symbol	Description
<i>Near real-time</i>	<i>Spectral</i>	a_{eff}	ESD
		n_z	EAC
	<i>Statistical</i>	\bar{E}	Mean of pixel intensity
		\bar{E}^2	Variance of pixel intensity
		\bar{E}^3	Skewness of pixel intensity
		\bar{E}^4	Kurtosis of pixel intensity
		\bar{E}^6	6 th moment of pixel intensity
		X	X-statistic
		U	U-statistic
		m	Nakagami
		α	Scatter clustering parameter
		κ	Structure parameter

The limited data available from the small samples at 25 MHz meant only an initial trial of the potential of the technique was conducted at this frequency using a SVM. The microultrasound scanning produced more robust data acquisition so there were more QUS results to allow a greater exploration. GBM samples were taken as the positive case and three classifiers were considered: a KNN with a number of neighbours of 5, linear SVM and Gaussian SVM. Two key subsets of parameters were considered: those obtainable in real-time, and specifically only the HK results.

5.4 RESULTS AND DISCUSSION

5.4.1 Acoustic Characterisation

5.4.1.1 Verasonics Results

The average SoS of healthy brain tissue was found to be 1551.8 ± 18.7 while that of GBM was slightly higher at 1560.4 ± 23.3 . The higher SoS suggests a slighter higher stiffness in the material, especially taking into account the fact that tissue with more internal structure may be expected to have a lower SoS. However, a t-test was conducted on the results, and this was not a significant difference ($P=0.33$). The source of the errors is most likely the thickness measurements, as any discrepancies in those would propagate an error in the SoS measurements. Care was taken to use data from the region where the most accurate thickness measurement was taken.

The attenuation of the larger, healthy brain samples using the LF Verasonics array is shown in the same diagram as the results for both smaller tissue samples in Fig. 5.14. A linear fit was ideal for the data as shown in Fig 5.14a, however when the graph was forced to have a zero intercept, a polynomial of order two was a more suitable fit. GBM sample 7 had abnormally low (near zero) attenuation results. This was the thinnest of the samples and upon further inspection, the tissue had been torn under the pressure of the tweezer used to handle it during the experiment. This sample was therefore discounted from the average results as the true path length was ambiguous. On average, the GBM samples had a higher attenuation value in the HF range but had significantly higher standard deviation on the mean. At the centre frequency, 25 MHz, the results were $29.9 \pm 1.6 \text{ dB cm}^{-1}$ and $34.8 \pm 4.3 \text{ dB cm}^{-1}$ for healthy tissue and GBM respectively, indicating a 4.9 dB cm^{-1} difference on average.

After a thorough literature search, it is thought this is the first report of attenuation measurements in human brain and GBM above 10 MHz, with comparable studies limited to animal tissues. At 10 MHz, the result for healthy brain is $14 \pm 2.02 \text{ dB cm}^{-1}$, which is similar to, although slightly higher than, the result of Schiefer in 1968, who found healthy brain to be around 10 dB cm^{-1} [85]. The results show there may be a possibility to use attenuation alone to distinguish the two tissue types at this frequency, so the attenuation value at the centre frequency for each scan was included as an additional QUS parameter.

There have been some reports of HF ultrasonic characterisation in mouse brain, which was found to have an attenuation value of 30.7 dB cm^{-1} at 32 MHz [78], lying 5 dB lower than the result from human healthy brain. The standard deviation increased with frequency in all measurements, perhaps due to the lower initial signal energy, as this is at the extreme of the transducer's bandwidth. Efforts were made to reduce this effect by maximising the number of measurements taken from each sample in the time available by utilizing the array as providing 40 - 60 independent attenuation estimates and taking acquisitions at five separate locations within the tissue.

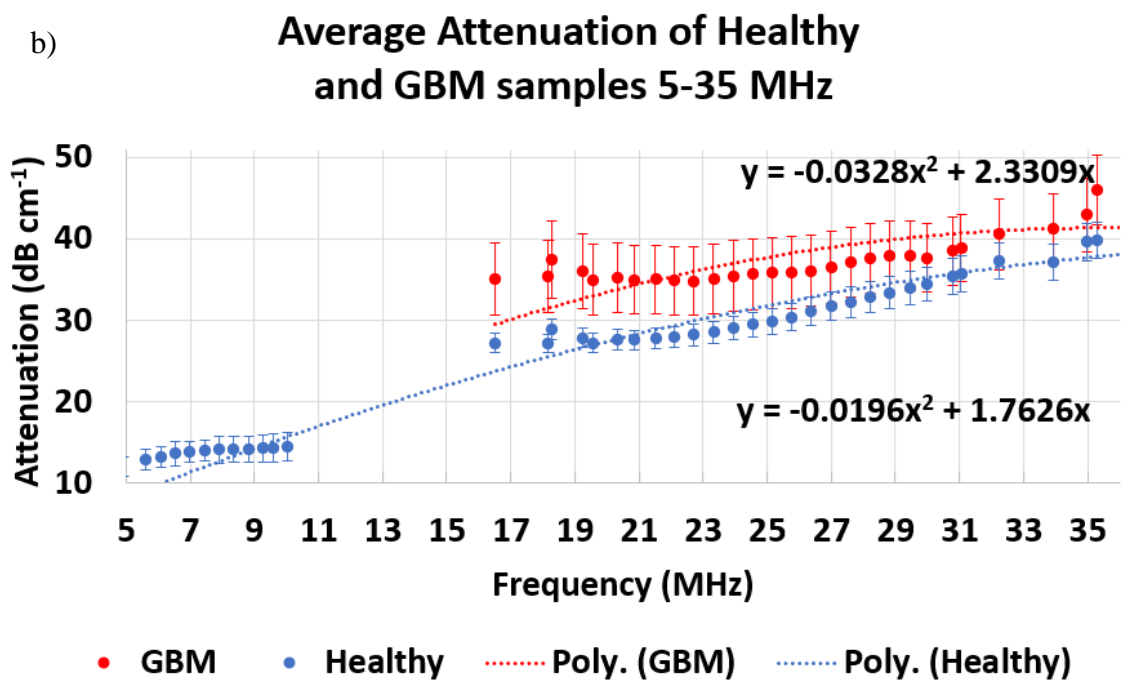
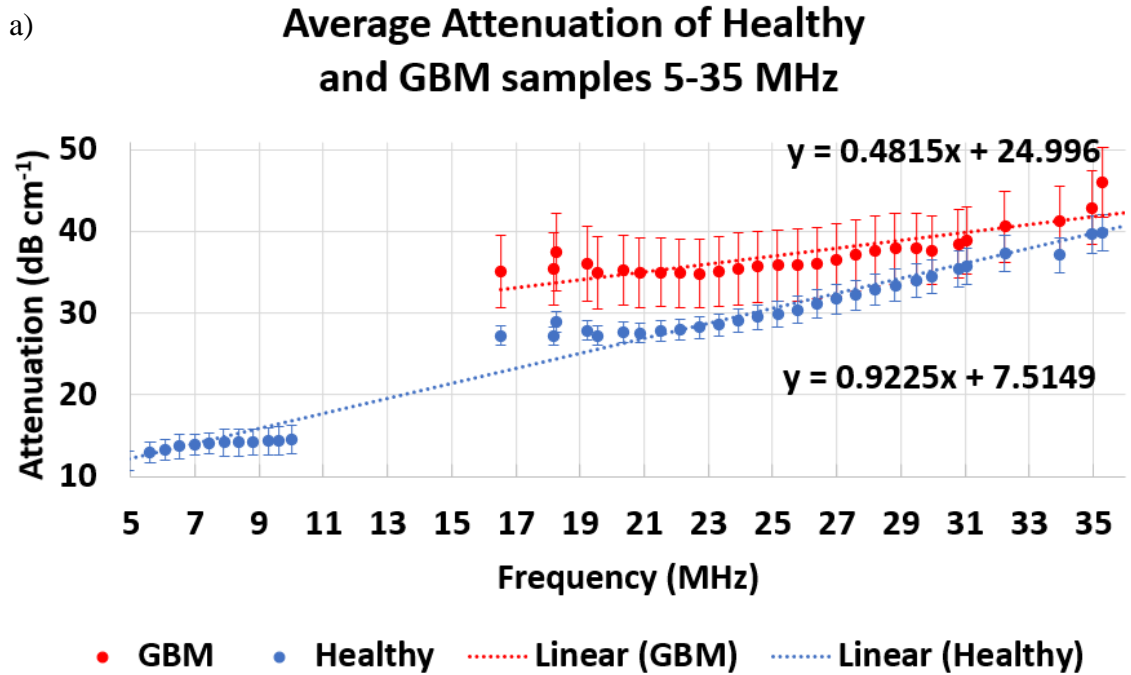


Figure 5.10: Average attenuation of healthy and GBM samples using L35-16 and L11-5 probes. a) The dotted line indicates a single ideal linear fit. b) Polynomial fit with zero intercept.

5.4.1.2 Microultrasound Results

Fig. 5.12 shows a set of 70 averaged A-scans from the microultrasound scanner through both a GBM sample (Fig. 12a) and a reference scan in Fig. 5.12b. Inspecting the magnitude of the received signal from the quartz flat in both cases, as indicated with blue arrows, shows it has remained the same with and without intervening tissue. The insertion of a small tissue

sample should cause a decrease in the received signal from the quartz flat, which is then used to calculate attenuation through the TL method. However, the initial results lead to a near zero attenuation measurement. Further investigation found that the data had been clipped, stopping abruptly at a limiting value, highlighted in Fig. 5.15a. Clipping is a type of distortion in digital signal processing often seen in the presence of high gain, where the hardware has a limitation on the range of values to which data can be assigned.

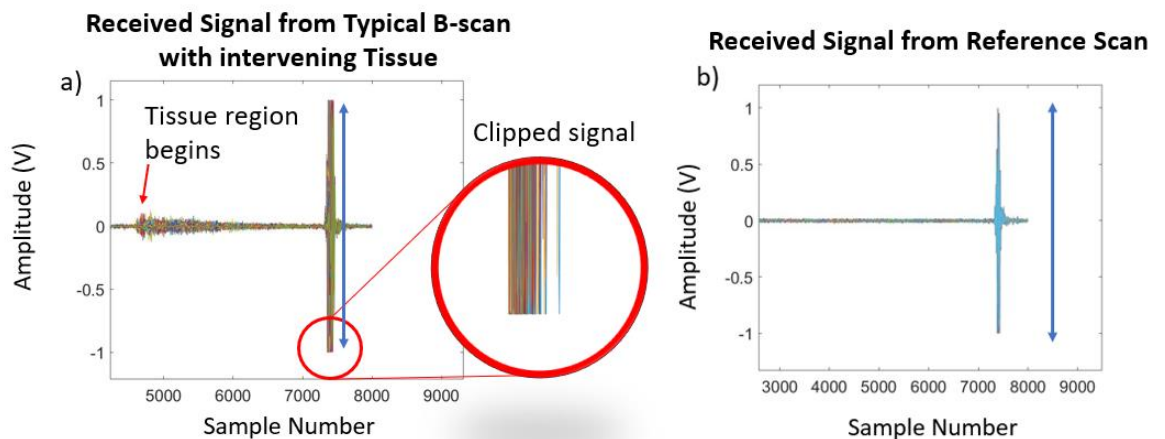


Figure 5.11: Pulse-echo response from LNO scanning set-up highlighting clipped data acquisition. a) Response with intervening tissue, as indicated in the red arrow. b) Reference response from only quartz flat.

As this gives a distorted magnitude of the reference signal, it was not possible to obtain the attenuation results through the TL method in this experimental set-up. Furthermore, the BSPS and associated spectral parameters rely on a calibrated measurement of the power spectrum of the system, which would be erroneous if the analysis were based on the clipped data. For this reason, the system independent spectral parameters and attenuation had to be omitted from this analysis. This issue was not noted in the scanning system set-up previously. The 40 dB gain was routinely used in microultrasound imaging, as it was necessary to extract scattering data from tissue above the noise floor. This is ultimately a drawback of spectral based QUS parameters based on the method of a reference from a quartz flat at HF; one solution is to procure a data acquisition system suitable for this specific application.

There is an alternate approach to estimate the attenuation via an *in-vivo* approach, which does not require a reference scan, and this is discussed in Chapter 7. Nonetheless, the magnitude of the tissue signal region is not affected by clipping so the statistical parameters can still be studied, and B-mode images can be created.

5.4.2 B-mode Images

5.4.2.1 Verasonics Results

B-mode images of healthy tissue brain samples at LF are displayed in Figure 5.13.

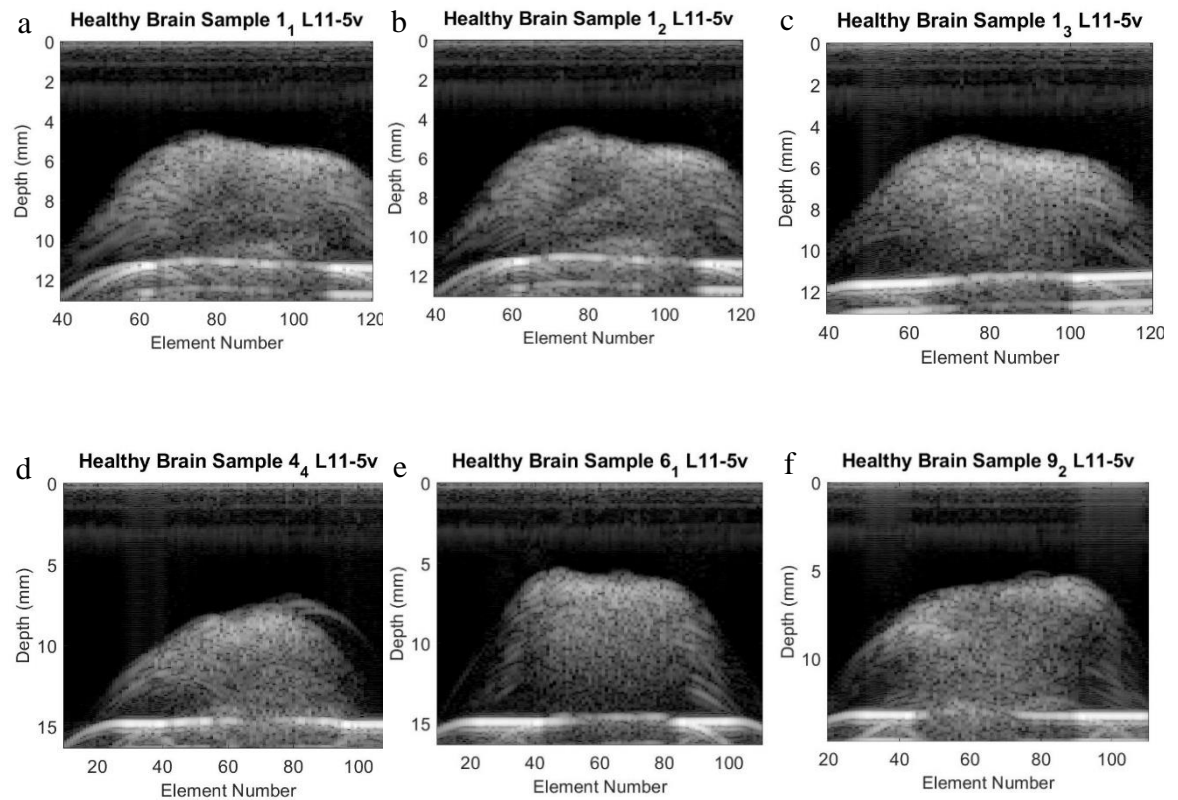


Figure 5.12: Six B-mode images of healthy human brain tissue from the LF Verasonics linear array. The scan number for a specific sample is indicated by the subscript of the sample number.

Fig. 5.12a-c show examples of three different slices of the same sample, highlighting minute inhomogeneities within the tissue over different locations within the same sample. The quartz flat appears as the bright horizontal line at 12 mm depth, yet the brightness is dramatically reduced over the regions of maximum thickness due to attenuation. d-f show one slice of three other samples, showing variations in size and shape of samples, and how all appear echogenic in the B-mode images. The effect of attenuation is observed even within the tissue sample, particularly in Fig. 5.11e, where the intensity of the pixels reduces with depth of tissue. The non-uniformity in thickness of sample is particularly evident in d and f. The B-mode images are essential to navigate to suitable regions of interest for bulk acoustic properties of the samples. Care was taken to choose regions where thickness is uniform in order to minimise thickness variations in SoS and attenuation measurements.

Typical B-mode images for healthy tissue and GBM samples at 25 MHz are shown in Fig. 5.13. When analysing the data, due to some asynchronies in the interleaving sampling

technique in the Verasonics, the data had to be manually checked to include only correctly processed frames. This reduced the number of frames from 20 to 12 and the averages of these were taken to form one B-mode image; this was found to be still sufficient to remove random noise.

All images have a dynamic range of 80 dB, however the appearance of the tissue samples varies significantly between samples of the same tissue type. For example, the healthy samples in Figs. 5.13a and 5.13c have significantly less visible scattering within the tissue than the sample in Fig. 5.13d. The magnitude of the PBS-tissue interface also varies depending on tissue type and sample size, but in general is brighter in the GBM samples, indicating a higher acoustic impedance in the material. Assuming the tissues have similar densities, this result would correspond with the higher SoS measurements in GBM found in the previous section. Fig. 5.13e-g have much brighter PBS-tissue interfaces when compared to 5.13h, which was the smallest of all samples received.

As these images are produced purely from single elements operating independently, they are not using the full potential of a linear array for imaging, but the tissue samples can still clearly be observed through this basic image processing. Commercial probes operating at this frequency using all elements to focus the beam over the tissue region would produce a more detailed image. Despite this, there may still be differentiation potential from the B-mode images alone in the larger samples as there tends to be higher echogenicity in the GBM samples. Additionally, it was necessary to utilise the array in the way described to explore QUS fully, given the small sample sizes. The variation in sample thickness is more evident in the HF images, and it would not have been meaningful to transmit and receive on the entire array to measure attenuation as there is up to a 50% uncertainty in tissue thickness over the entire sample. Similarly, the images are used to choose a suitable rectangular ROI for further QUS analysis.

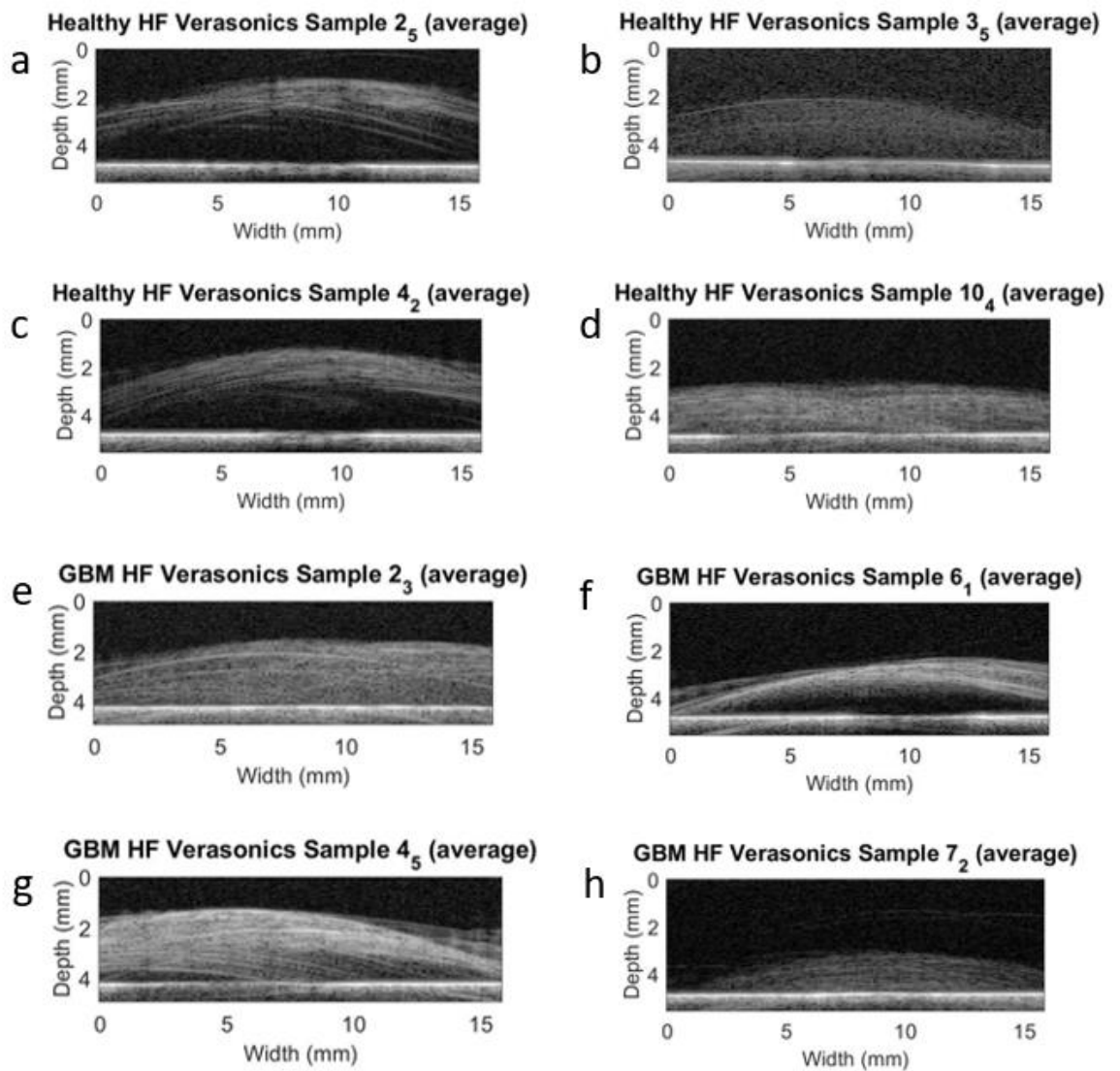


Figure 5.13: B-mode images of smaller samples of healthy tissue and GBM using L36-16 probe elements excited individually and 80 dB dynamic range.

5.4.2.2 LNO Results

Figure 5.14 shows the B-mode image results from three samples of both healthy and GBM tissue at three evenly spaced locations through the scanned tissue volume. Each image measures 8 mm (H) x 7 mm (D). The true shape of the samples is revealed, highlighting the non-uniformity of sample thickness and even possible tears in the sample, particularly GBM sample 1.

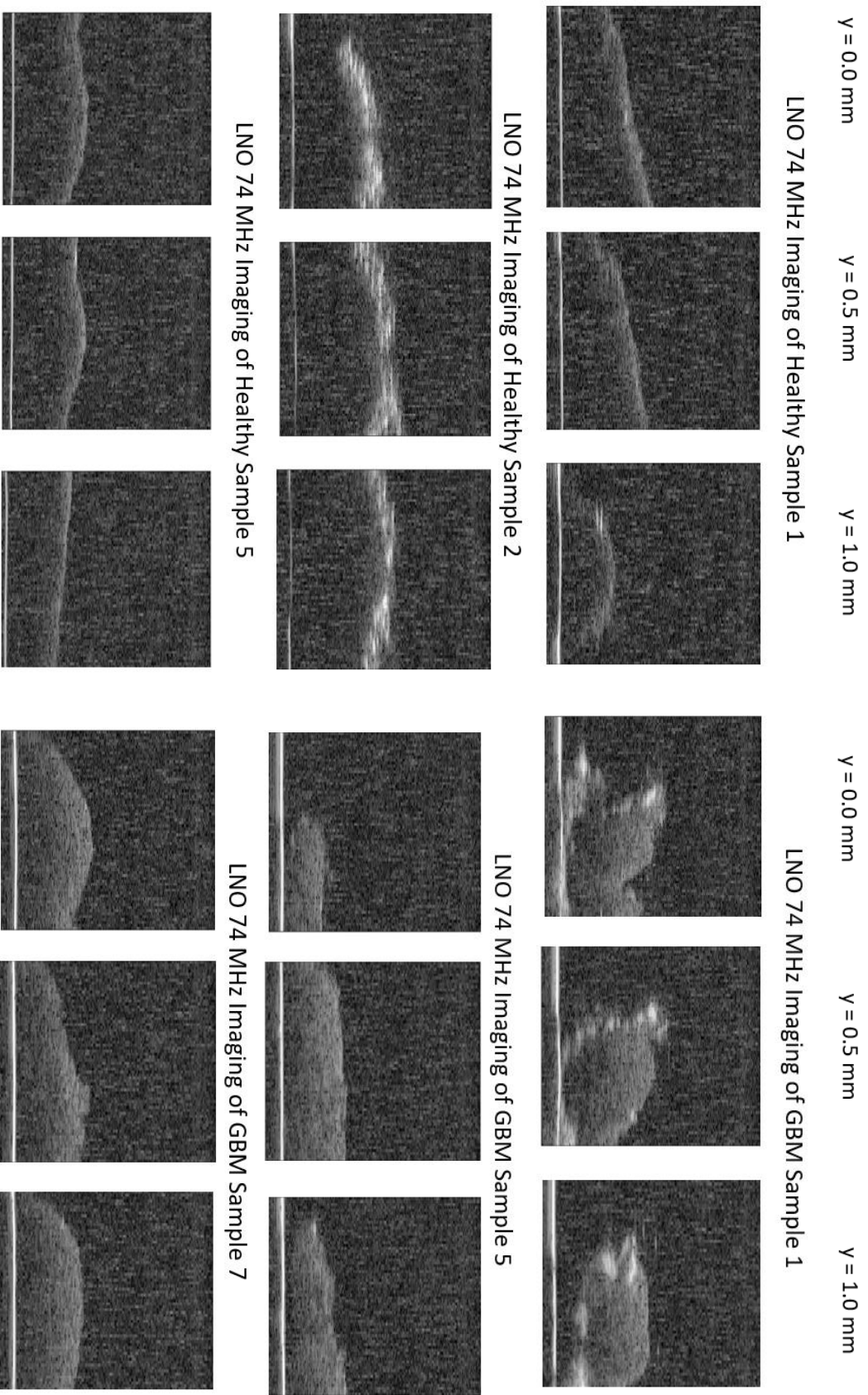


Figure 5.14: B-mode images of healthy tissue and GBM with LNO microultrasound scanning.

It is more evident in these scans that GBM samples show a higher echogenicity within the tissue than healthy tissue samples do, which would correspond to higher coherent scattering within that region. It was surprising to see the limited scattering in healthy brain tissue, where it is hard to distinguish any coherent scattering above the noise level. This suggests a gain of higher than 40 dB should have been used. However, another observation is that the tissue-PBS interface varies significantly within the tissue type and samples, though this may depend on the angle the tissue surface makes to the transducer surface. Healthy sample 2 shows the highest reflection and also appears to have the surface most parallel to the transducer aperture. In clinical practice, this variation should not be observed as the transducer would be in direct contact with the tissue with a layer of gel as couplant. In the present specific set-up, the difference in echogenicity within the tissue, while using the same dynamic range, makes it possible to differentiate between the tissue types from B-mode image alone.

5.4.3 QUS Results using Linear Array

The boxplots which follow show the average results from every scan of all samples in the analysis, healthy (n=48) and GBM (n=40). The full range is shown by the dotted lines and the median value is indicated by the red line. The result of the student t-test is also shown in red on each figure. The only two parameters which showed significant ($P < 0.05$) differences in the two tissue types were the mean value in the ROI and the EAC. The results from each system independent parameter are now discussed in more detail.

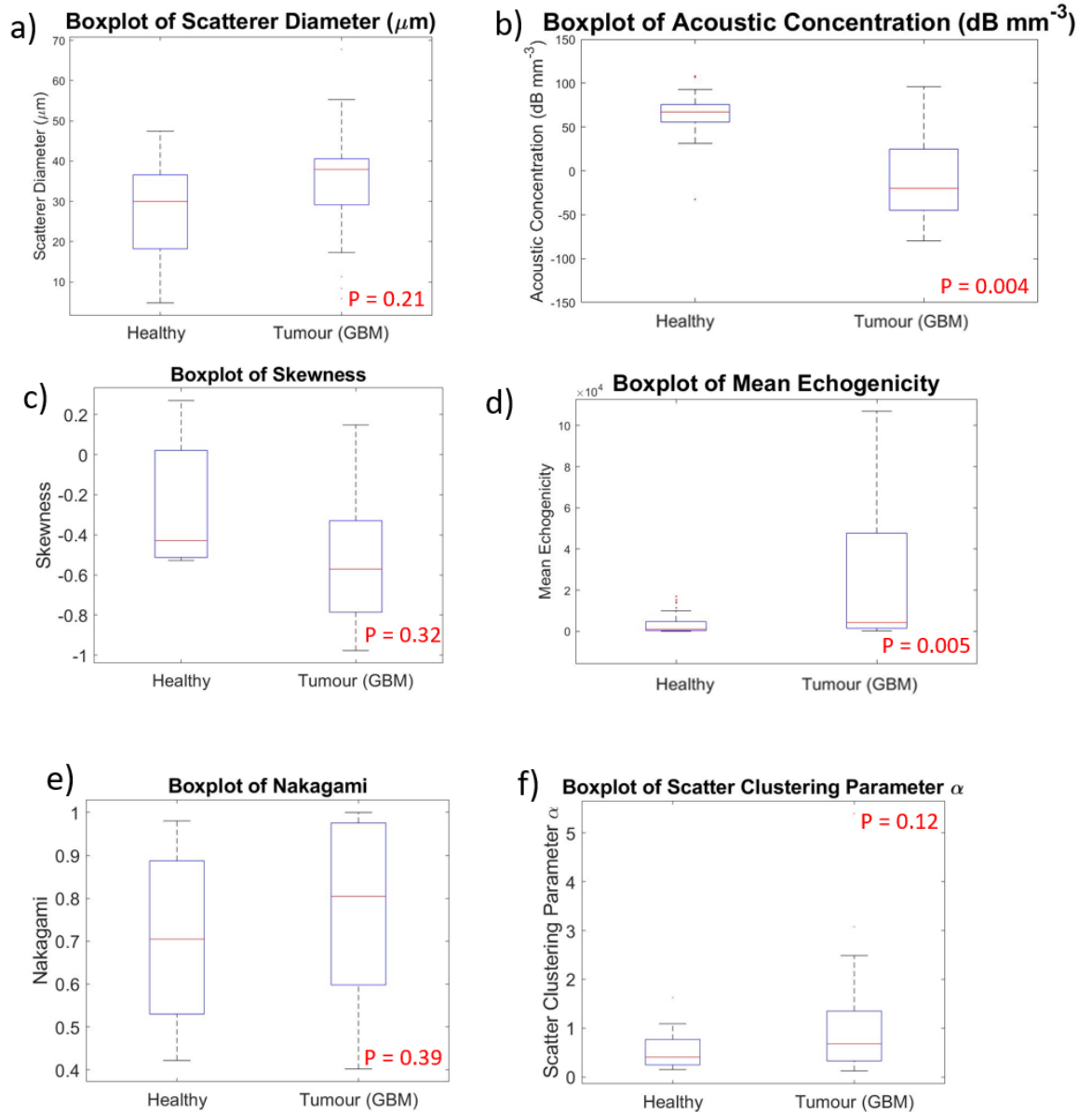


Figure 5.15: QUS parameters boxplots indicating the QUS results over each tissue scan for healthy ($n = 48$) and GBM ($n = 40$).

Fig. 5.15a-b show the results for spectral parameters. The scatterer diameter varied significantly in GBM, with the range spanning 18 - 57 μm . The mean result for healthy tissue was $27.7 \pm 11.6 \mu\text{m}$ and it was slightly higher for GBM at $35.1 \pm 14.9 \mu\text{m}$. For context, the wavelength of ultrasound at this frequency is 63 μm , and typical neuronal cell nuclei are much smaller, usually around 5 - 20 μm . One interpretation of a larger ESD is that the larger number of cells in a tissue volume in cancerous tissue causes the incident wave to behave as if a group of cells was a scattering source, which explains the ESD being larger than typical neuronal cells.

There were significant differences in the EAC, as shown in Fig. 5.15b. In particular, the values remained positive for healthy samples and were mostly negative for GBM samples. This relates physically to the acoustic impedance mismatch from scattering sources, and implies that, in GBM samples, the acoustic impedance of the scattering sources is lower than that of the surrounding material, whereas in healthy tissue the scattering sources have higher impedance. The change in sign between different tissue types has been reported in the literature in rat mammary tumour models and became a key parameter for differentiation [26]. Whilst there is clearly some potential for this parameter to differentiate the two tissue types, Chapter 4 showed that this is not an accurate measurement for *in vivo* tissue, as the EAC showed significant differences in fresh and frozen tissue.

Fig. 5.15c shows the skewness of the assigned echogenicity value, displaying a slight but not significant decrease in the case of GBM. Fig. 5.15d shows the mean echogenicity value, which was significantly higher in tumour tissue, aligning with the observation that tumour appears echogenic, or brighter compared to the surrounding brain tissue *in vivo*.

The mean Nakagami parameter values shown in Fig. 5.15e were 0.71 ± 0.18 and 0.78 ± 0.20 for healthy tissue and GBM respectively, which indicates they have both conformed to pre-Rayleigh statistics, except for a few cases of the GBM where it approached 1. A higher Nakagami parameter indicates GBM has a slightly higher concentration of scatterers globally [129]. The scatterer clustering parameter, from the HK-distribution is shown in Fig. 5.15f. There was an increase in the median result for the scatter clustering parameters in GBM, but this was not significant. A greater value indicates a greater acoustical homogeneity within the scattering medium [131] which, again, provides a quantitative measure of what may be physically true intuitively.

For eight cases of healthy tissue and eleven samples of GBM, it was not possible to obtain the EAC and ESD due to a break down in the theoretical model. The scatterer diameter depends only on the gradient of the, assumed linear, attenuation-compensated power spectrum from the tissue region. This study did not assume a linear frequency dependence, which is commonly used in the literature, and instead used the experimentally derived broadband attenuation function, which could vary from sample to sample. There was always a general increase in attenuation with frequency; however, in a minority of cases this fluctuated drastically over the bandwidth, which resulted in a non-linear power spectrum. The most extreme example of the resulting calibrated power spectrum is shown in Fig. 5.16b, with a more typical example shown in Fig. 5.16a. Where the power spectrum had poor correlation to the linear approximation, this would result in a small, or sometimes positive

gradient. From Equation 3.22, this resulted in an imaginary ESD, which makes no sense physically. This would propagate into an imaginary EAC, and thus these specific samples had to be omitted from the analysis. This is worth mentioning, as it is a fundamental limitation on the linear approximation in the theoretical framework of spectral based QUS and it not usually observed at lower frequencies. As additional work is done in future in attenuation measurements at HF in soft tissues, the most suitable power law compensation may be used to provide a more robust parameter estimation method when the linear approximation fails.

Linear Fit for Compensated Power Spectrum for Two Samples of GBM Tissue

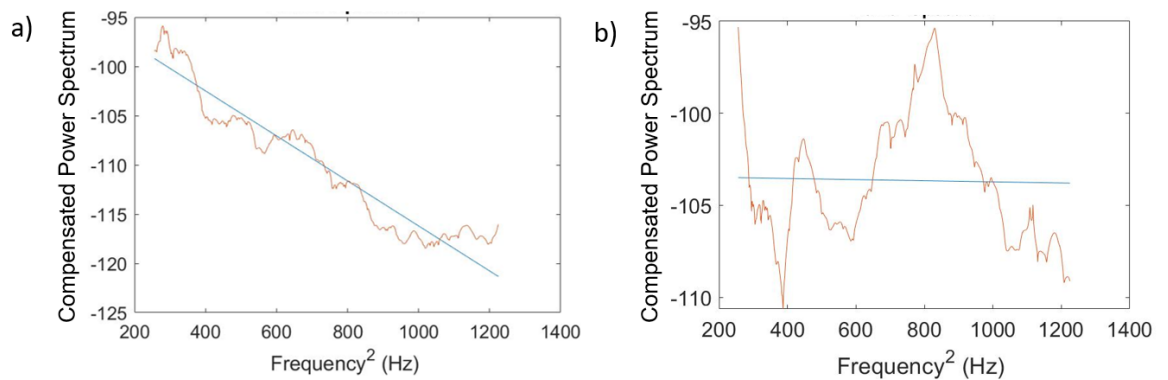


Figure 5.16: Compensated power spectrum of two samples of healthy tissue. a) Typical compensated power spectrum from soft tissue. b) Atypical power spectrum, seen in two samples of healthy tissue and eleven samples of GBM caused by a non-linear attenuation compensation function.

An initial look at the ML potential of several combinations of parameters is shown in Fig. 5.17. While none of the statistical combinations shows much delineation in the two tissue types in 2-D, Fig. 5.17b-c, the significantly lower values of acoustic concentration are evident in the tumour samples in Fig. 5.17a. Due to the uncertainty around the effect of freezing on the EAC parameter, two separate analyses were done where it was still included in the binary classification analysis.

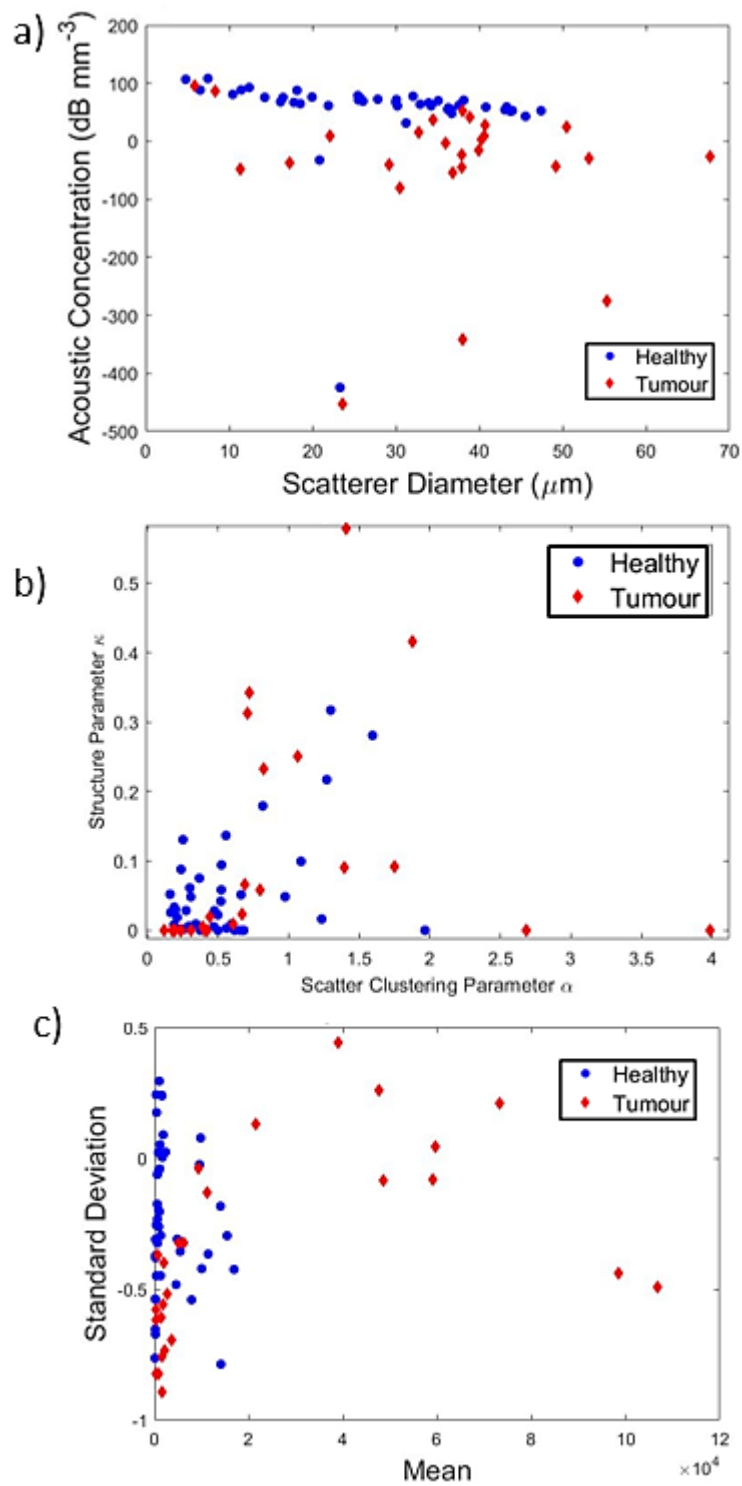


Figure 5.17: Scatter plots of several combinations of QUS parameters for healthy and GBM samples. a) ESD vs EAC. b) HK statistics. c) General statistics of pixel intensity.

HGG was taken as the positive case and the predicted results are shown in Table 5.3.

Table 5.3: Classification Results with Gaussian SVM

Instance	TP	FP	FN	TN	Accuracy	F1-score
Gaussian SVM (All parameters)	21	6	1	41	89.9	0.857
Gaussian SVM (EAC omitted)	20	7	2	40	87.0	0.82
Gaussian SVM (Only HK)	8	19	4	38	66.7	0.41

The total accuracy over 8-folds with all parameters was 89.9% with an F1-score of 0.857. This is an encouraging result regarding the potential of spectral-based QUS parameters at this frequency. When the EAC parameter was omitted from the analysis, the accuracy dropped to 87.0%. This is still a modest result considering there is no distinct clustering of the results in the 2D plots in Fig. 5.17b-c. The HK parameters alone do not show delineation in Fig. 5.17b, but a model using only these parameters was also tested, yielding an accuracy of 66.7%. This classifier had a particularly low sensitivity to detecting GBM samples, as evident in the low F1-score of 0.41. It can be concluded that at this frequency, the HK parameters were not able to delineate the two tissue types with useful accuracy.

Nevertheless, the results highlight the power of ML as a multiparametric approach, as utilising all parameters was able to accurately characterise the data. There were twelve parameters used in total, so the SVM would create an 11-dimensional hyperplane to best separate the data, which may see clearer clustering of the datatypes than the limits imposed by 3D.

The restricted sample sizes and small number of unique samples limited the amount of data available for testing. A full analysis comparing other ML strategies was not conducted on this data but is explored, with a much larger number of samples, in Chapter 6 through simulation.

5.4.4 LNO QUS Results

As discussed in Section 5.4.1, the limitations of the system hardware meant only statistical parameters could be considered to be derived from the microultrasound data. The results are displayed, as well as the significance values, in boxplots in Fig. 5.18.

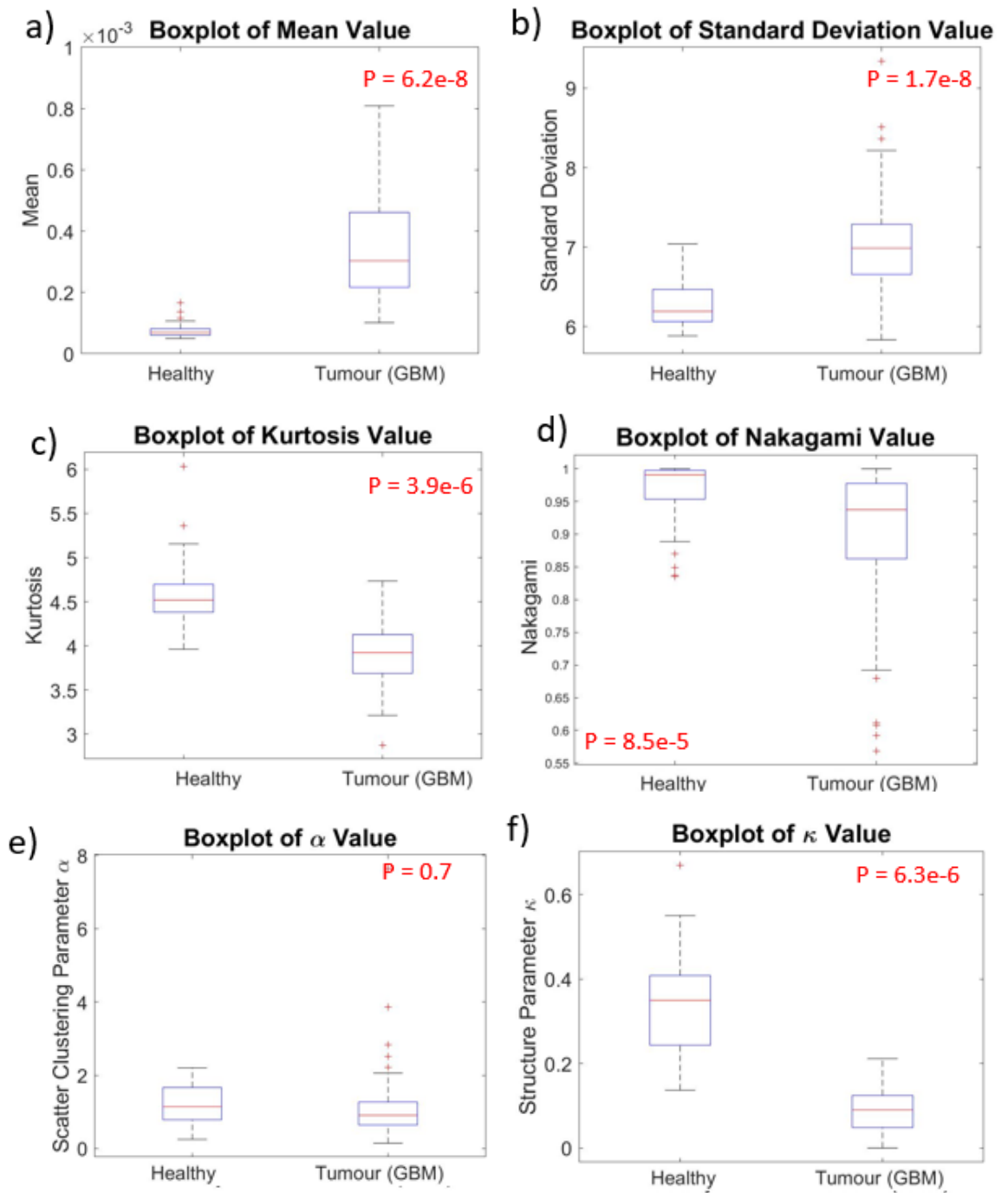


Figure 5.18: Statistical results of LNO QUS analysis. a) The mean value was significantly higher in tumour tissue. b) The echogenicity varied more in GBM. c) The kurtosis also showed to depend on tissue type. d) The structure parameter was significantly higher in healthy tissue.

The general statistical results in Fig. 5.18a-c all showed significant differences between the healthy tissue and GBM. The mean value was five times higher, on average, within GBM than healthy tissue. There were also significant differences with the standard deviation of the intensity within the GBM sample, as well as the kurtosis and higher order moments. Physically, the standard deviation can relate to the texture of the resulting greyscale image, and GBM samples exhibit a larger variance in that parameter than do healthy samples.

A parameter which increased substantially in this frequency regime, when compared to the results at 25 MHz, is the Nakagami parameter. It now takes an average value of 0.95 ± 0.04 for healthy tissue and 0.89 ± 0.09 for GBM. The values tend towards 1, however they only reached this value in five cases of healthy tissue and three of GBM. At a wavelength of $20 \mu\text{m}$, ultrasound could be probing a higher number of scattering sources, with the combination of their interference causing the echo envelope to move towards Rayleigh scattering. The majority of the results lie in the pre-Rayleigh regime and HK parameters are still relevant to consider.

The only parameter which did not demonstrate a significant difference between healthy tissue and GBM was the α parameter from the HK-distribution. This would indicate a similar level of acoustic inhomogeneity within healthy and GBM samples. The results here lie in the same range (1 - 5) to those obtained *ex vivo* in the liver of rats, with a higher α value corresponding to more severe cases of fatty liver disease [130]. A higher value of κ was found in the healthy tissue samples which reveals the presence of a larger coherent component, due to periodic, or highly structured spatial organisation of scatterers [35]. In the case of GBM, which had a lower value of κ , this infers a highly unstructured spatial organisation of scatterers [30].

The results of the HK parameters and mean value are visualised in a 3D scatter plot in Fig. 5.19, which also shows the X and U statistics.

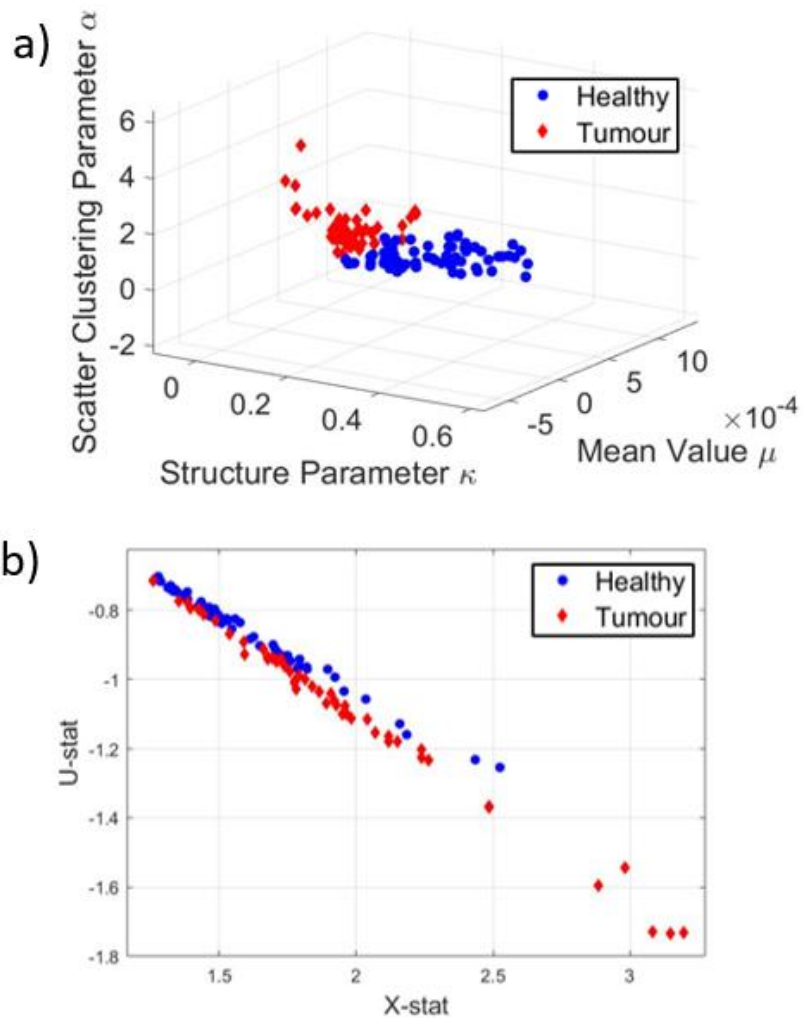


Figure 5.19: HK parameter results from LNO B-scans. a) α , κ and mean value. b) X and U statistics.

Binary classification seems very feasible from the 3D visualisation in Fig. 5.20a. The scatter clustering parameter alone does not hold much potential for classification, however combined with the mean and, importantly, the structure parameter, the two datasets group into distinct regions. Inspection of Fig. 5.19b shows the correlation between the X and U statistic and suggests a linear hyperplane could be found which could successfully separate the red and blue data points. The KNN and SVM will both be explored for these two parameters sets.

The ability of the HK parameters to correctly classify healthy and cancerous data was explored via binary classification over eight folds. The results using only the α and κ values are shown in Table 5.4.

Table 5.4: Classification results using only HK model parameters, α and κ .

Classifier	TP	FP	FN	TN	Accuracy	F1-score
SVM Linear	54	3	2	67	96.03175	0.955752
SVM Gaussian	54	3	2	67	96.03175	0.955752
KNN (k=5)	54	3	5	64	93.65079	0.931034

The highest performing classifiers were the SVM with linear and Gaussian kernels which both achieved accuracies of 96.0%. The KNN followed close behind at 93.7%, using five neighbours. The results show that the HK parameters alone are able to classify healthy and GBM in this *ex vivo* set-up. Computation with these parameters took 10.7 seconds, on average, to obtain from the X and U statistics, which cannot be considered a real-time result; however, they should not be ruled out for *in vivo* use.

X and U are defined in Equations 3.20 and 3.21 respectively and are efficient statistics for HK model parameter estimation but hold no physical interpretation. Nevertheless, they are obtainable in real time and so there is motivation, from a practical perspective, to consider the capability of these statistics alone to differentiate between healthy and cancerous samples, the results of which are given in Table 5.5.

Table 5.5: Classification results using only X and U statistic.

Classifier	TP	FP	FN	TN	Accuracy	F1-score
SVM Linear	50	7	2	67	92.85714	0.917431
SVM Gaussian	41	16	13	56	76.98413	0.738739
KNN (k=5)	45	12	11	58	81.74603	0.79646

The linear SVM outperformed the Gaussian SVM and KNN significantly in this study. This is due to the strong correlation between the X and U statistics as they are both dependent on the mean value, as observed in Fig. 5.19b. There is only a 3.2% reduction in accuracy while using these parameters, when compared to the system independent model parameters when considering the linear SVM. On the other hand, the Gaussian SVM and KNN saw reductions in accuracy of 19.1% and 12.1% respectively. In these cases, despite taking several seconds to obtain, there is diagnostic value in obtaining the model parameters, as even a 3.2% accuracy drop corresponded to four samples being incorrectly labelled. Besides, this time could be easily incorporated into the surgical environment, and the use of a more powerful computer or cloud computation could see a reduction. Whether parametric images, which will need 10.7 sec for each pixel, are feasible in real-time is a topic for future consideration.

Furthermore, the α and κ parameters hold an additional advantage as they are system independent, so a model used to train these could theoretically be implemented into any transducer system with different power and frequency, whereas a new model would have to be trained if the parameter values depend on the mean.

5.4.5 Limitations of this study

The tissue thickness is of fundamental importance in acoustic characterisation and ideally a larger tissue sample should be used to obtain an aggregate of the speed of sound or attenuation in a material. At 25 MHz, the samples were around 30 wavelengths in thickness, which may not be large enough to have confidence in the results. However, by utilising multiple single element acquisitions over different locations in the tissue, the data driven approach allowed greater confidence in these estimations.

Some improvements could be made to the Verasonics data acquisition, to automate a more efficient volume scan. Currently the transducer is held in place by a clamp-stand connected to a manual stage which was moved to five locations to acquire data from different locations. The Verasonics has a trigger function which means it could be incorporated into an automated scanning system to allow more systematic scanning, which would generate more data for the same sample size.

There were various hardware challenges associated with HF data acquisition. This was first encountered when using the Verasonics system, where the hardware was limited by a maximum sampling frequency of 62.5 MHz. The solution is to use an interleaved sampling technique, which will effectively double the frequency so it will then satisfy the Nyquist limit. This comes with an added complexity when programming acquisition events for a custom transmit and receive pattern. The second challenge was encountered using the microultrasound scanning system, as the gain required to analyse the tissue signal caused the large reflection from the quartz to be clipped. This meant attenuation and associated spectral parameters could not be accurately measured, suggesting further work in design of the experimental set-up.

The ML results should be taken as a preliminary study, especially in the case of the Verasonics, as the total number of data points used for testing was 29, which used half of all available data. Small fluctuations in performance will have a large effect on the percentage accuracy in such a small study, so it is imperative to explore this fully with adequate data.

5.5 CONCLUSIONS

The attenuation of GBM is higher than that of healthy brain at 25 MHz.

Bulk acoustic parameters were successfully obtained from *ex vivo* human tissue samples using two Verasonics linear arrays. GBM had a slighter higher speed of sound than the healthy samples, by 9 ms^{-1} on average. The values of attenuation at the centre frequency of 25 MHz were $29.9 \pm 1.6 \text{ dB cm}^{-1}$ and $34.8 \pm 4.3 \text{ dB cm}^{-1}$ for healthy and GBM respectively, indicating a 5.1 dB difference on average, however there were variations in each sample. The combination of LF and HF results allowed the attenuation of human brain to be mapped from 5 - 35 MHz, the first study in human tissue since the 1970s. Previous literature suggests a linear attenuation coefficient of $0.6 \text{ dB MHz}^{-1} \text{ cm}^{-1}$ in human brain, however the results presented here conclude that $0.9 \text{ dB MHz}^{-1} \text{ cm}^{-1}$ would be more accurate. This result has profound impact on the QUS analysis too, as often attenuation is mentioned only as a means to correctly estimate the spectral parameters, when in fact the attenuation measurement itself was found to be a potentially useful parameter for tissue characterisation.

ML-enabled QUS differentiates healthy brain and GBM at 25 MHz.

The Verasonics HF QUS analysis implemented two novel techniques. The first was to use an array with sequential single-element analysis, as a way to bridge the gap between microultrasound scanning and clinical imaging arrays. This allowed 40 - 60 independent A-scans of useful data from a rectangular tissue ROI to be used for subsequent QUS analysis. The second technique was in regard to the spectral parameters, where usually studies assumed a linear dependence on attenuation, however, the present study utilised an experimentally derived attenuation function. At the high frequencies studied, this had a huge effect on the compensated BSPS, which meant linear estimation broke down in these cases. A solution needs further work.

In this study there were significant differences only between the acoustic concentration and mean value in the ROI ($P < 0.05$). However, there were trends in the statistical QUS parameters which were sufficient to train a binary classifier, achieving an accuracy of 87% using attenuation, ESD and statistical parameters.

Values of HK parameters give near perfect classification at 74 MHz.

The microultrasound scanning allowed a more sophisticated set-up to acquire a complete volume scan of the tissue samples. However, acquisition issues with the clipping of data meant that the tissue signals could not be correctly calibrated, and consequently attenuation and spectral parameters could not be obtained. The importance of accurate, undistorted raw data collection must be emphasised for correct implementation of spectral techniques in the

future or, alternatively, a move towards a reference-free approach in the attenuation measurements.

The statistical measurements indicated that random and incoherent scattering increased in both tissues when moving to a smaller wavelength source. HK parameters allowed a physical description of scattering in tissues and, importantly, are a non-invasive technique which can correctly identify cancerous samples, achieving 96.0 % accuracy using α and κ alone. While there was value in understanding the model parameters from a physical perspective, when the analysis was repeated using only the X and U statistics, the accuracy did not greatly decrease, bringing to light a trade-off between computation time and accuracy.

Despite the small sample thickness and number of unique samples, this initial study supports the conclusion that QUS has the ability to aid HGG identification at 25 and 74 MHz. Only the GBM was explored in this study, as the most malignant type of primary brain tumour, which makes it the easiest to differentiate with a technique like QUS. A future study should explore the technique in the context of lower grade glioma and other tumours of the brain.

5.6 CHAPTER SUMMARY

This chapter described the implementation of innovative QUS techniques to distinguish healthy and HGG tissue. To start, it reported the bulk acoustic properties from human brain and GBM at what is believed to be above the highest frequency recorded in the literature, finding that both speed of sound and attenuation increased in cancerous tissue. The HF QUS analysis found that only the mean echogenicity value and the scatter clustering parameter were significantly different; however, combined with ML, this could still achieve a classification accuracy of 87%. Microultrasound scanning provided a more robust method of data acquisition but there were challenges encountered obtaining the attenuation estimates and spectral parameters. Nonetheless, the HK parameters alone were able to separate the data with near perfect accuracy, suggesting value in bringing forward this technique to an *in vivo* clinical trial. This chapter also necessitates future work with a larger dataset and exploration with differing grades of glioma to test ML-enabled QUS to its full potential.

6 DIFFERENTIATION OF LOW- AND HIGH-GRADE GLIOMA FROM HEALTHY BRAIN IN FINITE ELEMENT ANALYSIS

6.1 CHAPTER AIM

Chapter 5 demonstrated the ability of ML to accurately identify healthy and HGG samples using microultrasound. This chapter aims to extend the study to various malignancy levels of brain tumour through an *in-silico* study. To achieve this, 2D representations of the acoustic properties of cells and interstitial material within neural tissue were created, based on histopathology slides of healthy, LGG and HGG human brain samples. After image preparation, the models were imported into FEA modelling software to study the interaction of ultrasound with their microstructures. Specifically, the purpose was to obtain a database of QUS results *in silico* from healthy and cancerous brain tissue to determine the characteristics of ML - SVM vs KNN - best suited to classification using QUS results. It was also intended that the QUS results might be compared to those found in healthy and GBM samples in Chapter 5.

6.2 INTRODUCTION

The real potential of ML capability is tested when a study is extended to a larger number of samples. The main limitation of the studies described in Chapter 5 was the lack of available tissue. If an accurate model of healthy and cancerous brain tissue could be created, based on more readily available diagnostic slide images, then this would allow an increase in the size of the study. Furthermore, it need not be limited to only consider GBM samples, which is the name given to HGG. LGG could also be explored, corresponding to WHO grades I - III.

6.2.1 FEA Software

OnScale, previously PZFlex (Redwood City, CA, USA) is a software package which is commonly used for transducer design, development and material characterisation of novel piezoelectric materials. It is an explicit piezoelectric solver which makes it ideal for mechanical wave propagation [177]. In this study, the aim was to mimic the response from a Verasonics L35-16 MHz array element, for comparison with the previous study. Typically, FEA software packages will include a database of bulk material properties needed to model interaction with the wave equations at each time step, including stiffness, attenuation, and acoustic impedance. However, this suggests a constraint to model brain with only one

acoustic impedance, not accounting for the sub-wavelength fluctuations which give rise to scattering.

6.2.2 Acoustic Impedance of Brain Microstructure

It is well documented that the acoustic impedance of cell nuclei is higher than that of surrounding cytoplasm from acoustic impedance microscopy [178]. Measurement is possible using a technique frequently referred to as scanning acoustic microscopy (SAM) in the literature. This involves the use of a microultrasound scanner, typically operating at over 100 MHz, to determine the acoustic impedance of tissue with extremely high spatial resolution ($<10\ \mu\text{m}$) but having a maximum penetration depth of only a few mm [179]. There are no reports of SAM in human brain to date, however Soon et. al published the use of SAM to measure the effects of anti-cancer drugs on glioma management in a rat model [180]. The values for the acoustic impedance values, in MRayl, of the cell nuclei and surrounding material of healthy and cancerous rat glial tissue are given in Fig. 6.1.

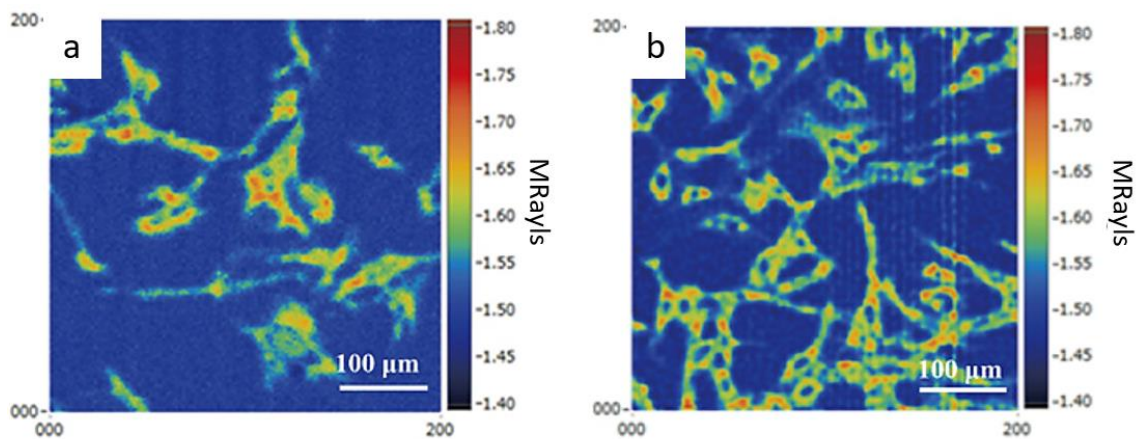


Figure 6.1: Acoustic impedance microscopy image from rat brain tumour model from [180]. a) healthy glial tissue and b) GBM tissue.

There are some key observations from Fig. 6.1. Firstly, there are clearly more features with higher acoustic impedance in the GBM tissue compared to healthy tissue due to the higher concentration of cell nuclei. Also, there is no increase in acoustic impedance in the cell nuclei in tumour, there are just more of them. Finally, there is around a 10% acoustic impedance difference between the cell nuclei (1.75 MRayl) and the surrounding tissue (1.55 MRayl). The cell bodies are denser, hence have a higher impedance, and the mid-range impedance values are tracks from glial cells. Assuming a similar acoustic impedance mismatch between cell nuclei and cytoplasm in human brain as in rat brain, 2D acoustic impedance maps can be created based on the distribution of cell nuclei in histopathologic images from human brain.

The method preferred by pathologists for viewing cellular structures in human tissues is haematoxylin and eosin (H&E) staining; haematoxylin is basic and stains acidic structures such as DNA and RNA of cell nuclei blue, while eosin is acidic and stains basophilic structures such as cytoplasm proteins pink [181]. An example of an H&E stained slide for healthy, LGG and HGG tissues is shown in Fig. 6.2.

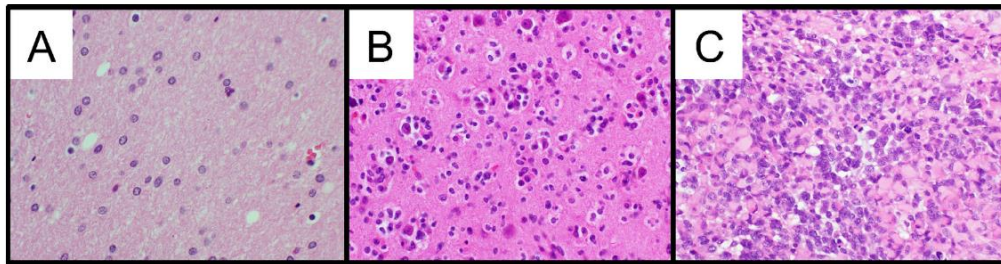


Figure 6.2: H&E stained diagnostic slide image of A) healthy brain tissue, B) LGG and C) HGG, from [182].

In general, within tumours there is a greater level of heterogeneity and an increased number of cell nuclei over a given region, up to four times as many in HGG when compared to healthy tissue [183]. In these diagnostic images, there is a clear distinction, but they require removal of the tissue and additional time, making the approach unsuitable for routine intraoperative use. The challenge is to determine which regions are cancerous using non-invasive techniques. Furthermore, the level of malignancy may not be known to the surgeon during operation, so combining LGG and HGG data to compare with healthy data is of interest from a clinical perspective.

The approach taken here is to use images such as those in Fig. 6.2 to isolate the cell nuclei from the surrounding material, to allow a binary acoustic impedance map to be created as an *in-silico* test sample. Ultrasound wave interaction can be studied in a pulse-echo setting, QUS analysis will be performed on the outputs, and parameters obtained will be used to train a classifier into three classes: healthy tissue, LGG and HGG.

6.3 METHODOLOGY

6.3.1 Pathology Image Preparation

Ten digitised microscope images of frontal healthy white matter were obtained directly from the lab of the Edinburgh Brain Bank and transferred via Dropbox in SVS format at 40x magnification. The level of detail in these files means one slide image is typically around

20 GB, hence requiring a process to follow for downloading the files. Microscope images of both LGG and HGG tissue were obtained from the Genomic Data Commons Portal, an online database for cancer researchers managed by the National Cancer Institute (Projects TCGA-LGG and TCGA-HGG) [184]. To access these high-resolution microscope images, the manifest for the project is downloaded from the database website, then the SVS files are retrieved using Openslide software in a Python script [185].

It would not be feasible to model an entire image in FEA. Instead, isolated samples were considered, of the same width as a typical single element transducer. This allowed many samples to be considered from only one image. The images were taken from random placement of 30 $500 \mu\text{m}^2$ tiles, as indicated in red squares in Fig. 6.3.

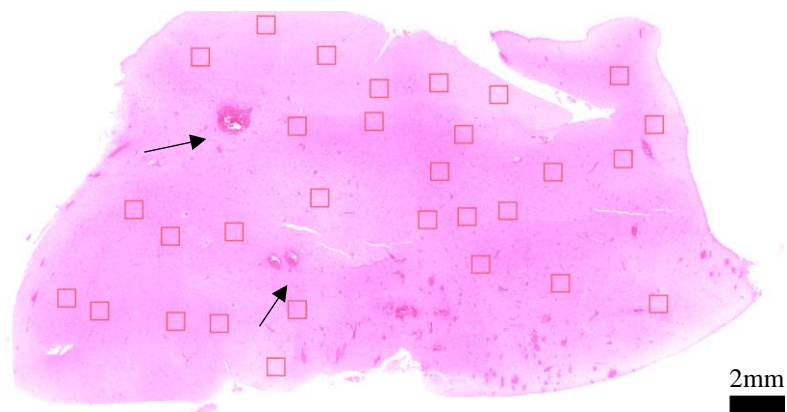


Figure 6.3: Selection of 30 $500 \mu\text{m}^2$ tiles in a LGG image, avoiding blood vessels (black arrow) and tissue breakages (white areas within tissue).

This placement allows a nonbiased selection of regions from all four quadrants of the full image, which is beneficial to account for the heterogeneity of the sample. It was achieved by initially generating random coordinates in MATLAB. Then a visual inspection was carried out to ensure all tiles covered tissue regions only, avoiding structures such as blood vessels and tissue tears. If a tile was created in an unsuitable area, the random coordinates were generated again until a suitable region was found.

As the original images were taken in different laboratories, the microscope used, thickness of sample and duration of staining varies for each slide. The pixel values must therefore be normalised for each slide image, to account for contrast variability, which can be achieved using QuPath, open source bioimage analysis software (University of Edinburgh, UK). After normalisation of pixel intensities in each image, QuPath enables filtering of haematoxylin

staining so only cell nuclei appear in the image, and cytoplasm and proteins are not displayed. Furthermore, minimum and maximum thresholding values can be set on the normalised image, which gives optimal delineation of cell nuclei. The differential staining allowed a binary image to be produced, with cell nuclei appearing white and the surrounding material as black. Examples are shown for healthy tissue, LGG and HGG in Fig. 6.4.

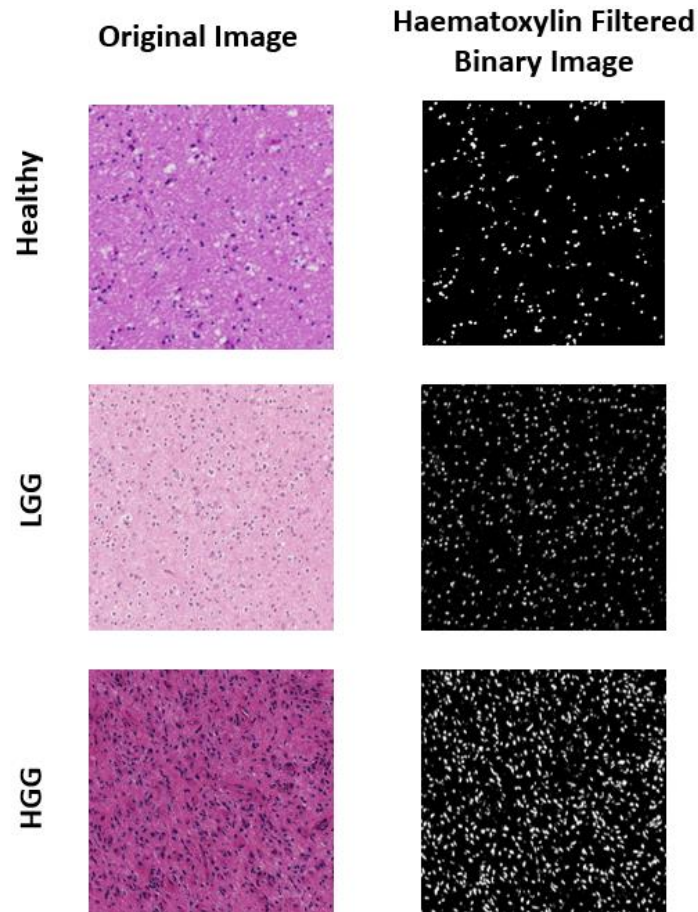


Figure 6.4: Binary image creation for 3 example tiles. The original image must be normalised to account for interlaboratory differences before filtering cell nuclei and creating a binary image.

A high resolution .tif file of each cropped region was exported using ImageJ (ImageJ v1.57, National Institute of Health, USA) and converted to greyscale. The greyscale image was then smoothed by a Gaussian filter to eliminate ambiguous regions and fill in cell nuclei where haematoxylin staining was uneven. After the image contrast settings were saved, 30 tiles of size $500 \mu\text{m}^2$ were saved using the following filename system: 'TissuetypeX_Y' where Y indicated the slide number, and X indicated the tile number. As 30 tiles were created from each slide, there are 300 tiles for each tissue type, allowing 900 total pulse-echo simulations.

6.3.2 Meshing

While the previous section explained the generation of 900 suitable tiled high-resolution images, a further step is required to make this geometry translatable into the grid of FEA. OnScale allows a table as an input to site material properties as a direct map from each row and column to the corresponding box location in the simulation. The following material properties were used for the cell nuclei and surrounding material, based on results of SAM.

Table 6.1: Acoustic Properties of Materials in the Model

Strucure	Material Name (Identifier)	Density	Velocity	Impedance
Cell Nuclei	Brain_scat (1)	1050	1560	1.65
Cytoplasm	Brain (2)	1030	1540	1.57

A program was developed in MATLAB (Version 2019b) which takes in the binary image, meshes it based on the box size required for the simulation and returns a table. This was achieved based on the mean pixel intensity of the pixels within the box, for example if more white pixels were present in a specific box location, it would be labelled as cell nuclei material and return '1'. The output is a table, of 1s and 2s, which has the exact number of rows and columns as x and y locations in the simulation, so a direct mapping can occur.

The mesh size was chosen which optimised resolution of circular structures, while still maintaining a reasonable computation time. Resolving the circular structures of cell nuclei with a square mesh meant a box size of 0.8333 microns was required, which corresponds to 60 elements per wavelength at 25 MHz, more than four times the minimum number required by the OnScale solver [177]. The scale of the geometry with mesh size is shown here in Fig. 6.5 for a small region.

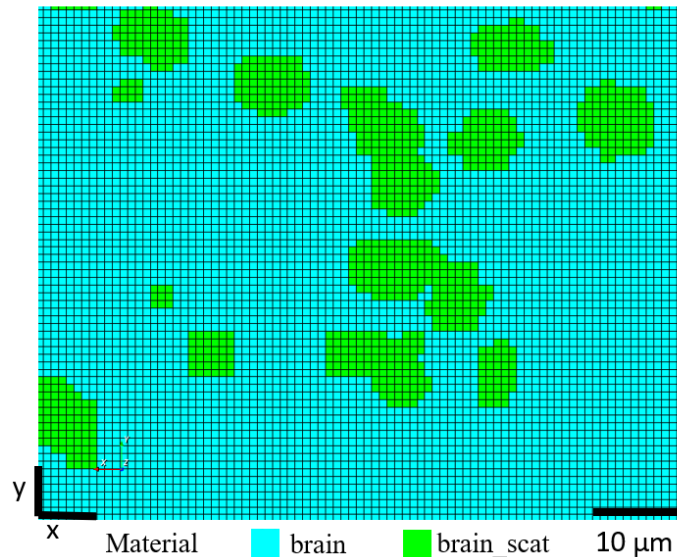


Figure 6.5: Optimised resolution of material geometry within simulation with gridlines representing model mesh size.

A visual summary of the steps involved in taking a microscope image and converting it into a mesh geometry for FEA is shown in Fig. 6.6.

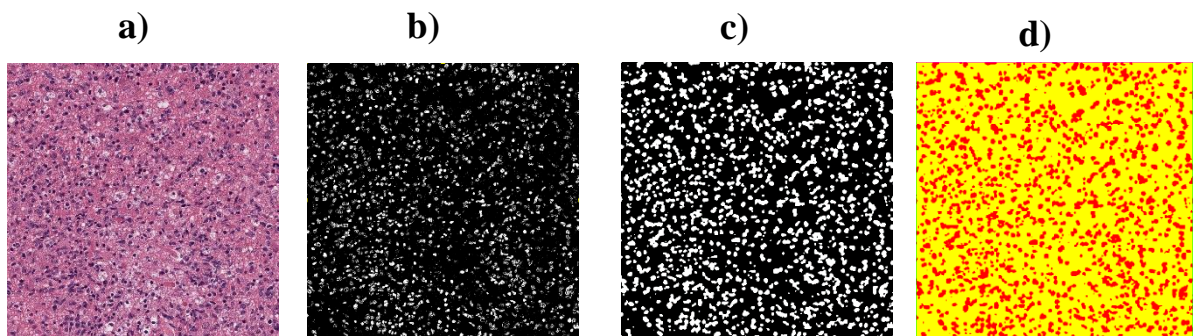


Figure 6.6: Steps involved for meshing pathology image into a binary acoustic impedance map for HGG. a) Original Image. b) Greyscale image filtered with Haematoxylin staining. c) Image smoothed with Gaussian filter. d) Final binary map in lower resolution used for acoustic impedance assignment in FEA.

6.3.3 Time-varying Pressure Input

Now a suitable tissue model could be generated, the ultrasound must be added to the simulation. One approach is to model an entire single-element transducer and optimise the piezoelectric material, backing and matching layer(s) to suit the application of interest. However, OnScale more simply allows a time-varying pressure input which can be used to model the pressure response from an ultrasound probe. In that way, the entire transducer could be removed from the simulation and replaced with a replica of the pressure from probe of interest. This also realises a smaller model, reducing simulation time. The HF Verasonics

probe from the previous study, Chapter 5, was chosen as the target probe, with an impulse response in the time and frequency domains given in Fig. 6.7.

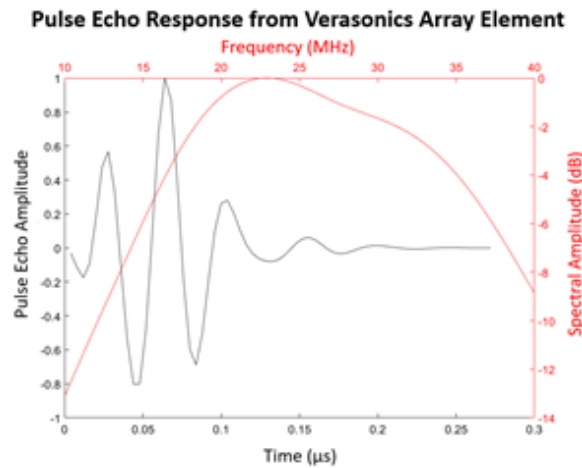


Figure 6.7: Pressure excitation used in pulse-echo simulation

This was measured by digitising the voltage response from one element of the linear array and resampling it to have the same sampling period as the time-step in the simulation. Since OnScale calculates the time-step as the minimum time needed to fully model one wavelength in each material at a particular frequency, it was easier to specify this explicitly in the code as 0.173793×10^{-8} seconds, the minimum required for the upper frequency limit.

6.3.4 Running the simulation

The base simulation consists of one pulse-echo burst, using the pressure input, over a region of water measuring $700 \times 500 \mu\text{m}^2$. Code was constructed in MATLAB which automatically generates a Flex table to overwrite the water area successively in the simulation for all 900 binary images required for the analysis. There was also a $200 \mu\text{m}$ layer of water in the simulation, to act as a couplant. MATLAB automated the process of running OnScale using the command prompt, so all 900 simulations would run automatically with only the geometry and output file name changing for each iteration. The resulting acoustic pressure at each node and at each time-step for the entire simulation was output in a Flex history file, typically 50 MB in size.

6.3.5 QUS analysis

The first step in QUS analysis is to convert the Flex history file into total pressure response incident on the transducer surface. The perceived transducer response was found by performing a line integral over the simulated transducer surface at each time-step.

Using this, for each of the 900 simulations and one reference scan which only contained water, QUS processing could proceed as described previously. A reference scan was carried out by replacing the tissue material with only water and creating a fixed boundary at the end of the simulation, i.e. with a reflection coefficient of 1.

The attenuation was found directly from the pressure measurements using the TL method and Equation 6.1.

$$\alpha_{TIS}(f) = \alpha_{WATER}(f) + \frac{20}{2d} \log \left(\frac{FFT(P_{TISSUE})}{FFT(P_{REF})} \right) \quad (6.1)$$

where

α_{TIS} = Attenuation of tissue (dB cm⁻¹)

d = Thickness of tissue in cm

P_{REF} = Pressure amplitude of reflection without tissue present

P_{TISSUE} = Pressure amplitude with tissue

α_{WATER} = Attenuation due to water displaced by tissue (dB)

This gives attenuation as a continuous function of frequency over the range 16 – 35 MHz. Two QUS parameters were obtained from this graph, the first being the value of the attenuation at the centre frequency and the second being the rate of change of this function at the centre frequency (25 MHz), termed ‘mid-band fit’.

The attenuation-compensated BSPS from the tissue scattering regions was determined using the derived attenuation function and Equation 3.20. In this study, as the transducer characteristics were not defined, it was not possible to obtain the system independent spectral parameters (ESD and EAC). Besides, considerations would have to be made as to the theoretical power spectrum to compensate for the 2D nature of the simulation. The spectral slope, $BSPS_M$, and intercept, $BSPS_I$, of the BSPS from the tissue region were estimated by applying linear regression to the compensated BSPS.

Statistical parameters were obtained by finding the central moments of the echo envelope distribution up to the 6th moment. More specific parameters were also obtained, including the Nakagami shape parameter, the X and U statistics and the system independent HK-distribution parameters, α and κ , using the techniques described in Section 3.3.4.

All QUS parameters were saved to a spreadsheet, with the columns corresponding to each QUS parameter and a final column added for the tissue label ‘Healthy’, ‘LGG’ or ‘HGG,’ in preparation for classification.

6.3.6 Machine Learning Classification

In this study, all suitable QUS parameters were used to explore 5 classification algorithms:

- SVM with Linear kernel
- SVM with Gaussian kernel
- KNN with 5 neighbours (fine)
- KNN with 10 neighbours (medium)
- KNN with 50 neighbours (coarse)

The final spreadsheets of QUS results were randomly separated into 8 subsections to perform an 8-fold validation. Briefly, 7 of the subsections were imported into the Classification Learner app (MATLAB Version 2019b) which can train all models simultaneously, and the remaining group was left to test the algorithm on unseen data. ‘Healthy’ was taken to be the negative case and glioma was the positive case in both HGG and LGG analysis. The confusion matrices for the three highest performing classifiers in each case were recorded. The accuracy and F1-score were then calculated for each fold and the average was taken. Three cases are considered: Healthy vs HGG, Healthy vs LGG, and a final case where LGG and HGG data are combined to produce a ‘Glioma’ class of 600 samples to determine the ability to identify Healthy vs Glioma.

6.4 RESULTS AND DISCUSSION

6.4.1 Running the Simulation

A single pulse-echo sequence had a runtime of around 3 min and the entire study of 900 samples took 45 hours to complete. Snapshots of the acoustic pressure over the entire simulation are shown in Fig. 6.8, with an example of each of the three tissue types. The pressure excitation is incident from the left and interacts with the tissue boundary. At $0.2 \mu\text{s}$, a percentage of the wave is transmitted through the tissue, while some is reflected to the left. At $0.6 \mu\text{s}$, interference patterns are observed to the left of the images as a result of reflections from the scattering sources within the material. There is an obvious increase in magnitude of scattering in cancerous tissue, especially in HGG.

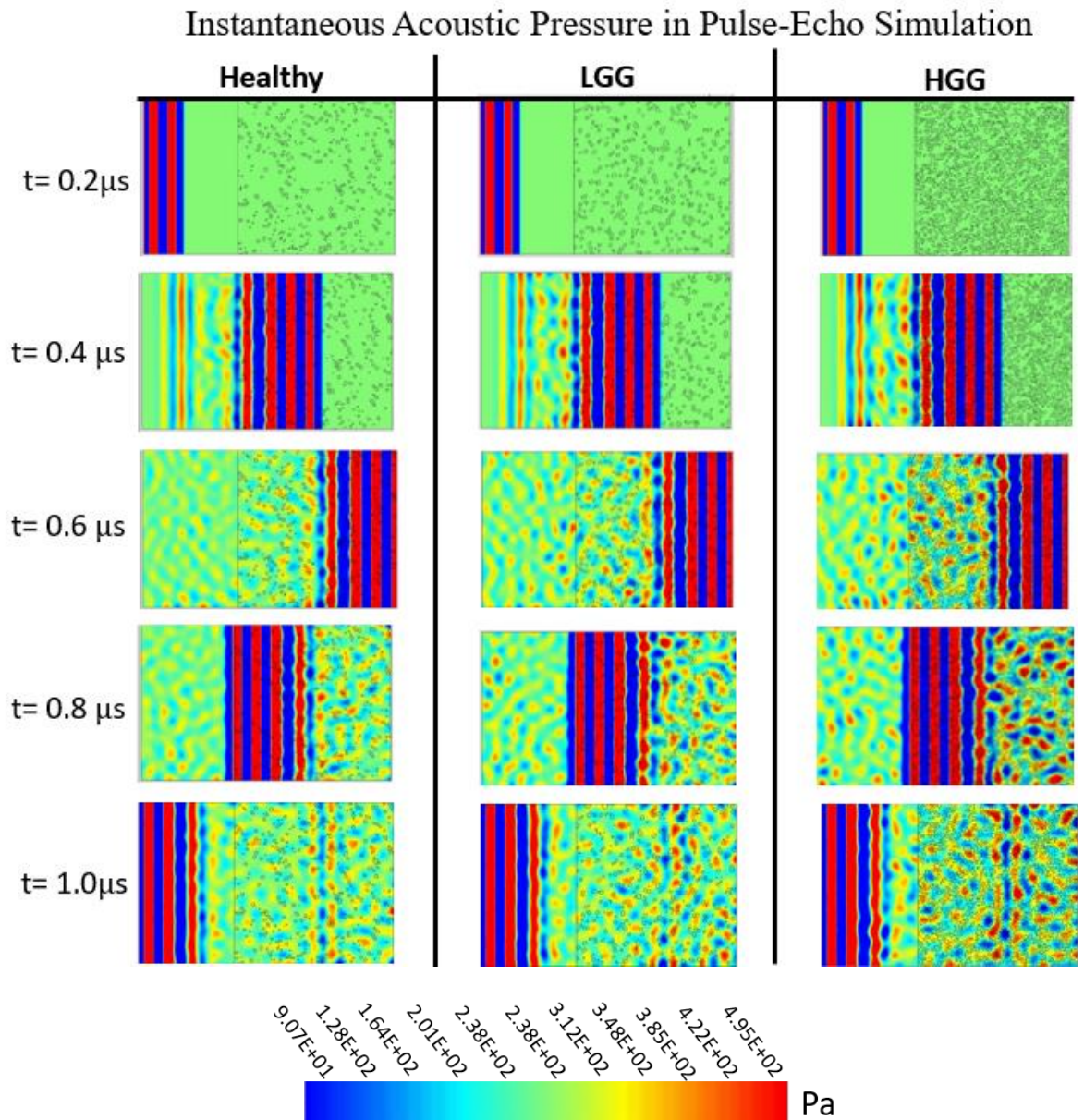


Figure 6.8: Pulse-echo responses of pressure waves incident from the left, showing interaction with tissue microstructure for the three tissue types over the entire simulation timeframe.

6.4.2 QUS Results

The QUS results for the 25 MHz pressure excitation are shown in Fig. 6.9a-d, with healthy tissue data shown in green, LGG in blue and HGG in red. Fig. 6.9a displays the attenuation and mid-band fit, the former falling into the narrow range of $20.3 - 20.8 \text{ dB cm}^{-1}$ which is attributed to the fact that attenuation was not modified in this simulation, and both materials used the OnScale database for material properties. In brain tissue attenuation is $0.6 \text{ dB MHz}^{-1} \text{ cm}^{-1}$. The attenuation values appear slightly lower on average for healthy tissue, with higher values for LGG and HGG, which is explained through more energy lost through scattering as evident in Fig. 6.8.

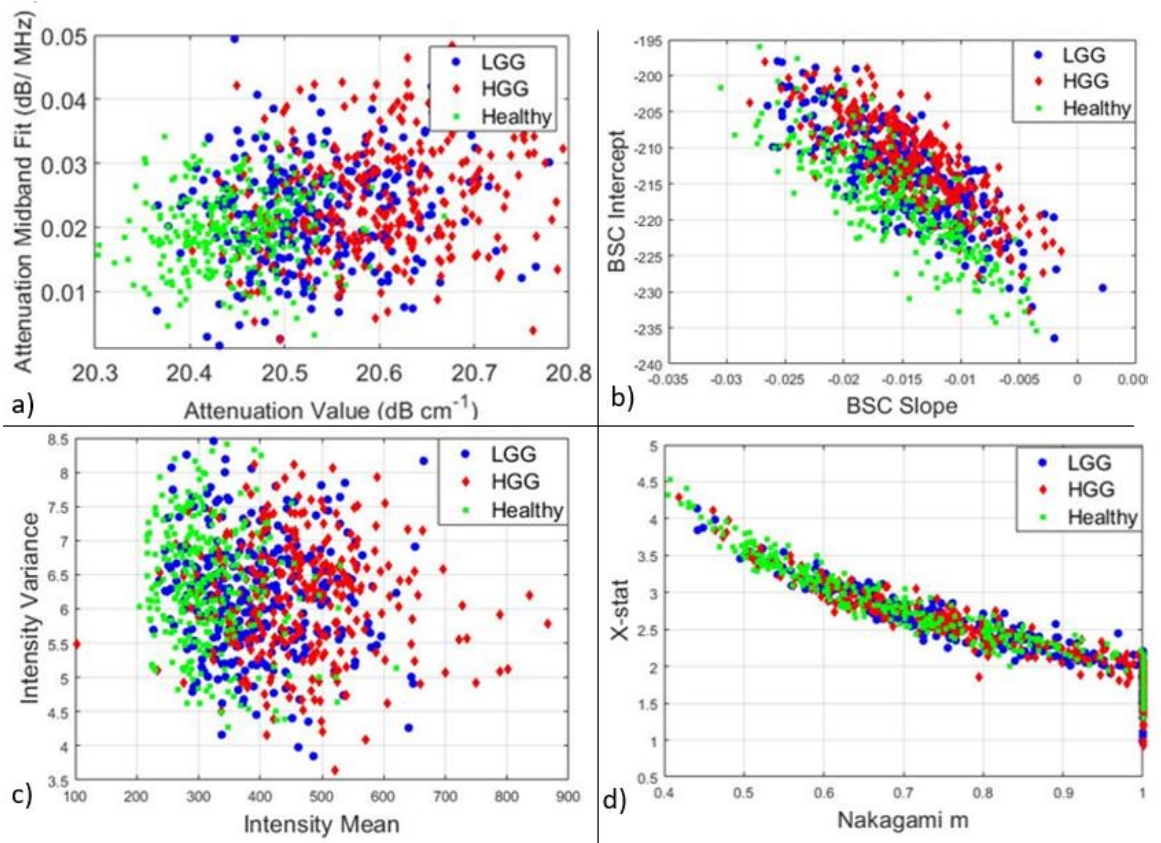


Figure 6.9: Paired QUS parameter results for healthy tissue (green), LGG (blue), and HGG (red). a) Attenuation Midband fit vs value at centre frequency. b) Lizzi parameters: BSPS intercept vs slope. c) Intensity statistics, variance vs mean. d) X-statistic vs Nakagami shape parameter.

Fig. 6.9b shows the intercept vs slope for the BSPS. The intercept is related to the overall magnitude of the BSPS, and this is highest in the red data points of HGG, but with significant overlap with LGG data. There is still a discernible linear trend, and subtle separation between healthy tissue and HGG, which may be suited to interpretation with a linear SVM.

The simple statistics of the mean and variance of the intensity within tissue scattering regions are displayed in Fig. 6.9c. Intuitively, the average values of the signals from the scattering regions should be higher in regions where there is a higher concentration of scatterers, which is observed. The variance is an example of a parameter which has no trend associated with tissue type.

The X statistic and Nakagami parameter are shown in Fig. 6.9d. This graph looks the least promising for classification, and a large portion of the results have a Nakagami shape parameter of 1, which means it reduces to the Rayleigh regime (see Fig 3.8 in Chapter 3) which means it is not meaningful to continue the analysis in the context of the HK-

distribution parameters (as $\kappa \rightarrow 0$). This may relate to a limitation of the study as every individual cell nucleus was modelled with a different acoustic impedance, which causes an artificially large number of scatterers. Since this is not observed in reality, it implies not every individual cell is seen as a scatterer, which has been discussed in the literature [186].

For this reason, only the attenuation, backscatter, 1st order moments and X and U statistics are used in the QUS classification algorithm, which is also convenient as they can be categorised as the near real-time parameters. In Figures 6.9a-c, there is an observable distinction between healthy and HGG results, while the LGG data in blue appear as a mid-range result.

Table 6.2: Summary of QUS Parameters used in Classification Algorithms.

<i>Symbol</i>	<i>Description</i>
α_{Centre}	Attenuation value at centre frequency
α_{Slope}	Attenuation slope at centre frequency
$BSPS_I$	Intercept of modelled BSPS
$BSPS_M$	Slope of modelled BSPS
$E[I] = \mu$	Mean of echoenvelope detected data
$E[I^2]$	Variance of echoenvelope detected data
$E[I^3]$	Skewness of echoenvelope detected data
$E[I^4]$	Kurtosis of echoenvelope detected data
$E[I^6]$	6 th Moment of echoenvelope detected data

6.4.3 Classification Performance

The results of the confusion matrix, accuracy and F1-score for the three cases (healthy tissue vs LGG, healthy vs HGG and healthy vs glioma) over 8 folds are shown in Tables 6.3 – 6.5. Figure 6.9 a and b show clear separation in red data (HGG) and green data (healthy) so the high classification results for Healthy vs HGG are unsurprising. This aligns with the results of the previous chapter which showed bulk attenuation could be a key parameter to distinguish the two tissue types at this frequency.

Table 6.3: Classifier results for healthy (negative) vs HGG (positive)

Healthy vs HGG	Gaussian SVM						Linear SVM						KNN (5 neighbours)					
	TP	FP	FN	TN	Accuracy	F1-score	TP	FP	FN	TN	Accuracy	F1-score	TP	FP	FN	TN	Accuracy	F1-score
Fold 1	60	0	1	59	99.16667	0.991736	59	1	2	58	97.5	0.975207	51	9	14	46	80.83333	0.816
Fold 2	59	1	2	58	97.5	0.975207	58	2	2	58	96.66667	0.966667	54	6	15	45	82.5	0.837209
Fold 3	58	2	0	60	98.33333	0.983051	58	2	3	57	95.83333	0.958678	55	5	13	47	85	0.859375
Fold 4	59	1	1	59	98.33333	0.983333	57	3	1	59	96.66667	0.966102	54	6	10	50	86.66667	0.870968
Fold 5	59	1	1	59	98.33333	0.983333	57	3	1	59	96.66667	0.966102	52	8	16	44	80	0.8125
Fold 6	60	0	4	56	96.66667	0.967742	58	2	2	58	96.66667	0.966667	55	5	11	49	86.66667	0.873016
Fold 7	58	2	2	58	96.66667	0.966667	60	5	0	60	96	0.96	53	7	15	45	81.66667	0.828125
Fold 8	58	2	1	59	97.5	0.97479	58	2	1	59	97.5	0.97479	54	6	8	52	88.33333	0.885246
Average					97.8%	0.979					96.7%	0.96					84.0%	0.85

Table 6.4: Classifier results for healthy (negative) vs LGG (positive)

Healthy vs LGG	Gaussian SVM						Linear SVM						KNN (5 neighbours)					
	TP	FP	FN	TN	Accuracy	F1-score	TP	FP	FN	TN	Accuracy	F1-score	TP	FP	FN	TN	Accuracy	F1-score
Fold 1	39	21	15	45	70	0.68421	45	15	23	37	68.33333	0.70313	49	11	14	46	79.16667	0.796748
Fold 2	42	18	13	47	74.1667	0.73043	42	18	21	39	67.5	0.68293	48	12	14	46	78.33333	0.786885
Fold 3	44	16	15	45	74.1667	0.7395	46	14	21	39	70.83333	0.72441	52	8	14	46	81.66667	0.825397
Fold 4	42	18	17	43	70.8333	0.70588	41	19	13	47	73.33333	0.7193	52	8	19	41	77.5	0.793893
Fold 5	49	11	12	48	80.8333	0.80992	50	10	18	42	76.66667	0.78125	47	13	16	44	75.83333	0.764228
Fold 6	43	17	10	50	77.5	0.76106	37	23	10	50	72.5	0.69159	49	11	11	49	81.66667	0.816667
Fold 7	41	19	19	41	68.3333	0.68333	44	16	18	42	71.66667	0.7171	50	10	17	43	79.02778	0.797303
Fold 8	41	19	16	44	70.8333	0.70085	39	21	17	43	72.08333	0.71943	52	8	18	42	79.00463	0.797395
Average					73.3333	0.7269					71.61458	0.71739					79.02488	0.797314

Table 6.5: Classifier results for healthy (negative) vs glioma (positive)

Healthy vs Glioma	Gaussian SVM						Linear SVM						KNN (5 neighbours)					
	TP	FP	FN	TN	Accuracy	F1-score	TP	FP	FN	TN	Accuracy	F1-score	TP	FP	FN	TN	Accuracy	F1-score
Fold 1	108	12	26	34	78.8889	0.85039	106	14	31	29	75	0.8249	51	9	14	46	80.83333	0.816
Fold 2	110	10	22	38	82.2222	0.87302	108	12	27	33	78.33333	0.84706	54	6	15	45	82.5	0.837209
Fold 3	103	17	25	35	76.6667	0.83065	98	22	29	31	71.66667	0.79352	55	5	13	47	85	0.859375
Fold 4	107	13	20	40	81.6667	0.8664	106	14	23	37	79.44444	0.85141	54	6	10	50	86.66667	0.870968
Fold 5	111	9	29	31	78.8889	0.85385	108	12	36	24	73.33333	0.81818	52	8	16	44	80	0.8125
Fold 6	108	12	22	38	81.1111	0.864	111	9	34	26	76.11111	0.83774	55	5	11	49	86.66667	0.873016
Fold 7	110	10	26	34	80	0.82305	100	20	23	37	76.11111	0.82305	53	7	15	45	81.66667	0.828125
Fold 8	110	10	28	32	78.8889	0.85271	106	14	28	32	76.66667	0.83465	54	6	8	52	88.33333	0.885246
Average					79.8	0.85					75.8	0.83					84.0	0.85

Consistently, the three highest performing classifiers were linear SVM, Gaussian SVM and fine KNN, using only 5 neighbours. All classifiers were significantly better at distinguishing HGG, as opposed to LGG, from healthy tissue.

Table 6.3 shows that the Gaussian SVM achieved a near perfect classification (98.7%) for HGG detection, followed closely by the linear SVM at 96.7%. The k=5 KNN algorithm consistently outperformed the other KNN algorithms using a higher number of neighbours by 3 - 5% but still the maximum accuracy achieved was only 85%. In the case of HGG identification, the SVM had the highest accuracy at 97%.

However, in the case of LGG identification, Table 6.4, the KNN was the highest performing classifier, achieving 79% accuracy while the Gaussian SVM sat at 73.3%. The F1-scores followed a similar trend, with KNN achieving the highest at 80%, then followed by Gaussian and linear SVM with 73% and 71% respectively. Despite the results being much lower than for HGG, it is still a moderate F1 score, indicating the QUS analysis did aid classification to a reasonable degree.

In the combined study of healthy tissue vs glioma, all algorithms improved on their score from LGG detection alone. The KNN achieved an accuracy of 84% which is slightly higher than SVM, which achieved 79.8% in this instance.

There is a noticeable imbalance between the FP and FN results in all classifiers in Table 6.5, with FN values higher in all three classifiers. The F1 score is a combination of the precision and recall of the diagnostic test. This indicates a significantly lower recall ability, so glioma samples were regularly incorrectly identified as healthy by the classifier. One reason for this could be that there is a noticeable difference between the cell densities in LGG and HGG, and so the classifier would mislabel LGG as healthy, as those samples did not exhibit such extreme scattering behaviours as HGG. Also, there was a level of heterogeneity in the healthy samples. The average number of scatterers varied significantly within each slide, and within different samples, despite all being a central white matter region. This resulted in the healthy samples having parameter results over a fairly large range.

Cancer detection in general requires a high specificity, or recall, as it is more detrimental for the patient to incorrectly label a cancerous sample as healthy but, for the application of brain tumours, both are argued to be equally important here and the goal is to increase overall accuracy. The KNN and SVM are among the simplest binary classifiers to implement, but there is a vast number of binary classification methods. Among them exist decision tree, random forest adaptive boosting and neural network, with particular recent interest in the

latter [139]. Nevertheless, it is clear that SVM can identify HGG samples with near-perfect accuracy, and both it and KNN are able to classify glioma samples with moderate accuracy. There is therefore every possibility that this could be a useful adjunct in neurosurgery as it will provide the surgeon with potentially beneficial information.

The results for each fold are shown for this study as it is useful to see the range of accuracies over each of the eight instances of classification. The data has been grouped into eight sections and sequentially, one group is used as the testing set, while the other seven are used to train the classifier. In the case of the Gaussian SVM HGG classification, the results for each fold vary from 96.9 - 99.1% which indicate this is a consistently high performing algorithm. Yet in the LGG classification the results varied from 68.3 – 80.8% accuracy which is a much larger variation over each fold. This is an important consideration in the case of healthy tissue vs glioma in Table 6.5. While the Gaussian SVM and KNN have a similar level of accuracy, the range of accuracies in the SVM are only 5% when compared to the 12% span of the KNN. When determining the most reliable classifier it may not always be the option with the highest average accuracy but instead the one with the most consistent performance. The variation in results shows the advantage of k-fold validation as a measure of performance over a single instance result.

6.4.4 Comparison to *ex vivo* results

Attenuation values at 25 MHz observed in Fig. 6.9a are much lower than those measured at the same frequency in the experimental work described in Chapter 5. The modelled tissue in OnScale was set to an attenuation of $0.6 \text{ dB cm}^{-1} \text{ MHz}^{-1}$ from the material library, which is assumed to be based on the literature measured to only 10 MHz. Future work at high frequencies should be used to confirm that an alternate model should be used for attenuation which is at the correct magnitude over a higher frequency range.

In the case of the Nakagami parameter, the results agree with the experimental data that healthy tissue has a lower value, on average. However, there were a larger number of samples of GBM in the simulation study than in practice where $m \rightarrow 1$. This could be caused by the oversimplification of scattering sources in the FEA model.

6.4.5 Limitations of this study

A key simplification in this study was isolating tissue sections to contain only cell nuclei as scattering sources. It is clearly an approximation that the complex material microstructure of tissues stained with eosin can be assigned a single impedance value representative of that region. In reality, there could be various causes of scattering in glial tissue. In a study in

biophantoms, researchers concluded that scatterers are most probably the whole cells or clusters of cells, rather than individual nuclei alone [187]. A more gradual change in acoustic impedance, as observed in Fig. 6.1 may have had greater suitability for the present study. Additionally, the study disregarded other structures such as blood vessels despite their presence containing some diagnostic potential. In fact, it was more difficult to select regions avoiding blood vessels in the HGG images than the LGG, which aligns with observation of increased microvasculature in HGG from techniques such as contrast enhanced ultrasound [103]. An improvement on this study would have seen the inclusion of acoustic properties of blood cells and vessels to provide a more extensive model of all scattering sources in soft tissue.

This study was also limited in its confinement to 2D. It is not clear whether incorporating a third dimension would improve the classification potential of this technique. A possibility for 3D modelling is to prepare histology slides in-house to provide fine slices of 2D data, which could then be extrapolated to 3D. This was achieved by Mamou in his PhD thesis, where he created 3D acoustic impedance maps of rat mammary tumours [188]. The SAM results allowed inclusion of up to five materials to be represented in the acoustic impedance map: cell nuclei, cytoplasm, fat, red blood cells and surrounding material. Without acquiring both SAM and H&E slide images in the lab, it would not be possible to allow a more complex mapping. When moving to 3D geometries, the model time or computing resources would need some additional consideration; however, if accomplished, the move would allow comparison with 3D scattering theories and estimations of system independent spectral parameters.

6.5 CONCLUSIONS

Upscaling the available QUS data from healthy and cancerous tissue gave an insight into the capabilities of simple binary classification for non-invasive tissue characterisation. The main conclusion was that it is far easier to differentiate between healthy tissue and HGG than between healthy tissue and LGG. A near perfect Gaussian SVM classifier could be created based on real-time QUS parameters including the attenuation slope and centre frequency value as a parameter for classification. However, when applying the same method to LGG classification, the accuracy dropped 24.5%, to 73.3%. Interestingly the KNN improved upon this result which gives the finding that it is not possible to resolve that one ML approach is more suitable for QUS analysis than another, with a major issue being that the choice is data specific.

An important finding with regard to the statistical modelling of the echo envelope was that the distribution collapsed to the Rayleigh distribution, which modelled a large number of random scatterers. As this is not what has been observed in practice, it is either a limitation of the binary acoustic impedance map or evidence that individual cell nuclei cannot be considered as scattering sources. Despite the limitations in this study concerning the oversimplification of microstructure, it was interesting to see that the combination of HGG and LGG to create a glioma group marginally improved the results to 84%. However, due to the large differences in LGG and HGG, the recall of the classifier was reduced and LGG was often incorrectly labelled as healthy. It is therefore fair to say that the small-scale structure differences in healthy and glioma tissue in reality will alter the received signal and this change is detectable and classifiable with QUS and ML.

6.6 CHAPTER SUMMARY

In this chapter, QUS parameters were able to distinguish between healthy tissue and HGG *in silico* with a 97.8% accuracy, while achieving only a 79% accuracy when classifying healthy tissue and LGG samples with the same approach. 900 tiles from diagnostic slide images of healthy tissue, LGG and HGG were used to create a binary acoustic impedance map in FEA by filtering the H&E staining to create a binary image meshed to a specific simulation geometry. The pulse-echo simulation mimicked that of a single element from the Verasonics L35-16v probe and pressure outputs throughout the entire simulation geometry were saved. The received pressure was used to estimate QUS parameters based on attenuation, the BSPS and statistics of the echo envelope. Utilising all parameters, the SVM outperformed the KNN technique and achieved a near perfect classification score to differentiate healthy tissue from HGG. However, the KNN technique was more accurate than a SVM in distinguishing between healthy tissue and LGG samples, though the accuracy was significantly lower at 79%. This study brought to light that the real challenge is to discern healthy tissue from LGG samples, as opposed to HGG, and this was accomplished with QUS and a binary classification algorithm.

7 CONCLUSIONS AND FUTURE WORK

7.1 AIM OF CHAPTER

This chapter aims to compile the main findings from the original work contained in this thesis and provide guidance for further progress of research in this field. The main conclusions and questions raised from each of the preceding chapters are discussed. Particularly, the novelty of applying the techniques to brain tissue warrants future work, namely in validation of results found and consideration of LGG brain tumours. The preliminary results are encouraging for an *in vivo* trial and the steps needed to realise this aim are suggested.

7.2 CONCLUSIONS

The primary objective of this thesis was to explore the ways in which ultrasound could be used to differentiate healthy and diseased neural tissue for reasons described in Chapter 2. The literature review confirms there is a need for an interoperative imaging tool to aid glioma detection, and ultrasound is an attractive solution. The potential of QUS, described in Chapter 3, to add an additional quantitative layer of information in the application of brain tumour characterisation was determined to be the area of the focus for the remainder of the project. Overall, this study lays the groundwork in the field of HF QUS applied to brain tissue and the following conclusions are drawn.

7.2.1 Machine Learning-enabled QUS for Tissue Characterisation

The phantom work presented in Chapter 4 was essential for setting up a ML-enabled tissue characterisation system. It was found that chicken liver and gizzard muscle were reasonable soft tissue phantoms to test the experimental set-up for QUS parameter estimation. This verified that a modern research ultrasound system can be used to implement QUS ultrasound techniques and display quasi-real time parametric images. However, an important finding was that it was not feasible to image a $1.5 \times 1.5 \text{ cm}^2$ region with a pixel size of $1 \times 1 \text{ mm}^2$ with the HK parameters intraoperatively. This is due to the time needed for computer solutions using the embedded binary search algorithms for each window, which took over 10 minutes. Using only real time parameters, QUS was able to correctly label liver and gizzard samples with an average accuracy of 95.5%. This chapter also noted that statistical QUS parameters did not change significantly when the tissue was fresh, frozen, or fixed, but the EAC did change in the case of fixed tissue. This result was used to aid the decision of which preserved *ex vivo* tissue to use in the following study as it would be highly

advantageous if acoustic properties were applicable in future comparisons to *ex vivo* measurements.

7.2.2 Acoustic Characterisation

The thesis contributed to current knowledge of the acoustic properties of healthy brain tissue and GBM through measurements of attenuation and speed of sound. The SoS estimates agree with current literature, but attenuation was slightly higher than the latest reports in human brain tissue at LF, indicating an attenuation coefficient closer to $0.9 \text{ dB MHz}^{-1} \text{ cm}^{-1}$. The frequency range was extended to 35 MHz for the first HF measurement of attenuation, which found the attenuation of GBM to be 5.1 dB higher than healthy tissue at a centre frequency of 25 MHz. The conclusion drawn from this was that the attenuation value itself can act as an additional QUS parameter to aid differentiation between healthy and cancerous tissue, so should be included in the binary classification results.

7.2.3 Differentiating Healthy and HGG Neural Tissue using QUS

The preliminary analysis of HF QUS results showed that a 25 MHz system is able to measure all QUS parameters successfully using a linear array exciting each element sequentially. This novel acquisition method was utilised as the simplest way to derive a large number of QUS results from the small tissue samples available, which allows an aggregate measure of the statistical parameters and provides five sets of results per sample. It is also applicable intraoperatively. The average results were found, and the EAC and mean echogenicity had significant differences in the two tissue types when analysed with conventional student's t-test. All results were then used to train a classifier which achieved an 89.9% accuracy, highlighting the benefits of a multiparametric approach.

7.2.4 Microultrasound Analysis

The analysis at 74 MHz pushed QUS beyond the boundaries of current knowledge with HF implementation, with several key findings. Firstly, it is imperative to ensure the data acquisition system is compatible with the high level of gain required to collect data from the tissue region in the presence of attenuation, without losing information through clipping distortion. Despite this main challenge, the images formed gave a crucial insight into the difference in scattering level observed through speckle at this scale. The general statistics from the B-mode pixel intensity found the mean value to be significantly higher in cancerous tissue, which is expected, and this additional quantitative layer may be useful on a clinical level. Using the HK-distribution parameters, the tissues could be categorised correctly with 96.0% accuracy. This supports the relevance of the model parameters of the HK-distribution

in the context of tissue characterisation. While the computation time limits the capability for real time imaging, it is still possible to obtain one set of HK parameters in a reasonable time, so these parameters should not be ruled out for clinical use. The availability of processing through network connection from the OR to the computing cloud is also worth considering.

7.2.5 QUS in FEA

Difficulties in data acquisition, in sourcing a large number of tissue samples and in working with them to obtain consistent data were overcome in the FEA analysis. This study simulated the HF QUS study with research ultrasound array elements but used over 900 2D tissue models in the analysis. The main finding was that ML-enabled QUS can identify HGG much easier than it can LGG. This agrees with the literature, that the acoustic contrast between healthy and LGG is much less, so it is harder to differentiate. This was quantified by an average of 10.2% lower classification accuracy for LGG when compared to HGG and brought into question whether the most valuable *ex vivo* tissue sample to source was the HGG.

After this study was conducted, discussions of the results with a neurosurgeon (Dr M.Draz, Queen Elizabeth University Hospital, Glasgow) revealed it is not necessarily harder to visualise HGG over LGG in the OR, as was the initial aim of this study. The detection of LGG would make the most impact on patient prognosis, as a full resection could make a large improvement to a patient's lifespan, which sadly is not the case for GBM. At this level of malignancy even several cells left unresected will continue to divide and multiply until eventually the cancer has returned. Patients with LGG have a better overall prognosis with complete resection and chemotherapy.

It was an essential step to conduct the *ex vivo* work using the most extreme differences in tissue microstructure, between healthy and HGG, to prove the capabilities of QUS in combination with HF ultrasound. Now, it must be applied to a more challenging differentiation task, which will require some innovative improvements through data acquisition, more sophisticated methods of binary classification, and utilisation of FEA to its full potential.

7.3 RECOMMENDATIONS FOR FUTURE WORK

7.3.1 *In vivo* QUS

Thus far, all experiments were carried out in a laboratory setting but, with intended application in an intraoperative device, it is imperative to test the feasibility of these

techniques *in vivo*. In particular, there is difficulty obtaining the attenuation of tissues, and thus spectral parameters, without a reference scan and excised tissue of known thickness. There have been several studies published on *in vivo* methods to determine attenuation through either the spectral shift method or amplitude decay using the B-mode image alone [189]. Recent techniques have been adopted, which are often used in the context of QUS, known as the reference phantom method. This uses a well-characterised material to estimate the linear attenuation coefficient and BSC of tissue from the ratios of signals received from the sample and reference phantom based on the frequency dependence at a given depth [190]. However, the phantoms can be difficult to manufacture and are not well characterised at high frequencies. There are some methods which allow an *in vivo* attenuation measurement using the unprocessed data, based on measuring average decay of the received signal through the tissue [191]. Most ultrasound systems in the OR are qualitative, so only an image is available, in which TGC may be applied. If access to raw data is required, then a system with research capabilities should be considered.

The full potential of the Verasonics Vantage System in an *in-vivo* setting must be explored. It has the capability to display real-time, high quality images, while still allowing parallel collection and processing of the RF data. This would allow an *in vivo* attenuation estimation and statistical approaches to be considered on the echo envelope. As well as this, there is almost limitless flexibility in transmission modes which could be explored. This work saw implementation of 60 elements of a linear array transmitting simultaneously in Chapter 4, then all elements transmitting and receiving sequentially in a HF array Chapter 5. Some examples of innovative methods for data acquisition in the context of QUS are listed here:

- Using a linear array to transmit and receive in a sweeping window sequence using a smaller aperture, for example, using only 8 elements to transmit and receive before shifting several elements and repeating the process over the full 128 elements. This would allow a larger signal to be directed to the tissue region at any given time while still maintaining high resolution in a QUS parametric image.
- Full matrix capture: where one array element transmits, and then all 128 receive. This is typically used in non-destructive testing [192] but, if incorporated into the context of BSC measurements with sufficient system sensitivity, it would maximise the information from the raw data received.

- Custom transducer design, powered by Verasonics. The system is not limited to using commercial probes, so a custom array specifically for neurosurgical application could be used, granted the upper frequency does not surpass 62.5 MHz.

As the next step towards *in vivo* QUS, it is recommended an animal trial is conducted, with the aim of using the Verasonics system on porcine brain, obtaining attenuation, spectral and HK parameters of healthy brain tissue.

It is also possible to use the Verasonics on human patients in the operating theatre, so long as relevant ethical approval and risk assessments are in place. This will require measurement of the output acoustic pressure of the transducer while it is operating for the required application, to ensure it does not exceed the maximum mechanical index (MI) deemed safe for human use. The MI quantifies the bioeffects from the acoustic beam and should not exceed 1.7 as stated in the guidelines for safe ultrasound imaging by the British Medical Ultrasound Society [193]. In preparation for this application, a measurement was made using a needle hydrophone placed 1 mm in front of the LF Verasonics array when exciting all elements at a maximum voltage of 50V. The output pressure measured by the hydrophone was used to calculate the MI over a 2D scan and the results are shown in Fig. 7.1.

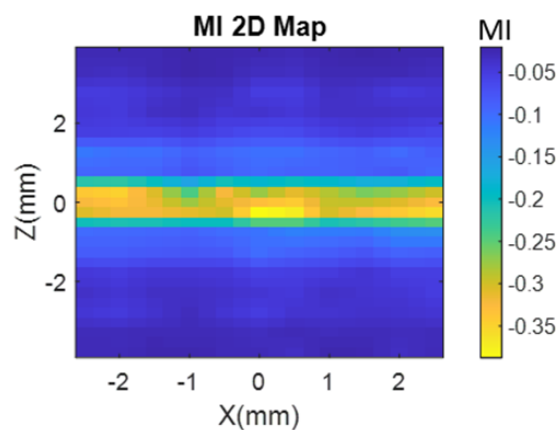


Figure 7.1: MI from Verasonics using acoustic pressure measurements from needle hydrophone. Image courtesy of Dr Alex Moldovan.

The results show that the pressure output is safe for use on human tissue, and may be feasible to utilise this probe in a clinical trial. However, especially at higher frequencies, considerations should also be made to the Thermal Index (TI), which measures the thermal bioeffects from the ultrasound source. A similar map should be made of the thermal effects from this probe before application for clinical trial. The ultimate aim would be to assess the

ability of ML-enabled QUS to correctly predict glioma regions *in vivo*. The binary classifier accuracy will be determined based on labels given by a clinician as the ground truth. If successful, this would act as a non-invasive aid to the neurosurgeon.

Alternative approaches to the method described above for measuring BSC include the reference phantom method, which allows a quick and simultaneous measure of the attenuation and BSC [194]. In short, signals are compared to a reference phantom, usually agarose with embedded scatterers of known attenuation and BSC is calculated from Faran's scattering theory [29][195]. Importantly the distribution of scatterers must be known, so the laboratory set-up involved to accurately prepare a suitable phantom is time-consuming [196].

7.3.2 Further FEA Exploration

One area in which FEA will have immense value is in custom device prototyping. Often, in neurosurgery a burrhole is used to conduct the surgery and so typical linear arrays may not be suitable for this application. As an extension to the study described in Chapter 5, a full 3-D piezoelectric device could be simulated, so parameters such as ESD and EAC could be found. FEA would allow easy manipulation of device configuration for proof of concept, such as the number of elements and centre operating frequency, which can then be optimised for this specific application. This would, however, require a representative 3-D model of healthy and cancerous brain tissue.

As discussed in Chapter 5 the model could be improved by considering other material properties present in the samples. The creation of 3D impedance maps could also be realised through histology slices.

7.3.3 Reference Free QUS

Traditional QUS and binary classification approaches were utilised in this thesis and shown in Chapter 3 to have a strong theoretical framework, which has developed over several decades. Fairly simple ML classification was used to explore their potential for. However, there are various improvements on the current study, namely optimisation of the feature selection. In the present study, all features received the same weighting, and different combinations of features were used to train different algorithms to determine the most valuable parameters. An improvement to this approach would be to incorporate feature weighting into the classification algorithm, which may improve accuracy. This is achieved by estimating the relative importance of each feature for the specific classification task, and assigning it a corresponding weight, in which higher weighting features have more influence

in the classification task. Another improvement could be use of an ensemble methods, which combines the predictions of several models, and has been shown to improve accuracy and robustness of a single model. This can be achieved either by averaging or boosting methods to produce an improved estimator [197].

To realise the full potential of ML in tissue characterisation with ultrasound, recent studies are moving away from traditional QUS methods. Both spectral and statistical methods have their drawbacks. It was noted that most implementations of spectral methods require a reference scan, which is a hindrance to its use *in vivo* as it could cause disruption in a clinical setting. Termed reference-free QUS, some initial studies are using a convolutional neural network (CNN) for tissue classification as a means of eliminating the need for a reference step.

CNNs are a type of supervised machine learning. A CNN learns a non-linear mapping from the input (backscattered RF data) to the output (pathologic index healthy tissue or tumour). It achieves this via stacking multiple connected convolutional filter layers at different resolutions. The learned features from the layers can then be concatenated into a vector and classified by fully connected layers. Recently, a CNN outperformed the classification utilizing the QUS parameters combined with a support vector machine in differentiating between low and high lipid liver levels, with accuracies of 74% versus 59% on the test data [198]. Therefore, although the CNN did not provide a physical interpretation of the tissue properties, e.g., attenuation of the medium or scatterer properties, it had much higher accuracy in predicting fatty liver state and did not require an external reference scan. Furthermore, there is no requirement for the input to the CNN to be raw data, and the image data alone could be used.

In the present study, work was carried out as a preliminary step to conduct a short, *in vivo* reference-free study in glioma patients at the Queen Elizabeth University Hospital, Glasgow. However, time constraints and the COVID-19 pandemic meant the study was not feasible. The research protocol is given as in Appendix V.

Briefly, images would be collected from glioma patients using a Flex Focus 800 clinical ultrasound machine (BK Medical, Denmark) with a specialised craniotomy probe with a bandwidth of 4 - 10 MHz (Probe 8862, BK Medical). Identical system settings would be used for all images and they would be saved in a specific pre-set. Then before tumour resection, the surgeon would identify the cancerous region in several B-mode images, which could be annotated. This procedure would be repeated over the course of tumour removal

until the surgeon stopped, then all the data would be used to train a ML algorithm to identify cancerous regions on the B-mode images, using the surgeon's initial judgement as ground truth.

ML has already shown to be powerful at aiding brain tumour detection in medical images [199]. However, most research has focused on CT and MRI data, so the use of ultrasound images features and ML, particular in brain tumour application is still in its early stages. Whether QUS-based or reference free, it is predicted that more ML technology will be integrated in tissue characterisation in the future. The ultimate goal is not that these will replace the judgement of the surgeon but rather aid them to increase the extent of tumour resected and improve patient prognosis.

References

- [1] D. J. Brat and A. Perry, *6 - Astrocytic and Oligodendroglial Tumors*, Second Edi. Elsevier Inc., 2018. doi: 10.1016/B978-0-323-44941-0.00006-0.
- [2] Q. T. Ostrom, N. Patil, G. Cioffi, K. Waite, C. Kruchko, *et al.*, “CBTRUS statistical report: Primary brain and other central nervous system tumors diagnosed in the United States in 2013-2017,” *Neuro. Oncol.*, vol. 22, no. Supplement_1, pp. IV1–IV96, 2020, doi: 10.1093/neuonc/noaa200.
- [3] S. Mahboob, R. McPhillips, Z. Qiu, Y. Jiang, C. Meggs, *et al.*, “Intraoperative Ultrasound-Guided Resection of Gliomas: A Meta-Analysis and Review of the Literature,” *World Neurosurg.*, vol. 92, pp. 255–263, 2016, doi: 10.1016/j.wneu.2016.05.007.
- [4] H. Onizuka, K. Masui, and T. Komori, “Diffuse gliomas to date and beyond 2016 WHO Classification of Tumours of the Central Nervous System,” *Int. J. Clin. Oncol.*, vol. 25, no. 6, pp. 997–1003, 2020, doi: 10.1007/s10147-020-01695-w.
- [5] I. Y. Eyüpoglu, M. Buchfelder, and N. E. Savaskan, “Surgical resection of malignant gliomas-role in optimizing patient outcome,” *Nat. Rev. Neurol.*, vol. 9, no. 3, pp. 141–151, 2013, doi: 10.1038/nrneurol.2012.279.
- [6] M. Lacroix, D. Abi-Said, D. R. Fourney, Z. L. Gokaslan, W. Shi, *et al.*, “A multivariate analysis of 416 patients with glioblastoma multiforme: prognosis, extent of resection, and survival,” *J. Neurosurg.*, vol. 95, no. 2, pp. 190–198, 2001, doi: 10.3171/jns.2001.95.2.0190.
- [7] N. L. Dorward, O. Alberti, B. Velani, F. A. Gerritsen, W. F. J. Harkness, *et al.*, “Postimaging brain distortion: magnitude, correlates, and impact on neuronavigation,” *J. Neurosurg.*, vol. 88, no. 4, pp. 656–662, 1998, doi: 10.3171/jns.1998.88.4.0656.
- [8] P. Schiavone, F. Chassat, T. Boudou, E. Promayon, F. Valdivia, *et al.*, “In vivo measurement of human brain elasticity using a light aspiration device,” *Med. Image Anal.*, vol. 13, no. 4, pp. 673–678, 2009, doi: 10.1016/j.media.2009.04.001.
- [9] M. N. Stienen, J. Fierstra, A. Pangalu, L. Regli, and O. Bozinov, “The Zurich checklist for safety in the intraoperative magnetic resonance imaging suite: Technical note,” *Oper. Neurosurg.*, vol. 16, no. 6, pp. 756–765, 2019, doi: 10.1093/ons/opy205.

- [10] C. Senft, A. Bink, K. Franz, H. Vatter, T. Gasser, *et al.*, “Intraoperative MRI guidance and extent of resection in glioma surgery: A randomised, controlled trial,” *Lancet Oncol.*, vol. 12, no. 11, pp. 997–1003, 2011, doi: 10.1016/S1470-2045(11)70196-6.
- [11] W. F. Chandler, J. E. Knake, J. E. McGillicuddy, K. O. Lillehei, and T. M. Silver, “Intraoperative use of real-time ultrasonography in neurosurgery,” *J. Neurosurg.*, vol. 57, no. 2, pp. 157–163, 1982, doi: 10.3171/jns.1982.57.2.0157.
- [12] C. R. Hill, J. C. Bamber, and G. R. Ter Haar, “Physical Principles of Medical Ultrasonics,” in *Physical Principles of Medical Ultrasonics*, 2nd ed. Wiley, 2005, pp. 1–511. doi: 10.1002/0470093978.
- [13] R. Sastry, W. L. Bi, S. Pieper, S. Frisken, T. Kapur, *et al.*, “Applications of Ultrasound in the Resection of Brain Tumors,” *J. Neuroimaging*, vol. 27, no. 1, pp. 5–15, 2017, doi: 10.1111/jon.12382.
- [14] P. D. Le Roux, M. S. Berger, K. Wang, L. A. Mack, and G. A. Ojemann, “Low grade gliomas: comparison of intraoperative ultrasound characteristics with preoperative imaging studies,” *J. Neurooncol.*, vol. 13, no. 2, pp. 189–198, 1992, doi: 10.1007/BF00172770.
- [15] O. Solheim, T. Selbekk, A. S. Jakola, and G. Unsgård, “Ultrasound-guided operations in unselected high-grade gliomas-overall results, impact of image quality and patient selection,” *Acta Neurochir. (Wien)*, vol. 152, no. 11, pp. 1873–1886, 2010, doi: 10.1007/s00701-010-0731-5.
- [16] A. G. Chacko, N. K. S. Kumar, G. Chacko, R. Athyal, V. Rajshekhar, *et al.*, “Intraoperative ultrasound in determining the extent of resection of parenchymal brain tumours - A comparative study with computed tomography and histopathology,” *Acta Neurochir. (Wien)*, vol. 145, no. 9, pp. 743–748, 2003, doi: 10.1007/s00701-003-0009-2.
- [17] A. V. Moiyadi, P. M. Shetty, A. Mahajan, A. Udare, and E. Sridhar, “Usefulness of three-dimensional navigable intraoperative ultrasound in resection of brain tumors with a special emphasis on malignant gliomas,” *Acta Neurochir. (Wien)*, vol. 155, no. 12, pp. 2217–2225, 2013, doi: 10.1007/s00701-013-1881-z.
- [18] J. Coburger, A. Scheuerle, D. R. Thal, J. Engelke, M. Hlavac, *et al.*, “Linear array ultrasound in low-grade glioma surgery: histology-based assessment of accuracy in

- comparison to conventional intraoperative ultrasound and intraoperative MRI,” *Acta Neurochir. (Wien)*, vol. 157, no. 2, pp. 195–206, 2015, doi: 10.1007/s00701-014-2314-3.
- [19] F. Prada and L. Solbiati, *Intraoperative Ultrasound (IOUS) in Neurosurgery*. Springer, 2016. doi: 10.1007/978-3-319-25268-1.
- [20] V. van Velthoven and L. M. Auer, “Practical application of intraoperative ultrasound imaging,” *Acta Neurochir*, vol. 105, no. 1–2, pp. 5–13, 1990, [Online]. Available: <http://www.ncbi.nlm.nih.gov/pubmed/2239380>
- [21] D. Nicholas, C. R. Hill, and D. K. Nassiri, “Evaluation of backscattering coefficients for excised human tissues: Principles and techniques,” *Ultrasound Med. Biol.*, vol. 8, no. 1, pp. 7–15, 1982, doi: 10.1016/0301-5629(82)90064-3.
- [22] G. Ghoshal, M. L. Oelze, and W. D. O’Brien, “Quantitative Ultrasound History and Successes,” in *Quantitative Ultrasound in Soft Tissues*, New York: Springer, 2013.
- [23] E. J. Feleppa, F. L. Lizzi, D. J. Coleman, and M. M. Yaremko, “Diagnostic spectrum analysis in ophthalmology: A physical perspective,” *Ultrasound Med. Biol.*, vol. 12, no. 8, pp. 623–631, 1986, doi: 10.1016/0301-5629(86)90183-3.
- [24] F. L. Lizzi, M. Greenebaum, E. J. Feleppa, M. Elbaum, and D. J. Coleman, “Theoretical framework for spectrum analysis in ultrasonic tissue characterization,” *J. Acoust. Soc. Am.*, vol. 73, no. 4, pp. 1366–1373, 1983, doi: 10.1121/1.389241.
- [25] M. L. Oelze, J. F. Zachary, and W. D. O’Brien, “Characterization of tissue microstructure using ultrasonic backscatter: Theory and technique for optimization using a Gaussian form factor,” *J. Acoust. Soc. Am.*, vol. 112, no. 3, pp. 1202–1211, 2002, doi: 10.1121/1.1501278.
- [26] M. L. Oelze, W. D. O’Brien, J. P. Blue, and J. F. Zachary, “Differentiation and characterization of rat mammary fibroadenomas and 4T1 mouse carcinomas using quantitative ultrasound imaging,” *IEEE Trans. Med. Imaging*, vol. 23, no. 6, pp. 764–771, 2004, doi: 10.1109/TMI.2004.826953.
- [27] L. Sannachi, H. Tadayyon, A. Sadeghi-Naini, W. Tran, S. Gandhi, *et al.*, “Non-invasive evaluation of breast cancer response to chemotherapy using quantitative ultrasonic backscatter parameters,” *Med. Image Anal.*, vol. 20, no. 1, pp. 224–236, 2015, doi: 10.1016/j.media.2014.11.009.

- [28] J. S. Paige, G. S. Bernstein, E. Heba, E. A. C. Costa, M. Fereirra, *et al.*, “A pilot comparative study of quantitative ultrasound, conventional ultrasound, and MRI for predicting histology-determined steatosis grade in adult nonalcoholic fatty liver disease,” *Am. J. Roentgenol.*, vol. 208, no. 5, pp. W168–W177, 2017, doi: 10.2214/AJR.16.16726.
- [29] M. F. Insana and T. J. Hall, “Parametric Ultrasound Imaging from Backscatter Coefficient Measurements: Image Formation and Interpretation,” *Ultrason. Imaging*, vol. 12, no. 4, pp. 245–267, 1990, doi: 10.1177/016173469001200402.
- [30] F. Destrepes, E. Franceschini, F. T. H. Yu, and G. Cloutier, “Unifying Concepts of Statistical and Spectral Quantitative Ultrasound Techniques,” vol. 35, no. 2, pp. 488–500, 2016.
- [31] R. F. Wagner, S. W. Smith, J. M. Sandrik, and H. Lopez, “Statistics of Speckle in Ultrasound B-Scans,” *IEEE Trans. Sonics Ultrason.*, vol. 30, no. 3, pp. 156–163, 1983, doi: 10.1109/T-SU.1983.31404.
- [32] H. G. Nasief, I. M. Rosado-Mendez, J. A. Zagzebski, and T. J. Hall, “A Quantitative Ultrasound-Based Multi-Parameter Classifier for Breast Masses,” *Ultrasound Med. Biol.*, vol. 45, no. 7, pp. 1603–1616, 2019, doi: 10.1016/j.ultrasmedbio.2019.02.025.
- [33] F. Destrepes and G. Cloutier, “A critical review and uniformized representation of statistical distributions modeling the ultrasound echo envelope,” *Ultrasound Med. Biol.*, vol. 36, no. 7, pp. 1037–1051, 2010, doi: 10.1016/j.ultrasmedbio.2010.04.001.
- [34] F. Destrepes and G. Cloutier, “Review of Echo Envelope Statistics Models for Quantitative Ultrasound Imaging and Tissue Characterisation,” in *Quantitative Ultrasound in Soft Tissues*, 1st ed. New York: Springer, 2013.
- [35] V. Dutt, “Ultrasound Echo Envelope Analysis Using a Homodyned K Distribution Signal Model,” *Ultrasonic Imaging*, vol. 16, no. 4, pp. 265–287, 1994. doi: 10.1006/uimg.1994.1016.
- [36] J. Mamou, A. Coron, M. Hata, J. Machi, E. Yanagihara, *et al.*, “Three-Dimensional High-Frequency Characterization of Cancerous Lymph Nodes,” *Ultrasound Med. Biol.*, vol. 36, no. 3, pp. 361–375, 2010, doi: 10.1016/j.ultrasmedbio.2009.10.007.
- [37] T. N. Nguyen, A. S. Podkowa, A. Y. Tam, E. C. Arnold, R. J. Miller, *et al.*, “Characterizing Fatty Liver in vivo in Rabbits, Using Quantitative Ultrasound,” *Ultrasound Med. Biol.*, vol. 45, no. 8, pp. 2049–2062, 2019, doi:

10.1016/j.ultrasmedbio.2019.03.021.

- [38] M. Strowitzki, S. Brand, R. Ketter, W. I. Steudel, and K. V. Jenderka, “Ultrasonic radio-frequency spectrum analysis differentiates normal and edematous brain tissue from meningioma intraoperatively,” *J. Neuroimaging*, vol. 18, no. 1, pp. 73–80, 2008, doi: 10.1111/j.1552-6569.2007.00173.x.
- [39] D. Rohrbach, B. Wodlinger, J. Wen, J. Mamou, and E. Feleppa, “High-Frequency Quantitative Ultrasound for Imaging Prostate Cancer Using a Novel Micro-Ultrasound Scanner,” *Ultrasound Med. Biol.*, vol. 44, no. 7, pp. 1341–1354, 2018, doi: 10.1016/j.ultrasmedbio.2018.02.014.
- [40] S. Mukherjee, *The Emperor of all Maladies*. Harper Collins.
- [41] D. J. Brat, *2 - Normal Brain Histopathology*, Second Edi. Elsevier Inc., 2018. doi: 10.1016/B978-0-323-44941-0.00002-3.
- [42] “Center for Functional MRI: Structural MRI.” <http://fmri.ucsd.edu/Howto/3T/structure.html> (accessed Dec. 20, 2017).
- [43] S. Ackerman, “Major Structures and Functions of the Brain,” in *Discovering the Brain*, National Academic Press, 1992.
- [44] J. A. Kiernan, “Cells of the Nervous System,” in *The Human Nervous System*, Lippincott Williams and Wilkins, 2005, pp. 13–37.
- [45] “Cancer Today.” <https://gco.iarc.fr/today/home> (accessed Dec. 21, 2017).
- [46] The Brain Tumour Charity, “The statistics about brain tumours.” <https://www.thebraintumourcharity.org/get-involved/donate/why-choose-us/the-statistics-about-brain-tumours/> (accessed Jan. 10, 2022).
- [47] C. C. Gotay, C. T. Kawamoto, A. Bottomley, and F. Efficace, “The prognostic significance of patient-reported outcomes in cancer clinical trials,” *J. Clin. Oncol.*, vol. 26, no. 8, pp. 1338–1345, 2008, doi: 10.1200/JCO.2007.13.9337.
- [48] P. C. Burger and S. B. Green, “Patient age, histologic features, and length of survival in patients with glioblastoma multiforme,” *Cancer*, vol. 59, no. 9, pp. 1617–1625, 1987, doi: 10.1002/1097-0142(19870501)59:9<1617::AID-CNCR2820590916>3.0.CO;2-X.
- [49] “Brain Tumour Statistics: Cancer Research.”

<http://www.cancerresearchuk.org/health-professional/cancer-statistics/statistics-by-cancer-type/brain-other-cns-and-intracranial-tumours#heading-Two> (accessed Dec. 21, 2017).

- [50] “American Brain Tumor Association.” <http://www.abta.org/about-us/news/brain-tumor-statistics/> (accessed Dec. 20, 2017).
- [51] O. Van Tellingen, B. Yetkin-Arik, M. C. De Gooijer, P. Wesseling, T. Wurdinger, *et al.*, “Overcoming the blood-brain tumor barrier for effective glioblastoma treatment,” *Drug Resist. Updat.*, vol. 19, pp. 1–12, 2015, doi: 10.1016/j.drug.2015.02.002.
- [52] Z. Z. Zhang, L. B. E. Shields, D. A. Sun, Y. P. Zhang, M. A. Hunt, *et al.*, “The Art of Intraoperative Glioma Identification,” *Front. Oncol.*, vol. 5, no. July, pp. 1–7, 2015, doi: 10.3389/fonc.2015.00175.
- [53] Mayo Clinic, “Burr hole approach offers minimally invasive option for resecting brain lesions.” <https://www.mayoclinic.org/medical-professionals/neurology-neurosurgery/news/burr-hole-approach-offers-minimally-invasive-option-for-resecting-brain-lesions/mac-20506910>
- [54] J. K. Burkhardt, C. Serra, M. C. Neidert, C. M. Woernle, and J. Fierstra, “High-frequency intra-operative ultrasound-guided surgery of superficial intra-cerebral lesions via a single-burr-hole approach,” *Ultrasound Med. Biol.*, vol. 40, no. 7, pp. 1469–1475, 2014, doi: 10.1016/j.ultrasmedbio.2014.01.024.
- [55] “Brain Tumour Symptoms: Mayo Clinic.” <https://www.mayoclinic.org/diseases-conditions/brain-tumor/symptoms-causes/syc-20350084>
- [56] M. Koshy, J. L. Villano, T. A. Dolecek, A. Howard, U. Mahmood, *et al.*, “Improved survival time trends for glioblastoma using the SEER 17 population-based registries,” *J. Neurooncol.*, vol. 107, no. 1, pp. 207–212, 2012, doi: 10.1007/s11060-011-0738-7.
- [57] T. Kaster, I. Sack, and A. Samani, “Measurement of the hyperelastic properties of ex vivo brain tissue slices,” *J. Biomech.*, vol. 44, no. 6, pp. 1158–1163, 2011, doi: 10.1016/j.jbiomech.2011.01.019.
- [58] C. R. UK, “PET Scan.” <https://www.cancerresearchuk.org/about-cancer/brain-tumours/getting-diagnosed/tests/pet-scan> (accessed May 07, 2023).

- [59] NHS, “CT Scan.” <https://www.nhs.uk/conditions/ct-scan/> (accessed May 07, 2023).
- [60] P. Hoskins, *Diagnostic Ultrasound: Physics and Equipment*. Greenwich Medical Media, 2003.
- [61] “National Institute of Biomedical Imaging and Bioengineering: What is Medical Ultrasound?” <https://www.nibib.nih.gov/science-education/science-topics/ultrasound#:~:text=One of the most common,organs%2C skin%2C and muscles.>
- [62] F. Prada and L. Solbiati, “Clinical Ultrasound: Historical Aspects.,” in *Intraoperative Ultrasound in Neurosurgery*, Springer, 2016, pp. 3–7.
- [63] I. Sudo, C. Martinoli, M. Panas-goworska, and K. Dussik, “History Page : Leaders in MSK Radiology Karl Dussik , 1908 – 1968 : Pioneer of MSK Ultrasonography,” pp. 184–185, 2021.
- [64] “History of Karl Dussik.”
- [65] K. T. Dussik, F. Dussik, and L. Wyt, “Auf dem Wege zur Hyperphonographie des Gehirnes (On the way to Brain Hyperphonography),” *Wien Men Wochenschr*, vol. 97, pp. 425–429, 1947.
- [66] I. Edler and K. Lindström, “The history of echocardiography,” *Ultrasound Med. Biol.*, vol. 30, no. 12, pp. 1565–1644, 2004, doi: 10.1016/S0301-5629(99)00056-3.
- [67] Z. Nazarchuk, V. Skalskyi, and O. Serhiyenko, “Propagation of Elastic waves in Solids,” in *Acoustic Emission*, 2017. doi: 10.1007/978-3-319-49350-3.
- [68] R. J. Dickinson and D. K. Nassiri, “Reflection and Scattering,” *Phys. Princ. Med. Ultrason.*, pp. 191–222, 2005, doi: 10.1002/0470093978.ch6.
- [69] J. D. . Cheeke, *Ultrasound for engineers*. 2000.
- [70] M. Morgan and Z. Vajuhudeen, “Acoustic Impedance Reference Article.,” *Radiopaedia.org*, 2022. <https://doi.org/10.53347/rID-32118>
- [71] “HyperPhysics - Quartz.” <http://hyperphysics.phy-astr.gsu.edu/hbase/Geophys/quartz.html>
- [72] J. C. Bamber, “Speed of Sound,” in *Physical Principles of Medical Ultrasonics*, 2nd ed. Wiley, 2004, pp. 167–190.
- [73] R. L. Johnston, S. A. Goss, and V. Maynard, “Elements of Tissue Characterisation.”

Ultrasonic Tissue Characterisation, 1979.

- [74] J. C. Bamber, "Attenuation and Absorption," *Phys. Princ. Med. Ultrason.*, pp. 93–166, 2004, doi: 10.1002/0470093978.ch4.
- [75] C. A. Guertler, R. J. Okamoto, J. L. Schmidt, A. A. Badachhape, C. L. Johnson, *et al.*, "Mechanical properties of porcine brain tissue in vivo and ex vivo estimated by MR elastography," *J. Biomech.*, vol. 69, pp. 10–18, 2018, doi: 10.1016/j.jbiomech.2018.01.016.
- [76] F. W. Kremkau, R. W. Barnes, C. P. McGraw, W. Krenkau, R. W. Barnes, *et al.*, "Ultrasonic attenuation and propagation speed in normal human brain," vol. 29, no. 1981, 1981.
- [77] A. K. Singh and G. R. Pandey, "Temperature Dependence of speed of Propagation of Ultrasound in soft biological tissues," vol. 5, no. 9, pp. 455–461, 2018.
- [78] A. Rabell-Montiel, A. J. Thomson, T. A. Anderson, S. D. Pye, and C. M. Moran, "Acoustic Properties of Small Animal Soft Tissue in the Frequency Range 12-32 MHz," *Ultrasound Med. Biol.*, vol. 44, no. 3, pp. 702–713, 2018, doi: 10.1016/j.ultrasmedbio.2017.11.003.
- [79] N. Jiménez, J. Redondo, V. Sánchez-Morcillo, F. Camarena, Y. Hou, *et al.*, "Nonlinear Acoustics FDTD method including Frequency Power Law Attenuation for Soft Tissue Modeling," no. January, 2014, [Online]. Available: <http://arxiv.org/abs/1401.6669>
- [80] F. A. Duck, *Physical Properties of Tissues: A Comprehensive Reference Book*. Academic Press, 2013.
- [81] J. M. Martínez and B. J. Jarosz, "3D perfused brain phantom for interstitial ultrasound thermal therapy and imaging: Design, construction and characterization," *Phys. Med. Biol.*, vol. 60, no. 5, pp. 1879–1900, 2015, doi: 10.1088/0031-9155/60/5/1879.
- [82] W. Schiefer, E. Kazner, and K. Zulch, "Proceedings in Echo-Encephalography: International Symposium on Echo-Encephalography," 1968.
- [83] J. C. Bamber, C. R. Hill, J. A. King, and F. Dunn, "Ultrasonic propagation through fixed and unfixed tissues," *Ultrasound Med. Biol.*, vol. 5, no. 2, pp. 159–165, 1979, doi: 10.1016/0301-5629(79)90084-X.

- [84] IEC, “IEC (International Electrotechnical Commission) Standard,” 1992.
- [85] W. Schiefer, E. Kazner, and K. Zülch, “Proceedings in Echo-Encephalography: International Symposium on Echo-Encephalography,” 1968.
- [86] D. Nicholas, C. R. Hill, and D. K. Nassiri, “Evaluation of backscattering coefficients for excised human tissues: Principles and techniques,” *Ultrasound Med. Biol.*, vol. 8, no. 1, pp. 7–15, 1982, doi: 10.1016/0301-5629(82)90064-3.
- [87] A. Cristea, “ULTRASOUND TISSUE CHARACTERIZATION ULTRASOUND TISSUE CHARACTERIZATION USING SPECKLE STATISTICS Délivrée par,” 2016.
- [88] S. C. Kak, “The Discrete Hilbert Transform,” *Proc. IEEE*, vol. 58, no. 4, pp. 585–586, 1970, doi: 10.1109/PROC.1970.7696.
- [89] A. V. Moiyadi, “Intraoperative Ultrasound Technology in Neuro-Oncology Practice—Current Role and Future Applications,” *WORLD Neurosurg.*, vol. 93, no. 93, pp. 81–93, 2016.
- [90] T. Selbekk, A. S. Jakola, O. Solheim, T. F. Johansen, and F. Lindseth, “Ultrasound imaging in neurosurgery: Approaches to minimize surgically induced image artefacts for improved resection control,” *Acta Neurochir. (Wien)*, vol. 155, no. 6, pp. 973–980, 2013, doi: 10.1007/s00701-013-1647-7.
- [91] J. Coburger, R. W. König, A. Scheuerle, J. Engelke, M. Hlavac, *et al.*, “Navigated high frequency ultrasound: Description of technique and clinical comparison with conventional intracranial ultrasound,” *World Neurosurg.*, vol. 82, no. 3, pp. 366–375, 2014, doi: 10.1016/j.wneu.2014.05.025.
- [92] F. Prada and L. Solbiati, “Ultrasound System Setup and General Semeiology,” in *Intraoperative Ultrasound in Neurosurgery*, p. 23.
- [93] O. Solheim, T. Selbekk, L. Løvstakken, G. A. Tangen, O. V. Solberg, *et al.*, “Intrasellar ultrasound in transsphenoidal surgery: A novel technique,” *Neurosurgery*, vol. 66, no. 1, pp. 173–185, 2010, doi: 10.1227/01.NEU.0000360571.11582.4F.
- [94] A. Boonruang, T. Thongchai, T. Button, and S. Cochran, “Microfabrication of 1-3 Composites with Photolithographically Defined Electrode Patterns for Kerfless Microultrasound Arrays,” *IEEE Int. Ultrason. Symp. IUS*, vol. 2019-Octob, pp.

1746–1749, 2019, doi: 10.1109/ULTSYM.2019.8925545.

- [95] L. Guasch, O. Calderón Agudo, M. X. Tang, P. Nachev, and M. Warner, “Full-waveform inversion imaging of the human brain,” *npj Digit. Med.*, vol. 3, no. 1, pp. 1–12, 2020, doi: 10.1038/s41746-020-0240-8.
- [96] D. Vordermark, G. Becker, M. Flentje, S. Richter, I. Goerttler-Krauspe, *et al.*, “Transcranial sonography: Integration into target volume definition for glioblastoma multiforme,” *Int. J. Radiat. Oncol. Biol. Phys.*, vol. 47, no. 3, pp. 565–571, 2000, doi: 10.1016/S0360-3016(00)00565-4.
- [97] G. Unsgaard, O. M. Rygh, T. Selbekk, T. B. Müller, F. Kolstad, *et al.*, “Intra-operative 3D ultrasound in neurosurgery,” *Acta Neurochir. (Wien)*, vol. 148, no. 3, pp. 235–253, 2006, doi: 10.1007/s00701-005-0688-y.
- [98] A. Gronningsaeter, A. Kleven, S. Ommedal, T. E. Aarseth, T. Lie, *et al.*, “SonoWand, an ultrasound-based neuronavigation system,” *Neurosurgery*, vol. 47, no. 6, pp. 1373–1380, 2000, doi: 10.1097/00006123-200012000-00021.
- [99] G. Unsgaard, T. Selbekk, T. Brostrup Müller, S. Ommedal, S. H. Torp, *et al.*, “Ability of navigated 3D ultrasound to delineate gliomas and metastases - Comparison of image interpretations with histopathology,” *Acta Neurochir. (Wien)*, vol. 147, no. 12, pp. 1259–1269, 2005, doi: 10.1007/s00701-005-0624-1.
- [100] O. M. Rygh, T. Selbekk, S. H. Torp, S. Lydersen, T. A. N. Hernes, *et al.*, “Comparison of navigated 3D ultrasound findings with histopathology in subsequent phases of glioblastoma resection,” *Acta Neurochir. (Wien)*, vol. 150, no. 10, pp. 1033–1041, 2008, doi: 10.1007/s00701-008-0017-3.
- [101] A. Von Herbay, J. Westendorff, and M. Gregor, “Contrast-enhanced ultrasound with SonoVue: Differentiation between benign and malignant focal liver lesions in 317 patients,” *J. Clin. Ultrasound*, vol. 38, no. 1, pp. 1–9, 2010, doi: 10.1002/jcu.20626.
- [102] F. Prada, A. Perin, A. Martegani, L. Aiani, L. Solbiati, *et al.*, “Intraoperative contrast-enhanced ultrasound for brain tumor surgery,” *Neurosurgery*, vol. 74, no. 5, pp. 542–552, 2014, doi: 10.1227/NEU.0000000000000301.
- [103] F. Prada, M. Del Bene, R. Fornaro, I. G. Vetrano, A. Martegani, *et al.*, “Identification of residual tumor with intraoperative contrast-enhanced ultrasound during glioblastoma resection,” *Neurosurg. Focus*, vol. 40, no. 3, p. E7, 2016, doi: 10.3171/2015.11.FOCUS15573.

- [104] D. C. Stewart, A. Rubiano, K. Dyson, and C. S. Simmons, “Mechanical characterization of human brain tumors from patients and comparison to potential surgical phantoms,” *PLoS One*, vol. 12, no. 6, pp. 1–19, 2017, doi: 10.1371/journal.pone.0177561.
- [105] P. Lu, V. M. Weaver, and Z. Werb, “The extracellular matrix: A dynamic niche in cancer progression,” *J. Cell Biol.*, vol. 196, no. 4, pp. 395–406, 2012, doi: 10.1083/jcb.201102147.
- [106] A. Nowicki and K. Dobruch-Sobczak, “Wprowadzenie do ultradźwiękowej elastografii,” *J. Ultrason.*, vol. 16, no. 65, pp. 113–124, 2016, doi: 10.15557/JoU.2016.0013.
- [107] T. Selbekk, R. Brekken, M. Indergaard, O. Solheim, and G. Unsgård, “Comparison of contrast in brightness mode and strain ultrasonography of glial brain tumours,” *BMC Med. Imaging*, vol. 12, no. 1, p. 11, 2012, doi: 10.1186/1471-2342-12-11.
- [108] C. E. Uff, L. Garcia, J. Fromageau, N. Dorward, and J. C. Bamber, “Real-time ultrasound elastography in neurosurgery,” *IEEE Int. Ultrasound Symp. Proc.*, pp. 467–470, 2009, doi: 10.1109/ULTSYM.2009.5441629.
- [109] C. Uff, L. Garcia, J. Fromageau, A. Chakraborty, N. Dorward, *et al.*, “Further characterization of changes in axial strain elastograms due to the presence of slippery tumor boundaries,” *J. Med. Imaging*, vol. 5, no. 02, p. 1, 2018, doi: 10.1117/1.JMI.5.2.021211.
- [110] T. Selbekk, J. Bang, and G. Unsgaard, “Strain processing of intraoperative ultrasound images of brain tumours: Initial results,” *Ultrasound Med. Biol.*, vol. 31, no. 1, pp. 45–51, 2005, doi: 10.1016/j.ultrasmedbio.2004.09.011.
- [111] K. J. Parker and N. York, “Shear Wave Imaging and Tissue Characterization Using Vibration Elastographic Techniques by of the Doctor of Philosophy Supervised by University of Rochester,” 2016.
- [112] T. Deffieux, J.-L. Gennisson, B. Larrat, M. Fink, and M. Tanter, “The variance of quantitative estimates in shear wave imaging: Theory and experiments.,” *IEEE Trans. Ultrason. Ferroelectr. Freq. Control*, vol. 59, no. 11, pp. 2390–410, 2012, doi: 10.1109/TUFFC.2012.2472.
- [113] M. Imbault, C. Demene, M. Mossad, J. Gennisson, M. Tanter, *et al.*, “Intraoperative quantitative measurement of brain tumor stiffness and intracranial pressure

- assessment using ultrasound shear wave elastography,” *2014 IEEE Int. Ultrason. Symp.*, pp. 201–204, 2014, doi: 10.1109/ULTSYM.2014.0051.
- [114] E. Mace, I. Cohen, G. Montaldo, R. Miles, M. Fink, *et al.*, “In Vivo Mapping of Brain Elasticity in Small Animals Using Shear Wave Imaging,” *IEEE Trans. Med. Imaging*, vol. 30, no. 3, pp. 550–558, 2011, doi: 10.1109/tmi.2010.2079940.
- [115] H. W. Chan, “Optimising the Use and Assessing the Value of Intraoperative Shear Wave Elastography in Neurosurgery,” no. September, 2016.
- [116] H. W. Chan, R. Pressler, C. Uff, R. Gunny, K. St Piers, *et al.*, “A novel technique of detecting MRI-negative lesion in focal symptomatic epilepsy: Intraoperative ShearWave Elastography,” *Epilepsia*, vol. 55, no. 4, pp. 30–33, 2014, doi: 10.1111/epi.12562.
- [117] Siemens, “ACUSON Juniper Ultrasound System.” <https://www.siemens-healthineers.com/en-uk/ultrasound/new-era-ultrasound/acuson-juniper>
- [118] B. J. Anderies, M. G. Sattur, M. E. Welz, L. K. Urday, K. R. Richter, *et al.*, “Photoacoustic Imaging for Maximizing Glioma Resection,” *World Neurosurg.*, vol. 107, pp. 906–907, 2017, doi: 10.1016/j.wneu.2017.09.044.
- [119] S. Dahal and B. M. Cullum, “Characterization of multiphoton photoacoustic spectroscopy for subsurface brain tissue diagnosis and imaging,” *J. Biomed. Opt.*, vol. 21, no. 4, p. 047001, 2016, doi: 10.1117/1.JBO.21.4.047001.
- [120] B. R. Masters, P. T. C. So, and E. Gratton, “Multiphoton excitation fluorescence microscopy and spectroscopy of in vivo human skin,” *Biophys. J.*, vol. 72, no. 6, pp. 2405–2412, 1997, doi: 10.1016/S0006-3495(97)78886-6.
- [121] F. L. Lizzi, M. Astor, T. Liu, C. Deng, D. J. Coleman, *et al.*, “Ultrasonic spectrum analysis for tissue assays and therapy evaluation,” *Int. J. Imaging Syst. Technol.*, vol. 8, no. 1, pp. 3–10, 1997, doi: 10.1002/(SICI)1098-1098(1997)8:1<3::AID-IMA2>3.0.CO;2-E.
- [122] M. F. Insana, R. F. Wagner, and D. G. Brown, “Describing small-scale structure in random media using pulse-echo ultrasound,” pp. 179–192, 1990.
- [123] M. L. Oelze and J. Mamou, “Review of Quantitative Ultrasound: Envelope Statistics and Backscatter Coefficient Imaging and Contributions to Diagnostic Ultrasound,” *IEEE Trans. Ultrason. Ferroelectr. Freq. Control*, vol. 63, no. 2, pp. 336–351,

2016, doi: 10.1109/TUFFC.2015.2513958.

- [124] J. Mamou and M. L. Oelze, *Quantitative Ultrasound in Soft Tissues*, 1st ed. Springer, 2013.
- [125] F. Destrempes, J. Porée, and G. Cloutier, “Estimation method of the homodyned K-distribution based on the mean intensity and two log-moments,” *SIAM J. Imaging Sci.*, vol. 6, no. 3, pp. 1499–1530, 2013, doi: 10.1137/120875727.
- [126] S. O. Rice, “Mathematical analysis of random noise.,” *Bell Syst. Tech. J.*, vol. 24, pp. 46–156, 1945.
- [127] P. M. Shankar, J. M. Reid, H. Ortega, C. W. Piccoli, and B. B. Goldberg, “Use of Non-Rayleigh Statistics for the Identification of Tumors in Ultrasonic B-Scans of the Breast,” *IEEE Trans. Med. Imaging*, vol. 12, no. 4, pp. 687–692, 1993, doi: 10.1109/42.251119.
- [128] Nakagami M., “Study of the resultant amplitude of many vibrations whose phases and amplitudes are at random. ;,” *J Inst Elec Commun Engrs Japan*, vol. 24(202):17, 1940.
- [129] P. H. Tsui, C. K. Yeh, C. C. Chang, and Y. Y. Liao, “Classification of breast masses by ultrasonic Nakagami imaging: A feasibility study,” *Phys. Med. Biol.*, vol. 53, no. 21, pp. 6027–6044, 2008, doi: 10.1088/0031-9155/53/21/009.
- [130] Z. Zhou, J. Fang, A. Cristea, Y. H. Lin, Y. W. Tsai, *et al.*, “Value of homodyned K distribution in ultrasound parametric imaging of hepatic steatosis: An animal study,” *Ultrasonics*, vol. 101, no. January 2019, p. 106001, 2020, doi: 10.1016/j.ultras.2019.106001.
- [131] M. H. Roy-Cardinal, F. Destrempes, G. Soulez, and G. Cloutier, “Assessment of Carotid Artery Plaque Components with Machine Learning Classification Using Homodyned-K Parametric Maps and Elastograms,” *IEEE Trans. Ultrason. Ferroelectr. Freq. Control*, vol. 66, no. 3, pp. 493–504, 2019, doi: 10.1109/TUFFC.2018.2851846.
- [132] M. L. Oelze, “Quantitative ultrasound techniques and improvements to diagnostic ultrasonic imaging,” *IEEE Int. Ultrason. Symp. IUS*, pp. 232–239, 2012, doi: 10.1109/ULTSYM.2012.0058.
- [133] M. A. S. Trowitzki, S. E. B. Rand, and K. L. I. J. Enderka, “ULTRASONIC

RADIO-FREQUENCY SPECTRUM ANALYSIS OF NORMAL BRAIN TISSUE,” vol. 33, no. 4, pp. 522–529, 2007, doi: 10.1016/j.ultrasmedbio.2006.09.004.

- [134] I. M. Rosado-Mendez, K. K. Noguchi, L. Castañeda-Martinez, G. Kirvassilis, S. H. Wang, *et al.*, “Quantitative ultrasound and apoptotic death in the neonatal primate brain,” *Neurobiol. Dis.*, vol. 127, no. April, pp. 554–562, 2019, doi: 10.1016/j.nbd.2019.03.032.
- [135] R. M. Vlad, S. Brand, A. Giles, M. C. Kolios, and G. J. Czarnota, “Quantitative ultrasound characterization of responses to radiotherapy in cancer mouse models,” *Clin. Cancer Res.*, vol. 15, no. 6, pp. 2067–2075, 2009, doi: 10.1158/1078-0432.CCR-08-1970.
- [136] A. I. L. Namburete, B. Rahmatullah, and J. A. Noble, “Nakagami-Based AdaBoost Learning Framework for Detection of Anatomical Landmarks in 2D Fetal Neurosonograms,” vol. 2013, no. 2, pp. 1–16, 2013, [Online]. Available: <http://citeseerx.ist.psu.edu/viewdoc/download?doi=10.1.1.412.8941&rep=rep1&type=pdf>
- [137] R. O. J. L. Avarello, W. I. R. R. Idgway, S. A. S. S. Arwate, and M. I. L. O. Elze, “Characterization of Thyroid Cancer in Mouse Models Using High-Frequency Quantitative Ultrasound Techniques,” vol. 39, no. 12, pp. 2333–2341, 2013, doi: 10.1016/j.ultrasmedbio.2013.07.006.
- [138] B. Kumar, K. Verma, L. Panigrahi, and A. S. Thoke, “Integrating radiologist feedback with computer aided diagnostic systems for breast cancer risk prediction in ultrasonic images : An experimental investigation in machine learning paradigm,” *Expert Syst. Appl.*, vol. 90, pp. 209–223, 2017, doi: 10.1016/j.eswa.2017.08.020.
- [139] R. Kumari and S. Kr., “Machine Learning: A Review on Binary Classification,” *Int. J. Comput. Appl.*, vol. 160, no. 7, pp. 11–15, 2017, doi: 10.5120/ijca2017913083.
- [140] C. Marzban, “The ROC curve and the area under it as performance measures,” *Weather Forecast.*, vol. 19, no. 6, pp. 1106–1114, 2004, doi: 10.1175/825.1.
- [141] VisualSonics, “M Series Transducers,” 2023. <https://www.visualsonics.com/product/transducers/custom-designed-linear-array-transducers-vevo-2100>
- [142] R. F. Wagner, D. G. Brown, and T. J. Hall, “Describing small-scale structure in

- random media using pulse-echo [1] R. F. Wagner, D. G. Brown, and T. J. Hall, ‘Describing small-scale structure in random media using pulse-echo ultrasound,’ *J. Acoust. Soc. Am.*, vol. 87, no. 1, pp. 179–192, 1990, doi: 10.1121/1.399283.
- [143] M. L. Oelze and W. D. O’Brien, “Frequency-dependent attenuation-compensation functions for ultrasonic signals backscattered from random media,” *J. Acoust. Soc. Am.*, vol. 111, no. 5, p. 2308, 2002, doi: 10.1121/1.1452743.
- [144] T. A. Bigelow and Y. Labyed, “Attenuation Compensation and Estimation,” in *Quantitative Ultrasound in Soft Tissues*, 2013, pp. 71–93. doi: 10.1007/978-94-007-6952-6.
- [145] M. F. Insana, R. F. Wagner, B. S. Garra, D. G. Brown, and T. H. Shawker, “Analysis Of Ultrasound Image Texture Via Generalized Rician Statistics,” *Intl Conf Speckle*, vol. 0556, no. 6, p. 153, 1986, doi: 10.1117/12.949535.
- [146] P. Mohana Shankar, “A general statistical model for ultrasonic backscattering from tissues,” *IEEE Trans. Ultrason. Ferroelectr. Freq. Control*, vol. 47, no. 3, pp. 727–736, 2000, doi: 10.1109/58.842062.
- [147] R. W. Prager, A. H. Gee, G. M. Treece, and L. Berman, “Speckle Detection in Ultrasound Images Using First Order Statistics,” *CUED/F-INFENG/TR 415*, no. July, p. 11, 2001.
- [148] D. P. Hruska and M. L. Oelze, “Improved parameter estimates based on the homodyned K distribution,” *IEEE Trans. Ultrason. Ferroelectr. Freq. Control*, vol. 56, no. 11, pp. 2471–2481, 2009, doi: 10.1109/TUFFC.2009.1334.
- [149] M. R. Murty and A. Zaytseva, “Transcendence of generalized euler constants,” *Am. Math. Mon.*, vol. 120, no. 1, pp. 48–54, 2013, doi: 10.4169/amer.math.monthly.120.01.048.
- [150] G. Arfken, “Digamma and Polygamma Functions,” in *Mathematical Methods for Physicists*, 6th ed. Academic Press, 2005, pp. 549–555.
- [151] W. . Bailey, “Generalized Hypergeometric Series,” *Cambridge Univ. Press*, no. 32, 1964.
- [152] Wikipedia, “Standardised Moments,” 2022. https://en.wikipedia.org/wiki/Standardized_moment

- [153] K. Binmore, *The Foundations of Topological Analysis: A Straightforward Introduction: Book 2 Topological Ideas*. 1980.
- [154] A. Saini, “Support Vector Machine(SVM): A Complete guide for beginners,” 2021. <https://www.analyticsvidhya.com/blog/2021/10/support-vector-machinessvm-a-complete-guide-for-beginners/>
- [155] T. Evgeniou and M. Pontil, “Support vector machines: Theory and applications,” *Lect. Notes Comput. Sci. (including Subser. Lect. Notes Artif. Intell. Lect. Notes Bioinformatics)*, vol. 2049 LNAI, no. January 2001, pp. 249–257, 2001, doi: 10.1007/3-540-44673-7_12.
- [156] “Introduction to Kernel Methods in Machine Learning,” 2021. <https://www.section.io/engineering-education/introduction-to-kernel-methods-in-machine-learning/>
- [157] M. Deisenroth, A. Aldo Faisal, and C. Soon Ong, “Classification with Support Vector Machines,” in *Mathematics for Machine Learning*, Cambridge University Press, 2020, pp. 335–356.
- [158] Y. Sasaki, “The truth of the F-measure,” *Teach Tutor mater*, pp. 1–5, 2007, [Online]. Available: <http://www.cs.odu.edu/~mukka/cs795sum09dm/Lecturenotes/Day3/F-measure-YS-26Oct07.pdf>
- [159] C. M. Troy and G. S. Salvesen, “Caspases on the brain,” *J. Neurosci. Res.*, vol. 69, no. 2, pp. 145–150, 2002, doi: 10.1002/jnr.10294.
- [160] A. F. Carlos, T. E. Poloni, V. Medici, M. Chikhladze, A. Guaita, *et al.*, “From brain collections to modern brain banks: A historical perspective,” *Alzheimer’s Dement. Transl. Res. Clin. Interv.*, vol. 5, pp. 52–60, 2019, doi: 10.1016/j.trci.2018.12.002.
- [161] G. Cortela, N. Benech, W. C. A. Pereira, and C. Negreira, “Characterization of acoustical properties of a phantom for soft tissues (PVCP and Graphite Powder) in the range 20-45°C,” *Phys. Procedia*, vol. 70, pp. 179–182, 2015, doi: 10.1016/j.phpro.2015.08.107.
- [162] J. Joy, “Models for Testing Contemporary Ultrasound Systems,” no. January, p. 190, 2015.
- [163] CIRS, “Multipurpose Soft Tissue Phantom.”

- [164] B. Phantom, “Blue Phantom Ultrasound Training Model.”
- [165] Delta Neurosurgical, “Rowena Ultra, complete head for Ultrasound Machine,” 2016. <https://neurosurgical-training-simulator.com/rowena-individual-parts/>
- [166] “E-mail communication with Jon, Delta Neurosurgical.”
- [167] Stryker Neurosurgical, “Sonopet Ultrasonic Aspirator.” <https://neurosurgical.stryker.com/products/sonopet-ultrasonic-aspirator/>
- [168] S. Rajagopal, N. Sadhoo, and B. Zeqiri, “Reference Characterisation of Sound Speed and Attenuation of the IEC Agar-Based Tissue-Mimicking Material Up to a Frequency of 60MHz,” *Ultrasound Med. Biol.*, vol. 41, no. 1, pp. 317–333, 2015, doi: 10.1016/j.ultrasmedbio.2014.04.018.
- [169] A. Hurrell, “Voltage to pressure conversion: are you getting ‘phased’ by the problem?,” *J. Phys. Conf. Ser.*, vol. 1, pp. 57–62, 2004, doi: 10.1088/1742-6596/1/1/014.
- [170] J. Krautkrämer and H. Krautkrämer, *Ultrasonic Testing*. Springer-Verlag, 1990.
- [171] M. F. Insana, T. J. Hall, L. T. Cook, and A. F. Patterns, “Backscatter Coefficient Estimation Using Array Transducers,” vol. 41, no. 5, 1994.
- [172] T. Oguri, K. Tamura, K. Yoshida, J. Mamou, H. Hasegawa, *et al.*, “Estimation of scatterer size and acoustic concentration in sound field produced by linear phased array transducer,” *Jpn. J. Appl. Phys.*, vol. 54, no. 7, 2015, doi: 10.7567/JJAP.54.07HF14.
- [173] K. A. Topp, J. F. Zachary, and J. O’Brien, “Quantifying B-mode images of in vivo rat mammary tumors by the frequency dependence of backscatter,” *J. Ultrasound Med.*, vol. 20, no. 6, pp. 605–612, 2001, doi: 10.7863/jum.2001.20.6.605.
- [174] “Edinburgh Brain bank.” <https://www.ed.ac.uk/clinical-brain-sciences/research/edinburgh-brain-and-tissue-bank>
- [175] Editors of Encyclopaedia Britannica, “Osmosis,” *Encyclopaedia Britannica*, 2019. <https://www.britannica.com/science/osmosis>
- [176] J. L. Raymond, K. J. Haworth, K. B. Bader, K. Radhakrishnan, J. K. Griffin, *et al.*, “Broadband attenuation measurements of phospholipid-shelled ultrasound contrast agents,” *Ultrasound Med. Biol.*, vol. 40, no. 2, pp. 410–421, 2014, doi:

10.1016/j.ultrasmedbio.2013.09.018.

- [177] C. Allison, “OnScale Introduction: The Basics,” 2019.
<https://support.onscale.com/hc/en-us/articles/360015653612-The-Basics>
- [178] M. Fadhel, “Ultra-High Frequency Acoustic Impedance Imaging of Cancer Cells,” pp. 1912–1915, 2014.
- [179] Y. Saijo, “Recent Applications of Acoustic Microscopy for Quantitative Measurement of Acoustic Properties of Soft Tissues,” in *Quantitative Ultrasound in Soft Tissues*, M. L. Oelze and J. Mamou, Eds., Springer, 2013, pp. 291–313.
- [180] T. T. K. Soon, T. W. Chean, H. Yamada, K. Takahashi, N. Hozumi, *et al.*, “Effects of anticancer drugs on glia-glioma brain tumor model characterized by acoustic impedance microscopy,” *Jpn. J. Appl. Phys.*, vol. 56, no. 7, 2017, doi: 10.7567/JJAP.56.07JF15.
- [181] Lecia Biosystems, “H&E Staining Overview: A Guide to Best Practices.”
<https://www.leicabiosystems.com/en-gb/knowledge-pathway/he-staining-overview-a-guide-to-best-practices/>
- [182] M. G. Ertosun and D. L. Rubin, “Automated Grading of Gliomas using Deep Learning in Digital Pathology Images: A modular approach with ensemble of convolutional neural networks,” *AMIA ... Annu. Symp. proceedings. AMIA Symp.*, vol. 2015, pp. 1899–1908, 2015.
- [183] Y. Jiao, H. Berman, T. Kiehl, and S. Torquato, “Spatial Organization and Correlations of Cell Nuclei in Brain Tumors,” vol. 6, no. 11, 2011, doi: 10.1371/journal.pone.0027323.
- [184] National Cancer Institute, “Genomic Data Commons Data Portal.”
- [185] A. Goode, B. Gilbert, and J. Harkes, “OpenSlide: A vendor-neutral software foundation for digital pathology,” 2013. doi: 10.4103/2153-3539.119005.
- [186] E. Franceschini, R. De Monchy, and J. Mamou, “Quantitative Characterization of Tissue Microstructure in Concentrated Cell Pellet Biophantoms Based on the Structure Factor Model,” *IEEE Trans. Ultrason. Ferroelectr. Freq. Control*, vol. 63, no. 9, pp. 1321–1334, 2016, doi: 10.1109/TUFFC.2016.2549273.
- [187] E. Franceschini, R. Guillermin, F. Tourniaire, S. Roffino, E. Lamy, *et al.*, “Structure factor model for understanding the measured backscatter coefficients from

- concentrated cell pellet biophantoms,” *J. Acoust. Soc. Am.*, vol. 135, no. 6, pp. 3620–3631, 2014, doi: 10.1121/1.4876375.
- [188] J. M. Mamou, “Ultrasonic Characterization of three animal mammary tumors from 3D acoustic tissue models,” 2005.
- [189] R. Waag and S. Member, “Comparison of Techniques for In Vivo Attenuation Measurements,” vol. 35, no. 12, pp. 1064–1068, 1988.
- [190] K. Nam, J. A. Zagzebski, and T. J. Hall, “Simultaneous backscatter and attenuation estimation using a least squares method with constraints,” *Ultrasound Med. Biol.*, vol. 37, no. 12, pp. 2096–2104, 2011, doi: 10.1016/j.ultrasmedbio.2011.08.008.
- [191] C. N. Steffel, S. Salamat, T. D. Cook, S. M. Wilbrand, R. J. Dempsey, *et al.*, “Attenuation Coefficient Parameter Computations for Tissue Composition Assessment of Carotid Atherosclerotic Plaque in Vivo,” *Ultrasound Med. Biol.*, vol. 46, no. 6, pp. 1513–1532, 2020, doi: 10.1016/j.ultrasmedbio.2020.02.015.
- [192] P. D. Wilcox, J. Zhang, and B. W. Drinkwater, “Defect characterization using ultrasonic arrays,” *Heal. Monit. Struct. Biol. Syst. 2008*, vol. 6935, no. April 2008, p. 69350X, 2008, doi: 10.1117/12.776235.
- [193] G. ter Haar, “The new British Medical Ultrasound Society guidelines for the safe use of diagnostic ultrasound equipment,” *Ultrasound*, vol. 18, no. 2, pp. 50–51, 2010, doi: 10.1258/ult.2010.100007.
- [194] K. Nam, J. A. Zagzebski, and T. J. Hall, “Simultaneous backscatter and attenuation estimation using a least squares method with constraints,” *Ultrasound Med. Biol.*, vol. 37, no. 12, pp. 2096–2104, 2011, doi: 10.1016/j.ultrasmedbio.2011.08.008.
- [195] T. J. Hall, M. F. Insana, L. A. Harrison, and G. G. Cox, “Ultrasonic measurement of glomerular diameters in normal adult humans,” *Ultrasound Med. Biol.*, vol. 22, no. 8, pp. 987–997, 1996, doi: 10.1016/S0301-5629(96)00142-1.
- [196] I. M. Rosado-Mendez, “Private Correspondence.” Mexico, 2019.
- [197] S. Learn, “Ensemble Methods.” <https://scikit-learn.org/stable/modules/ensemble.html> (accessed May 16, 2023).
- [198] T. Nguyen and M. Oelze, “Reference free quantitative ultrasound classification of fatty liver,” *IEEE Int. Ultrason. Symp. IUS*, vol. 2019-Octob, pp. 2424–2427, 2019, doi: 10.1109/ULTSYM.2019.8925666.

- [199] M. Afridi, A. Jain, M. Aboian, and S. Payabvash, “Brain Tumor Imaging : Applications of Artificial Intelligence,” *Semin. Ultrasound, CT, MRI*, vol. 43, no. 2, pp. 153–169, 2022, doi: 10.1053/j.sult.2022.02.005.
- [200] D. P. Hruska, J. Sanchez, and M. L. Oelze, “Improved diagnostics through quantitative ultrasound imaging,” *Proc. 31st Annu. Int. Conf. IEEE Eng. Med. Biol. Soc. Eng. Futur. Biomed. EMBC 2009*, pp. 1956–1959, 2009, doi: 10.1109/IEMBS.2009.5333465.
- [201] E. J. Feleppa, J. Mamou, C. R. Porter, and J. MacHi, “Quantitative ultrasound in cancer imaging,” *Semin. Oncol.*, vol. 38, no. 1, pp. 136–150, 2011, doi: 10.1053/j.seminoncol.2010.11.006.

APPENDIX I: *In situ* and 3D *ex vivo* Imaging of Porcine Brain over Frequency Range 14-30 MHz.

Aim: To test the ability of current state of the art ultrasound imaging systems to image the neuroanatomy of a porcine brain using two probes operating at centre frequencies of 14 MHz and 30 MHz respectively. This was carried out both *in situ* and *ex vivo* using a SonixTouch Q+ (BK Medical, 2015) clinical ultrasound machine.

Methodology: During an *in vivo* pig trial for the Sonopill program at Dryden Farm, University of Edinburgh, there was an opportunity to image one porcine brain *in situ*, and harvest two brains for *ex vivo* imaging. Directly after euthanasia, the skull was removed by the mortician to reveal the brain as shown in Fig. 1.

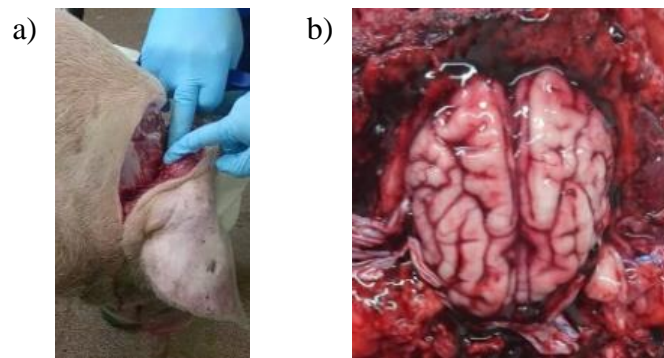


Fig. 1 (a) Base of skull before removal
(b) Exposed brain tissue after dura removal.

Ultrasound scans were performed by using both the linear 5 - 14 MHz and linear 15 - 40 MHz probes. Sagittal and coronal scans were captured in static images and video. Several landmarks were identified such as the cerebellum, ventricles, central sulcus, blood vessels and *corpus callosum*. All image and video data was saved onto the BK machine and could be transferred to a PC. After scanning the brain was removed from the cranial cavity by the mortician. The tissue specimen was washed and placed in a sealable container which was then filled with a solution of 2% formaldehyde diluted with PBS solution. The container was then placed in a fridge while the second pig trial took place.

The same procedure was carried out on Pig 2, and both brains were triple packaged and labelled 'EXEMPT ANIMAL SPECIMEN' along with suitable warnings regarding the formaldehyde. They were transported to the University of Glasgow in a journey that took approximately 80 mins. The following day, one brain was removed from the formaldehyde solution and placed in PBS. The structure of the brain had been maintained and the tissue did not feel artificially hard but had a stiffer texture than fresh tissue.

The footprint of the transducer was smaller than the width of the brain, so to obtain a full volume acquisition, the probe was clamped to a 2-axis motor and scanned over the entire tissue volume (Fig. 2). This was beneficial as it allowed a steady acquisition at the same distance to the brain tissue. For the strain elastography acquisition, the brain was incased in agar and the motor lowered the transducer to provide a pressure on to the agar to allow strain imaging to occur.

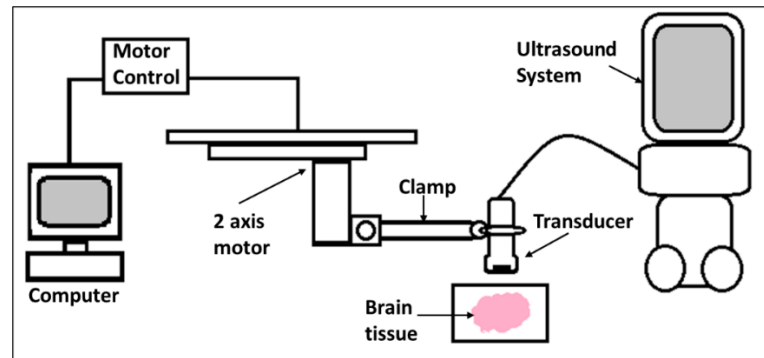
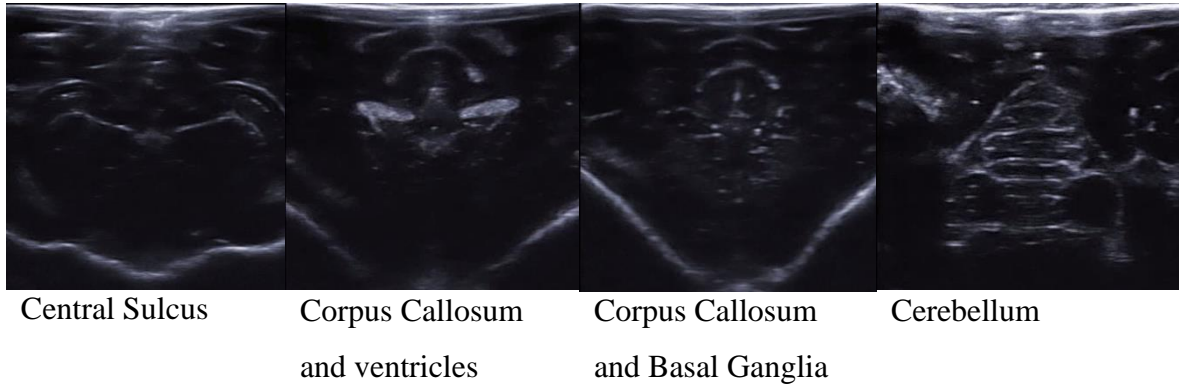


Figure 2: Motorised scanning of porcine brain with commercial ultrasound system.

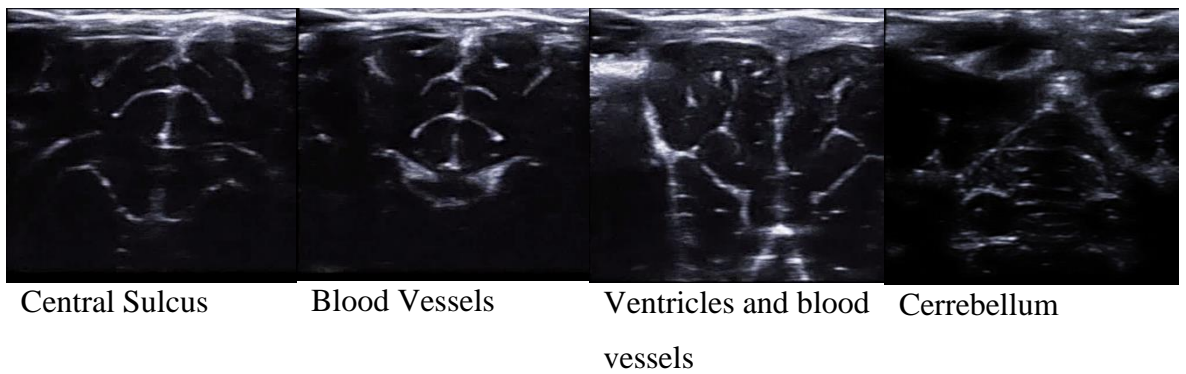
Videos of the scans from the SonixTouchQ+ were processed in MATLAB (The MathWorks, 2017b) to extract each frame and concatenate parallel scans. ImageJ was used to create an interactive 3D volume, which were then processed to be shown in the coronal, sagittal and axial planes.

Results: Images shown below were taken using the 14 MHz probe *in situ*, the image depth is 5 cm for all images. Clear structures can be seen from main blood vessels in the centre of the brain. The cerebellum, which is the structure located toward the spinal cord, can also be seen in final image in the coronal scans in Fig. 3a. In the sagittal scans, the folds of the cerebral hemisphere can be seen. The dynamic range is only 40 dB, which may have been too low to pick up any scattering in brain parenchyma.

Brain 1 Coronal *in situ* scans. Images taken from a video moving from the eyes to the back of the skull



Brain 2 Coronal *in situ* scans, again scanning from eyes to back



Brain 1 Sagittal *in situ* scans from left to right.

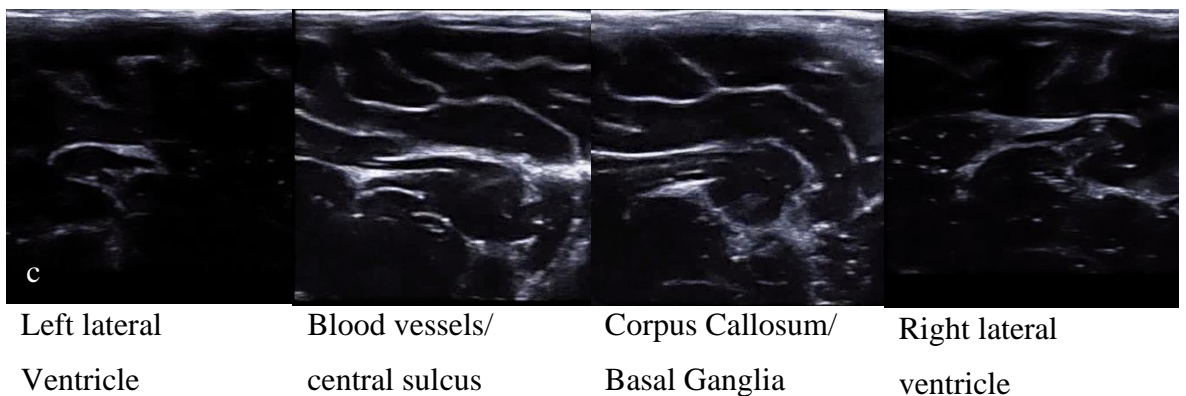


Figure 3: 14 MHz array scanning of porcine brain *in situ*. a-b are coronal views whereas c is achieved by rotating the probe 90°.

The results of the motorised scanning are shown in Fig. 4, which used a dynamic range of 70 dB.

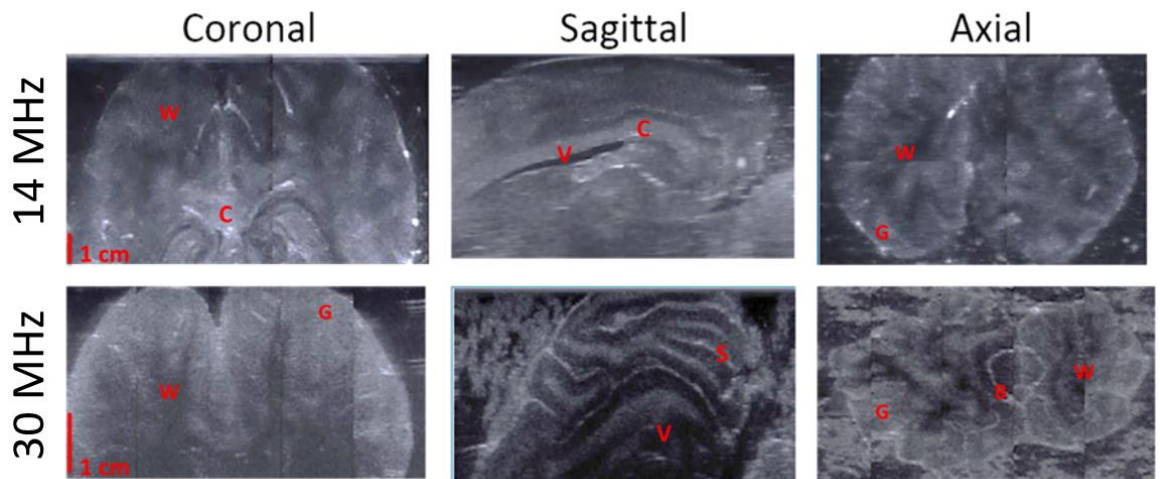


Figure 4: B-mode images using two transducers. Key for anatomical structures: Ventricles (V), Corpus Callosum (C), Blood vessels (B), Sulci (S), White Mater (W), Grey Mater (G)

The key difference between the scans at 14 MHz and 30 MHz, particularly in the coronal view is the delineation of white and grey matter only occurs at the higher frequency. The various gyri and sulci (folds in the cerebral hemisphere) are much more pronounced in the sagittal scans at HF. The ventricle is shown clearly at 14 MHz, but the HF scan shown did not occur deep enough into the brain to show these. Ultimately, it is clear there is increased resolution, yet comparable scattering observed with the two probes.

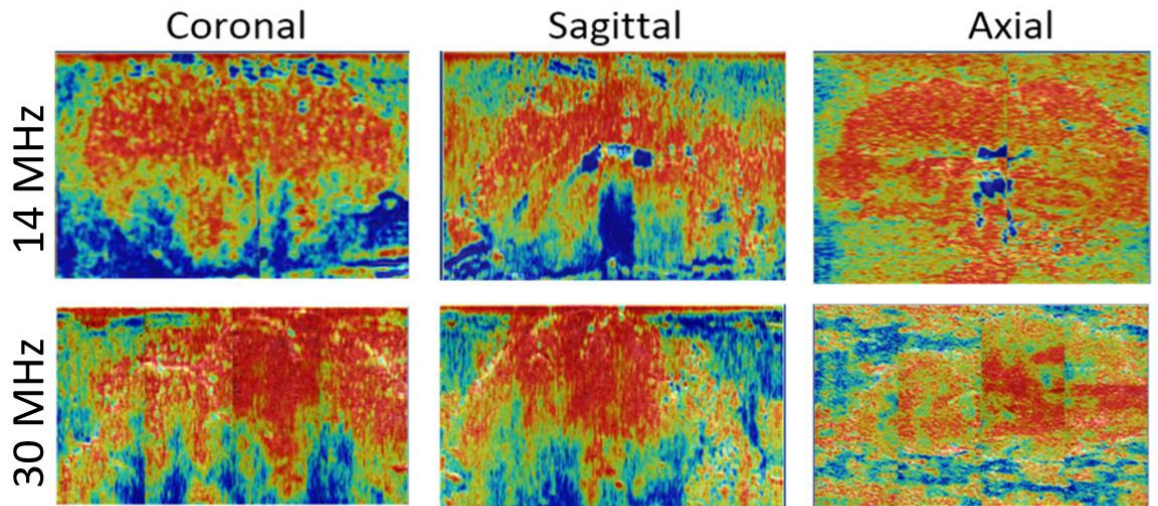


Figure 5: Elastography images of porcine brain. Red indicates regions of higher stiffness, whereas blue shows regions of lower stiffness.

The elastography images show the brain is stiffer than the surrounding agar encasing it, however the resolution is significantly reduced, especially in the 30 MHz scans. The ventricle is observed as the blue region within the brain in the sagittal view using the 14

MHz. The resolution dropped considerably with depth, as the force may not have been enough to deform deeper structures in the brain due to its material properties.

Conclusions: The 30 MHz scans show superior resolution but cannot reach structures deeper than 3cm. It was sufficient to delineate white and grey matter, so could be of use in identifying healthy and cancerous regions *in vivo*. However, this scanning technique did not yield high quality elastography images as more compressional force is required.

APPENDIX II: Algorithms involved in computation of HK parameters from X and U statistic.

% Algorithm for calculating function gamma alpha X - Figure 4 Flow

```
function gam_out = gam_alphaX(alpha,X)
    gam_1 = 0;
    gam_2 = 1;
    T = 0.0001;

    while solve_X(alpha,gam_2) >= X
        gam_2 = gam_2 + 1;

    end

    while abs(gam_2-gam_1)>T
        gam = (gam_1+gam_2)/2;
        if solve_X(alpha,gam) <= X
            gam_2=gam;
        else
            gam_1= gam;
        end
    end
    gam_out(1) = gam_1;
end
```

% Algorithm for HK-distribution parameters - Figure 5 flow chart

```
function [a_out,g_out]= find_gam_alpha(X,U)
    a_1=0;
    a_0 = 1/(X-1);
    T=0.0001995;
    if X<= 1
        a_2 =1;
        gam = gam_alphaX(a_2,X);

        while solve_U(a_2,gam) >= U
            a_2= a_2 +1;
            gam=gam_alphaX(a_2,X);
        end

    else
        a_2= a_0;
    end

    while abs(a_2-a_1)>T
        a = (a_1+a_2)/2;
        gam = gam_alphaX(a,X);

        if U>=solve_U(a,gam)
            a_2=a;
        else
            a_1=a;
        end
    end
```

```

end
a_out = a;
g_out = gam;
end

%Algorithm for HK dist - flow 6
function [eps,sig,alpha] = find_parameters(X,U,I)
    a_max = 59.5;
    if X<=1
        a_star = a_max;
    else
        a_0 = 1/(X-1);
        a_star= min(a_0,a_max);
    end
    g_star =gam_alphaX(a_star,X);
    if U>= solve_U(a_star,g_star);
        [alpha_sol,gamma_sol] = find_gam_alpha(X,U);
    else
        gamma_sol = gam_alphaX(a_star,X);
        alpha_sol = a_star;
    end

    eps = I*gamma_sol/(gamma_sol+alpha_sol);
    sig = I/(2*(gamma_sol+alpha_sol));
    alpha = alpha_sol;

%Function to calculate X-Statistic for given alpha and gamma
values
function X_out =calc_X(alpha,gam)
    X_out = (1+2*alpha)/(gam+alpha) -
    2*gam^(alpha/2+1/2)*besselk(alpha+1,2*sqrt(gam))/((gam+alpha)
    *gamma(alpha)+(gam/(gam+alpha))*(hypergeom([1,1],[2,2,1-
    alpha],gam)-(pi/sin(pi*alpha))*gam^(alpha-1)
    *hypergeom(alpha,[1+alpha,1+alpha],gam)/(gamma(alpha)*gamma(1
    +alpha))+(pi/sin(pi*(alpha+1)))*gam^alpha*hypergeom(1+alpha,[
    2+alpha,2+alpha],gam)/(gamma(alpha)*gamma(2+alpha)*(1+alpha))
    -alpha/(alpha-1)*hypergeom([1,1],[2,2,2-alpha],gam));

end
%Function to calculate U-Statistic for given alpha and gamma
function U_out = calc_U(alpha,gam)
    U_out = -double(eulergamma) -
    log(gam+alpha)+psi(alpha)+pi*gam^alpha*hypergeom(alpha,[1+alp
    ha,1+alpha],gam)/(sin(pi*alpha)*alpha*gamma(alpha)*gamma(alph
    a+1))+gam*hypergeom([1,1],[2,2,2-alpha],gam)/(alpha-1);
end

```

APPENDIX III: Application form for Human Tissue samples.

Name of Research Study: *Quantitative Ultrasound Differentiates High Grade Glioma and Healthy Brain Tissue ex vivo*

Principal Investigator (PI) Contact Information

Name: Hannah Thomson	
Name of Organisation: University of Glasgow	
Division or Department: Centre for Medical and Industrial Ultrasonics, School of Engineering	
Contact email: h.thomson.3@research.gla.ac.uk	Contact telephone: xxxxx
Full Postal Address:	Hannah Thomson James Watt School of Engineering, James Watt South Building, Engineering Way, University Avenue, Glasgow, G12 8QQ

Contact Person (if different from PI named above)

Name: Sandy Cochran	
Name of Organisation: University of Glasgow	
Division or Department: Centre for Medical and Industrial Ultrasonics, School of Engineering	
Contact email: sandy.cochran@glasgow.ac.uk	Contact telephone:
Full Postal Address:	Sandy Cochran James Watt School of Engineering, James Watt South Building, Engineering Way, University Avenue, Glasgow, G12 8QQ

Name of Research Governance Sponsor *:

University of Glasgow

**This is usually the institution where the research is taking place (not BRAIN UK). It is to ensure compliance with and support from the sponsoring local institute and needs to be done before the study becomes active.*

Has the study received a favourable opinion from a UK Research Ethics Committee? Yes/No

If 'yes' please provide a copy of the approval letter from the Ethics Committee.

Has the study secured funding? Yes/No

If yes please provide the source and period of funding:

UK Engineering and Physical Sciences Research Council (EPSRC) National Productivity and Investment Fund studentship, with Stryker Medical Devices

1. Details of tissue and/or data requirements

Please summarise the cases you require and include all of the following information:

- Number of cases
- Diagnosis
- Data relating to the cases that you require
- If you have identified potential cases, please provide the details

Number of cases: Min 5, ideal 10:
Diagnosis: Glioblastoma Multiforme
Data: Age,sex, PM delay
Cases identified: None

Type of tissue required **Please highlight those that apply*

Post-mortem

Biopsy (from living patients)

Formalin Fixed Paraffin Embedded (FFPE)

Frozen

None (Data Only)

Other **Please specify*

2. Study Protocol

Please complete the sections below thoroughly and concisely. Omissions and incomplete sections will result in a delayed review process. If available, please also attach a copy of local or external peer review of the study. Please feel free to contact us for advice.

- **Study Title: Quantitative Ultrasound Differentiates High Grade Glioma and Healthy Brain Tissue *ex vivo***

- **Contacts And Co-Investigators (If Applicable)**

Both investigators are listed above.

- **Lay Summary**

When someone is having an operation on their brain to remove cancerous tissue, it can be difficult for the surgeon to know where the cancerous tissue ends and the healthy tissue begins. Ultrasound is a useful tool which can quickly provide images to help visualise different tissues in the body, including the brain. However, it is currently limited in resolution, so the images are not very clear at showing all the cancerous areas the surgeon should remove. When ultrasound is introduced into tissue, it scatters in all directions because of the very small cells that make up the tissue, just as light scatters in mist or fog. However, the ultrasound will scatter differently in cancerous areas because there are more cells grouped closer together in these regions. If these signals are carefully analysed in samples of healthy and cancerous brain tissue, that may allow us to pin down certain values, called quantitative ultrasound parameters, which will tell us more about the underlying organisation of the cells in the tissue. A notable difference in these values in tissue may then tell us if it is healthy or cancerous, allowing us to improve the normal ultrasound images. It may even be possible to train a computer program to advise the surgeon whether or not tissue is cancerous or healthy, allowing them to carry out more complete removal of brain tumours.

- **Abbreviations**

QUS **Quantitative Ultrasound**

MRI **Magnetic Resonance Imaging**

RF **Radio-frequency**

- **Background**

- Literature review

Brain shift causes errors when using high resolution preoperative MRI images during tumour removal surgery, so there is need for a real-time update [7]. Furthermore, as

tumour surgery proceeds, especially in glioma resection, the margins of tumour boundaries can become difficult to determine due to lack of acoustic contrast between the tumour and healthy tissue. There is evidence showing that the use of ultrasound as a real-time update can increase the completeness of tumour resection in neuro-oncology [13]; however, there is still difficulty to completely delineate the most infiltrative tumour types. Quantitative ultrasound (QUS) infers properties describing tissue microstructure by using mathematical scattering theory and statistical modelling to model ultrasound interaction with tissue structures [200]. QUS has shown success in identifying cancerous regions including ocular tumours, detecting lymphatic metastases, classifying breast masses, and identifying tumours in the prostate [32][201]. To date, there has been only one report of measurement of attenuation and backscatter coefficients in the human brain and meningioma *in vivo*, with promising results [133]. There has been no report of any of other QUS parameters in any mammalian brain, *ex vivo* or *in vivo*, or tumour for differentiation.

- Clear explanation of research

Scattering arises when ultrasound is incident upon an acoustic inhomogeneity smaller than its wavelength (< 200 microns at 7.5MHz). Tissue constituents, when modelled mathematically, can cause ultrasound to scatter incoherently and the backscattered data can be used to obtain specific parameters (e.g. scatterer size, structure parameters).

The list of quantitative ultrasound parameters that are planned to be measured are as follows:

- Bulk properties - attenuation and backscatter coefficient;
- Echogenicity parameters - moments of the distribution of echogenicity values assigned;
- Spectral parameters of US signals received - Lizzi parameters, scatterer size and acoustic concentration
- Statistical parameters - Nakagami parameters, scatter clustering parameters, homodyned K-distribution parameters

Direct examination and machine learning will be used to determine whether any combination of these parameters can differentiate glioma from healthy tissue.

- Potential benefits

A short-term benefit of this research is to allow the first application of QUS in neural tissue, which will help understanding whether ultrasound scattering in brain tissue can be described by general ultrasonic scattering models.

If key differences are found in the distribution and size of scattering sources in healthy and cancerous neural tissue then a medium-term benefit of this study will be to support trials to study the technique *in vivo*.

Furthermore, a related study is planned to look at the effect of freezing on these QUS parameters. If the results from frozen tissue can be translated to *in vivo* measurements, then a long-term benefit from this study will be improved glioma resection as a result of tissue classification based on real-time QUS imaging, if the hypothesis is proved.

Feasibility/time scale

- A MATLAB framework has already been developed to calculate the QUS parameters from small samples of tissue phantoms.
- The necessary QUS measurements on the glioblastoma tissue will take only one day.
- The data from healthy samples will depend on availability in the Edinburgh Tissue bank and are expected to be available in early 2021.
- Once all the data are acquired, the analysis can begin: various machine learning classifiers will be tested to differentiate the tissue types, with plans to have a manuscript for publication prepared by April 2021.

- **Aims**

The first aim of this study is to measure QUS parameters accurately from small sections of *ex vivo* glioblastoma. This will be achieved by analysing raw ultrasound data scattered back to an ultrasonic array transducer after insonation by plane waves using code written in MATLAB. The second aim is to use these results to test the ability of QUS to differentiate between healthy tissue samples and glioblastoma *ex vivo*. This will be achieved by repeating the measurement process for healthy white matter tissue from another MRC institute

- **Study Design and Methods**

- Inclusion and exclusion criteria

Inclusion: Samples which are histologically verified as being wholly glioblastoma

Exclusion: Samples should have a minimum size of 3 mm x 3 mm x 3 mm.

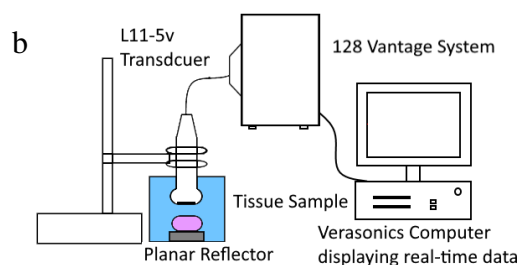
- Methodology - use of tissue

To achieve the aims, we will use a Verasonics research ultrasound system (Vantage 128, Verasonics, Kirkland, WA, USA) (Fig. 1a) to test tissue samples and store unprocessed radio-frequency data from the insonated tissue. Data is acquired first from a reference reflector and then from the tissue sample placed above the reference reflector (Fig 1b). QUS parameters are calculated over 3 mm x 3 mm regions, using a sliding window technique for the entire tissue volume, with digital signal processing

code written in MATLAB. The sliding window technique will allow maximum data acquisition for the small tissue volume, which will reduce variance in the QUS parameters. The measurements will be made with a probe operating at conventional medical ultrasound frequencies (L11-5 MHz) and with one operating at high frequency (L35-16 MHz) to probe smaller acoustic inhomogeneities in the tissue. Average estimates will be obtained for each sample by conducting multiple data acquisitions for each scan (100 averages). Then these scans will be repeated over the entire tissue region to obtain the estimates over a different acoustic path in the tissue. At least 20 different 'slices' through the tissue volume will be used to ensure the estimates obtained from limited tissue sizes still have the statistical power to carry out this research



Fig. 1 Verasonics Vantage system with 5 - 11 MHz probe



Experimental Set-up for data acquisition from tissues

- Justification for sample size
In order to obtain an accurate statistical representation of ultrasound scattering in tissue, the region studied should be at least 10x the wavelength of ultrasound in the medium [26]. This corresponds to around 3 mm in brain tissue at the lowest ultrasound operating frequency. The heterogeneous nature of both brain and brain tumour means there could be high inter-sample variability in the QUS measurements. Therefore, ten samples are requested to ensure there is sufficient data to train and test a machine learning classifier.
- **Analysis**
Using the sliding window technique, repeated measurements and different orientations of the sample we will maximise the amount of QUS data from each sample. Both intra- and inter- sample variability will be assessed by first preparing a Q-Q plot to confirm that the results are normally distributed for each QUS parameter, followed by the appropriate hypothesis test.

The ability of the binary classifier to correctly identify whether a result comes from a healthy sample or glioblastoma will be analysed using 80% of the results for training and 20% for testing. The accuracy of the predicted class will be

determined by generating a confusion matrix and calculating the area under the receiver operating characteristic (ROC) curve [140].

- **Publication**

This study will include novel research in the field of QUS in neuro-oncology and will advance the topic of real-time tissue differentiation significantly. A reviewed journal paper detailing the ability of QUS to differentiate high grade glioma and healthy brain tissue *ex vivo* will be prepared for publication in a high-impact technology journal such as IEEE Transactions on Medical Imaging (IF 9.7) or a specialised journal such as Ultrasound in Medicine and Biology (IF 2.5).

- **Further Work**

This *ex vivo* trial is the first step toward *in vivo* application. Another study is planned to compare QUS measurements *in vivo*, *ex vivo* and in tissue that has been frozen to study the extent at how the QUS parameters change in these three situations. This will be done on healthy ovine or porcine brain tissue. Depending on the results, we plan to move towards an *in vivo* human trial in 2022, with data obtained from ultrasound scans on patients' brains during neurosurgery.

APPENDIX IV: Ethical Approval Letter



Hannah Thomson
James Watt School of
Engineering James Watt
South Building Engineering
Way, University Avenue
Glasgow
G12 8QQ

UK BRAIN ARCHIVE
INFORMATION NETWORK
Director: Prof James AR
Nicoll Deputy Director:
Dr David Hilton email:
brainuk@soton.ac.uk
Phone : +44 23 8120
8560
www.brain-uk.org

11th December 2020

Dear Hannah (cc: Prof Cochran),

BRAIN UK Ref: 20/013 Quantitative Ultrasound Differentiates High Grade Glioma and Healthy Brain Tissue ex vivo

After review of the information provided by you, I am pleased to inform you that the above study has been granted approval by BRAIN UK. As this study conforms to the criteria laid down by the South Central – Hampshire B Research Ethics Committee (REC) it may proceed under the generic Ethical Approval given by this REC. A copy of these acceptance criteria is attached for your information and records.

I will forward the contact details for Participating Centres that are able to potentially provide you with tissue for your study once they have confirmed their participation. Please note that you must register your study with the relevant Research and Development office prior to being able to obtain tissue from any of these sites.

Please note that you must obtain separate ethical approval for any cases obtained outside of BRAIN UK.

Once you have received the tissues, please email brainuk@soton.ac.uk confirming the lab numbers and supplying centre/s of the received samples. This allows us to enhance the service both in terms of improving the sample information held within BRAIN UK and by encouraging collaboration amongst researchers using similar samples. We will not share any details but may highlight that other research is being done either on the same samples or in the same area of research in order for you to consider if collaboration is appropriate.

Additionally, you are also obliged to provide BRAIN UK with annual updates concerning the progress of your study and to deliver evidence of the conclusion of your study. Any material published as a result of the use of tissue derived via BRAIN UK must also be acknowledged accordingly. Please do not feel that you must wait until the annual report to tell us about any publications or research output for this study; you can email details to brainuk@soton.ac.uk at any time and we will include these within a pre-filled annual report for your convenience.

Further information regarding these obligations is covered in greater detail in the attached Terms and Conditions which you have agreed to abide by. If you have any further questions or

require further clarification then please do not hesitate in contacting BRAIN UK.

We would like to thank you for using BRAIN UK and we would like to wish you every success with your current and future research undertakings.

Yours sincerely,

Prof. James A R
Nicoll BRAIN
UK Director

Mailpoint 825, Level F, Laboratory and Pathology Block, Southampton General Hospital, SO16 6YD

APPENDIX V: Research Protocol: Reference free QUS in GBM patients



Research Protocol – Quantitative Ultrasound in Neuro-oncology

Hannah Thomson , Prof. Sandy Cochran and Dr Mohammed Draz

Title: Reference Free Quantitative Ultrasound for Intraoperative Brain Tumour Identification

Chief Investigator:	Hannah Thomson , PhD Student, University of Glasgow h.thomson.3@research.gla.ac.uk , xxxxxxxxxxxx
Investigators:	Professor Sandy Cochran , University of Glasgow Sandy.Cochran@glasgow.ac.uk Dr Mohammed Draz , Queen Elizabeth University Hospital
Funder:	European Research Council (EPSRC) Stryker Medical Devices

Lay Summary

During brain tumour removal surgery, the high quality MRI images become out of date as the brain moves during the operation[7]. Ultrasound is routinely used as a real-time imaging technique to locate the tumour accurately, however, it can be difficult to see the boundaries of the tumour clearly using conventional ultrasound images. The speckled appearance of an ultrasound image is caused by scattering within the tissue when ultrasound interacts with tissue microstructure. These speckled patterns may be difficult for humans to interpret, but it is hypothesised that a computer could analyse the images and detect differences in the speckled pattern between healthy and cancerous regions. If a large number of images are used, the computer could learn to classify regions of the image into healthy and cancerous areas in almost real time, to provide valuable information to help the neurosurgeon detect any residual tumour. This would maximise the amount of tumour safely removed and improve patient prognosis.

Introduction

Rationale

Ultrasound is a useful real-time imaging modality used to localise the brain tumour after craniotomy. A real-time image is needed due to brain shift, where the high resolution MRI images become out of date as the surgery proceeds, meaning it can be difficult to localise the tumour using the registered images alone[97]. However, the resolution of ultrasound images is less than MRI, and particularly in glioma cases, the lack of acoustic contrast

between healthy and cancerous tissues means ultrasound fails to clearly depict the margins of the tumour [100]. There is the need for a high resolution imaging tool which can detect cancerous regions of tissue intraoperatively to improve the extent of resection and hence patient prognosis [6].

Background

Ultrasound is completely safe to use directly on the human brain with commercial equipment and has been shown to aid tumour differentiation and improve the extent of tumour resected in brain tumour surgery[4-5], however fails to clearly depict glioma margins after surgery proceeds.

Ultrasound images typically have a grainy structure to them, and these patterns arise from scattering in tissue, when ultrasound encounters an acoustic boundary of a size smaller than its wavelength [60]. Tissue can be modelled mathematically in terms of scattering sources, such as cell nuclei, and surrounding material. The scattering of ultrasound in soft tissues has been studied extensively and parameters relating to tissue microstructure can be found which hold valuable diagnostic information [25]. The concentration of scatterers in cancerous tissue is hypothesised to be higher than that of healthy tissue, and these parameters can be used into a machine learning algorithm to characterise tissue. So far it has shown success in differentiating healthy and cancerous tissue of different types, such as ocular tumours [23], breast masses [32] and prostate cancer detection [39]. The raw ultrasound data is needed to relate the tissue to the theoretical background, however a preliminary study into the ability of ‘reference-free’ quantitative ultrasound would be extremely valuable for this field. This is where the images alone can be used to define regions of interest, conduct a statistical analysis on the pixel values of the regions, and detect patterns which the human eye cannot in order to classify the tissues. This would involve obtaining a large data set of ultrasound images of glioma tumour intraoperatively, before surgical resection, to train a classifier to detect which speckled patterns in the image correspond to the cancerous tissue, and which are healthy. The ability of the classifier will be assessed by using 80% of the data obtained to train and the remaining data to test. The surgeons initial label of the tumour region will be used as ground truth.

Potential risk and benefits

This study will add no additional risk to the patient to carry out as we are obtaining ultrasound images prior to tumour resection, and after craniotomy, which is already routine practice. Yet, it would be extremely valuable as it is the first test of reference free quantitative ultrasound to detect brain tumours. The long term benefits, based on the results of this study, would be the development of a tool which can accurately detect residual tumour intraoperatively, allowing a larger percentage of tumour to be removed, which improves patient prognosis in both low and high grade glioma [5].

Aims and Objectives

The aim of this study is to assess the ability of quantitative ultrasound and machine learning classification to correctly identify cancerous glioma tissue using a data set of B-mode images from 30 glioma patients.

The objectives required to meet this aim are:

- Obtain at least 10, high quality ultrasound B-mode images, from glioma patients before tumour resection with identical system settings in each case.
- Carefully label, with help from attending neurosurgeon, the image of regions of healthy neural tissue, oedema, and tumour.

- Use this information to train a machine learning classifier, based on the statistics of the pixel values in the labelled regions.
- Form classification images from these results, where regions which are likely to be cancerous are clearly identified.

Methodology

Equipment

This study will use the BK flex Focus 800 ultrasound machine with the craniotomy 8862 probe operating between 4 and 10 MHz, which is currently used in the neurosurgical theatre as shown in Figure 1.



Figure 1: BK Flex Focus Ultrasound Machine (left) with craniotomy probe (right).

The system settings (gain, dynamic range, focus, brightness) must be identical over all participants. These settings can be saved onto the BK system as a custom pre-set named ‘HTOncologyStudy’ to allow this imaging mode to be easily switched to in the operating theatre, while keeping all settings identical.

Data Acquisition

During glioma removal surgery, the neurosurgeon will use the BK machine with this pre-set to localise the tumour as is the standard practice after craniotomy. A clean image will be taken, allowing them to identify the region most likely to be cancerous on the B-mode image and an annotated image will also be saved which clearly labels the glioma tissue. Each image acquisition should take no more than 30 seconds. This will be repeated 10 times, to image the tumour from different locations and angles, and to allow a larger training data-set while still causing minimal disruption to the surgery.

Anonymisation of Data

The image data set held on the BK machine will be given an anonymous ID based on case type and the date. The data will then be transferred to a University of Glasgow PC to allow data analysis to take place.

Inclusion/ Exclusion criteria

This study will include all adult cases of low and high grade glioma tumour removal surgery where the craniotomy scheduled is greater than 3cm x 1cm to allow the use of the BK Craniotomy 8862 probe over a 3-4 month period. Metastasis and meningiomas will not be considered in this study as they are generally more encapsulated, whereas the real

value would come from the more invasive nature of glioma. The proposed number of cases is 30 to allow a full assessment of the potential of this technique and based on the report from last year's surgeries this is a viable number of cases to occur over a 4 month timeframe.

Data Processing

The images will be divided into regions of 1mm x 1mm, corresponding to 10 pixels by 10 pixels. These 100 pixels will be analysed and the statistical distribution which describes the intensity values will be modelled to determine parameters for binary classification. 80% of the images will have labels ('Healthy' or 'Cancerous') associated to the pixels, and this information will be used to predict the cancer likelihood map on the remaining 20% of the images.

Safety considerations

Imaging will be carried out using a commercial ultrasound system operating at acoustic powers which cause no additional damage to humans. The only safety consideration is the time taken to acquire the images, if we are advised there is any potential risk to the patient by taking the five minutes to acquire the data, then this patient will not be included.

Statistical considerations

The ability of this technique to detect glioma tissue in a conventional ultrasound image will be tested by training with 80% of the data and testing with 20%. For the study to have statistical power, it would be ideal to have 5 images to test the classification algorithm. This corresponds to 25 cases minimum, and the requested sample size is 30. The method of analysis, to find the accuracy of the classification results, is determined by generating a confusion matrix and calculating the area under the receiver operating characteristic (ROC) curve [140].

Funding

This study will be part of the final year experiments of Hannah Thomson's PhD project at the University of Glasgow entitled 'Ultrasonic Differentiation of Healthy and Diseased Neural Tissue' and is fully funded, with budget allowance, until June 2022 by the European Research Council and Stryker Medical Devices (award reference number 00395278). This study requires no additional equipment or software to carry out, therefore no additional costs are anticipated.

Expected Outcomes of the Study

This study will include novel research in the field of QUS in neuro-oncology and will advance the topic of real-time tissue differentiation significantly. A reviewed journal paper detailing the ability of QUS to differentiate high grade glioma and healthy brain tissue *ex vivo* will be prepared for publication in a high-impact technology journal such as IEEE Transactions on Medical Imaging (IF 9.7) or a specialised journal such as Ultrasound in Medicine and Biology (IF 2.5). Further to the publication arising from this work, the study will indicate if there is potential for an intraoperative tool which can be trained in real-time to allow a patient specific imaging device which can aid neurosurgeons in the decision of healthy or cancerous tumour. The long term benefits, such as greater extent of tumour resection and improved prognosis for glioma patients, could be possible with some further work in this field, thanks to this study which was the first assessment of QUS for cancer detection in glioma patients.